UNIVERSITY OF SOUTHAMPTON

FACULTY OF NATURAL AND ENVIRONMENTAL SCIENCES

School of Chemistry

Sol-gel preparation of solid and porous films of titanium oxide and metal titanates

By

Wafa Shamsan Al-Arjan

Thesis for the degree of Doctor of Philosophy

October 2015

UNIVERSITY OF SOUTHANPTON

ABSTRACT

FACULTY OF NATURAL AND ENVIRONMENTAL SCIENCES

CHEMISTRY

Doctor of Philosophy

SOL- GEL PREPARATION OF SOLID AND POROUS FILMS OF TITANIUM OXIDE AND METAL TITANATES

By Wafa Shamsan Al-Arjan

TiO_2 films and powders have been synthesised using sol-gel methods with a number of sol formulation, including $Ti(O^iPr)_4$ and $Ti(O^nbu)_4$- based sols modified with diethanolamine (DEA), and a $Ti(O^iPr)_4$ based sol with HCl-catalyst. Mass spectrometry (MS) and nuclear magnetic spectroscopy (NMR) were used to interrogate the species present in solution.

$BaTiO_3$ and $Bi_2Ti_2O_7$ films were prepared using sols based on titanium alkoxides, acetic acid, acetylacetone and methoxyethanol with simple barium or bismuth salts.

Mesoporous TiO_2, $BaTiO_3$ and $Bi_2Ti_2O_7$ films were prepared using different block copolymer templates and a hard template route based on carbon infiltration into MCM-41 mesoporous silica was investigated.

Tetragonal $BaTiO_3$ and pyrochlore $Bi_2Ti_2O_7$ inverse opal films were synthesised by using 500 nm PS spheres as a template.

DECLARATION OF AUTHORSHIP

I, ……Wafa Shamsan Al-Arjan……., declare that the thesis entitled 'Sol-gel preparation of solid and porous films of titanium oxide and metal titanates" and the work presented in the thesis are both my own, and have been generated by me as the result of my own original research. I confirm that:

☐ this work was done wholly or mainly while in candidature for a research degree at this University;

☐ where any part of this thesis has previously been submitted for a degree or any other qualification at this University or any other institution, this has been clearly stated;

☐ where I have consulted the published work of others, this is always clearly attributed;

☐ where I have quoted from the work of others, the source is always given, this thesis is entirely my own work;

☐ I have acknowledged all main sources of help;

☐ where the thesis is based on work done by myself jointly with others, I have made clear exactly what was done by others and what I have contributed myself;

☐ this work was presented in a number of conferences:

1. Solid State Chemistry Group Christmas Meeting 2011, Department of Chemistry, University of Liverpool, UK.
2. 6th Saudi scientific international conference 2012 at the Brunel University.
3. Electrochem 2013 at Southampton, UK.
4. Nanotechnology 2013 at University of Birmingham, UK.
5. 11th International Conference On Materials Chemistry (MC11)2013 at University of Warwick, UK.
6. 7th Saudi student conference 2014 at the Edinburgh University, UK.
7. 65th Annual Meeting of the International Society of Electrochemistry 2014 at Lausanne, Switzerland.
8. 8th Saudi student conference 2015 at Queen Elizabeth 11 Conference Centre in London, UK.
9. E-MRS 2015 Spring Meeting at Lille Grand Palais, France.

☐ part of this works has been published as:

Sol-gel preparation of well-adhered films and long range ordered inverse opal films of $BaTiO_3$ and $Bi_2Ti_2O_7$.

Wafa S. Al-Arjan, Mohammed M. F. Algaradah, Jack Brewer and Andrew L. Hector. *Mater. Res. Bull.*, 2015.

☐ during my PhD study I received 5 awards from Saudi Cultural Berue from 2011- 2015.

ACKNOWLEDGEMENTS

I would like to thank several people for supporting me in the last four years of my Ph.D. First of all, I extend great thanks to my supervisor Prof. Andrew L. Hector who has spent a massive amount of time on the project. During the time that I have spent in his group, he has provided me with intensive supervision, considerable time to discuss the results and valuable suggestions. At the end of my Ph.D. period I feel that I have acquired several skills from him, especially the organisational skills and the ability to solve problems. I am very lucky to have had the opportunity to work with him.

I would like to thank my co-supervisor Prof. Gill Reid for her useful feedback in the transfer report.
I would like to thank Prof. Bill Levason for his help in solving NMR problems.
I would like to thank Mr. Alistair Clark for his help with the SEM instrument.
I would like to thank my project student Jack Brewer for his commitment in the lab.

Also take this opportunity to gratefully thank King Abdullah bin Abdulaziz for giving me the scholarship to carry on studying of the higher education, as well as thanks to the University of King Faisal for the job opportunity to work with them.

Thanks to the members of the group and lab-mates, Imran, Mahboba, Li and Calum and new postdoc, Andy for their useful discussion and having fun during my study. Also I would like to thank people who helped me in level 3(organic department).

It is with a feeling of great pleasure that I would like to express my most sincere heartfelt gratitude to my dad Shamsan for his love and accompanying me during my study, as submitting this thesis would have been a Herculean job, without the constant help, encouragement, limitless support, mentally and financially from him. I would like to specially thank my mum, Fatimah for encouraging and keeping me in good spirits. Even far away from them, their loves make me never feel lonely and helpless. I would like to dedicate this thesis solely to them.

I should also thank Dr. Mohammed Diaa for advising in the pursuit my Ph.D. and helping me to be relaxed and be in a good mood all the time.

I would like also express my sincere thanks to my brothers, Teacher Adel, Eng. Abdullah, Eng. Khaled, Teacher Mohammed and my younger brother Abdualziz, and my lovely sisters Seham and Nouf for their tremendous support, love, patience and understanding. My special deepest feeling and thanks go to my lovely niece, Sadeem for having fantastic and fun time with her when I travelled to Saudi Arabia with always reminding me to keep smiling without stress. So, special thanks to my brothers Adel and Abdullah.

I would like to thank all my friends and especially, Sybrriah, Eman and Muna for their love, support and having fun during my Ph.D. study and special thanks to my friend Sahra who accompanied and supported me when I needed her, and I will miss her when I go back to my home country. I really thank them. Also, I would like to thank all my friends in Saudi Arabia specially, Fatimah Al-Amer.

To my parents

ABBREVIATIONS

Methylene blue	MB
zirconate titanate	PZT
Dynamic random access memories	DRAMs
Bismuth zinc niobate	BZN
Metal organic chemical vapour deposition	MOCVD
Hexadecyl-trimethylammonium bromide	CTAB
Critical micelle concentration	CMC
Three dimensional	3D
Polystyrene	PS
Polymethyl methacrylate	PMMA
X-ray diffraction	XRD
Scanning electron microscopy	SEM
Nuclear magnetic resonance spectroscopy	NMR
Mass spectrometry	MS
Powder X-ray diffraction	PXD
Grazing incidence X-ray diffraction	GIXRD
Grazing incidence small angle X-ray scattering	GISAXS
Electron dispersive energy X-ray spectroscopy	EDX
Electrospray ionisation	ESI
Tetramethylsilane	TMS
Acetylacetone	acac
Diethanolamine	DEA
Pluronic surfactant	P123
Evaporation induced self-assembly	EISA
Saturated calomel electrode	SCE
Cyclic voltammogram	CV
Two dimensional	2D
Ultra violet	UV

FIGURES

TABLES

CONTENTS

1. Introduction

1.1 The sol-gel method

The sol-gel technique can produce a variety of different morphologies such as dense monoliths, fibres, films and mesoporous structures and nanostructured materials. Its advantages include simplicity, low equipment cost, low consumption of energy, and large area coatings on various substrates including glass. It provides homogeneity, reproducibility and the optical characteristics (transparency).[1] The products can be used for photocatalytic,[2] optical, electrical, catalytic,[3] capacitance[4] and solar energy conversion[5] applications.

The sol-gel process consists of a series of steps: hydrolysis, condensation, gelation, ageing and drying. It is based on the formation of a colloidal suspension of particles (sol) and gelation of the sol to form a three dimensional solid network in a continuous liquid phase (gel). The mechanism[6] (Fig. 1.1) typically involves the hydrolysis of a metal precursor such as $[M(OR)_4]$ (R = Me, Et or Pr and M = metal) followed by condensation to form polymeric particles containing M-O-M linkages. The reaction takes place either in a base or an acid-catalysed process, which promotes the rates of reactions drastically and also, supplies a particular degree of control over the structural properties of the sols.

a) Hydrolysis:

$$M(OR)_X + H_2O \longrightarrow M(OR)_{X-1}(OH) + ROH$$

b) Condensation (water elimination):

$$2M(OR)_{X-1}(OH) \longrightarrow M_2(OR)_{2X-2} + H_2O$$

c) Condensation (alcohol elimination):

$$2M(OR)_{X-1}(OH) \longrightarrow M_2(OR)_{2X-3}(OH) + ROH$$

Fig.1. 1 Hydrolysis and condensation of metal tetra-alkoxides.

The hydrolysis reaction mechanism in both cases follows nucleophilic substitution, which requires a penta-coordinated intermediate. Water is a poor nucleophile and thus the reaction can be sterically hindered. In reaction (a), the hydrolysis can be performed by replacing the alkoxide group with OH group from water. Reactions (b and c) show polymerization by condensation. Two partially hydrolyzed molecules can be linked together by condensation eliminating small molecules (e.g. water or alcohol). This type of reaction can continue forming larger and larger molecules by polymerization to 3D structures. The condensation reactions are dependent on the pH.

However, as with acid catalysis, highly cross-linked systems are produced, whereas under basic catalytic conditions dense particles are formed (Fig. 1.2). Thus, the reaction conditions (acid or base) can be modified to control the properties of the produced materials (gel or sols).

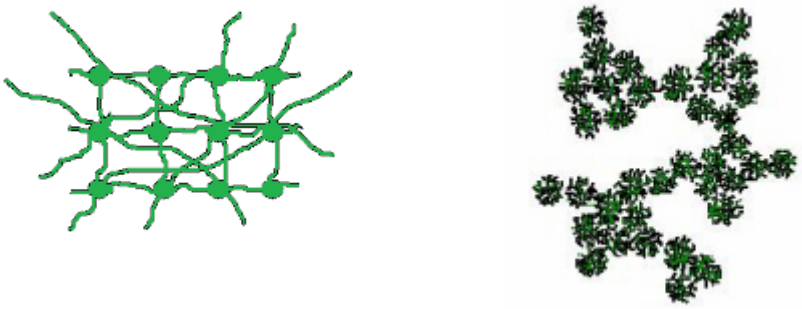

Fig.1. 2 The products of acid-catalysed (left) and base-catalysed (right) condensation.

The viscosity is increased as more linkages form until the gelation point, when a high viscosity gel extends across the container supporting the solvent, and a series of chemical and physical changes then occur due to further increases in cross-linking via trans-pore condensation reactions of pore surface hydroxide groups.

During the aging process further cross-linking takes place in the gel which forms a more robust gelled sample. Finally, gels are dried and then many stages can be distinguished during the liquid evaporation.[7] The loss of the solvent through ageing takes place by expulsion of the liquid from the gel. After this process has completed, solvent trapped within the pore structure can be lost through normal evaporation. If the gel is still soft, it will contract in proportion to the volume of the solvent that evaporates. After ageing and drying the gelled sample becomes strong enough to counter further shrinkage. Cracking of the gel network can occur due to capillary stress resulting from the surface tension of the solvent in the small pores of the gel. Powders can be produced by conventional evaporative drying processes. Eventually, pyrolysis techniques take place to densify the materials for the production of dense glasses and ceramic materials and remove the remaining substituent groups from the original precursor.[7]

1.2 Sol-gel chemistry for TiO_2

Sol-gel methods have been used to produce oxide materials with controlled shapes and sizes on all length scales. In addition, micro- and meso-porous materials with high effective surface areas and small pore sizes with a narrow size distribution can be achieved.[8]

Different processing routes based on sol-gel chemistry can produce a variety of materials as demonstrated in Fig. 1.3. From the sol, powders can be obtained by spray-drying, fibres spun or drawn and coating techniques such as spin-or dip-coating can be used to generate films.

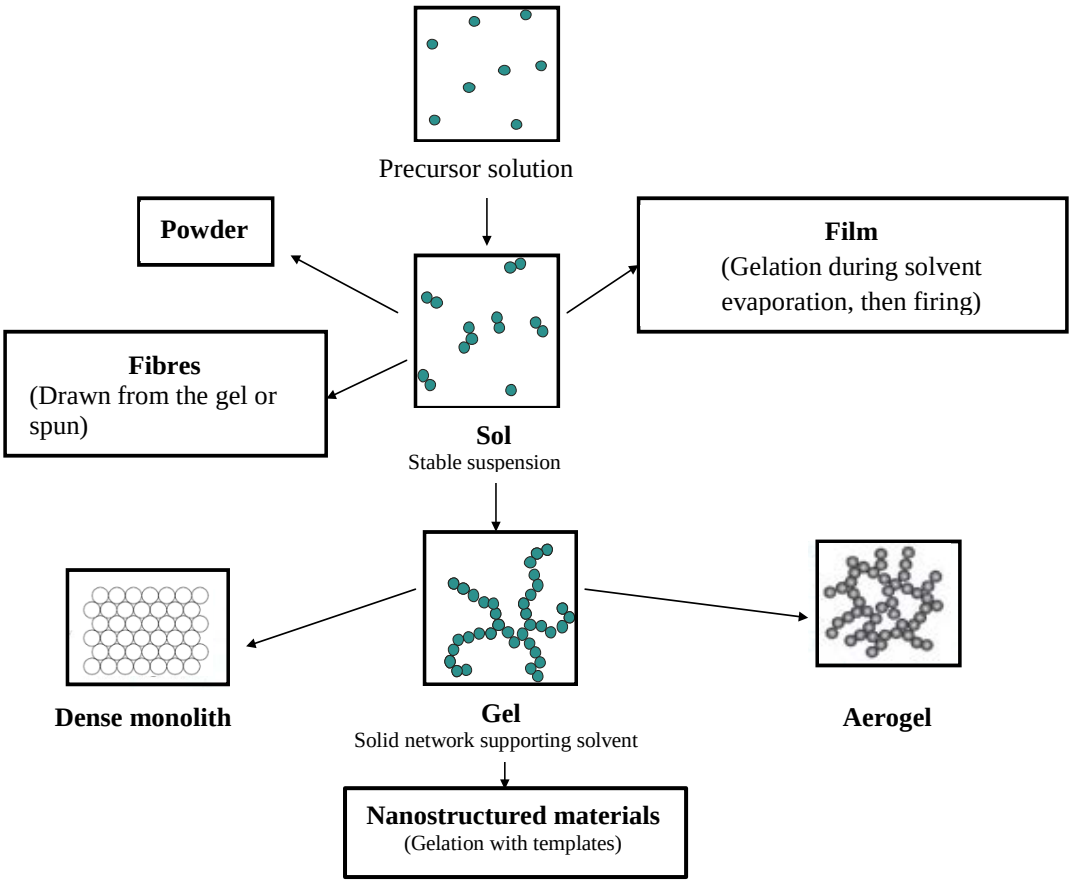

Fig.1. 3 Processing routes to different forms using sol-gel method.

1.2.1 Titanium dioxide (TiO_2)

TiO_2 exists in three forms: rutile, anatase and brookite and all have six-coordinated titanium.[1, 9] Anatase and rutile phases have been obtained in this study. Anatase and rutile have the same tetragonal symmetry in spite of possessing different structures.

The structure of rutile (Fig. 1.4) is based on octahedra of titanium oxide which share two edges of the octahedron with other octahedra to create chains and the chains themselves are set into a four-fold symmetry. In an anatase (Fig. 1.5) the octahedra share four edges and create a fourfold axis. Rutile is known to be the most thermodynamically stable phase of TiO_2. At higher temperature (T > 600 °C) the metastable anatase and brookite phases convert directly to rutile.[10]

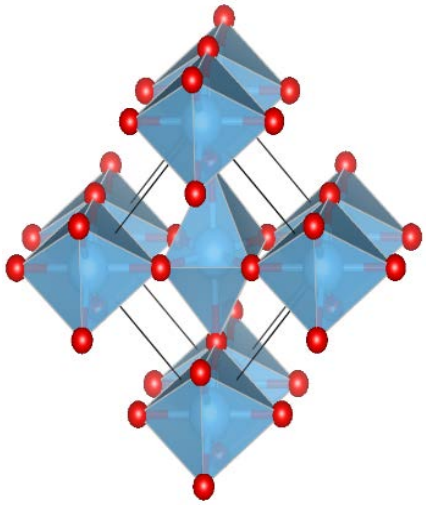

Fig.1. 4 Structure diagram of rutile TiO_2 showing the unit cell (tetragonal, space group P42/mmm). The structure with distorted TiO_6 octahedra, edge and corner sharing.

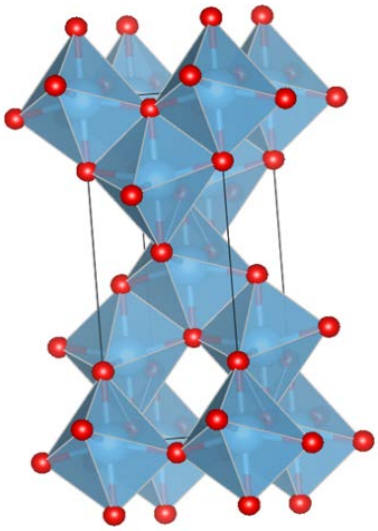

Fig.1. 5 Structure diagram of anatase TiO_2 showing the unit cell (tetragonal, space group $I4_1/amd$). The structure with distorted TiO_6 octahedra, all edge sharing.

1.2.2 Applications of titanium dioxide

TiO_2 is a very useful semiconducting transition metal oxide material and it provides materials with a variety of product morphologies and surface area for industrial applications. It is part of our everyday life in cosmetics, foods and drugs. In particular, it is widely used as a white pigment in paint due to its high refractive index and strong light scattering. TiO_2 exhibits unique characteristics for various applications due to its resistance to photochemical and chemical corrosion, and its chemical inertness and its photocatalytic activity as well low cost, easy handling and nontoxicity.[11]

1.2.2.1 Photovoltaics

Photovoltaics can achieve the direct conversion of light into electricity. Some materials display a property of photoelectric effect that leads them to absorb photons of light and release electrons. When these free electrons are captured, electric current is produced and can be utilised as electricity.

Photovoltaic cells are also known as solar cells. A novel solar cell concept using dye-sensitized nanocrystalline TiO_2 films and an iodine/iodide electrolyte was published by Grätzel in 1990s.[12, 13] By using dye-sensitized TiO_2 films, the power conversion efficiencies out of 10-12% reached, this is analogous to conventional solar cells based on amorphous silicon.[14] Pichot et al.[15] obtained a photocurrent density of 2 mA cm^{-2} by using 1 μm thick TiO_2 films. Kashyout et al.[14] studied the influence of preparation conditions on the solar cell performance of TiO_2 nanoparticles prepared using a sol-gel technique. The authors observed the efficiency of the solar cell was increased with an increase in the temperature, and that the photocurrent was increased from 8.9 mA cm^{-2} to 14.9 mA cm^{-2} with $TiCl_4$ treatment.

1.2.2.2 Photo-catalysis

Photocatalysis relies on the interaction of electrons and holes in semiconductor materials. TiO_2 films and nanoparticles can be used for the photocatalysis process; however the films have an advantage over the nanoparticles due to easier photocatalyst separation from reaction mixtures. Xagas et al.[16] demonstrated that the photocatalytic activities of TiO_2 thin films towards the degradation of 2, 4-dichlorophenol in acidic aqueous solutions are strongly dependent on their synthesis conditions. Murugan et al.[17] showed the best photocatalytic activity on degradation of methylene blue (MB) by using an optimum ratio of anatase to rutile phase content of TiO_2 film.

1.3 Dielectrics

Dielectric materials are electrical insulators and offer very large resistance to the flow of electric current. However, the most important property of dielectrics is that they can be polarized under the action of an externally applied field. The idea of dielectric polarization was raised for the first time by Faraday. The magnitude of polarization (P) is directly proportional to the intensity of the electric field, E.[18]

$$P = \varepsilon_0 \chi_e E \qquad (1.1)$$

where χ_e is the electric susceptibility which is defined as a constant of proportionality and is a dimensionless quantity, ε_0 is the electric constant of free space and the E is the total electric field.

In a linear dielectric, the electric displacement (D) is related to E and P and given as:

$$D = \varepsilon_0 E + P \qquad (1.2)$$

$$= \varepsilon_0 E + \varepsilon_0 \chi_e E \qquad (1.3)$$

$$= \varepsilon_0 (1+\chi_e) E \qquad (1.4)$$

And therefore, P and D are proportional to E:

$$D = \varepsilon E \qquad (1.5)$$

Where $\varepsilon = \varepsilon_o (1+\chi_e)$ (1.6)

where ε is called the dielectric constant of the material. In the case of a vacuum, there is no matter to polarize, so the susceptibility χ_e is zero and the dielectric constant is equal to ε_0. The relative permittivity (ε_r) can be written as:

$$\varepsilon_r = (1+\chi_e) \qquad (1.7)$$

By substituting the value of ε_r from equation (1.7) in (1.6):

$$\varepsilon_r = \varepsilon / \varepsilon_0 \qquad (1.8)$$

And hence, ε_r is known as the dielectric constant of a material and is a dimensionless quantity.

1.4 Ferroelectricity

Ferroelectric materials have no linear polarization correlation between the polarization and the external electric field. Ferroelectricity is explained by reorientation of polarization by an external electric field and was first discovered in 1921 by Valasek, in Rochelle's salt (potassium sodium tartrate) and potassium dihydrogen phosphate.[19]

Examples of the more common significant materials that exhibit ferroelectric properties, include: barium titanate ($BaTiO_3$),[20] lead titanate ($PbTiO_3$)[21] and lead zirconate titanate (PZT).[22]

When the ideal dielectric material is subjected to an electric field, there is no long-range movement of charge, however some rearrangement of charge occur leading to a dipole moment and then the material is polarised. This process is named spontaneous polarization in which the polarization occurs in the absence of the external electric field. However, in the presence of the external electric field a reorientation of the polarization is produced. These two cases are essential in a material to classify it as a ferroelectric.[23]

The spontaneous polarization changes with temperature. There is a specific point recognised as the Curie temperature that marks the transition from a state that is electrically neutral to a spontaneous polarization state. Above the Curie temperature, the paraelectric cubic phase and the crystal is electrically neutral; below the Curie temperature (on cooling), a non-cubic polar-ferroelectric crystal structure is obtained.[24]

1.4.1 Importance of ferroelectric materials

Ceramic ferroelectrics are divided into four main groups depending on their crystal structure, (a) perovskites (e.g. $BaTiO_3$) (b) pyrochlores (e.g. $Bi_2Ti_2O_7$) (c) tungsten bronze materials (e.g. $PbNb_2O_9$) and (d) the bismuth layer-structure group (e.g. $PbBi_2Nb_2O_9$).

The ABO_3 perovskites group is by far the most studied. Most technologically significant ferroelectrics are oxides with a perovskite structure.

1.4.2 Applications of ferroelectrics

Ferroelectric materials enable many modern technologies. Due to their superior properties such as large piezoelectric effects, high pyroelectric coefficient and large dielectric constants, they can be used for a wide range of applications such as sensors,[25] thermal

imaging[26] and dynamic random access memories (DRAMs) with very large scale integration.[27]

Currently there is a huge interest in next generation non-volatile high density random access memories (FeRAM) using a ferroelectric layer instead of the dielectric materials in the DRAMs.[28] Therefore, the data is stored digitally in the direction of the spontaneous polarization. The FeRAM used to build the memory in the capacitor from the ferroelectric materials is sandwiched between two electrodes and then it is connected to the transistors. By applying a suitable voltage to a capacitor in order to switch the remanent polarization between two polarization directions, the function of the memory can be gained. The advantage of this memory is that it is a non-volatile memory, resulting from the ability of the ferroelectric layers to hold the polarization in the absence of an external field. In addition, FeRAMs provide a fast writing speed, high endurance, compatibility with integrated silicon-based semiconductor devices and low operating voltage.[29]

1.5 Barium titanate ($BaTiO_3$), its properties

$BaTiO_3$ is a white to grey powder. It is soluble in different acids, such as hydrofluoric, sulphuric and hydrochloric acids. It is insoluble in alkalis and water. It has five different crystal structures (Fig. 1.6); listing from higher temperature to lower temperature, hexagonal, cubic, tetragonal, orthorhombic, and rhombohedral (all of the structures show ferroelectric behaviour except the hexagonal and cubic phases as they are paraelectric.[30]

Pure $BaTiO_3$ is an electrical insulator. However, it becomes a semiconductor material if doped with small amounts of metals, most commonly scandium, and samarium.[30]

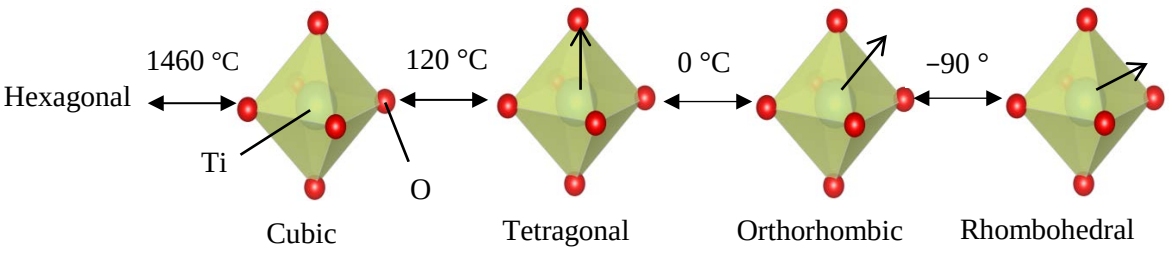

Fig.1. 6 The crystal structures of $BaTiO_3$.

1.5.1 Structure of $BaTiO_3$

$BaTiO_3$ is isostructural with the mineral perovskite ($CaTiO_3$) and is a ternary compound of formula ABO_3 in which the A and B cations differ in size. It consists of a corner-linked network of oxygen octahedra with Ti^{4+} ions of the centre (B sites, smaller) within the octahedral cage and the Ba^{2+} ions (A sites, larger) situated in the interstitial sites created by the linked octahedral (Fig. 1.7). It can be seen that the coordination number of A (Ba^{2+} barium) is 12, whereas the coordination number of B (Ti^{4+} titanium) is 6. In the perovskite structure it is not restricted that the anion is oxygen, as it can be fluoride, chloride, carbide, nitride, hydride and sulphide. The perovskite structure materials give to important roles such as dielectric ceramics.[31]

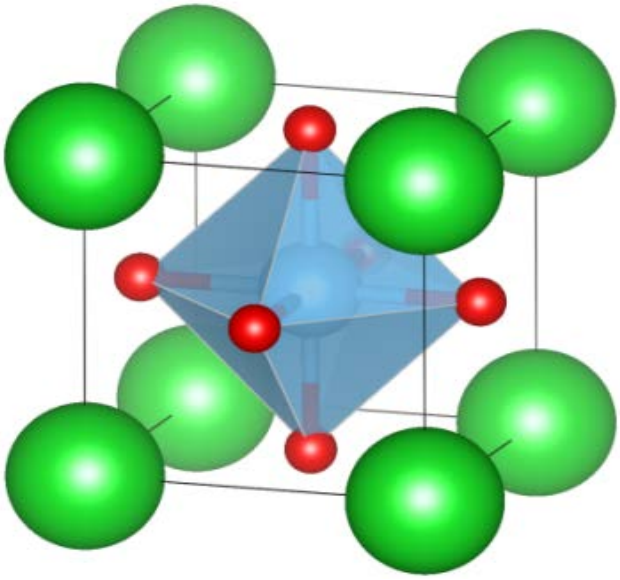

Fig.1. 7 Perovskite ABO_3 unit cell for $BaTiO_3$, where the Ba^{2+} (green spheres), Ti^{4+} (blue sphere) and O^{2-} (red spheres).[32]

1.5.2 Dielectric properties of $BaTiO_3$

The crystallographic dimensions of the $BaTiO_3$ lattice respond to electric field, temperature and pressure. The hexagonal $BaTiO_3$ structure is stable above 1460 °C. On cooling $BaTiO_3$ below 1460 °C, hexagonal phase to cubic phase transformation occurs

with a centro-symmetric space group and hence this phase shows no spontaneous dipole moment (paraelectric). The most important change relating to its dielectric constant is the paraelectric-ferroelectric transition which occurs at the Curie temperature (~120 °C).[33]

Thus above its Curie temperature the unit cell is cubic and below 120 °C the structure is slightly distorted to the tetragonal phase and therefore a dipole moment is obtained. Other transformations occur on cooling close to 0 °C and −90 °C: below 0 °C the unit cell is orthorhombic and below −90 °C is rhombohedral (Fig. 1.6).

When an electric field is applied to these unit cells, the Ti^{4+} ion in $BaTiO_3$ can undergo a significant displacement to a new position along the direction of the applied field and relative to its anionic neighbours. These charge displacements produce a spontaneous polarisation and the high dielectric constants characteristic of ferroelectrics with values depending on the synthesis procedure, purity, density, grain size and temperature.[34]

1.5.3 Applications of $BaTiO_3$

$BaTiO_3$ is commonly used as a ferroelectric material. It is the first piezoelectric transducer ceramic ever developed and is used for microphones resulting from its strong piezoelectric characteristics.[35]
Recently, attention has been shifted from transducer applications (due to its relatively low T_c of 120 °C, which limits its use in high-power transducers) to the major use being in dielectrics for discrete and multilayer capacitors due to its high dielectric constant, low dispersion and wide frequency response for multilayers ceramic capacitors in the thick and thin films form.[36]

The cubic $BaTiO_3$ phase shows high dielectric constant and therefore can be used for multilayer capacitors and integral capacitors in printed circuit boards.[37]

1.5.3.1 $BaTiO_3$ for capacitors

A capacitor consists of a parallel metal plates separated by free space (dielectric materials) such as, air, oil, paper and ceramic. When a voltage is passed across the plates, the charges are created on them and are proportional to the applied voltage (Fig. 1.8).

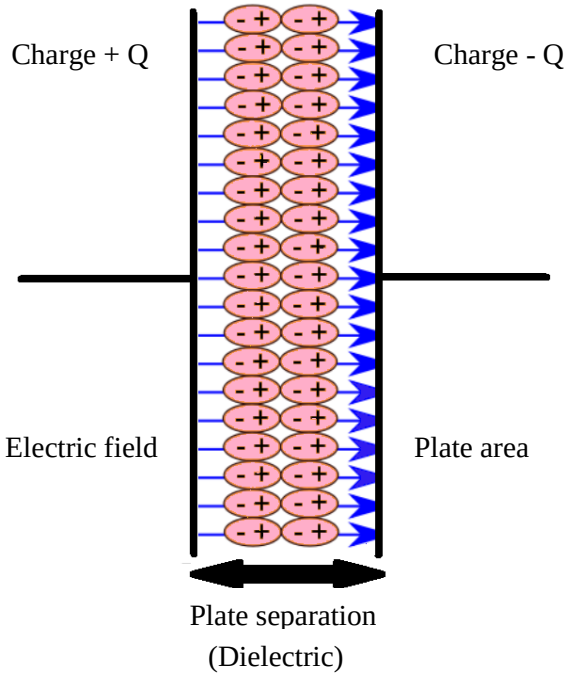

Fig.1. 8 A capacitor construction.

Multilayer ceramic capacitors consist of alternate metal and $BaTiO_3$ ceramic layers, with alternate metal layers connected to a common lead. These are common components in electrical devices and are important in our everyday lives due to their excellent high frequency characteristics, good reliability, high breakdown voltage, low price and high volumetric capacity.[38] The first multilayer capacitors synthesised from polycrystalline $BaTiO_3$ ceramics were released in the early 1950s.[39]

Multilayer ceramic capacitors manufacturers have focused on development of products with smaller size and higher capacitance. Therefore, film manufacture is important.

1.6 Bismuth titanate

Bismuth titanate is a type of a wide band -gap semiconductor with varied crystal structures, such as $Bi_{12}TiO_{20}$ which has been used for photorefractive application.[40] The dielectric pyrochlore phase $Bi_2Ti_2O_7$ has displayed quite promising properties in DRAM capacitor dielectric[41] and ferroelectric Aurivillius phase $Bi_4Ti_3O_{12}$ is utilised for piezoelectric and pyroelectric applications due to its low ε and high T_c.[42]

Stojanovic et al. [43] prepared nano-sized $Bi_4Ti_3O_{12}$ ceramic powders by a mechanochemical method and obtained ~90 % of the electric density. Pinheiro et al.[44] gained denser $Bi_4Ti_3O_{12}$ powders and better electrical properties by modifying the synthesis process. It can be concluded by that the grain morphology may be the factor for improving the electric properties.

1.6.1 Bismuth based pyrochlores

Pyrochlores are a class of material which usually has the ideal stoichiometric chemical composition of $A_2B_2O_7$. It consists of an interpenetrating A_2O' tetrahedral framework with linear bonds (O'–A–O'), corner sharing BO_6 octahedra that links together to create six membered of rings. The six membered rings have six O'- anions also available for bonding with the A cation, so A is overall in a distorted 8-coordinate site (Fig. 1.9).[45]

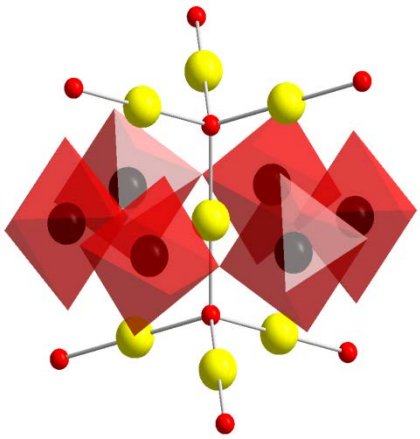

Fig.1. 9 Simplified view of the pyrochlore structure, showing interpenetrating sublattices in a cubic pyrochlore structure of A_2O' and forming a ring of six BO_6 octahedra. BO_6 octahedra (red prism), and A_2O' network (red = O, yellow = A cation).[46]

The ideal cubic pyrochlore structure (Fig. 1.10) adapts the centrosymmetric space group $Fd\bar{3}m$ with face-centered structure. The structure is based on an anion-defective calcium fluorite structure.[47]

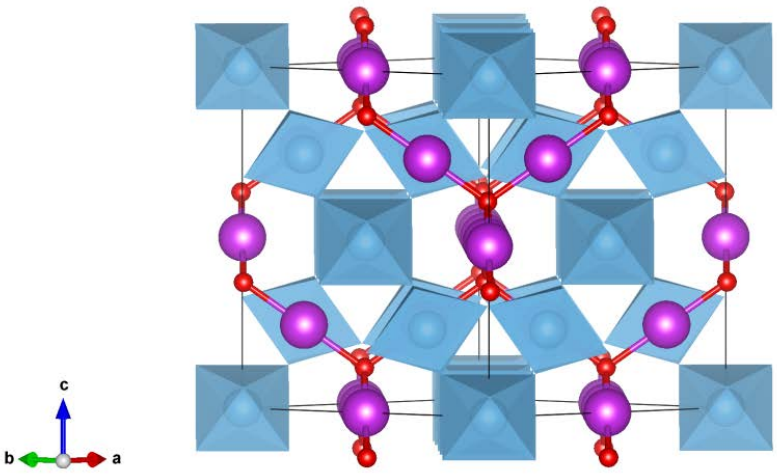

Fig.1. 10 Ideal pyrochlore structure (viewed along the [110] axis (A purple, O' red, and BO_6 octahedra in blue).[48]

Fig. 1.11 shows the fluorite structure and an idealised 1/8 unit cell of pyrochlore, with all the oxygen ions at the same position as the fluorite except in one 8a site. It is obvious that one of the oxygen ion positions that was occupied in the fluorite structure is now missing in the pyrochlore structure.[46]

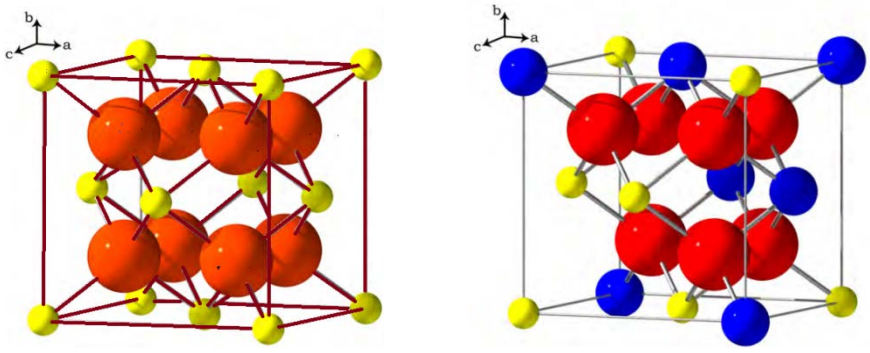

Fig.1. 11 The fluorite structure. Small yellow spheres are B ions; large red spheres are O^{2-} ions (left). The pyrochlore structure ($1/8^{th}$ of the unit cell). Blue spheres = A ions, yellow = B ions and the red spheres are O^{2-} ions (right).[49]

Bi_2O_3–ZnO–Nb_2O_5 (BZN) based pyrochlore ceramics were first studied by Chinese engineers in 1970s for multilayer capacitors[50] and have attracted further attention more recently as they exhibit high dielectric constants, low dielectric losses, and low firing temperatures (below 1000 °C). They are considered as promising candidates for low temperature coefficient of capacitance materials in multilayer capacitors exhibiting high tunability with the electric field. For example $Bi_{1.5}ZnNb_{1.5}O_7$ crystallizes in the cubic pyrochlore structure.[51]

It has been reported that the high dielectric constant and low-temperature dielectric relaxation are shown by pyrochlore phase due to the local hopping of Bi atoms and O' positions from the ideal pyrochlore arrangement. The random distribution of Zn atoms between Bi and Nb sites leads to non-uniform fields which contribute to the dielectric relaxation. Therefore, the dielectric constant of BZN has been calculated as 80 – 150.[52] Substitution of Ti atoms to the B sites in BZN leads to a massive increase in the dielectric constant as it is increased linearly from 150 to 200 with increasing the titanium concentration.[51] $Bi_2Ti_2O_7$ is the most promising of other bismuth based pyrochlores compounds due to the larger disordered Bi^{3+} displacements (0.43 Å)[46] in comparison to BZN (0.39 Å).[53]

Bismuth based pyrochlores ($Bi_2Ti_2O_7$), have been attracting interest for many applications such as ceramic capacitors and dynamic random access memories, due to their high dielectric constants. These useful applications have been proposed due to the substantial displacive disorder of Bi cations of pyrochlores and this displacement takes place away from the center of the six membered rings (Fig. 1.12).

Displacement of Bi and (O') atoms off the ideal pyrochlore sites is predominantly due to the Bi active lone pair.[52] Nino et al.[54] showed in calcium titanium niobate ($Ca_{1.47}Ti_{1.47}Nb_{1.04}O_7$) that pyrochlores can exhibit dielectric relaxation even in the absence of a highly polarizable Bi atoms or a lone-pair, as well in the absence of cation substitution such as Bi_2InNbO_7.[55] The other mechanism proposed for displacement is the relief of metal under-bonding. The precise explanation in $Bi_2Ti_2O_7$ remains unclear.

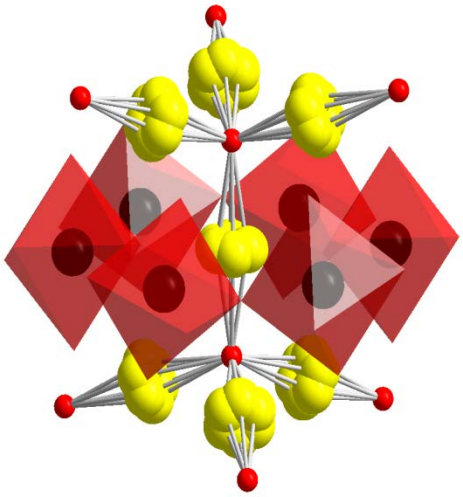

Fig.1. 12 Representation of the A cation environments in $Bi_2Ti_2O_7$, Bi cation sites in yellow, Ti cations in black, and O′ in red. O atoms are at the corners of octahedral coordination to Ti cations.[46]

1.6.2 $Bi_2Ti_2O_7$ thin films

Although $Bi_2Ti_2O_7$ powders are good for some applications such as multilayer capacitors, they are not sufficient for other applications in electric bias fields due to the low decomposition temperature into $Bi_2Ti_4O_{11}$ and $Bi_4Ti_3O_{12}$.[56] Therefore the need for good routes to $Bi_2Ti_2O_7$ films is very crucial for its applications and solving the major problems associated with dielectric measurements.

As mentioned earlier, pyrochlore $Bi_2Ti_2O_7$ exhibits a wide variety of functional properties. $Bi_2Ti_2O_7$ films are attractive due to their high dielectric constant, good insulating properties for low leakage current, and thus could be used as the gate material for advanced transistors as an alternative to SiO_2.[57] Moreover, the high dielectric constant can be retained in thin $Bi_2Ti_2O_7$ films better than in powder form.[58] Wang et al.[59] showed the inverse relation between the leakage current density and the annealing temperature and direct proportionality to the annealing period.

Photocatalytic studies of $Bi_2Ti_2O_7$ films have shown some attractive properties. McInnes et al.[60] demonstrated that $Bi_2Ti_2O_7$ films are suitable for photoelectrochemical water splitting due to a narrower band gap (~2.8 eV) compared with anatase TiO_2 (~ 3.2 eV).

Gupta et al.[61] obtained smaller band gap of 2.1 eV by modifying the $Bi_2Ti_2O_7$ structure with Mn, leading to a 140 % increase in the water splitting efficiency.

1.7 Sol-gel chemistry for ternary oxides

The sol-gel method mentioned previously in section 1.1 is a liquid phase process for the preparation of ceramic and thin film materials. The preparation of ternary films is a key technological process and many fabrication routes have been proposed so far, including metal organic chemical vapour deposition (MOCVD),[62] and wet processes such as hydrothermal[63] and sol-gel.[64] Thin films with good properties can be prepared by these methods. Although MOCVD can be used for depositing semiconductors, metals and dielectrics due to its flexibility, the environmental cost is high on account of its highly toxic and very expensive source materials.[65] Sol-gel methods provide simplicity, low equipment cost, environmental friendliness and flexibility concerning the substrate size.[64]

The high reactivity of metal alkoxides results in a need to control hydrolysis and condensation rate. 2-methoxyethanol ($CH_3OCH_2CH_2OH$) is the most widely used solvent in the chemical fabrication of perovskite materials as it leads to the formation of the metal-oxygen-metal (M-O-M) bonds as well as results in a decrease in the hydrolysis sensitivity of starting reagent such titanium isopropoxide by the alcohol-exchange reaction. However, it has a significant safety concern and must be used cautiously.[66] Chelating processes depend on the molecular modification of the alkoxide groups by reactions with a modifier, such as acetic acid and acetylacetone (acac, 2, 4-pentanedione). Chelate processes share several common characteristics with 2-methoxyethanol-based sol-gel methods, most significantly the creation of small oligomeric species through solution synthesis. The main reason for using the modifier is to decrease the hydrolysis sensitivity of the alkoxides compounds towards water. However, the understanding of its mechanism with titanium alkoxides is still lacking. Chelating reagents such as acac also modify the structure and properties of the product.

Xiaoli et al.[67] prepared transparent $BaTiO_3$ thin films by dissolving barium isopropoxide and titanium tetrabutoxide in isopropanol, while acetylacetone and glacial acetic acid were used as a modifier to block the coordination sites in order to supress the hydrolysis. Kamalasanan et al.[68] used barium 2-ethyl hexanoate and titanium isopropoxide as precursors in the presence of methanol, acetyl acetone and water to synthesise $BaTiO_3$ thin films. Kumazawa et al.[69] described the preparation of 3 μm thicknesses of $BaTiO_3$ films made from titanium isopropoxide and barium isopropoxide, water, and acetylacetone followed by glacial acetic acid.

Lee et al.[70] applied a chelate acetate sol-gel process to prepare nano-crystalline $BaTiO_3$ thin films with a grain size of 30-60 nm by mixing barium acetate with acetic acid and then titanium bis (ammonium lacto) dihydroxide were added. 2-methoxyethanol and acetic acid was used to dissolve barium acetate and titanium isopropoxide by Solanki et al.[71], whereas Liebrecht et al.[72] dissolved barium acetate in acetic acid and titanium isopropoxide in 2-methoxyethanol and small amount of water was added to the mixture to start the hydrolysis. Ashiri et al.[20] they produced a crack-free, dense film by dissolving barium acetate in acetic acid at 65 °C, then 2-propanol and titanium isopropoxide were added to the solution. Deionized water was mixed with the mixture after it was cooled to 2-3 °C.

There are a limited number of sol-gel reports for preparing $Bi_2Ti_2O_7$ films. Wang et al.[59] synthesised crack-free $Bi_2Ti_2O_7$ thin films by dissolving bismuth nitrate in glacial acetic acid, adding titanium butoxide and diluting with 2-methoxyethanol. Wang et al.[73] fabricated a high-quality $Bi_2Ti_2O_7$ film using the same precursors but replacing 2-methoxyethanol with ethylene glycol monomethyl ether and adding a little acetylacetone to control the hydrolysis. Kidchob et al.[74] prepared bismuth titanate films by dissolving bismuth (III) chloride in ethanol containing a few drops of concentrated hydrochloric acid to give a clear solution, and then titanium tetrachloride in ethanol solution was added to the bismuth titanate solution. They concluded that the synthesis based on chloride precursors has many advantages such as the possibility to control synthesis conditions and film morphology without adding any other chemical compound to adjust the reactivity.

1.7.1 Sol-gel film deposition

There are a number of different processes to apply precursor sols onto different types of substrates, including spin coating, spray coating and dip coating. Each one has its advantages and disadvantages.

1.7.1.1 Spin coating

Spin coating is executed with photoresist spinner which can be rotated at high speed (2000-8000 rpm). The substrates are commonly silicon or other materials positioned on a vacuum chuck. The precursor solution is dispensed on the substrate. When the substrate is accelerated, centrifugal forces cause the liquid to spread to the edge of the substrate leaving a thin film on its surface.
An advantage of the spin-coating method is that thin and uniform thickness coatings can be achieved due to the high spin speed which results in the high airflow and fast drying times and then leads to high consistency in the thickness. The main drawback is its relatively low throughput when substrate sizes are larger. Larger substrates cannot be rotated at a sufficiently high speed to allow the film to thin and dry in a short time, so material efficiency drops due to a large amount of the precursor solutions flying off into the coating bowl hence it is not an economical process due to the disposal cost. This process is also not effective for some experiments that require a period of time during drying for example, the synthesis of pore structure.[75]

1.7.1.2 Spray coating

Spray coating is used for conformal film deposition on non-planar surfaces, such as stepped and cylindrical surfaces and curved substrates.[76] It uses a nebulizer with a spray nozzle to generate a distribution of droplets of micrometer size. The fine liquid particles ejected by the nebulizer are carried into the deposition chamber by a carrier gas onto the substrate by gravitation or by the application of an electrostatic field. Spray coating has advantages such as, the deposition in three dimensional fabrications[77] and has been applied for optical quality coatings with controlled thicknesses of approximately 200 nm.[78]

On the other hand, a limitations of the spray-coating process is that variations in coating thickness can occur if the substrate has cavities with different size and feature with different dimensions.[79]

1.7.1.3 Dip-coating

Dip-coating is accomplished with substrates being drawn from a precursor solution and allowed to drain to a certain thickness. Film thickness is controlled by the evaporation rate of the solvent and the viscosity of the precursor solution more directly than for spin and spray coating, as well as by the withdrawal rate.

Most of the materials synthesised for this thesis were prepared using some variation on a sol gel dip-coating technique and it is essential to discuss the theoretical parts of this technique. The dip-coating process is crucial to the final film properties. The dip- coating procedure can be divided into five stages: (a) immersion, (b) start up, (c) deposition, (d) drainage and (e) evaporation.[19]

Fig. 1.13 provides a schematic representation of the withdrawal process for film formation that take place during a sol-gel dip-coating process. When the solvent evaporates and the withdrawal speed equals that of the recession in the drying line, the process is referred to as steady state with respect to the liquid bath surface. During gravitational draining, evaporation and condensation reactions provide a concentrated solution of the polymeric species onto the glass substrate.

During the deposition stage there is a competition between solvent evaporation, which acts to compact the film, and the condensation process, which stiffens the structure of the network and counteracts this shrinkage. The aggregation, gelation and the drying occur within seconds to minutes during the dipping.[80]

Although dip-coating is simple, has a low consumption of energy, can coat large area with internal and external surfaces and provides good thickness control, it also has drawbacks including the variation in the film thickness from top to bottom, and dense edges at the bottom of the film where excess coating fluid drains.[81]

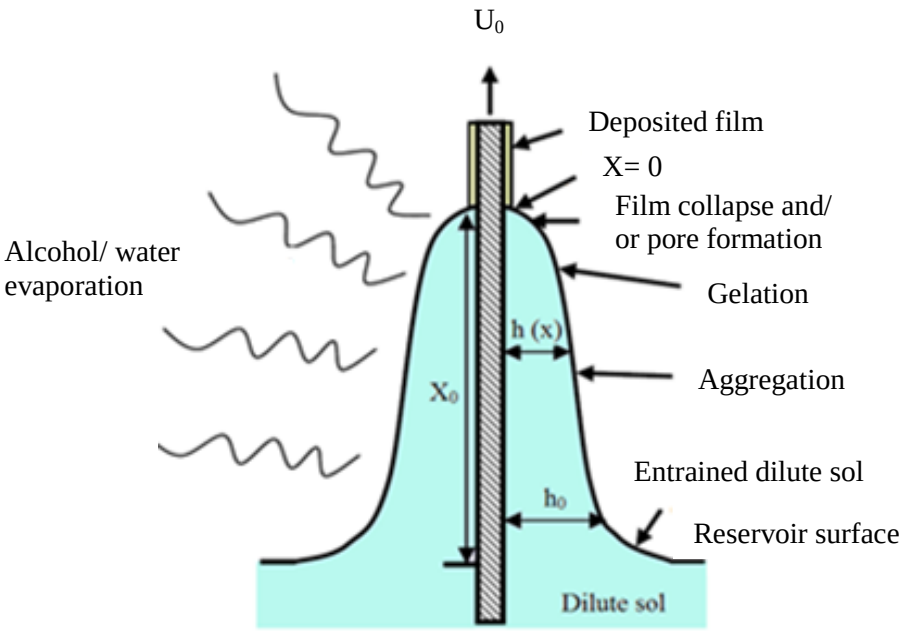

Fig.1. 13 Schematic of the sol-gel dip coating process, redrawn from.[82]

1.7.2 Film thickness

The evolution of the thickness of a liquid film deposited on the substrate can be controlled by some parameters, such as the liquid viscosity (μ) and the withdrawal speed (U). When the liquid viscosity and the withdrawal speed are low as often occurs under experimental condition utilised generally in sol-gel process, the film thickness (h) is dependent upon the viscous drag ($\mu U_0/h$), gravity force (ρgh) and liquid vapour surface tension (γ_{LV}) in accordance with the equation derived by Landau and Levich[83]:

$$h = \frac{0.94(\mu\, U_0)^{2/3}}{\gamma_{LV}^{1/6}\,(\rho g)^{1/2}} \qquad (1.9)$$

where ρ is the liquid density and g is the acceleration due to the gravity.

This equation demonstrates that the thickness of any film deposited by a dip coating technique will rely on the solution viscosity and the withdrawal speed.

1.8 Porous materials

Porous materials can be produced with controllable dimensions of voids at the atomic, molecular or nanometer scales, allowing them to distinguish and interact with molecules and clusters. These include geomaterials, metals, ceramics and polymers. The properties of porous materials, such as high surface area and low thermal conductivity, have been of major practical concern in various areas including catalysis,[84] electrical properties and capacitance and separation.[85] The critical features for such applications are pore accessibility and a narrow pore size distribution.

The International Union of Pure and Applied Chemistry (IUPAC) break down nanoporous materials into three broad categories depending on their pore size[86]:

a. Microporous materials which have a pore size of ≤ 2 nm.
b. Mesoporous materials which have medium size pore of 2-50 nm.
c. Macroporous materials which have large pores of > 50 nm.

The sol-gel process is one of the most important technologies for the preparation of porous metal and multimetal oxide materials. Incorporating a template adjusts the sol-gel process and controls the pore size towards the production of mesoporous and macroporous materials.

Thus the templating method is one of the most widely used to fabricate materials with structural units ranging from nano-to micrometers. The templates can take a great diversity of forms including molecules, surfactant assemblies and colloids. The organic molecules are utilised as soft templates to stimulate the generation of porous solids of diverse types of materials. Accordingly, these porous solids then can be utilised as hard templates (hosts) to direct the insertion of guest molecules, predominantly leading to precise or inverse replicas of the host.[87]

The selection of the right template is essential to ensure successful templating, including being robust enough to form the desired nanostructural framework, and then simply be removed without destruction of the structure formed.

1.8.1 Mesoporous material

Mesoporous materials have been recognised for a long time, however their possible applications were highly limited because of the heterogeneity in pore size and disorganized pore arrangements. The first ordered mesoporous material was announced in a patent in 1969.[88] Kresge and co-workers[89] (Fig. 1.14) discovered the first material which is recognised as MCM-41 (Mobil Corporation Material 41) and it comprises of a hexagonal arrangement of channels. MCM-48 was the second material and possesses a complex network of three dimensional channels systems, whereas the third material is MCM-50, contains stacked silica sheets.

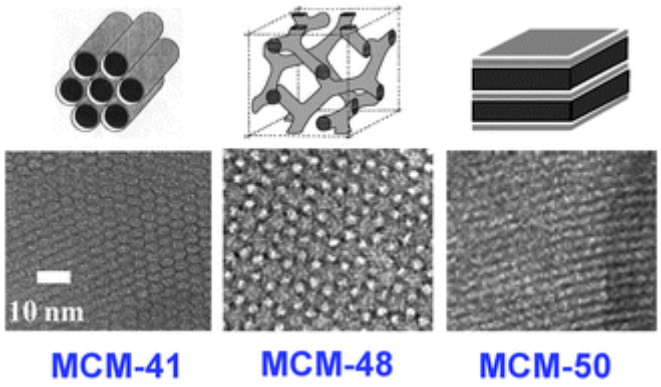

Fig.1. 14 TEM images of mesoporous silica: hexagonal pore structure (left), cubic (middle), and lamella (right) taken from reference[90] with permission from the publisher.

The fabrication of these materials uses self-assembled surfactant aggregates as structure directing agents. The properties of high surface area and narrow pore sizes were among the many required properties that made these materials the subject of a great deal of research over the following years. Different elements, such as aluminium and titanium, can be incorporated by partially substituting together with silicon into the framework of MCM-41 molecular sieves that varied the physico-chemical properties of the material.

Mesoporous materials containing aluminium, such as Al-MCM-41 can have improved catalytic properties.[91] Very soon after their initial synthesis for Al-MCM-41, many laboratories spent much effort to prepare titanosilicates.[91]

The extension of the surfactant templating procedure to the formation of non-silica mesoporoous inorganic oxides such as, Al_2O_3, ZrO_2, and TiO_2, or even more complex multi-metallic oxides (ternary compounds) such as $BaTiO_3$, and $LiTaO_3$, however have been less wide spread, although these mesoporous metal or multi metallic oxides possess more promise in electron transport, catalytic and separation applications.

The extension of mesoporous silica synthesis to transition metal based system is much more difficult, due to the great differences in chemistry between Si and most transition metals, as well as interactions with metal-structure directing agents and flexibility. Among the metal oxides titanium dioxide is one of the most studied materials, due to its applications in catalysis. Most of the proposed syntheses of mesoporous titania depend on the control of the high reactivity of Ti in terms of hydrolysis and condensation. One appropriate solution is the employment of a moderator to slow down the condensation reactions to avoid the rapid precipitation. Another solution to reduce the reactivity of transition metal is the use of non-aqueous solvents[92] with low amounts of water being supplied by moisture or impurities.[93]

One serious issue for synthesis of mesoporous metallic oxides is thermal instability of the porous structures as they often collapse during the transition from amorphous to crystalline phase by annealing. Stabilisation has been achieved by prefilling the pores with carbon prior to crystallization in inert gas and then removing the carbon matrix by calcination.[94] However, the preparation of mesoporous multimetallic oxide materials by the integration into mesoporous silica could offer some advantages, such as the preserving its properties due to confinement.[95]

1.8.1.1 Surfactants and liquid crystal phases

Mesoporous materials are typically prepared via templating around surfactant aggregates as structure directing agents in sol-gel method. To understand how these ordered structures are produced, it is necessary to comprehend how surfactants behave in aqueous solutions. Fig. 1.15 displays a schematic image of a surfactant molecule. The molecule involves a hydrophilic head group which is water soluble and a hydrophobic tail group that is water insoluble.[96]

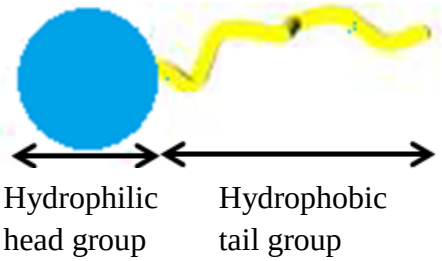

Fig.1. 15 Schematic diagram of surfactant molecule.

Regulated by the so-called the amphiphilic nature of surfactant molecules in aqueous solution, the polar head groups interact with water molecules and the inorganic species existing in the solution and the hydrocarbon tails are directed towards the centre which is only occupied by low polarity species. Therefore, the surfactant molecules self-assemble to form micelles (Fig. 1.16). The aggregation only happens after a certain concentration is reached which is known as the critical micelle concentration (CMC) which is typically around 1 wt % of surfactant.[97]

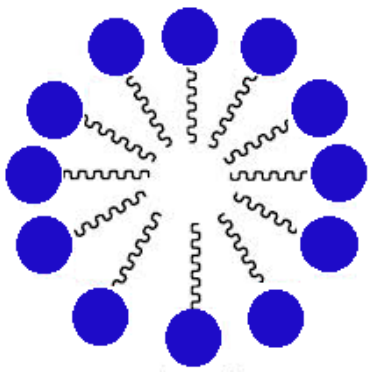

Fig.1. 16 Schematic representation of a spherical micelle.

Further increases in the surfactant concentration above the CMC result in the formation of more micelles, and these can self-assemble into various thermodynamically stable structures. Initially a hexagonal arrangement of micellar rods can be observed. At higher concentration, lamellar micelles are created and consist of bilayers separated from each other by water[97] (Fig. 1.17).

At the extreme concentration of the surfactant inverse phases are formed, for instance the inverse hexagonal and inverse micellar phase. The inverse micellar phase also comprises of spherical micelles however the hydrocarbon tails are pointed outwards whilst the polar head groups face inwards and surround small pockets of water[97] (Fig. 1.17).

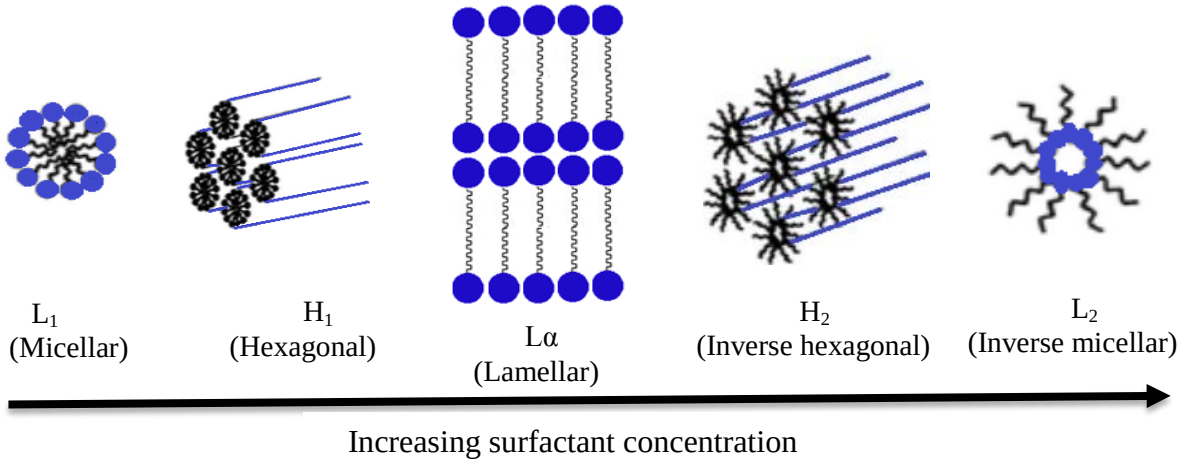

Fig.1. 17 The aggregation of amphiphiles into micelles in a lyotropic system.

At extremely high concentration, the randomly disordered micelles spontaneously assemble into different structures, such as cubic, hexagonal and lamellar. These are known as liquid crystalline phases as the materials are oriented into preferred directions. The molecules in a liquid crystal phase possess shared features of both a crystal and a liquid, they do not possess the positional and orientational order of a solid, but neither do they have the total disorder related to a melt.

Three types of surfactant are commonly used as templates: ionic, neutral and non-ionic surfactants. The ionic surfactants are divided into cationic and anionic types, relying on the nature of charge on the hydrophilic group.

The most commonly used cationic surfactants in mesoporous materials include alkylammonium salts such as hexadecyl-trimethylammonium bromide (C_{16}TMABr) while the most used anionic surfactants are alkylcarboxylic acids such as $C_{17}H_{35}COOH$. Primary amines (in which the hydrophilic group is not charged) are an important example of neutral surfactants. Non-ionic surfactants, such as polyethylene oxide, are block copolymers such as pluronic P-123, F-127. The selection of surfactant leads to control of the pore size and pore orientation

1.8.1.2 Mechanisms of self-assembly

Several mechanisms have been suggested to define the formation of mesoporous materials. Most suggested mechanisms take into account the type of template molecules, condensation degree and the precursor composition.[98] Though the proposed models offer some elucidation of mesostructure formation, the templating method is still not totally understood. The mesostructure fabrication reaction consists of multiple and complicated species and equilibria, diffusion, nucleation, and growth which is influenced by concentration, temperature, pH and reaction time.

There are different mechanisms in which the surfactants can self-assemble into suitable mesophases, however the evaporation induced self-assembly mechanism has been extensively applied for the fabrication of mesoporous films.[98]

Evaporation induced self-assembly (EISA)

There is a diversity of applications for which a mesoporous film would be required. EISA was first proposed by Ogawa[99] and extensively used to synthesise mesoporous films by coating a substrate by spin or dip coating with a homogeneous solution of a metal alkoxide, surfactant and water diluted in an alcohol, in which the surfactant is below the CMC.

During the film preparation, ethanol evaporates increasing the surfactant concentration up to the CMC, inducing the self- assembly of the surfactant molecules into micelles. Hence the experimental state changes continuously during evaporation.

The films are then aged for a period of time, followed by a heat treatment step to remove the surfactant and crystallise the mesoporous material into the required phase. The calcination step is crucial for the preparation of mesoporous materials as it removes the surfactant and then gives rise to the pores in the material and to crystallise the wall inside the pores. The consequence of this process is the rapid formation of thin film mesophases which are highly ordered with the consideration of the substrate surface.[100]

1.8.2 Applications of mesoporous materials

Ordered mesostructured porous solids have important advantages, such as increased surface area and site activity, high adsorptivity, high mass transport potential and high dielectric constants in mesoporous multimetal oxides. Therefore, the range of applications of these templated mesoporous oxide materials has increased during recent years in many areas, notably catalytic,[84] electrical and capacitance applications.[101]

The applications of mesoporous materials in the fields of capacitance and catalysis will be discussed in the following sections as they are the most significant applications of mesoporous materials reported in the literature.

1.8.2.1 Capacitance

One of the most studied metal oxides in mesoporous form is TiO_2 due to its huge surface area and good accessibility of the pores. Brezesinski et al.[102] obtained 340 F g^{-1} of the total capacity in the nanocrystal mesoporous TiO_2 films with pore size of 17 nm and the capacity was increased by almost 1.7 times compared to the highly ordered films for Li^+. Hamaguchi etal.[103] demonstrated Li^+ storage with 4 nm pore diameter mesoporous titanias with a maximum capacity of 225 F g^{-1}.

Although the ferroelectric-based nanocomposites with other functional constituents, such as carbon, metal have been described for ultrahigh dielectric constant power storage applications, no reports exist using mesoporous multimetalic oxides pure (without modification), in films or powders for energy storage applications.

Moniruzzaman et al.[101] found the capacitance of porous amine modified $BaTiO_3$ in multi wall carbon nanotubes composites as 32.65 F g^{-1}.

1.8.2.2 Photo catalysis

Mesoporous films have vastly grown and have caught interest in a wide range of catalytic applications. The interest results from the unique properties of mesoporous materials such as high specific surface area; high content of surface-active groups and narrow pore size distribution.[104]

In recent times a few studies have focused on mesoporous titania films in order to enhance the photocatalytic properties. The catalyst morphology affects the transport of reactants and yields to or from the catalytic active sites, in addition to the light absorbance for the photo-excitation of the catalyst and the production of electron-hole pairs.[104]

Yu et al.[105] reported the photocatalytic activity increased by increasing the firing temperature of mesoporous TiO_2 films with respect to the mesoporous structure. Choi et al.[104] studied the effect of photocatalytic activity as a function of the particle size of mesoporous TiO_2 films; they concluded the photocatalytic activities are enhanced by decreasing the particle size.

On the other hand, although mesoporous multimetal oxides have many advantages in mechanical, photocatalytic and electrical applications, very little development has been accomplished in terms of the syntheses of mesoporous multimetal oxides either in powders or films. Fan et al.[106] synthesised crystalline mesoporous $SrTiO_3$ and $BaTiO_3$ powders of 5.4 nm pore size with high specific surface areas, narrow pore-size distributions, and higher photocatalytic activities.

1.9 Macroporous materials (inverse opal)

The largest pore diameter that can be obtained during liquid crystal templating is approximately 50 nm. Macroporous materials have very large pore size (> 50 nm) that leads to an ease of mass transfer of guest molecules. Macroporous materials are synthesized by a variety of methods including colloidal crystal templating with large three dimensionally ordered (3D) arrays of close packed polymer microspheres.

The colloidal crystal template materials are called inverse opals because they show a periodic structure complementary to that of an opal. These materials have been considered for many potential applications such as catalyst supports, separation materials and thermal insulators.[107]

1.9.1 Colloidal crystal templating

The general theory of colloidal crystal templating includes three steps. (a) A close packed array of ordered monodisperse spheres is packed and assembled into an ordered array, (b) the interstitial voids between the spheres is infiltrated with a suitable liquid precursor of the desired material and the allowance of the hydrolysis and condensation around the sphere and then subsequently dried to solidify the structure and (c) The template can then be removed by dissolution with a suitable solvent or thermal degradation of the composite, and a framework with ordered macropore is shown as an inverse replica of the spheres.[108] A schematic of macroporous materials is shown in Fig. 1.18.

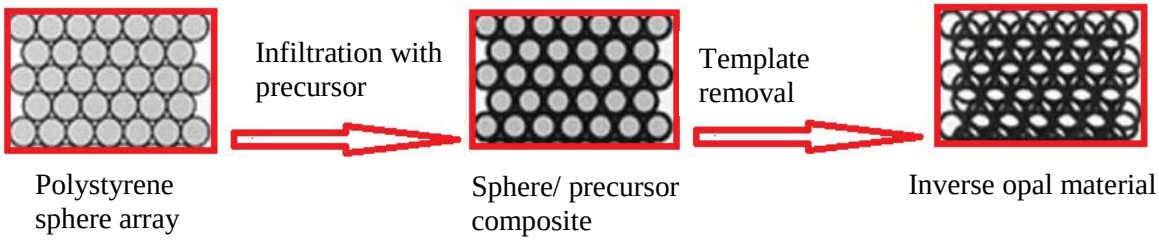

Fig.1. 18 The three main stages involved in colloidal crystal templating.

1.9.2 Assembling the template

The microspheres are typically composed of polystyrene (PS), polymethyl methacrylate (PMMA) or silica; they are cheap and simply fabricated with sizes ranging from tens of nanometres up to several microns and with very narrow size distributions. Also microspheres can be obtained commercially with a various range of sizes and functionalities. PS and PMMA spheres are commonly favoured in the formation of macroporous materials due to their ease of removal after the colloidal crystal architecture has been applied as a template.[109]

There are various techniques that can be employed to order the colloidal sphere into colloidal crystals; some of them are explained in the next section:

1.9.2.1 Self-assembly by physical confinement

Once monodisperse microspheres undergo to physical confinement, they will predominantly organise themselves into highly ordered 3D structures in spite of their size, bulk properties and surface properties. The advantages of this process are that it is simple, can be applied to relatively large areas, and provides tight control over the film thickness of the achieved arrays and number of the layers of the crystalline assemblies in the film.[110]

1.9.2.2 Self-assembly by vertical deposition

The substrate is fixed vertically into a suspension of colloidal spheres. The suspension is driven by capillary forces at the substrate-solvent-air interface. The spheres assemble on the substrate as this interface moves, i.e. by water evaporation is the driving force for this phenomenon. The quality of spheres self-assembled can be controlled by the quality of the suspension, cell cleanliness and wettability, atmosphere around the cell and substrate type. Also the degree of monodispersity of the particles in the suspension and which then finally will be absorbed onto the substrate.[111]

1.9.3 Macroporous films

Template-assisted methods using colloidal crystals have gained considerable interest for synthesis of three dimensionally ordered macroporous films. The pore sizes of the films are dependent on the size of the colloidal crystals used. Therefore, applying polystyrene (PS) colloidal crystals as a template offers an approach to effectively adjust the pore size of the achieved film. The morphology and thickness of macroporous films can be simply controlled through adjusting of the deposition parameters and time.

This technique has allowed materials with a variation of pore size to be created and thus generating new desirable materials. An et al.[112] fabricated high quality inverse opal films of yttria stabilized zirconia (YSZ) using template-assisted growth based on polystyrene (PS) colloidal crystals. The same method was used by Wijnhoven et al.[113] and Ding et al.[114] to prepare inverse opal films of titania and Cu_2O, respectively.

1.9.4 Methods for infiltration

To successfully template around a colloidal crystal, it is necessary to infiltrate the interstices between the spheres in the colloidal crystal with material, and then eliminate the colloidal spheres by thermal treatment or dissolution.
The infiltration method affects the morphology of the inverse opal materials significantly, while imperfect infiltration results in collapsing of the inverse opal structure. Various infiltration techniques have been accomplished to accurately control the infiltration process, and therefore to produce different ranges of inverse opal materials.

1.9.4.1 Organic polymerization

Polymerization of organic precursors around a colloidal crystal sphere is used for the generation of a large variety of macroporous polymers. This method is applied as the colloidal crystal shapers are infiltrated with a liquid monomer. The silica spheres/ oxide are infiltrated by polymer support which is then polymerized by heat treatment or UV irradiation in order to produce rigid inverse opal materials while preserving the structure. At the end the extraction is achieved by dissolution in HF solution.

The type of material for the microspheres is critical to secure the final material has a perfect structure and has not been damaged e.g. SiO_2 colloidal crystal.[115]

Turner et al.[116] fabricated inverse opal titania films by using a SiO_2 colloidal crystal template. The process of capillary forces is achieved to draw the monomer to the interstitial between the silica spheres. The capillary as well used to fill the space between the spheres and the oxide. Exposure to UV light for 6 hours caused the cross-linking of the monomers into a polymer species, followed by immersing in ~10 % aqueous HF solution. The HF solution leads to penetrate the silica sphere/oxide coating structure and remove away all silica, generating highly ordered inverse opal film.

1.9.4.2 Liquid phase infiltration

One of main methods to fabricate inverse opal materials is liquid phase infiltration and that is applied for sol-gel processes. As previously discussed (section 1.1), a sol involves a metal oxide complex in a liquid that can be impregnated into the voids of a colloid crystal template analogous to that discussed for the organic polymerisation method.

Hydrolysis and condensation of the metal alkoxide in the interstitial space between the spheres of the colloidal crystal result in the evolution of a metal oxide network. Capillary force allows infiltration into the voids. The microsphere based template is often removed by calcination, however inverse opal materials undergo shrinkage by 15-30 % as a result of large volume loss through the sol-gel dip or spin-coating process as the alcohol is evaporated.

This shrinkage leads to a clear cracking of the final inverse opal material.[98] Kuai et al.[117] prepared large-area 309 nm inverse opal titania thin-film through a dip-infiltrating sol-gel process using a colloidal crystal template.

1.9.5 Macroporous ternary compounds

Inverse opal $BaTiO_3$ and pyrochlore $Bi_2Ti_2O_7$ are one of the particularly beneficial materials in the microelectronics industry, catalysis,[118, 119] separation[120] and molecular hosting of organic and inorganic such as for inserting lithium ion battery.[121]

To the best of our knowledge, a few papers have been focused on the preparation of inverse opal $BaTiO_3$ and no literature was found for $Bi_2Ti_2O_7$ films. Lei et al.[122] prepared inverse opal $BaTiO_3$ powders by sol-gel method using a PS spheres as template and they reported the shrinkage of the spheres by 50 % smaller than the original spheres used. Li et al.[123] obtained 25 % of the spheres shrinkage during his fabrication by sol-gel electrophoretic deposition, whereas Xiang et al.[124] gained 25 % ~30 % of the shrinkage in the pores diameters. Jin et al.[125] prepared cerium-doped inverse opal $BaTiO_3$ films with shrinkage of 32.65 %. Matsuura et al.[126] synthesised Pb-doped inverse opal $Ba_{0.7}Sr_{0.3}TiO_3$ films and the shrinkage of the spheres were 17 % of the original spheres utilised.

Zhou et al.[127] prepared inverse opal $BaTiO_3$ from SiO_2 colloid- crystal to enhance the photonic band gap. Soten et al.[128] prepared inverse opal $BaTiO_3$ films with pore size ranged from 280-330 nm and the shrinkage was 17 %.

Yan et al.[129] synthesised inverse opal $Bi_2Ti_2O_7:Er^{3+},Yb^{3+}$ powders by sol-gel process, whereas, Cun et al.[130] have doped Li^+ ions to inverse opal $Bi_2Ti_2O_7:Er^{3+}$, Yb^{3+} films by sol-gel method. Kim et al.[131] prepared inverse opal La-doped $Bi_{3.25}La_{0.75}Ti_3O_{12}$ films and 20 % of the shrinkage was observed. Kim et al.[132] prepared inverse opal $La_{0.7}Ca_{0.3}MnO_3$, $BaTiO_3$, $PbZr_{0.2}Ti_{0.8}O_3$, and $Bi_4Ti_3O_{12}$ powders using poly (methyl methacrylate) (PMMA) colloidal crystal templates with large shrinkage.

1.9.6 Applications of macroporous materials

Macroporous materials prepared from colloidal crystal templating have various promising applications, some of which are discussed in further detail below:

1.9.6.1 Photonic crystals

The major feature that distinguishes macroporous materials from their meso and microporous counterparts is that, if ordered, they can act as a photonic crystal. The concept behind photonic crystal materials has its origin in two articles by Yablonovitch and John in 1987[133] who suggested that a material with a periodic modulation of refractive index can affect the photonic properties in a material giving rise to a photonic band gap (PBG).

The PBG is similar to a band gap in a semiconductor in which a particular range of energies of light cannot propagate through the photonic crystal. This advantage results in several exciting potentials for PBG materials. Previously manipulation of light depended on internal reflections, though the improvement of photonic crystal waveguides can enable light to be monitored in a way parallel to the control of electrons by the electronic band gap of semiconductors.[134]

There are some conditions that must be achieved to ensure a complete PBG, including a low solid fraction approximately 20-30 % solid by volume, for materials that possess a close packed spheres structure the minimum refractive index contrast must be 2.8 and the periodicity must be uniform with a lattice spacing comparable to the desired PBG wavelengths. Any undesirable defects result in destruction of the photonic band gap.[98] These issues make it hard to generate a complete photonic band gap material via colloidal crystal templating, however some reports show partial stop bands which are displayed as different coloured reflections. The spectral position of these stop bands can be controlled by altering of the pore sizes and the pore walls refractive index. The presence of a partial stop band implies these materials are still beneficial for optoelectronic application.[135]

1.9.6.2 Lithium insertion electrode material

Pioneering work for the lithium battery started in 1912 by G. N. Lewis,[136] however it was not available commercially until 1970's when the first non-rechargeable lithium batteries became popularly utilised as stationary power storage units for portable electronic equipment and for electric vehicles with long ranges.

Current densities are limited by activation and concentration polarizations at fast charge/discharge rates that result from low diffusion rules in the electrodes, resistance of the electrolyte and electrical resistance of active materials.[121] In order to improve electrodes, nanostructuring is an extremely attractive method for improving current densities. Nanosized and nanoporous electrodes possess large surface areas in comparison to the counter bulk electrodes, which help in reducing the polarization. Electrodes with increased electrolyte accessible surface areas have more opportunity for reactions with Li^+ ions and thin pore walls minimise the diffusion lengths in these materials, which implies that the diffusion time for Li^+ is reduced.

Since Li^+ is capable of fast diffusion over an electrode with nanoscale grains, the kinetic limitations of solid-state diffusion are absent and thus high current densities can be obtained. Additionally, a high surface area leads to interfacial charge storage making a larger contribution to overall capacity. This technique allows lithium-ion cells to realise high power densities.[137]

Ke et al.[138] demonstrated that electrodes of inverse opal Sn–Ni alloy prepared from a polystyrene sphere template improved effectively the cycling performance of the electrode when used as an anode for a rechargeable lithium battery. Esmanski et al.[139] prepared amorphous inverse opal silicon films with promising cycling characteristics, and the amorphous nature of silicon can be beneficial for reducing stresses associated with large volume changes through electrochemical lithium insertion-removal.

1.10 Objectives

The aim of this project was to investigation of production of porous titanate ceramics in thin films form. It is hoped these will be good hosts for electro-deposition at offer materials to produce composite devices.

This work started with syntheses of TiO_2 thin films and powders by sol–gel methods, using a dip-coating process to produce films. Sol composition was varied to determine the effect on morphology and particles size, and also on the crystallization and phase transformation behaviour. Then the work has been moved in attempt to prepare mesoporous TiO_2 thin films with surfactant -templated method to obtain experience of synthesis of porous films. NMR and MS were used to demonstrate TiO_2 precursor in diethanolamine containing sols.

Thin film of titanate electroceramics are often examined for capacitor applications. The high sintering temperature of $BaTiO_3$ and low thermal stability of $Bi_2Ti_2O_7$ make film formation challenging.

$BaTiO_3$ and $Bi_2Ti_2O_7$ films were prepared from a well-controlled sol system sol in acetic acid/methoxyethanol mixtures. Films with a thickness of ~5 μm were obtained by dip coating once and firing the dried films, and multiple dip/dry cycles resulted in larger thicknesses.

Porous $BaTiO_3$ and $Bi_2Ti_2O_7$ films were initially attempted by adding a surfactant such as pluronic F-127 into the sol to generate mesoporosity of hexagonal ordering with a pore size of 2.5- 4.0 nm. The work then shifted to use of a hard template by incorporating $BaTiO_3$ into a mesoporous silica based carbon template to produce the corresponding mesoporous $BaTiO_3$ powders and films.

The final aspect of the work has been the fabrication of macroporous materials with highly ordered, tuneable pore structures by using the colloidal spheres as templates with self-assembly on vertical substrates techniques and sol-gel method to infiltrate the precursors between the spheres.

Sacrificial polystyrene sphere templates were employed to synthesise macroporous $BaTiO_3$ and $Bi_2Ti_2O_7$ with a defined pore size depending on the diameter of the polystyrene spheres used.

1.11 References

1. D. J. Kim, S. H. Hahn, S. H. Oh and E. J. Kim, *Mater. Lett.*, 2002, **57**, 355-360.
2. B. I. Kharisov, O. V. Kharissova and H. V. R. Dias, *Nanomaterials for Environmental Protection*, Wiley, 2014.
3. A. L. Hector, *Chem. Soc. Rev.*, 2007, **36**, 1745-1753.
4. N. B. Chaure, A. K. Ray and R. Capan, *Semicond. Sci. Technol.*, 2005, **20**, 788.
5. K. Kalyanasundaram, *J. Phys. Chem. C*, 2014, **118**, 16303-16306.
6. J. D. Wright and N. A. J. M. Sommerdijk, *Sol-Gel Materials: Chemistry and Applications*, Gordon and Breach Science Publishers, 2001.
7. J. D. Wright and N. A. J. M. Sommerdijk, *Sol-Gel Materials: Chemistry and Applications*, Taylor & Francis, 2000.
8. G. Hasegawa, *Studies on Porous Monolithic Materials Prepared Via Sol-Gel Processes*, Springer Japan, 2012.
9. K. K. Saini, S. D. Sharma, Chanderkant, M. Kar, D. Singh and C. P. Sharma, *J. Non-Cryst. Solids.*, 2007, **353**, 2469-2473.
10. M. A. Carpenter, S. Mathur and A. Kolmakov, *Metal Oxide Nanomaterials for Chemical Sensors*, Springer, 2012.
11. M. Naya, N. Kobayashi, M. Ema, S. Kasamoto, M. Fukumuro, S. Takami, M. Nakajima, M. Hayashi and J. Nakanishi, *Regul. Toxicol. Pharm.*, 2012, **62**, 1-6.
12. M. K. Nazeeruddin, A. Kay, I. Rodicio, R. H.Baker, E. Mueller, P. Liska, N. Vlachopoulos and M. Graetzel, *J. Am. Chem. Soc.*, 1993, **115**, 6382-6390.
13. M. Wang, N. Chamberland, L. Breau, J.-E. Moser, R. Humphry-Baker, B. Marsan, S. M. Zakeeruddin and M. Grätzel, *Nat Chem*, 2010, **2**, 385-389.
14. A. B. Kashyout, M. Soliman and M. Fathy, *Renewable Energy*, 2010, **35**, 2914-2920.
15. F. Pichot, J. R. Pitts and B. A. Gregg, *Langmuir*, 2000, **16**, 5626-5630.
16. A. P. Xagas, E. Androulaki, A. Hiskia and P. Falaras, *Thin Solid Films*, 1999, **357**, 173-178.
17. K. Murugan, T. N. Rao, G. V. N. Rao, A. S. Gandhi and B. S. Murty, *J. Mater. Chem. Phys.*, 2011, **129**, 810-815.
18. R. K, *Engineering Physics*, Prentice-Hall Of India Pvt. Limited, 2007.
19. S. M. Aygun and N. C. S. University, *Processing Science of Barium Titanate*, North Carolina State University, 2009.
20. R. Ashiri, A. Nemati and M. Sasani Ghamsari, *Ceram. Int.*, 2014, **40**, 8613-8619.
21. R. Sirera, M. L. Calzada, F. Carmona and B. Jiménez, *J. Mater. Sci. Lett.*, 1994, **13**, 1804-1805.
22. D. A. Barrow, T. E. Petroff, R. P. Tandon and M. Sayer, *J. Appl. Phys.*, 1997, **81**, 876-881.
23. T. Shimizu, D. Suwama, H. Taniguchi, T. Taniyama and M. Itoh, *J. Phys. Condens. Matter.*, 2013, **25**, 226-8503.
24. K. Byrappa and T. Ohachi, *Crystal. Growth. Technology*, Springer, 2003.

25. Z. Hong, J. Britson, J.-M. Hu and L.-Q. Chen, *Acta Mater.*, 2014, **73**, 75-82.
26. J. Chen, F. Wang, Q. Huang, L. Hu, X. Song, J. Deng, R. Yu and X. Xing, *Sci. Rep.*, 2013, **3**, 2045-2322.
27. Q. Zhang, S. Corkovic, C. P. Shaw, Z. Huang and R. W. Whatmore, *Thin Solid Films*, 2005, **488**, 258-264.
28. H. S. Nalwa, *Handbook of Low and High Dielectric Constant Materials and Their Applications, Two-Volume Set*, Elsevier Science, 1999.
29. H. Ishiwara, M. Okuyama and Y. Arimoto, *Ferroelectric Random Access Memories: Fundamentals and Applications*, Springer, 2004.
30. A. Alper, *Phase Diagrams 6-V: Materials Science and Technology*, Elsevier Science, 2012.
31. R. E. Smallman and R. J. Bishop, *Modern Physical Metallurgy and Materials Engineering: Science, Process, Applications*, Butterworth-Heinemann, 1999.
32. R. Buttner and E. Maslen, *Acta Crystallogr., Sect. B: Struct. Sci.*,1992, **48**, 764-769.
33. R. B. R. M. Eichhorn, *Engineering Dielectrics Volume Iia Electrical Properties of Solid Insulating Materials: Molecular Structure and Electrical Behavior*, ASTM International.
34. A. Soukiassian and T. P. S. University, *Growth of Nanoscale Barium Titanate/strontium Titanate Superlattices by Molecular-beam Epitaxy*, Pennsylvania State University, 2007.
35. G. H. Haertling, *J. Am. Ceram. Soc.*, 1999, **82**, 797-818.
36. A. Visinoiu, R. Scholz, M. Alexe and D. Hesse, *Appl. Phys. A*, 2005, **80**, 229-235.
37. M. Frey and D. Payne, *Appl. Phys. Lett.*, 1993, **63**, 2753-2755.
38. Q. Feng and C. McConville, *J. Electroceram.*, 2005, **14**, 45-52.
39. *Electronic Ceramics: Properties: Devices, and Applications*, Taylor & Francis, 1987.
40. S. Chehab, P. Conflant, M. Drache, J. C. Boivin and G. McDonald, *Mat. Res. Bull.*, 2003, **38**, 875-897.
41. G. W. Hwang, W. D. Kim, Y. S. Min and C. S. Hwang, *J. Electrochem. Soc.*, 2006, **153**, F20-F26.
42. N. Ichinose and Y. Takahashi, *Ferroelectrics*, 2001, **258**, 31-36.
43. B. D. Stojanovic, A. Z. Simoes, C. O. Paiva-Santos, C. Quinelato, E. Longo and J. A. Varela, *Ceramics International*, 2006, **32**, 707-712.
44. A. G. Pinheiro, G. D. Saraiva, J. Mendes Filho and A. S. B. Sombra, *Mater. Sci. Appl.*, 2013, **4**, 549-555.
45. J. A. Alonso and X. Turrillas, *Dalton Trans.* , 2005, 865-867.
46. A. Salamat, A. L. Hector, P. F. McMillan and C. Ritter, *Inorg. Chem.*, 2011, **50**, 11905-11913.
47. S. S. Kim, M. H. Park, J. K. Chung and W. J. Kim, *J. Appl. Phys.*, 2009, **105**, 061641-061641-061645.
48. A. L. Hector and S. B. Wiggin, *J. Solid. State. Chem.*, 2004, **177**, 139-145.
49. W. L. W. Ludekens and A. J. E. Welch, *Acta. Crystallogr.*, 1952, **5**, 841-841.
50. M. T. Sebastian, *Dielectric Materials for Wireless Communication*, Elsevier Science, 2010.
51. H. Wang, S. Kamba, H. Du, M. Zhang, C. T. Chia, S. Veljko, S. Denisov, F. Kadlec, J. Petzelt and X. Yao, *J. Appl. Phys.*, 2006, **100**, 014105.
52. S. J. Henderson, O. Shebanova, A. L. Hector, P. F. McMillan and M. T. Weller, *Chem. Mater.*, 2007, **19**, 1712-1722.
53. T. A. Vanderah, M. W. Lufaso, A. U. Adler, I. Levin, J. C. Nino, V. Provenzano and P. K. Schenck, *J. Solid. State.Chem.*, 2006, **179**, 3467-3477.

54. C. G. Turner, J. R. Esquivel-Elizondo and J. C. Nino, *J. Am. Ceram. Soc.*, 2014, **97**, 1763-1768.
55. J. Luan, S. Zheng, X. Hao, G. Luan, X. Wu and Z. Zou, *J. Brazil. Chem. Soc.*, 2006, **17**, 1368-1376.
56. J. Cagnon, D. S. Boesch, N. H. Finstrom, S. Z. Nergiz, S. P. Keane and S. Stemmer, *J. App. Physics.*, 2007, **102**, 102-105.
57. S. W. Wang, W. Lu, N. Li, Z. F. Li, H. Wang, M. Wang and X. C. Shen, *Mar. Pollut. Bull.*, 2002, **37**, 1691-1697.
58. D. P. Shoemaker, R. Seshadri, A. L. Hector, A. Llobet, T. Proffen and C. J. Fennie, *Phys. Rev. B: Condens. Matter.*, 2010, **81**.
59. S. W. Wang, W. Lu, N. Li, Z. F. Li, H. Wang, M. Wang and X. C. Shen, *Mater. Res. Bull.*, 2002, **37**, 1691-1697.
60. A. McInnes, J. S. Sagu and K. G. U. Wijayantha, *Mater. Lett.*, 2014, **137**, 214-217.
61. S. Gupta, L. De Leon and V. Subramanian, *Phys. Chem. Chem. Phys.*, 2014, **16**, 12719-12727.
62. I. T. Kim, C. H. Lee and Soon J. Park, *Jpn. J. Appl. Phys.*, 1994, **33**, 5125.
63. J. M. Han, M. R. Joung, J. S. Kim, Y. S. Lee, S. Nahm, Y. K. Choi and J. H. Paik, *J. Am. Ceram. Soc.*, 2014, **97**, 346-349.
64. T. M. Stawski, W. J. C. Vijselaar, O. F. Gobel, S. A. Veldhuis, B. F. Smith, D. H. A. Blank and J. E. ten Elshof, *Thin Solid Films*, 2012, **520**, 4394-4401.
65. J. H. Park and T. S. Sudarshan, *Chemical Vapor Deposition*, A S M International, 2001.
66. N. Y. Turova, *The Chemistry of Metal Alkoxides*, Springer US, 2002.
67. X. Xiang, L. Hou and F. Gan, Sol-gel-derived $BaTiO_3$ thin films, Shanghai-DL tentative conference, 1991.
68. M. N. Kamalasanan, N. D. Kumar and S. Chandra, *J. Appl. Phys.*, 1993, **74**, 5679-5686.
69. H. Kumazawa and K. Masuda, *Thin Solid Films*, 1999, **353**, 144-148.
70. B. Lee and J. Zhang, *Thin Solid Films*, 2001, **388**, 107-113.
71. A. Solanki, S. Choudhary, V. R. Satsangi, R. Shrivastav and S. Dass, *J. Alloys Compd.*, 2013, **561**, 114-120.
72. L. J. H. Liebrecht, *MSc thesis "Sol-Gel Derived Barium Titanate Thin Films" , University of Twente,*, 2006.
73. Z. Wang, C. H. Yang, D. L. Sun, J. F. Hu, H. Wang, H. C. Chen and C. S. Fang, *Mater. Sci. Eng., B*, 2003, **102**, 335-338.
74. T. Kidchob, L. Malfatti, D. Marongiu, S. Enzo and P. Innocenzi, *J. Am. Ceram. Soc.*, 2010, **93**, 2897-2902.
75. H. S. Nalwa, *Handbook of Advanced Electronic and Photonic Materials and Devices: Semiconductor devices*, Academic Press, 2001.
76. A. J. McKerrow and M. R. S. Meeting, *Materials, technology and reliability for advanced interconnects and low-k dielectrics,2003: symposium held April 21-25, 2003, San Francisco, California, U.S.A*, Materials Research Society, 2003.
77. M. Ichiki, L. Zhang, Z. Yang, T. Ikehara and R. Maeda, *Microsystem Technologies*, 2004, **10**, 360-363.
78. A. Aegerter, *Sol-Gel Technologies for Glass Producers and Users*, Springer, 2004.
79. P. Nga Phuong, E. Boellaard, J. N. Burghartz and P. M. Sarro, *J. Microelectromech. Syst.*, 2004, **13**, 491-499.
80. H. J. Moon, *Development of Thin Film Inorganic Membranes for Oxygen Separation*, Forschungszentrum, Zentralbibliothek, 2012.
81. M. N. Rahaman, *Ceramic Processing and Sintering*, Taylor & Francis, 2003.

82. C. J. Brinker, G. C. Frye, A. J. Hurd and C. S. Ashley, *Thin Solid Films*, 1991, **201**, 97-108.
83. N. Barati, M. A. F. Sani, H. Ghasemi, Z. Sadeghian and S. M. M. Mirhoseini, *Appl. Surf. Sci.*, 2009, **255**, 8328-8333.
84. Y. Tsuge, K. Inokuchi, K. Onozuka, O. Shingo, S. Sugi, M. Yoshikawa and S. Shiratori, *Thin Solid Films*, 2006, **499**, 396-401.
85. Q. Huo, D. Zhao, J. Feng, K. Weston, S. K. Buratto, G. D. Stucky, S. Schacht and F. Schüth, *Adv. Mater.*, 1997, **9**, 974-978.
86. V. Piemonte, M. De Falco and A. Basile, *Sustainable Development in Chemical Engineering: Innovative Technologies*, Wiley, 2013.
87. N. Pal and A. Bhaumik, *Adv. Colloid Interface Sci.*, 2013, **189**, 21-41.
88. V. Valtchev, S. Mintova and M. Tsapatsis, *Ordered Porous Solids: Recent Advances and Prospects*, Elsevier Science, 2011.
89. M. Baerns, *Basic Principles in Applied Catalysis*, Springer, 2004.
90. C. T. Kresge and W. J. Roth, *Chem. Soc. Rev.*, 2013, **42**, 3663-3670.
91. E. Antonakou, A. Lappas, M. H. Nilsen, A. Bouzga and M. Stöcker, *Fuel*, 2006, **85**, 2202-2212.
92. P. Yang, D. Zhao, D. I. Margolese, B. F. Chmelka and G. D. Stucky, *Chem. Mater.*, 1999, **11**, 2813-2826.
93. D. Grosso, G. J. de A. A. Soler-Illia, F. Babonneau, C. Sanchez, P. A. Albouy, A. Brunet-Bruneau and A. R. Balkenende, *Adv. Mater.*, 2001, **13**, 1085-1090.
94. R. Hou, P. Ferreira and P. Vilarinho, *Microporous Mesoporous Mater.*, 2008, **110**, 392-396.
95. M. Kinka, J. Banys, W. Bohlmann, E. Bierwirth, M. Hartmann, D. Michel, G. Volkel and A. Poppl, *Ultrasonics, Ferroelectrics, and Frequency Control, IEEE Transactions on*, 2006, **53**, 2305-2308.
96. J. Texter, *Reactions And Synthesis In Surfactant Systems*, Taylor & Francis, 2001.
97. S. T. Hyde, *Handbook of applied surface and colloid chemistry*, 2001, 299-332.
98. S. M. Hant, *Characterization and fabrication of nanoporous materials by template-directed sol-gel methods.* PhD thesis. University of Southampton, 2008.
99. H. Ishikawa and T. Kikuchi, *J. Mater. Chem.*, 1998, **8**, 1783-1786.
100. T. Brezesinski, M. Groenewolt, A. Gibaud, N. Pinna, M. Antonietti and B. Smarsly, *Adv. Mater.*, 2006, **18**, 2260-2263.
101. M. Moniruzzaman and C. K. Das, *Macromol. Symp.*, 2010, **298**, 34-42.
102. T. Brezesinski, J. Wang, J. Polleux, B. Dunn and S. H. Tolbert, *J. Amer. Chem. Soc.* , 2009, **131**, 1802-1809.
103. S. Hamaguchi and H. Yoshitake, *Electrochemistry*, 2009, **77**, 373-378.
104. H. Choi, E. Stathatos and D. D. Dionysiou, *Appl. Catal., B*, 2006, **63**, 60-67.
105. J. C. Yu, X. Wang and X. Fu, *Chem. Mater.*, 2004, **16**, 1523-1530.
106. X. Fan, Y. Wang, X. Chen, L. Gao, W. Luo, Y. Yuan, Z. Li, T. Yu, J. Zhu and Z. Zou, *Chem. Mater* , 2010, **22**, 1276-1278.
107. B. Mattiasson, A. Kumar and I. Y. Galeaev, *Macroporous Polymers: Production Properties and Biotechnological/Biomedical Applications*, Taylor & Francis, 2009.
108. A. K. Srivastava, *Oxide Nanostructures: Growth, Microstructures, and Properties*, Pan Stanford, 2014.
109. M. Sadakane, T. Horiuchi, N. Kato, K. Sasaki and W. Ueda, *J. Solid. State. Chem.*, 2010, **183**, 1365-1371.

110. V. Shklover and H. Hofmann, *Handbook of Semiconductor Nanostructures and Nanodevices*, 2006.
111. J. Fang, Y. Xuan and Q. Li, *Chin. Sci. Bull.* , 2011, **56**, 2156-2161.
112. Y. An, S. J. Skinner and D. W. McComb, *J. Mater.Chem.*, 2010, **20**, 248-254.
113. J. E. Wijnhoven, L. Bechger and W. L. Vos, *Chem. Mater.*, 2001, **13**, 4486-4499.
114. Y. Ding, L. Yang, Y. Li, X. Wu, Y. Lu and J. Zhao, *J. Porous. Mater.*, 2013, **20**, 601-605.
115. A. Stein, B. E. Wilson and S. G. Rudisill, *Chem. Soc. Rev.*, 2013, **42**, 2763-2803.
116. M. E. Turner, T. J. Trentler and V. L. Colvin, *Adv. Mater.*, 2001, **13**, 180-183.
117. S. L. Kuai, X. F. Hu and V. V. Truong, *J. Cryst. Growth.*, 2003, **259**, 404-410.
118. W. Fan, H. Bai, G. Zhang, Y. Yan, C. Liu and W. Shi, *Cryst. Eng. Comm.*, 2014, **16**, 116-122.
119. C. F. Blanford, H. Yan, R. C. Schroden, M. Al-Daous and A. Stein, *Adv. Mater.*, 2001, **13**, 401-407.
120. M. E. Davis, *Nature*, 2002, **417**, 813-821.
121. R. E. Hummel, *Electronic Properties of Materials*, Springer, New York, 2011.
122. Z. Lei, J. Li, Y. Zhang and S. Lu, *J. Mater. Chem.*, 2000, **10**, 2629-2631.
123. B. Li, J. Q. Wang, R. Fujiwara, M. Kuwabara, M. Fu and J. Zhou, *Key Eng. Mater.*, 2010, **434**, 247-252.
124. A. Xiang, G. Jian Ping, C. Hong Kui, Y. Jiu Gao and R. X. LIU, *Chin. Chem. Lett.*, 2004, **15**, 228-230.
125. Y. Jin, Y. Zhu, X. Yang, C. Li and J. Zhou, *J. Solid. State. Chem.*, 2007, **180**, 301-306.
126. N. Matsuura, S. Yang, P. Sun and H. E. Ruda, *Appl. Phys. A*, 2005, **81**, 379-384.
127. J. Zhou, C. Q. Sun, K. Pita, Y. L. Lam, Y. Zhou, S. L. Ng, C. H. Kam, L. T. Li and Z. L. Gui, *Appl. Phys. Lett.*, 2001, **78**, 661-663.
128. I. Soten, H. Miguez, S. M. Yang, S. Petrov, N. Coombs, N. Tetreault, N. Matsuura, H. E. Ruda and G. A. Ozin, *Adv. Funct. Mater.*, 2002, **12**, 71-77.
129. I. S. Amiri and J. Ali, *Chin. Opt. Lett.*, 2013, **11**, 041901.
130. Y. Cun, Z. Yang, J. Liao, J. Qiu, Z. Song and Y. Yang, *Mater. Lett.*, 2014, **131**, 154-157.
131. J. K. Kim, C. Mao and J. Kim, *J. Phys. Chem. Solids.*, 2008, **69**, 1468-1470.
132. Y. N. Kim, E. O. Chi, J. C. Kim, E. K. Lee and N. H. Hur, *Solid. State. Commun.*, 2003, **128**, 339-343.
133. J. D. Joannopoulos, S. G. Johnson, J. N. Winn and R. D. Meade, *Photonic Crystals: Molding the Flow of Light (Second Edition)*, Princeton University Press, 2011.
134. K. Edagawa, *Sci. Technol. Adv. Mater.*, 2014, **15**, 1-15.
135. M. Sadakane, R. Kato, T. Murayama and W. Ueda, *J. Solid. State. Chem.*, 2011, **184**, 2299-2305.
136. C. Glaize and S. Genies, *Lithium Batteries and other Electrochemical Storage Systems*, Wiley, 2013.
137. J. C. Lytle, H. Yan, N. S. Ergang, W. H. Smyrl and A. Stein, *J. Mater. Chem.*, 2004, **14**, 1616-1622.
138. F. Ke, L. Huang, H. Jiang, H. Wei, F. Yang and S. Sun, *Electrochem.Commun.*, 2007, **9**, 228-232.
139. A. Esmanski and G. A. Ozin, *Adv. Funct. Mater.*, 2009, **19**, 1999-2010.

2. Instrumental techniques

2.1 Introduction

This chapter describes the techniques that have been used for the characterisation of films and powders produced during this project. X-ray diffraction (XRD) and scanning electron microscopy (SEM) were used to characterise the phase composition, morphology and thickness of the films. Sol speciation was also investigated using nuclear magnetic resonance (NMR) spectroscopy and mass spectrometry (MS).

2.2 X-Ray diffraction

X-ray diffraction (XRD) by crystals was discovered in 1912,[1] and the first collection of X-ray diffraction patterns of a copper sulphate penta-hydrate crystal was carried out in the same year by Friedrich and Knipping.[2] XRD is a non-destructive technique and is routinely used to study and determine the crystallographic structure and chemical composition of solid state materials. It provides information on structural parameters, for example the crystallite size, degree of crystallinity, and crystal defects.[3]

X-ray photons are produced when a beam of electrons from a heated filament with high-speed bombard a metal target. Thus, any X-ray tube necessarily comprises of a source of electrons (cathode), a high accelerating voltage and a metal target (anode). The electrons are accelerated to the anode, and then eject an electron in the metal atom out of its orbital, leaving a hole. An electron from another orbital in the atom can relax into this hole, releasing X-ray radiation in the transition (Fig. 2.1). Commonly a Cu $K_{\alpha 1}$ radiation source is used for powder XRD with wavelength λ=1.5406 Å.[3]

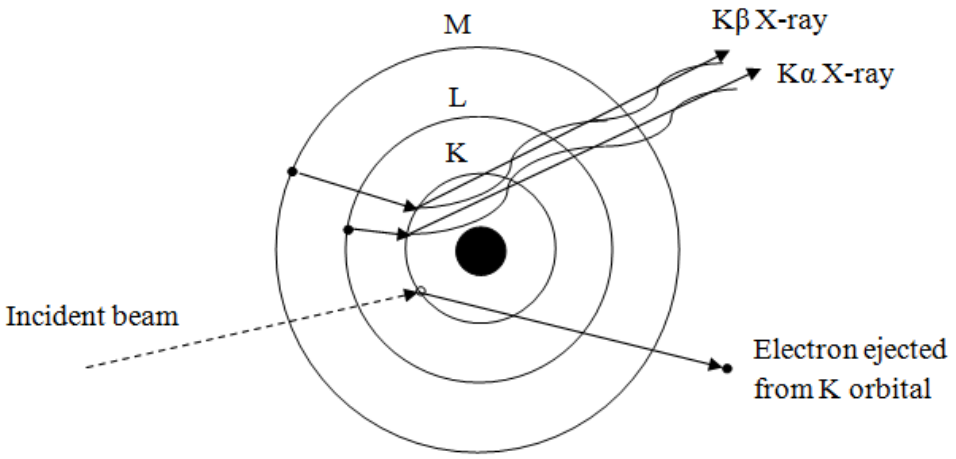

Fig. 2. 1 Theoretical diagram of the generation of X-rays.

A single-crystal monochromator is often used to produce a beam of radiation with a single X-ray wavelength for diffraction experiments. The monochromator is positioned in series between the incident X-ray beam source and the sample. This crystal monochromator is fixed in the correct orientation to diffract only X-ray photons of the preferred wavelength. The monochromated beam is collimated by an aperture diaphragm and before hitting the sample.[4] Alternatively a mirror may be used to focus the beam and remove most wavelengths apart from the $K\alpha_1$ and $K\alpha_2$ peaks. This set up allows a higher X-ray intensity.

Diffraction can be seen when monochromatic beam of X-rays is scattered by specific atoms within the target materials by constructive interference. The diffraction of X-rays by crystals is described according by Bragg's Law, which is:

$$n\lambda = 2d \sin\theta \qquad (2.1)$$

where n is an integer (1, 2, 3, ..); λ is the X-ray wavelength; θ is the angle of incidence ; d is the inter-planar separation in the crystalline material (the lattice spacing).

If incident X-ray beams, 1 and 2 strike the crystal at an angle of θ onto a set of parallel planes A and B and may be scattered by atoms lying on the planes separated by a distance *d*. When the conditions described by Braggs low are met the scattered photons are in phase and hence can interfere constructively. The d value can be calculated by measuring the diffraction maxima when $2d \sin\theta = 1\lambda, 2\lambda, 3\lambda \ldots n\lambda$ (Fig. 2.2).

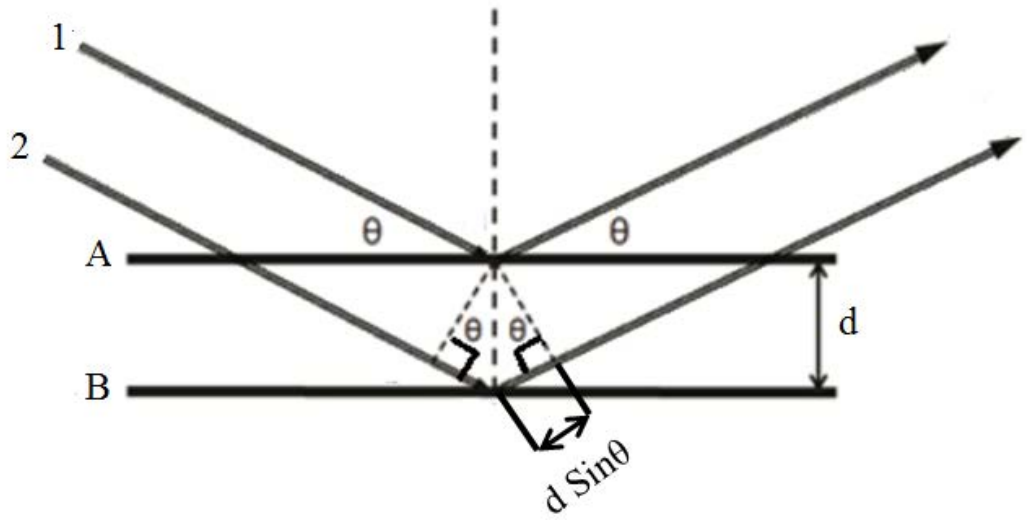

Fig. 2. 2 Schematic diagram of X-ray diffraction.

The powder X-ray diffraction (PXD) data collection for this study was carried out with a Siemens D5000 diffractometer (Cu $K_{\alpha 1}$). The PXD sample was ground to a fine powder to obtain a random distribution of small crystallites. A scintillation detector was scanned through different positions in Bragg-Brentano geometry in which the goniometer of the sample was rotated at a constant angular velocity while the detector was moved at double this velocity in order to ensure the incidence angle (θ) is fixed at half the diffraction angle (2θ). Fig. 2.3 shows a typical powder diffractometer. The collected data were analysed by using the Bruker Diffract Evaluation program (Eva) interfaced with PDF (Powder Diffraction File) to match and identify the unknown phase in the sample.

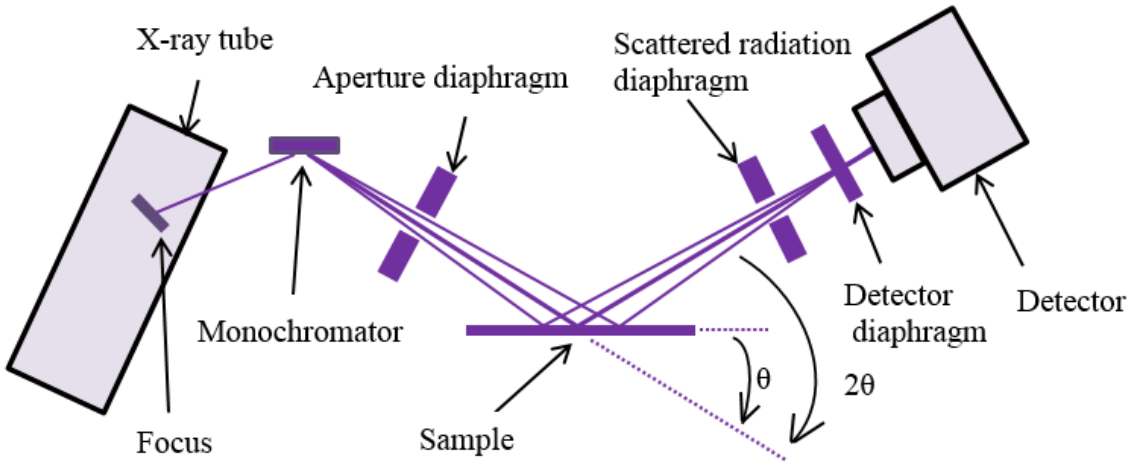

Fig. 2. 3 A schematic diagram of a powder X-ray diffractometer.

2.2.1 Thin film diffraction geometry

2.2.1.1 Grazing incidence X-ray diffraction (GIXRD)

To understand the crystallisation and phase information of the film, GIXRD geometry was employed, which is widely used for characterizing thin films to enhance the scattering contribution sensitivity from the film and decrease the observed substrate scattering[5] (Fig. 2.4). Using GIXRD, any phase change in the active film can be observed.

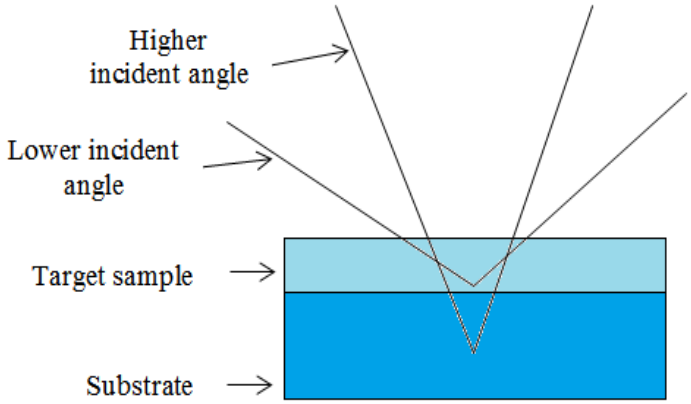

Fig. 2. 4 GIXRD geometry for thin film showing the effect of incident angle on path length within the film.

GIXRD measurement is based on irradiating the film with X-rays at small incidence angles (typically several degrees or less) with respect to the film surface and the detector is scanned across a range of 2θ angles to record diffraction intensities (Fig. 2.5). The travelling path of X-ray photons through the films is maximised and the path length (L) is determined by layer thickness (D) and the incidence angle (θ_{inc}), L = D / sin θ_{inc}. Very small X-ray incidence angles can contribute to the total external reflection from the surface Therefore, optimum GIXRD measurements are performed around the critical angle, which is the incident angle below which total external reflection occurs. The critical angle is a function of the X-ray wavelength and the density of the matter.[6]

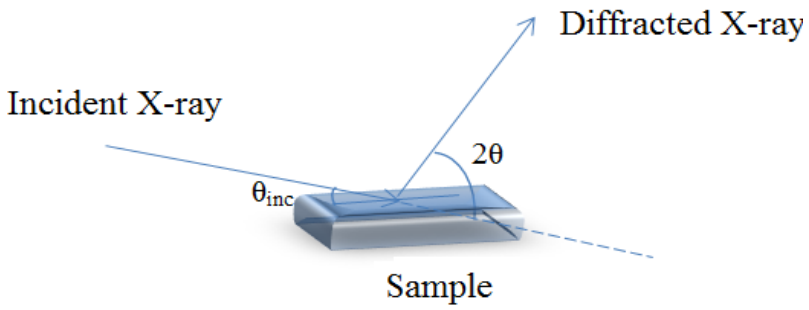

Fig. 2.5 A Schematic representation of grazing incidence X-ray diffraction measurement.

The XRD results were collected using grazing incidence X-ray diffraction (GIXRD) with Cu-K_α radiation using a Rigaku Smart lab Thin Film diffractometer and a Bruker D8 Discover powder diffractometer with General Area Detector Diffraction system (GADDS**).** The optical device used for Rigaku Smart lab is medium resolution parallel beam (PB) with a 0.1 mm incident slit and a 5 mm line delivered to the film surface at atypical incident angle of 1°. The optics used 5° incident and receiving soller slits and a DTex 250 1D detector. The patterns were collected in the 2θ range of 20-100°.

2.2.1.2 Grazing incidence small angle X-ray scattering (GISAXS)

GISAXS measurement was applied in this project to investigate the pore structure in the materials. It involves the X-ray photons being diffracted from pore wall normal to the sample surface (Fig. 2.6). It is a very useful measurement in thin film characterisation and it minimises the diffraction and background intensities from the substrate.[7]

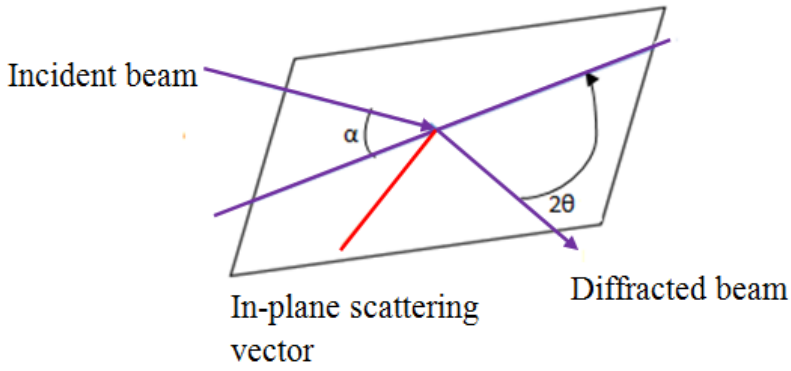

Fig. 2. 6 A Schematic representation of grazing incidence small angle X-ray scattering.

All XRD results of mesoporous films were collected using grazing incidence small angle X-ray scattering (GISAXS) with 9 kW Cu-K_α and Cu-K_α radiation using a Rigaku Smart lab Thin Film diffractometer and a Bruker D8 Discover powder diffractometer. For Smart lab, the in-plane arm and a DTex 250 1D detector with 0.25° incident angle, 0.5 º in-plane slit on the incident side and 0.228° parallel-slit analyser (PSA) in the detector side, and the data were collected from 1-10° 2θ. A Bruker D8 Discover powder diffractometer was used with 0.1° incident angle for the same studies.

2.2.2 Rietveld refinement

Since powder diffraction data (PXD) contains overlapping diffraction peaks, the structure information extracted from the pattern is difficult to obtain. H.M. Rietveld[8] realised that though many reflections did overlap and hence could not easily be modelled as single entities, the total intensity and the peak shape of a cluster of reflections can be determined by using simple peak shape parameters. Structural analysis in this thesis was routinely carried out using the General Structure Analysis Suite (GSAS).[8, 9]

The refinement was used to minimize the difference between the experimental diffraction pattern and the calculated data from the model by varying different parameters, includeding[10]:

- Application of an approximate model of the structure (e.g. from the ICSD database).
- Refinement the scale factor, zero point and lattice parameters.
- Refinement of the atom positions in the structure.
- Refinement of the isotropic thermal parameters.
- Refinement of peak shape and width (Lorentzian) to determine crystallite size and strain

Gaussian peaks were kept at values obtained by refining a LaB_6 or silica standard to define an instrumental peak shape for the specific film or powder diffraction geometry.

2.2.2.1 Crystallite size estimation from GSAS Refinement

Crystallite size can be estimated by a Rietveld refinement method in particular related to the peak shape. The equation for calculating the crystallite size (equation 2.2) can be achieved after rearrangement the complex expressions that applied to model the peak shape (mostly instrumental broadening) and Lorentzian (mostly sample broadening).[11]

$$p = \frac{18000K\lambda}{\pi X} \qquad (2.2)$$

where K is the Scherrer constant, λ is the X-ray wavelength usually (1.54 Å) and X is the Lorentzian component value that is extracted from a GSAS refinement.

The equation 2.2 was applied to calculate the particle size of the materials prepared in this work. The products that were annealed at low temperature possessed low crystallinity. In order to gain the best shape for the peaks of the patterns and good resolution, the samples have been collected using 0.02° step size to improve signal: noise ratio.

2.3 Scanning electron microscopy (SEM)

SEM is a high resolution surface investigation method with the ability to examine surface structure down to nanometre scale.[12] The microscope includes an electron gun (Fig. 2.7) that emits an electron beam therm-ionically from a heated tungsten filament; usually tungsten is used because it has a high melting point. The filament acts as cathode, the electrons emitted from it are accelerated by a positive charge placed down the gun column towards the anode and this generates a beam of high energy electrons. A negative potential is applied to the 'Wehnelt Cap' so that any emitted electron from the filament is repelled by that cap to the horizontal centre. The electrons are collected in the space between filament tip and Wehnelt Cap, called a space charge. Those electrons at the bottom of the space charge nearest to the anode can leave the gun area through a small hole moving down the column be used in imaging.[13]

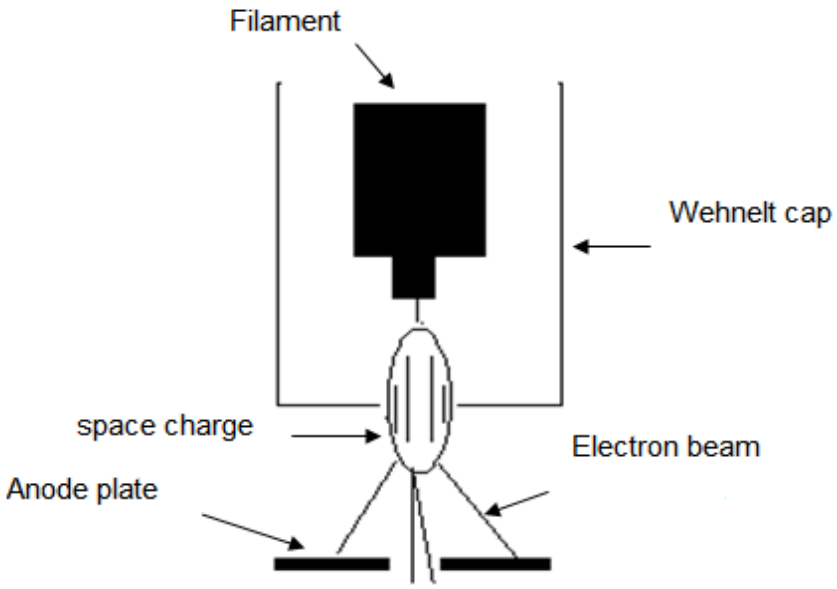

Fig. 2. 7 The electron gun in electron microscopy.

The beam of electrons is passed between two electromagnetic condenser lenses (demagnified). The first condenser lens is used to control the diameter of the beam and get rid of the high angle electrons and it limits the amount of current flowing in the beam whereas the second condenser lens forms the electrons into a thin, coherent beam. The objective lens focuses the scanning beam onto the part of sample to be examined[14] (Fig. 2.8).

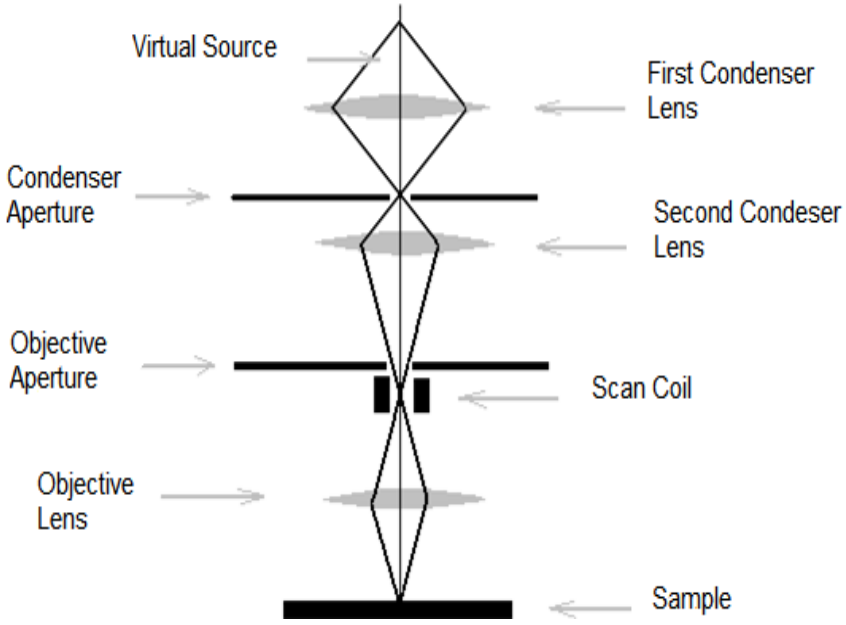

Fig. 2. 8 A schematic representation of the SEM system.

SEM was carried out using a XL30-ESEM microscope to examine surface morphologies and the cross- section of the films. High vacuum was used for semiconducting or conductive materials. Therefore, the electric current has electrical path to pass through to the sample. Environmental mode (E-SEM), in which a small pressure of water vapour is allowed to inter the measurement chamber, was applied for dielectric materials to prevent sample charging. Titania films were characterised by high vacuum SEM. Samples were stuck onto aluminium stubs using conductive carbon pads to provide the conductivity between the stub and the films.

2.4 Electron dispersive energy X-ray spectroscopy (EDX)

EDX is an analytical technique used to detect and identify the elemental composition of a specimen. This technique is utilised in combination with SEM. The measurements are based on the identification of the energy distribution of the X-ray photons. When the electron beam strikes a sample surface electron in an inner shell of one of the constituent atoms is excited by the X-ray beam. Removal from its orbital creates an electron vacancy and an electron from an outer, higher energy shell will fill that hole. The difference in energy between the higher -energy orbital and the lower one results in emission of energy in the form of an X-ray photon. The energy of these photons is measured in the EDX detector. Since these energies are a fingerprint of the atomic structure of the element from which they were emitted, the elemental composition of the sample can be examined.[15 16]

To combine EDX with SEM, it needs an X-ray detector, pulse processor, as well as an analyser system. A histogram of X-ray energy against intensity is the detection outcome in EDX system created by the detector. The detector converts the received X-ray photons to proportional amplitude of electronic pulses.[17] EDX is able to detect elements in compositions down to 0.1% atomic concentration. The high detection capability forms EDX an exceptional technique in detecting and quantifying small concentrations of elements in very small samples.

In this project the EDX spectra used for the films were collected using a Thermofisher Ultradry detector with Noran System 7 (NS7) analysis platform on a Philips XL30-ESEM. The spot size was increased from the SEM monitor until for high magnifications of around 1000x and a detector counts on the EDX monitor revealed a value of above 10,000. In the EDX experiments the live time was fixed at 100 seconds.

2.5 Mass Spectrometry (MS)

Mass spectrometry (MS) is an analytical technique is used to allow qualitative (structure) and quantitative (molecular structure) for small organic molecule and large molecular species such as proteins by converting the individual molecules to ions. The target molecules are ionised in the ionisation source by inducing either gain or loss of a charge from a neutral compound. Then the ions are moved directly to the mass analyser where they are separated according to their charge to mass (*m/z*) ratio and eventually detected.[18] The results of these processes, useable signals are displayed and recorded by a computer system. These signals are plotted against their intensities to show the molecular mass and the relative abundant of each ion according to their m/z ratio. Thus the structural information can be calculated.[19]

Electrospray ionisation (ESI) is a 'soft ionisation' technique and is widely used to produce gas phase ions without fragmentation. It can be used in conjunction with different mass analysers, such as it is widely used in combination with time-of-flight mass analyser (TOFMS). ESI techniques tend to prevent the problems that are associated with sample decomposition during the electron ionisation process.[20]

ESI works at atmospheric pressure. A sample dissolved in a polar, volatile solvent is injected through stainless steel capillary (75 -150 micrometers i.d) at a flow rate of 1–20 μL/minute with a high voltage (2-6 kV) applied to the tip of the capillary metal, resulting in producing an aerosol of highly charged droplets.[19] Positive and negative ions can be detected. In positive ion mode, the functional group of the sample analyte is protonated by H^+ or sodiated by Na^+ to confirm if the sample contains either of them , whereas the negative ion mode relies on deprotonation by loss of the protons.[21]

In this study the spectra of TiO_2 sols were collected using a Bruker maXis ESI-TOF. The mass data within 50 ppm were analyzed by using the MassLynx NT software to generate fragmentation in the mass range 50-2500 *m/z*. By matching the experimental *m/z* values to the *m/z* value from the computer programme, possible titania structures were evaluated.

2.6 Nuclear Magnetic Resonance Spectroscopy (NMR)

2.6.1 Basic principle

NMR spectroscopy relies on the spin quantum number, I, of a nucleus. Nuclei of particular isotopes have angular momentum. The total angular momentum relies on the spin number I with value range from 0, 1/2, 1, 3/2,…. depending on the certain nucleus. If I=0, the nucleus does not possess a spin and therefore can't be seen by this technique. Nuclei of I >0 have characteristic magnetic moments. When a magnetic nucleus is placed in an external magnetic field, a discrete set of (2I + 1) orientations could be adopted. For example, in nuclei with I=1/2 one of two orientations is possible that correspond to energy level ± μH in applied magnetic field, where H is the strength of the external magnetic field and μ is the magnetic moment of the spinning nucleus. NMR spectroscopy uses the magnetic spin energy of atomic nuclei of I= ½ such as ^{1}H, ^{13}C, ^{19}F, ^{29}Si and ^{31}P. A transition between these two energy levels can be and may be affected by the absorption or emission of amount of energy.[22]

2.6.2 Chemical shift

Each nucleus in a compound is surrounded by a cloud of electrons. When a magnetic field of H is subjected to a sample these electrons are circulated to oppose the field. This action will cause shielding the nucleus from the external field value and the effective magnetic field H_{eff} resulting from nuclei will not be equal.[23]

This shielding constant will vary based on the variation of local environment, particularly for the electron density around the nucleus under study. This will influence the energy required to be applied to make a transition and hence the resonance frequency characterises the surrounding environment of the nucleus.

The chemical shift (δ) is the resonant frequency of the nucleus relative to a standard. It expressed in ppm.

$$\delta = \frac{H_{sample} - H_{reference}}{H_{reference}}$$

where H_{sample} is the resonance frequency of the sample and $H_{reference}$ is the resonance frequency of a standard reference compound measured in the same magnetic field.

Tetramethylsilane, $(CH_3)_4Si$, usually referred to as TMS is used as a reference compound for proton and carbon NMR as it is chemically unreactive and easily removed from the sample after the measurement.[23]

When the level of atomic nucleus shielding is decreased the resonance frequency will be increased. Thus, the signal will be shifted to higher ppm value. For example, CH_3X where X is a highly electronegative element, have reduced electron density around the protons, and they resonate at lower field strengths that imply increasing δ values.[24] Since the shielding of the nucleus is affected by the atoms type surrounding it, so the chemical shift of nucleus under study will be possible to determine the type of chemical envirnment.[24]

NMR spectra were used in this study to invistugate the TiO_2 speciation in the sol and were collected using a Bruker AV400. The samples were prepareds in the glove-box by dissolving in deuterated chloroform ($CDCl_3$) and ^1H and $^{13}C\{^1H\}$ spectra collected using an autosampler. Low temperature experiments used CD_2Cl_2 solutions and were run manually.[25]

2.7 References

1. V. K. Pecharsky and P. Y. Zavalij, *Fundamentals of Powder Diffraction and Structural Characterization of Materials*, Springer, 2005.
2. B. D. Cullity, *Elements of X Ray Diffraction*, BiblioBazaar, 2011.
3. W. H. Zachariasen, *Theory of X-Ray Diffraction in Crystals*, Dover Publications, 2004.
4. E. Lifshin, *X-ray Characterization of Materials*, Wiley, 2008.
5. M. Birkholz, *Thin Film Analysis by X-Ray Scattering*, Wiley, 2006.
6. P. Dutta, *Curr. Sci.*, 2000, **2000**, 1478-1483.
7. A. Ogi and K. Inaba, *Rigaku J.*, 2011, **27**, 1-5.
8. H. M. Rietveld, *Acta Crystallogr.*, 1966, **20**, 508-513.
9. C. R. Brundle, C. A. Evans and S. Wilson, *Encyclopedia of materials characterization : surfaces, interfaces, thin films*, Butterworth-Heinemann ; Manning, Boston; Greenwich, CT, 1992.
10. H. Z. Morawiec and H. M. D. Stróż, *Applied Crystallography: Proceedings of the XIX Conference : Kraków, Poland, 1-4 September 2003*, World Scientific, 2004.

11. A. C. Larson and R. B. V. Dreele, *Los Alamos National Laboratory Report LAUR* 2004, 86-748.
12. G. McMahon, *Analytical Instrumentation: A Guide to Laboratory, Portable and Miniaturized Instruments*, Wiley, 2008.
13. J. Goldstein, D. E. Newbury, P. Echlin, D. C. Joy, C. Fiori and E. Lifshin, *Scanning Electron Microscopy and X-Ray Microanalysis: A Text for Biologists, Materials Scientists, and Geologists*, Springer US, 2013.
14. R. J. Ross and E. D. R. Committee, *Microelectronics Failure Analysis Desk Reference, 6th Ed (Book and CD Set)*, ASM Press, 2011.
15. R. J. Ross, *Microelectronics Failure Analysis: Desk Reference*, ASM International, USA, 2011.
16. A. Naranjo, M. P. Noriega, T. Osswald, A. R-Alzate and J. D. Sierra, *Plastics Testing and Characterization: Industrial Applications*, Carl Hanser Verlag, Munich.
17. P. H. Holloway, P. N. Vaidyanathan, C. R. Brundle and C. A. Evans, *Characterization of Metals and Alloys*, Momentum press, LLC,, New York, 2010.
18. R. K. Boyd, *Rapid Commun. Mass Spectrom.*, 1997, **11**, 948-948.
19. S. Banerjee, *J. Mass Spectrom.* , 2013, **48**, 193-204.
20. L. Latourte, J. C. Blais, J. C. Tabet and R. B. Cole, *Anal. Chem.*, 1997, **69**, 2742-2750.
21. T. D. Veenstra and R. D. Smith, *Proteome Characterization and Proteomics*, Elsevier Science, 2003.
22. J. Keeler, *Understanding NMR Spectroscopy*, Wiley, 2011.
23. Q. T. Pham, *Proton and carbon NMR spectra of polymers*, Wiley, 2003.
24. M. L. Naklicki, S. I. Gorelsky, W. Kaim, B. Sarkar and R. J. Crutchley, *Inorg. Chem.*, 2012, **51**, 1400-1407.
25. T. Sakai, H. Yano, H. Shibata, T. Endo, K. Sakamoto, H. Fukui, N. Koshikawa, H. Sakai and M. Abe, *Colloids and Surfaces A: Physicochemical and Engineering Aspects*, 2010, **371**, 29-39.

3. Sol-gel route for titanium dioxide (TiO_2) films, powders and mesoporous films

3.1 Introduction

TiO_2 has been widely studied in the form of thin films or powders due to the stability of its chemical structure, physical, optical ,electrical and photocatalytic properties.[1] Applications include the decomposition of unwanted and harmful organic compounds,[2] self-cleaning surfaces,[3] solar energy conversion[4] and charge storage.[5] Some applications in catalysis[6] and photocatalysis[7] can be improved by incorporating a template into the solid film and producing mesoporous structures.

The crystal structure of TiO_2 naturally is composed of three crystallographic phases, rutile (tetragonal), anatase (tetragonal), and brookite (orthorhombic). Although anatase is not as stable thermodynamically as rutile, it is often the preferred form due to its high photocatalytic activity (band gap: 3.2 eV), non-toxicity, high surface area and low price. The transformation of anatase to rutile phase depends on starting material, deposition method and calcination temperature. TiO_2 films and powders can be transformed from amorphous phase into crystalline anatase (~ 400 °C) and from anatase to rutile (~800 °C).[2]

A variety of physical and chemical approaches have been used for preparing TiO_2 powders and films. Dry processes include physical or chemical vapour deposition,[8, 9] e.g. the latter was used by Chimupala to synthesise TiO_2 thin films that were then annealed at 600 °C. Wet processes include hydrothermal methods[10] and sol-gel.[11-14] Sol-gel routes have been used extensively in the preparation of oxide films and powders, and mesoporous films[15] due to their low cost, simple operating procedures, purity and homogeneity. In film synthesis they can cover large areas and the thickness can be controlled easily by changing the withdrawal speed (dip-coating and spin-coating) and concentration of the sol. The sol-gel process can be controlled by many factors, such as pH, catalyst, alkoxide/water ratio and temperature.[16]

Typically in metal oxide sol-gel processes it is necessary to include a reaction moderator to block coordination sites and therefore reduces reactivity. These include ethanolamine,[17] acetylacetone[18] and acetylacetone with polyethylene glycol[19] and controlled amounts of water can then be added if it is needed.

Acetylacetone (acac) has been used in the preparation of TiO_2 films on silicon substrates by dip coating. The structural characterisation of these films revealed the anatase phase of TiO_2 after heating at 400 °C, whereas at 800 °C the coexistence of the anatase and rutile phases was observed. In contrast, the rutile phase appeared at 700 °C in the xerogel. The authors[20] attributed of delay of crystallization of the rutile phase in the films to the presence of the silicon substrate and to acetic acid modification that stabilises the anatase phase by about 100 °C.

Diethanolamine (DEA) has been used to prepare TiO_2 powders from ethanolic solutions of titanium isopropoxide ($Ti(O^iPr)_4$)[21] and the transition between anatase and rutile occurred at 561 °C. Similar work by Murugan et al.[17] showed the threshold of TiO_2 rutile formation in powders to be at 600 °C and the percentage of the rutile was increased by increasing the amount of DEA. Another study has been conducted using isopropanol as a solvent by Takahashi and Matsuoka[22] and they reported the transformation from anatase to rutile start from 550 to 600 °C. Also, Hu et al.[23] and Yu et al.[24] have utilised titanium butoxide ($Ti(O^nBu)_4$) as a precursor to prepare TiO_2 thin films, with no observation for rutile up to the highest temperature of 400 or 500°C. DEA had the effect of increasing the rutile transformation temperature.

No literature exists on using $Ti(O^iPr)_4$ with DEA in ethanolic solutions to prepare TiO_2 films except the work of Verma et al.[21] who produced TiO_2 films by spin coating and observed no rutile for films annealed up to 560 °C.

TiO_2 thin films and powders can also be prepared under acidic solution without moderation. Nishide et al.[25] investigated the effect of HNO_3 as a catalyst on the crystallisation and they reported the rutile was transformed at temperatures between 550 °C and 600 °C, with the rutile content increasing gradually with increasing temperature.

Kim et al.[26] used HCl as a catalyst and anatase-to-rutile phase transformation occurred at 1000 °C, the authors have concluded the phase transition depends on the materials used and the catalyst concentration.

Limited studies into the mechanism of hydrolysis and polycondensation in titania sol-gel processes exist. Knowledge of the speciation in the TiO_2 sols is critical to understanding why the differences in the film morphology and phase behaviour observed in TiO_2 occur and could allow us to improve the behaviour of TiO_2 as well as of ternary compounds, such as $BaTiO_3$. Mass spectrometry (MS) and nuclear magnetic resonance (NMR) are obvious options to interrogate species in solutions.

Mass spectrometry in general and electrospray ionisation mass spectrometry (ESI-MS) in particular is an important analytical tool that allows the determination of accurate molecular masses of organic and inorganic species. The ESI method is capable of measuring large molecular species[27] and allows mass spectral analysis of the species in the gas phase with minimum fragmentation. Coupling ESI with time of flight measurement is of even greater for the characterization of complicated sol-gel system by isolating single ions from an analyte. Simonsen et al.[28] used ESI-MS to identify the titanium clusters in solution from different titanium alkoxides at various pH values. They found the pH did not significantly affect the nature of the titanium clusters. The same group[29] concluded that the number of titanium atoms in the cluster relied on the alkoxide used. With titanium isopropoxide 11-12 Ti atoms were observed whereas with titanium butoxide this fell to 10-11 Ti atoms and with titanium tetraethoxide ($Ti(OEt)_4$) to 5-7 Ti atoms.

NMR can improve the understanding of polymeric systems, such as sols, by following the species present via their ^1H and ^{13}C NMR shifts.[30] Jung et al.[31, 32] have followed by ^1H and ^{13}C NMR spectroscopy on the preparation of modified $Ti(O^iPr)_4$ with different modifiers such as acac, ethylacetoacetate (Etac) and methylacetoacetate (Mtac). They found there was coordination of the modifier to titanium and that the degree of coordination decreased in the sequence Ti- Mtac > Ti-Etac > Ti-acac. Benfer et al.[33] have concluded that by using ^{13}C NMR spectroscopy, the isopropoxide groups have been substituted by DEA from the reaction of $Ti(O^iPr)_4$ with DEA.

Ordered mesoporous TiO_2 films can be obtained by surfactant- templating through the well-known evaporation induced self-assembly (EISA) process. This is a heavily used technique due to the ability to control precisely both the pore dimensions and their spatial organisation by adjusting the composition and molecular weight of the surfactant.[34] This method was first used by Brinker and co-workers in 1992 for synthesis of mesoporous silica film and it is also effective for the preparation of ordered mesoporous TiO_2 thin films.[35]

The fabrication of mesoporous TiO_2 thin films is strongly dependant on the film preparation conditions, variation of the composition of reaction components, precursor and template type. However, the formation of mesoporous TiO_2 films have suffered from some drawbacks, such as the collapsed mesoporosity during crystallisation of the framework.Yu et al.[36] prepared cubic ordered mesoporous TiO_2 films with 4.6 nm pores by the thermal treatment of films prepared using a polyethyleneoxide-polypropyleneoxide–polyethyleneoxide block copolymer of EO_{20}-PO_{70}-EO_{20} (Pluronic P123). Koh et al.[37] obtained TiO_2 films with 10-25 nm pores by using an amphiphilic graft copolymer. Whereas Gan et al.[38] synthesised 7.9 nm mesoporous TiO_2 films using a tri-block copolymer (Pluronic F127) , the same surfactant was used by Hing pan to prepare hexagonal mesoporous TiO_2 film with pore size of 16.9 nm.[39]

The prime aim of this chapter was the comparison between different speciation of TiO_2 sols prepared by sol-gel process in either presence of modifier or catalyst without modifier in terms of the crystallization behaviour and their morphologies by XRD and SEM. NMR and MS were used to demonstrate TiO_2 species in the sols. There were also many attempts to prepare hexagonal order structure of mesoporous TiO_2 with dense crystalline pore walls by P123 on glass substrate by using dip-coating sol-gel method.

3.2 Experimental procedures

All reagents were purchased from Sigma-Aldrich and solvents from Fisher Scientific. Titanium dioxide powders and films were prepared using moderated sol-gel techniques. The DEA- moderated processes (T2 and T3-DEA) were adapted from that reported on TiO_2 powders by Murugan et al.[17] and this method have been developed to synthesise TiO_2 films successfully.

3.2.1 Preparations of TiO_2 sols

TiO_2 sols in each experiment were prepared by mixing the titania precursors with alcoholic solution in the presence of the modifier or catalyst (Table 3.1). The solution was stirred for 2 hours and the resultant transparent sol was aged in a sealed bottle at room temperature for 24 hours.

Table 3.1 Contents of TiO_2 sols.

Sol type	Titanium reagent, amount	Solvent, amount	Modifier /catalyst, amount
T1-HCl	$Ti(O^iPr)_4$, 10 mL	^iPrOH, 50 mL	HCl, 0.4 mL of 2M solution
T2-DEA	$Ti(O^iPr)_4$, 10 mL	EtOH, 30 mL	DEA, 3mL
T3-DEA	$Ti(O^iPr)_4$, 10 mL	EtOH, 30 mL	DEA, 7mL
T4-DEA	$Ti(O^nBu)_4$, 7 mL	EtOH, 30 mL	DEA, 1.5 mL

3.2.2 Preparations of TiO_2 films and powders

Microscope glass slides (10 × 20 mm) were used as substrates for sol-gel dip-coating. The slides were immersed in dilute nitric acid (1 M) for one hour in order to remove organic contamination and dirt, ultrasonically cleaned with distilled water and dried in an oven at 130 °C for 24 hours. Using a Nima Technology D1L dip-coater, a 10 × 10 mm region of the substrate was immersed once into the coating sol for 30 minutes and removed at a constant withdrawal speed of 60 mm minutes^{-1}.

The drop of excess sol at the bottom of the substrate was removed with tissue and then immediately the deposited films on the glass were wiped off from one side using ethanol while keeping the film on the other side. The films were placed horizontally on a petri dish to age/dry in air for ~ 60 minutes before calcining in air by placing into a pre-heated furnace at 600 °C for 5, 10, 20 or 40 minutes.
TiO_2 powders were prepared by drying and evaporating the remaining sols of each precursor in a Petri dish at room temperature after production of coatings. The resultant solid was ground by mortar and pestle and calcined as for the films at 600 °C for 5, 10, 20 or 40 minutes.

3.2.3 TiO_2 sol preparation for MS

Sols were prepared as described in section 3.2.1, and then diluted to 50 ppm concentration in dry acetonitrile using standard Schlenk and vacuum line techniques. The vials were sealed in the glove-box under a dry nitrogen atmosphere.

In some cases $NaNO_3$ (0.00061 g) was dissolved into TiO_2 sol (0.1 mL, T3-DEA) before addition of dry acetonitrile to achieve the described 50 ppm concentration. This was to provide sodium ions in an attempt to control the positive ion formation and simplify the mass spectra.

3.2.4 TiO_2 sol from $Ti(O^iPr)_4$ with 2 equivalents of DEA for NMR

In a Schlenk tube, $Ti(O^iPr)_4$ (5mL) was mixed with 2 equivalents of DEA (3.8 mL) in EtOH (15 mL).The mixture was stirred for 2 hours under nitrogen atmosphere and aged for 24 hours at room temperature. The solvent was removed completely under vacuum. In the glove-box, 2 drops of the product was mixed with chloroform ($CDCl_3$, 1 mL) for NMR study.

3.2.5 TiO_2 sol from $Ti(OEt)_4$ with 2 equivalents of DEA for NMR

In order to study the effect of $Ti(OEt)_4$ in the TiO_2 sol, the same experiment as section 3.2.4 was repeated by replacing $Ti(O^iPr)_4$ with $Ti(OEt)_4$ (3.54 mL).

3.2.6 $Ti(OEt)_4$ preparation

Due to (~20 %) impurities of $Ti(O^iPr)_4$ observed in commercial $Ti(OEt)_4$, pure $Ti(OEt)_4$ was prepared. A solution of $TiCl_4$ (12 mL) in C_6H_{14} (50 mL) and EtOH (40 mL) was cooled in a Schlenk flask under nitrogen atmosphere using a salted ice bath. After 30 minutes, 52 mL of Et_3N was added to the yellow suspension and the mixture was stirred for 10 minutes. C_6H_{14} (100 mL) was added to the suspension and left stirring for 30 minutes. The suspension was filtered, and the solvent was evaporated in vacuo at ~ 40 °C. The viscous liquid product after solvent removal was distilled *in vacuo*. In the glove-box, 2 drops of the product was mixed with chloroform ($CDCl_3$, 1 mL) for NMR study.

3.2.7 $Ti(OEt)_4$ with variation DEA

Various equivalents of DEA were used in sequence and waiting for 1 hour between the next sample to study their effect on the Ti ion. Under inert atmosphere in a Schlenk tube, (0.6 mL) of commercial or synthesised (section 3.2.6) $Ti(OEt)_4$ was mixed with sequentially increasing molar equivalents of DEA over a time period (Table 3.2) in $CDCl_3$ or CD_2Cl_2 (9.4 mL). After running the first sample by taking 1 mL of the sol, the calculated DEA amount was added to increase number of mol equivalent in 0.25 steps. Samples were allowed to equilibrate for 1 hour and then 1 mL was taken for NMR experiment. Two different temperatures were used for this experiment, ambient temperature (22 °C) or lower temperature (< 0 °C).

Table 3. 2 Different molar equivalents of DEA.

Time (hour)	$Ti(OEt)_4$: DEA (Molar ratio)	Volume (mL) of DEA added
0	0.25	0.06
1	0.5	0.054
2	0.75	0.048
3	1	0.042
4	1.25	0.036
5	1.5	0.03
6	1.75	0.024
7	2	0.018

3.2.8 Synthesis of mesoporous TiO_2 films using P123 surfactant

In a round bottom flask containing a solution of P123 (average *n*/*m* = 20/70, MW = 5800) was prepared in EtOH (8.7 mL) and deionised water (0.9 mL). The mixture was stirred until all the solid had dissolved. A solution of $Ti(O^iPr)_4$ (3 mL) in HCl (concentrated, 37%, 0.5 mL) was added slowly to the template solution. The mixture was stirred for 5 minutes. The resulting solution was aged at 4 or 34 °C for 10 minutes. The transparent and stable solution was used for dip-coating. The slides were immersed 3 times into the templated sol for 10 seconds then withdrawn at a constant withdrawal speed of 60 mm minutes^{-1}. After each dip-coating, the slides were kept horizontally to dry for 300 seconds before dipping again. Once coating was complete the films were aged at 4 °C for 24 hours. Alternatively the dipping and aging process were carried out at 34 °C. The TiO_2 films were exposed to NH_3 vapour for 10 seconds to enhance the thermal stability of the pore structure[40] before drying for 12 hours at 60, 80, 120 or 200 °C. The dried TiO_2 films were calcined at 300, 400, 500 or 600 °C for 4 hours (1 °C minutes^{-1} ramping rate) in air.

The crystallisation and phase transformation of TiO_2 films were examined by grazing incidence X-ray diffraction (GIXRD) using a Rigaku Smartlab Thin Film diffractometer with Cu-K_α radiation. Mesoporous films were collected using grazing incidence small angle X-ray scattering (GISAXS) by a Bruker D8 Discover powder diffractometer with 0.1° incident angle. TiO_2 powders were examined by powder X-ray diffraction (PXD) using a Siemens D5000 with Cu $K_{\alpha1}$. Rietveld fitting used the GSAS package[41] and structural models from ICSD.[42] Crystallite sizes were extracted from the GSAS particle size broadening term as described in the GSAS manual.[43] Film thickness and surface morphology were studied using a Philips XL30-ESEM microscope. Energy dispersive X-ray (EDX) spectroscopy used a ThermoFisher Ultradry probe. ^1H and $^{13}C\{^1H\}$NMR spectra were collected using a Bruker AV-300 with an autosampler (ambient temperature) or an AV-400 (low temperature) and deuterated chloroform or dichloromethane solvents. Mass spectra were collected from diluted acetonitrile solutions with a Bruker maXis ESI-TOF spectrometer operating in ES^+ mode.

3.3 Phase behaviour of TiO_2 films and powders

TiO_2 films and powders were synthesised from a number of sols recipes based on titanium alkoxide in the presence of a modifier (DEA) or with an acidic catalyst (HCl) and no modifier. The comparison between these sols in terms of films morphologies and their crystallisation behaviour will be discussed in the following sections using SEM and XRD data. MS and NMR were used to study the species in the solution, due to the interest in speciation in the TiO_2 sols and understanding their behaviour to understand the behaviour of TiO_2 deposition. The interest was extended to prepare mesoporous TiO_2 films using a series of surfactant compositions based on block copolymer (P123).

3.3.1 Effect of sols preparation on the TiO_2 films and powders morphology

TiO_2 films and powders were prepared using different sols preparation types (Table 3.1) and annealed at 600 °C due to it is the crystallisation temperature for the TiO_2 and their effects on the morphology were discussed in the following steps.

3.3.1.1 HCl catalyst

TiO_2 films and powders were prepared from $Ti(O^iPr)_4$ with ^iPrOH solution in the presence of HCl catalyst (T1-HCl). The SEM of the surface and cross-section of TiO_2 films and annealed at 600 °C for 5 minutes is shown in Fig. 3.1.The surface displayed cracking could be from the chemical reaction of drying shrinkage of TiO_2 particles or from the difference in the thermal expansion coefficients between glass and the TiO_2 films. The other reason can be contributed in cracked film was the thickness, as the thickness was measured as 1.6 µm resulting from the concentration of HCl (2 M) used which can be contributed in producing thicker films.[22, 44] The film has reduced in its thickness when it annealed for 40 minutes due to loss of organic mass during the annealing process which promote the densification in the TiO_2 film particles by sintering[45] (Fig. 3.1).

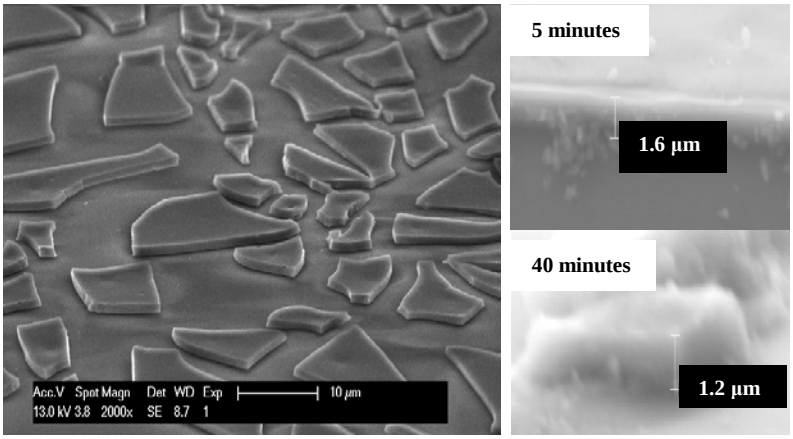

Fig. 3.1 SEM image of the TiO_2 films prepared by T1-HCl and annealed at 600 °C for 5 minutes (left), and cross section of films annealed for 5 minutes and 40 minutes (right).

3.3.1.2 DEA modifier

TiO_2 films and powders were prepared from $Ti(O^iPr)_4$ or $Ti(O^nBu)_4$ in ethanolic solution with DEA modifier. Fig. 3.2 shows the surface morphology of different TiO_2 films made using sols T2-DEA, T3-DEA and T4-DEA (Table 3.1) and annealed for 5 minutes. It was evident from the micrographs that the films produced from 7 mL DEA (T3-DEA) were flat and crack free with a thickness of 961 nm. Cracks appeared more significant when reducing the DEA amount to 3 mL (T2-DEA) and thinner films were obtained (540 nm). However, by using 1.5 mL DEA the film has some irregular shape in the top surface and the thickness value of 404 nm.

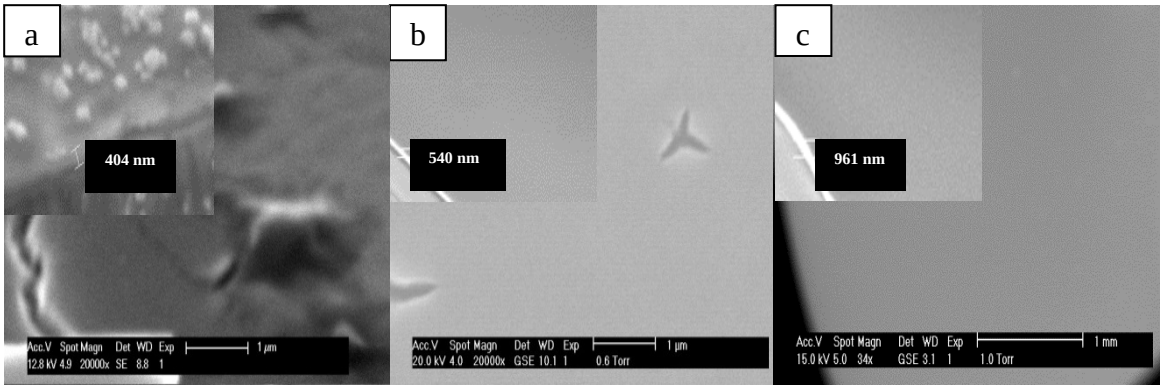

Fig. 3. 2 SEM images of the TiO_2 films prepared by (a) 1.5 mL DEA (T4-DEA), (b) 3 mL DEA (T2-DEA) and (c) 7 mL DEA (T3-DEA) and their thicknesses (inset).

3.3.1.3 Thickness of TiO_2 films

The thickness of TiO_2 films were controlled by several parameters:

1- The number of coating cycles
2- The concentration of the sol
3- The substrate withdrawal speed
4- The annealing treatment

The relation between the TiO_2 film thicknesses and the number of coating cycles is directly proportional, Cernigoj et al.[46] reported the TiO_2 thickness was increased by repeating the immersion and annealing treatment cycle five times. The effect of the concentration of the TiO_2 sol on the thickness of TiO_2 films was also examined, and at higher concentration of DEA caused higher viscosity of the solution. Therefore higher viscosity of the sol is contributing to produce thicker films as observed in Fig. 3.2 and it was in agreement with Chen et al.[47].

Based on the Landau –Levich[48] equation, 1.9 (section 1.7.2, introduction), the variation of the pull-up rate of the substrate from the sol and the thickness of film are directly proportional.

TiO_2 films prepared with DEA modifier produced the best films, however the optimum amount of DEA also needed to be found.

3.3.2 XRD refinement approach

Rietveld refinement of the XRD pattern was performed using GSAS.[49, 50] Standard patterns were obtained from ICSD,[42] and data from TiO_2 films and powders prepared using sol, T1-HCl, T2-DEA, T3-DEA and T4-DEA (Table 3.3), and fired at 600 °C for 5, 10, 20 or 40 minutes (appendix) were examined. The phase fractions of each film and powder, and their calculated average crystallite size from the Lorentzian components, were obtained from the corresponding Rietveld refinement.

3.3.3 XRD data for T1-HCl

The XRD patterns of TiO_2 films and powders prepared from sol T1-HCl, using an acidic catalyst, are shown in Fig. 3.3. The diffractogram revealed that the TiO_2 films and powders are single phase anatase. As the heating period increased from 5 to 40 minutes, the intensities of the anatase peaks for TiO_2 powders and films were increased slightly.

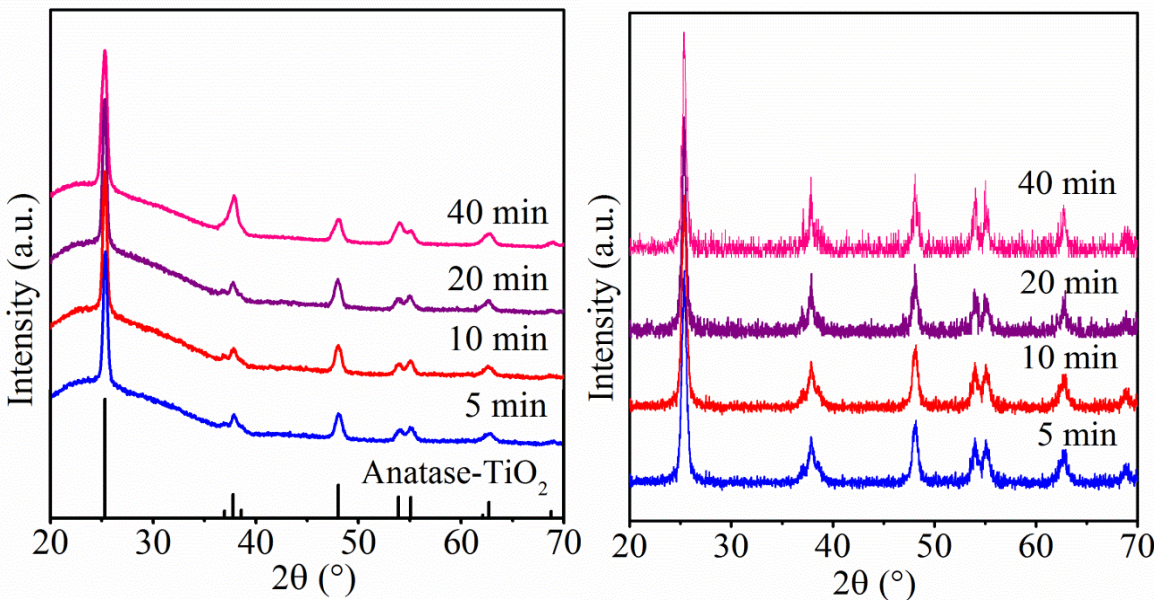

Fig. 3. 3 XRD patterns of TiO_2 films (left) and powders (right) prepared from sol T1-HCl and calcined at 600 °C for shown periods, compared with standard TiO_2 pattern from ICSD.[51]

Rietveld refinement of the film and powder XRD patterns were refined and (Fig. 3.4) shows a good fit of the anatase phase and a refined crystallite size for film and powder was 32.2 (8) nm and 46.5 (8) nm, respectively.

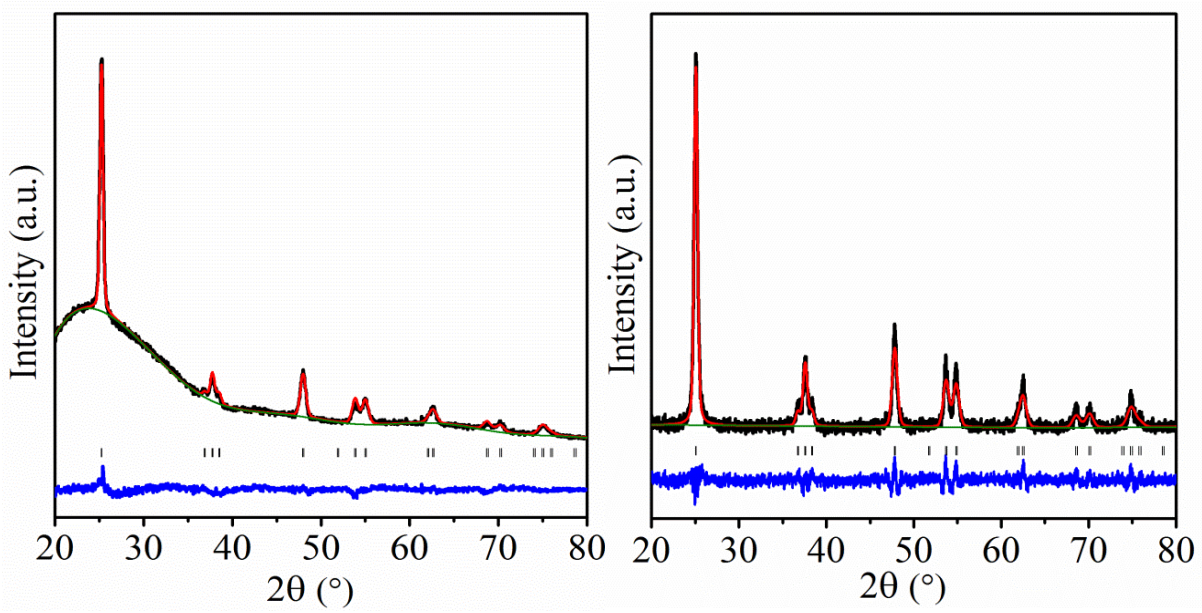

Fig. 3. 4 A Rietveld fit to the XRD for a film and a powder and heated at 600 °C for 20 minutes. Rietveld fit results for films (left): R_{wp} = 3 %, R_p = 2 %, U_{iso} = 0.01. Rietveld fit results for powders (right): R_{wp} = 10 %, R_p = 8 %. The black line shows the data points, the red solid line the fit and the lower continuous line the difference. Tick marks show the allowed positions of reflections for anatase TiO_2 in $I4_1/amd$.[51] The atom positions were not refined.

Based on Table 3.3, the average refined lattice parameters of each XRD refined pattern of films and powders are closed to previously reported values a = 3.7842(13) and c = 9.5146(15) Å.[51] Refined crystallite sizes of films and powders annealed at 600 °C for various periods are given in Table 3.3. The crystallite size increased with firing time.

Table 3. 3 Rietveld refined parameters and analytical data for T1-HCl films and powders.

Time (min)	Film			R_p/R_{wp} (%)	Powder			R_p/R_{wp} (%)
	a / Å	*c* / Å	Crystallite size/nm		*a* / Å	*c* / Å	Crystallite size/nm	
5	3.7829(8)	9.4926(1)	26.2(5)	3/2	3.7874(9)	9.5104(6)	31(4)	17/20
10	3.7853(6)	9.5058(2)	28.1(6)	2/3	3.7833(7)	9.5069(3)	39.3(3)	10/14
20	3.7871(3)	9.5112(5)	32.2(8)	2/3	3.7849(6)	9.5108(5)	46.5(8)	8/10
40	3.7850(6)	9.5070(2)	41(9)	2/2	3.7905(10)	9.5303(8)	62.4(2)	2/3

3.3.4 XRD data for T2-DEA, T3-DEA and T4-DEA

XRD patterns (Fig. 3.5) for TiO_2 films obtained from T2-DEA (Table 3.1) show mixed phase of anatase and rutile at 600 °C for various time. Anatase peaks are the most intense for these fired films and the anatase peaks decreased in intensity with increasing firing temperature, while rutile peak intensities increased.

XRD patterns were refined with the reported anatase phase $I4_1/amd$ [51] and rutile phase $P4_2/mnm$.[52] The fit to the crystalline TiO_2 film (Fig. 3.6) is good. Table 3.4 demonstrates annealing for longer periods (from 5 to 40 minutes) and this led to the growth of rutile phase content from 3 % to 11 %. The average of refined lattice parameters for all TiO_2 film are closed to the standard value of anatase a = 3.7842(13) and c = 9.5146(15) Å,[51] and rutile a = 4.5937 and c = 2.9587 Å.[52] Refined crystallite sizes for anatase and rutile are shown in Table 3.4.

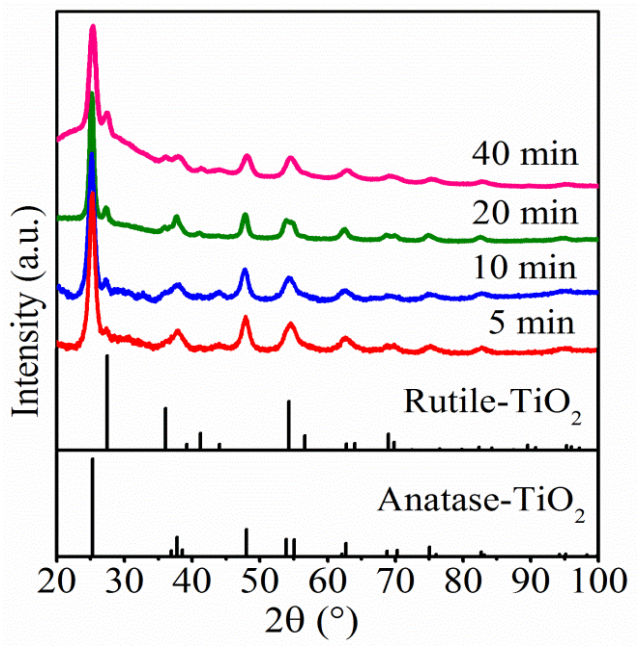

Fig. 3. 5 XRD patterns of TiO_2 films prepared by sol T2-DEA,and heated at 600°C for shown periods, compared with standard TiO_2 patterns for anatase[51] and rutile[52] from ICSD.

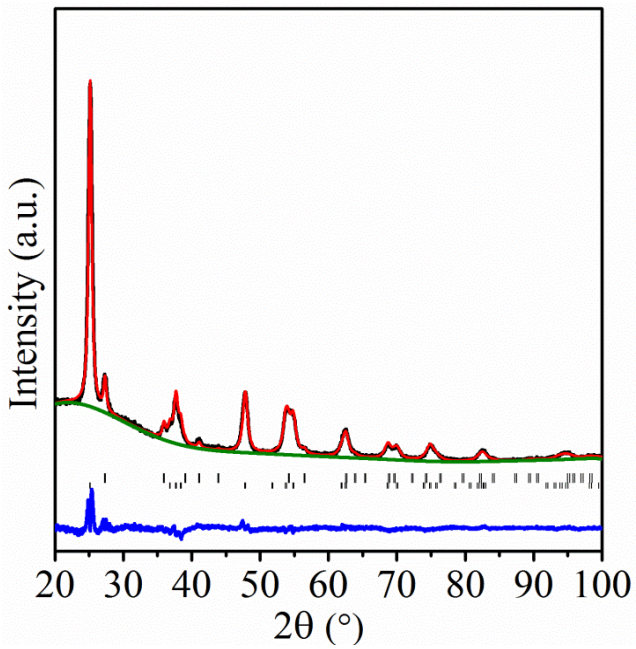

Fig. 3. 6 A Rietveld fit (R_{wp} = 9%, R_p = 7%) to the mixed phase anatase and rutile TiO_2 film XRD. Films were heated at 600 °C for 20 minutes. Anatase TiO_2 (93%, lower tick marks), $I4_1/amd$ [51] and rutile TiO_2 (7%, upper tick marks), $P4_2/mnm$.[52] The black line shows the data points, the red solid line the fit and the lower continuous line the difference. The atom positions were not refined.

Table 3. 4 Rietveld refined parameters and analytical data for T2-DEA film.

Time / min	Anatase (A)			Rutile (R)			A/R (%)	R_p/R_{wp} (%)
	a / Å	*c* / Å	Crystallite size/nm	*a* / Å	*c* / Å	Crystallite size/nm		
5	3.7868(13)	9.4722(7)	11.2(3)	4.5786(9)	2.9442(8)	17.8(4)	97/3	11/13
10	3.7884(2)	9.4723(4)	13.5(4)	4.5780(1)	2.9671(7)	20(29)	96/4	5/9
20	3.7775(1)	9.4709(1)	19.6(5)	4.5740(5)	2.9527(3)	26.2(5)	93/7	7/9
40	3.791(6)	9.5147(2)	35.7(4)	4.5978(6)	2.9627(8)	32(7)	89/11	6/9

Refined pattern for TiO_2 powder prepared by sol T2-DEA and annealed at 600 °C for 20 minutes (Fig. 3.7). The phase fractions, refined lattice parameters and crystallite size are given in Table 3.5. So, the lattice parameters for anatase and rutile were higher for powder fired for 5 and 20 minutes than the previous report value of anatase *a* = 3.7842(13) and *c* = 9.5146(15) Å,[51] and rutile *a* = 4.5937 and *c* = 2.9587 Å.[52]

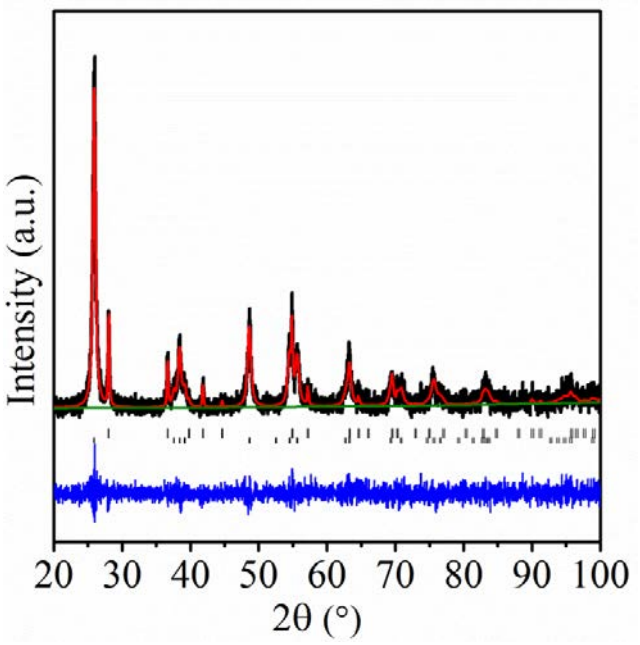

Fig. 3. 7 A Rietveld fit (R_{wp} = 10 %, R_p = 8 %) to the mixed phase anatase and rutile TiO_2 powder XRD heated at 600 °C for 20 minutes. Anatase TiO_2 (92 %, lower tick marks), $I4_1/amd$[51] and rutile TiO_2 (8%, upper tick marks), $P4_2/mnm$.[52] The black line shows the data points, the red solid line the fit and the lower continuous line the difference. The atom positions were not refined.

Table 3. 5 Rietveld refined parameters and analytical data for T2-DEA powders.

Time /min	Anatase (A)			Rutile (R)			A/R (%)	R_p/R_{wp} (%)
	a / Å	*c* / Å	Crystallite size/nm	*a* / Å	*c* / Å	Crystallite size/nm		
5	3.7907(4)	9.4866(5)	13.5(2)	4.6040(3)	2.9666(5)	19.6(5)	96/4	10/12
10	3.7866(1)	9.5017(7)	16.1(2)	4.5953(9)	2.9620(3)	34.2(3)	94/6	6/7
20	3.7925(7)	9.5255(8)	22.4(3)	4.6026(3)	2.9658(1)	60.5(2)	92/8	13/17
40	3.7874(9)	9.5183(1)	34.6(1)	4.5948(9)	2.9600(7)	104(2)	63/37	10/14

The diffraction patterns for TiO_2 film prepared from sol T3-DEA and annealed at 600 °C for various time are shown in Fig. 3.8. The intensity of rutile phase was increased by prolonging the firing time up to 40 minutes. The Rietveld fit of the sample fired at 600 °C for 20 minutes (Fig. 3.9). Table 3.6 shows the refined lattice parameters are closed to the literature value for anatase a = 3.7842(13) and c = 9.5146(15) Å,[51] and rutile a = 4.5937 and c = 2.9587 Å[52] for film fired for 10 minutes, while higher for other films. Crystallite sizes (Table 3.6) were obtained from the Lorentzian broadening using the adaptation of the Scherrer equation given in the GSAS manual.[49, 50] Increasing the amount of DEA was increased the rutile content up to 30% by firing for 40 minutes.

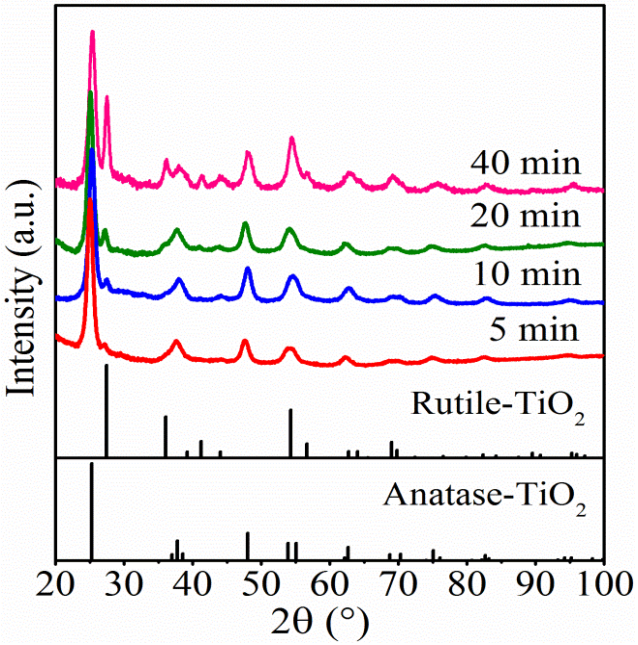

Fig. 3. 8 XRD patterns of TiO_2 films prepared by sol T3-DEA and heated at 600°C for periods shown, compared with standard pattern for anatase[51] and rutile[52] from ICSD.

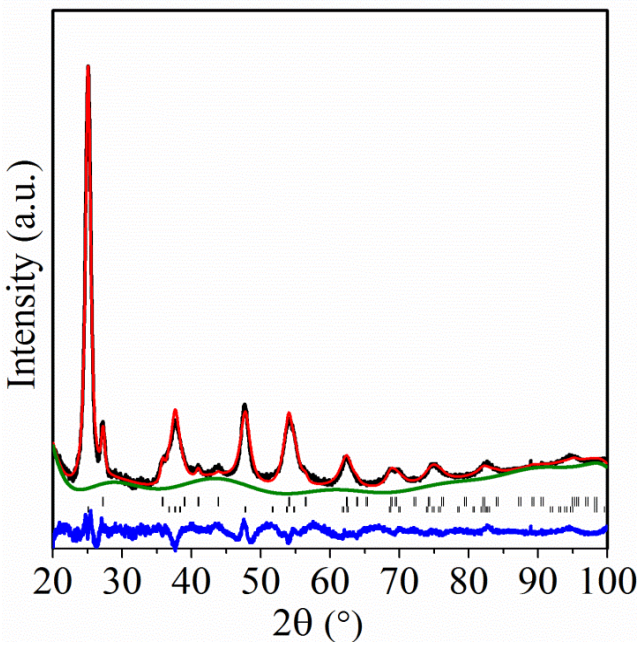

Fig. 3. 9 A Rietveld fit (R_{wp} = 5%, R_p = 4%) to the mixed phase anatase and rutile TiO_2 film XRD heated at 600 °C for 20 minutes. Anatase TiO_2 (92%, lower tick marks), $I4_1/amd$ [51] and rutile TiO_2 (8%, upper tick marks), $P4_2/mnm$.[52] The black line shows the data points, the red solid line the fit and the lower continuous line the difference. The atom positions were not refined.

Table 3. 6 Rietveld refined parameters and analytical data for T3-DEA films.

Time /min	Anatase			Rutile			A /R	R_p/R_{wp}
	a / Å	*c* / Å	Crystallite size/nm	*a* / Å	*c* / Å	Crystallite size/nm	(%)	(%)
5	3.7961(9)	9.5726(1)	14.8(2)	4.5940(1)	2.9585(9)	19.3(5)	97/3	0.1/0.2
10	3.7847(1)	9.4684(3)	17.1(3)	4.5798(3)	2.9537 (9)	20.2(3)	95/5	9/12
20	3.7957(1)	9.5162(6)	23.9(5)	4.5998(7)	2.9708(1)	28.1(8)	92/8	4/5
40	3.7718(7)	9.4320(4)	36(7)	4.5764(1)	2.9578(5)	39.3(8)	70/30	15/23

XRD pattern for TiO_2 powder prepared by T3-DEA and annealed at 600 °C for 20 minutes were refined and showed good fit (Fig. 3.10). Refined lattice parameters and the crystallite sizes are given in Table 3.7. All lattice parameters are closed to the value stated in the literature for anatase a = 3.7842(13) and c = 9.5146(15) Å,[51] and rutile a = 4.5937 and c = 2.9587 Å.[52]

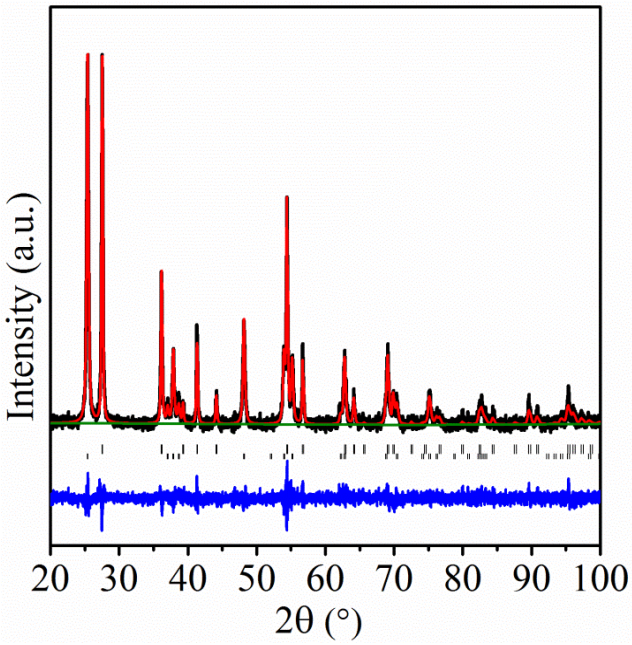

Fig. 3. 10 A Rietveld fit (R_{wp} = 13%, R_p = 10%) to the mixed phase anatase and rutile TiO_2 powders XRD heated at 600 °C for 20 minutes. Anatase TiO_2 (50%, lower tick marks), $I4_1/amd$ [51] and rutile TiO_2 (59%, upper tick marks), $P4_2/mnm$.[52] The black line shows the data points, the red solid line the fit and the lower continuous line the difference. The atom positions were not refined.

Table 3. 7 Rietveld refined parameters and analytical data for T3-DEA powders.

Time /min	Anatase (A)			Rutile (R)			A/R (%)	R_p/R_{wp} (%)
	a / Å	c / Å	Crystallite size/nm	a / Å	c / Å	Crystallite size/nm		
5	3.7861(8)	9.4963(1)	15.7(5)	4.5942(3)	2.9567(8)	20.4(3)	93/7	9/12
10	3.7848(4)	9.5114(2)	21.5(4)	4.5934(3)	2.9594(4)	41.4(3)	76/24	10/12
20	3.7848(2)	9.5202(9)	34.2(2)	4.5945(3)	2.9599(2)	83.8(6)	50/50	10/13
40	3.7847(3)	9.5209(9)	52.4(7)	4.5946(2)	2.9606(2)	112.1(7)	37/63	11/14

Mixed anatase and rutile XRD pattern of TiO_2 film prepared from T4-DEA and fired at 600 °C for 20 minutes were refined and shows a good fit (Fig. 3.11). The refined lattice parameters and crystallite sizes were shown in Table 3.8. The lattice parameters for film fired for 10 minutes are lower and higher for film fired for 20 minutes than the literature value for anatase a = 3.7842(13) and c = 9.5146(15) Å,[51] and rutile a = 4.5937 and c = 2.9587 Å.[52]

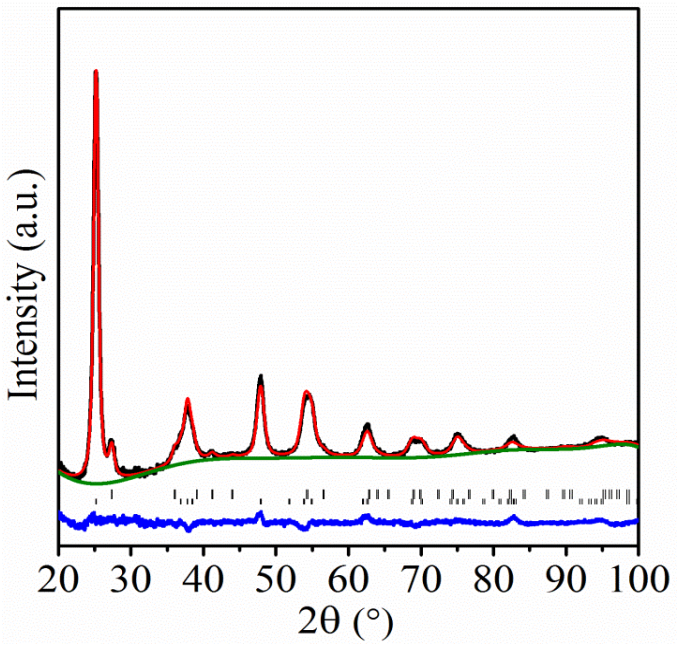

Fig. 3. 11 A Rietveld fit (R_{wp} = 4 %, R_p = 6 %) to the mixed phase anatase and rutile TiO_2 film XRD heated at 600 °C for 20 minutes. Anatase TiO_2 (90%, lower tick marks), $I4_1/amd$ [51] and rutile TiO_2 (10%, upper tick marks), $P4_2/mnm$.[52] The black line shows the data points, the red solid line the fit and the lower continues line the difference. The atom position not refined.

Table 3. 8 Rietveld refined parameters and analytical data for T4-DEA films.

Time /min	Anatase (A)			Rutile (R)			A/R (%)	R_p/R_{wp} (%)
	a / Å	*c* / Å	Crystallite size/nm	*a* / Å	*c* / Å	Crystallite size/nm		
5	3.7836(1)	9.4617(1)	12.3(7)	4.5743(6)	2.9483(3)	12.3(5)	98/2	8/10
10	3.7669(9)	9.4457(7)	16.7(4)	4.5491(3)	2.9336(9)	21.9(5)	96/4	8/10
20	3.7918(8)	9.5005(1)	23(2)	4.5953(8)	2.9529(6)	25.3(9)	90/10	4/6
40	3.7881(7)	9.4822(1)	26.2(3)	4.5920(1)	2.9461(8)	34.1(5)	89/11	13/19

The fitted XRD pattern to the Rietveld refinement of anatase and rutile powder prepared from T4-DEA fired at 600°C for 20 minutes is showed in Fig. 3.12. Refined lattice parameters and the crystallite sizes are provided in Table 3.9. The lattice parameters for all TiO_2 powder are closed to the value reported in the paper previously for anatase a = 3.7842(13) and c = 9.5146(15) Å,[51] and rutile a = 4.5937 and c = 2.9587 Å.[52]

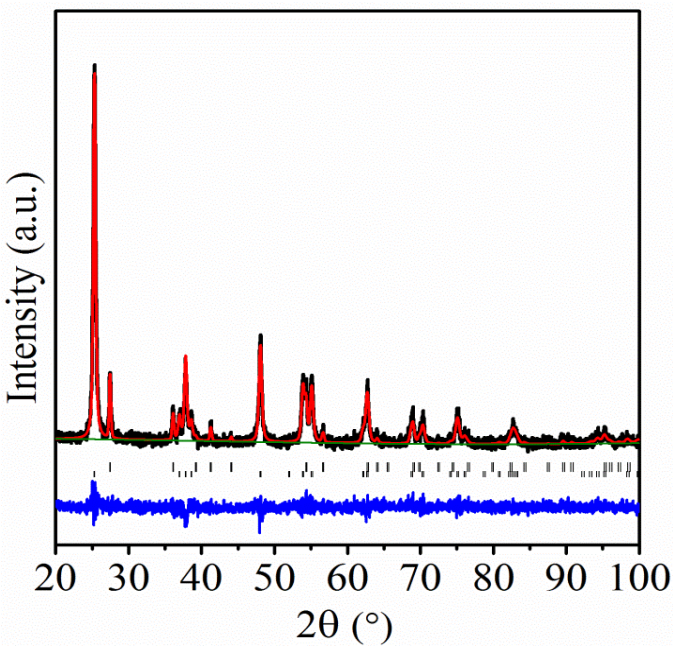

Fig. 3. 12 A Rietveld fit (R_{wp} = 12 %, R_p = 10 %) to the mixed phase anatase and rutile TiO_2 powder XRD heated at 600 °C for 20 minutes. Anatase TiO_2 (87 %, lower tick marks), $I4_1/amd$ [51] and rutile TiO_2 (13 %, upper tick marks), $P4_2/mnm$.[52] The black line shows the data points, the red solid line the fit and the lower continuous line the difference. The atom position were not refined.

Table 3. 9 Rietveld refined parameters and analytical data for T4-DEA powders.

Time /min	Anatase (A)			Rutile (R)			A/R	R_p/R_{wp}
	a / Å	*c* / Å	Crystallite size/nm	*a* / Å	*c* / Å	Crystallite size/nm	(%)	(%)
5	3.7860(2)	9.5011(6)	12.6(3)	4.5929(4)	2.8529(2)	19(8)	96/4	8/10
10	3.7879(4)	9.5182(1)	26.1(1)	4.5978(1)	2.9623(3)	48.5(8)	90/10	9/12
20	3.7861(3)	9.5180(1)	40.2(3)	4.5962(7)	2.9603(7)	87.5(10)	87/13	10/12
40	3.7851(7)	9.5155(1)	82.7(8)	4.5952(1)	2.9599(8)	157.1(26)	78/22	18/20

3.3.5 Discussion for different preparation of TiO_2

As mentioned earlier in Table 3.1, sol T1-HCl prepared with an acidic catalyst and no modifier produced single anatase TiO_2 films and powders when fired at 600 °C for various temperatures. There was no observation of rutile phase in these films and powders at this temperature. This could be due to the lack of HCl concentration to promote the hydrolysis and initiate the nucleation of rutile,[53] or may be related to the surface energy of anatase that increases with small crystallite size.[54] Kim et al.[26] and Ahn et al.[53] obtained single phase anatase when using a $Ti(O^iPr)_4$ based sol with 0.7 M HCl catalyst to prepare TiO_2 films. The rutile phase appeared when they increased the temperature at 1000 °C. They referred to the delay in the transition temperature from anatase to rutile as being due to the concentration of the HCl catalyst. Nishide et al.[25] and Hashimoto et al.[55] have used HNO_3 as a catalyst to prepare TiO_2 films by sol-gel process and obtained single anatase phase with no change of the crystalline phase up to 900 °C. Negishi et al.[56] attributed delay in the transformation from anatase-rutile to the large crystallite size of TiO_2 when it was fired at 850 °C.

The variation in crystallite size of TiO_2 films and powders prepared from T1-HCl and fired at 600 °C for various periods was studied. The crystallite size for anatase films and powders increased smoothly with increasing firing period (Table 3.3). The anatase crystallite size for the film and (powder) fired at 600°C for 5 minutes was 26.2 nm (31 nm) and increased to 41 nm (62.4 nm) when it was fired for 40 minutes. Therefore, the anatase crystallite size in the films and powders increased gradually by ~2 and ~8 nm every 5 minutes constantly, respectively.

The current work is in good agreement with the above literature and with Sayilkanl et al.[57] and So et al.[58] in which they obtained single anatase phase. So, the stability of anatase phase of TiO_2 can be caused by the HCl concentration or the crystallite size.

TiO_2 films and powders prepared with DEA modifier (Table 3.1) were shown to contain a mixture of anatase and rutile phase. The process of the anatase and rutile formation can be explained. The TiO_6 octahedra are subjected to distortion during the heating process resulting in breaking Ti-O bonds and recreation of new Ti-O bonds. This takes place at the interface between two anatase particles. The breaking of Ti-O bonds results in removal of oxygen ions and formation of defects, along with creation of new Ti-O bonds for the rutile phase.[59] Therefore, the rutile phase is created from the anatase phase.

The current study has observed that the rutile percentage depended on the quantity of DEA modifier. In films and powders, the addition of 7 mL of DEA (Table 3.6 and Table 3.7) led to an increase the phase fraction of rutile compared with using 3 mL of DEA (Table 3.4 and Table 3.5). The content of rutile phase was reduced when DEA was decreased to 1.5 mL (Table 3.8 and Table 3.9). Verma et al.[21] obtained anatase phase by using 1 mL of DEA and annealing at 560 °C, but observed a transformation from anatase to rutile at 561 °C, Takahashi et al.[22] increased the quantity of DEA up to 2 mL and the transition temperature was 500 °C. Murugan et al.[17] have confirmed the transformation temperature from anatase to rutile phase was increased by increasing DEA quantity to 3 mL. The optimum amount of DEA produced denser and thicker powders and films which led the small particles to be in contact to each other and thus interface boundary defects to form at the interfaces between neighbouring anatase nanocrystallites.[1, 17] These boundary defects can then continue to form between the interfaces of anatase and rutile crystallites and removal of the particle defects which generates only rutile phase.

So, in order to study the effect of the crystallite size on the transformation of the anatase into rutile, the films and powders prepared from T2-DEA, T3-DEA and T4-DEA were studied as a function of temperature. In general, the anatase and rutile crystallite size was increased by prolonging the firing time (Table 3.4-3.8).

However, the larger rutile crystallite size compared with anatase could be due to the formation of the rutile phase from the anatase phase. The anatase and rutile crystallite sizes were increased as a function of temperature.[22] An example to demonstrate the increasing of rutile crystallite size of the films and powders prepared from T2-DEA as a function of firing time is shown in Fig. 3.13.

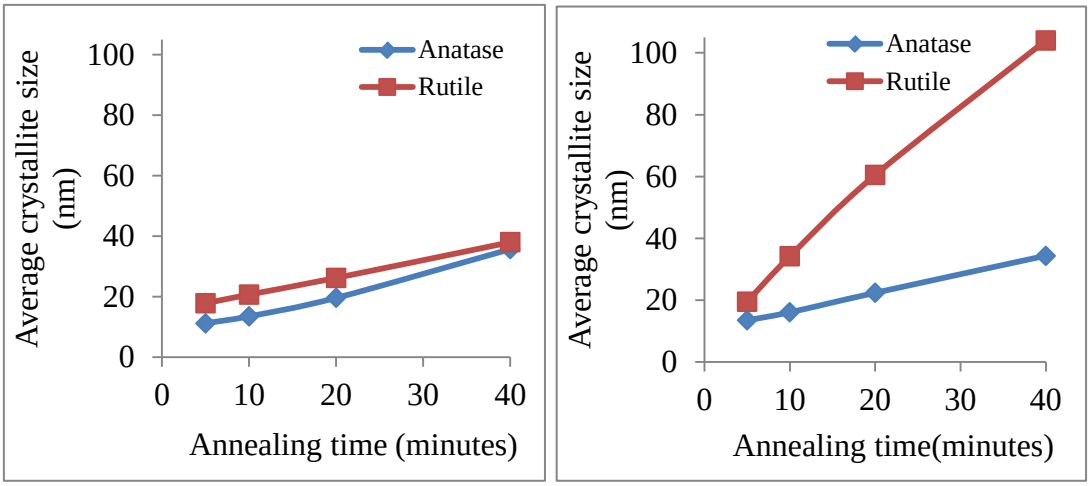

Fig. 3. 13 Average crystallite size of mixed phase anatase and rutile TiO_2 for films (left) and powders (right) prepared from sol T2-DEA and fired at 600 °C for time shown.

As well, the rutile crystallite size of powders prepared by DEA modifier (Table 3.1) was significantly larger than films under the same condition (Fig. 3.14). As the transition temperature from anatase to rutile in the films was increased possibly due to the effect of the substrate and the presence of SiO_2 in the substrate.[56] Based on Nechache et al.[60] and Yu et a.[61] reported that the anatase phase was stabilised by the surrounding SiO_2 phase through the Ti-O-Si interface resulted from the substitution of Ti into the tetrahedral SiO_2 lattice creating Ti sites. During the interaction between the tetrahedral Ti groups and the Ti sites in the anatase phase was expected to delay the transformation from anatase into rutile unless higher temperature was applied due to the SiO_2 lattice locks the Ti-O-Si at the interface with TiO_2 preventing the formation of rutile nucleus.

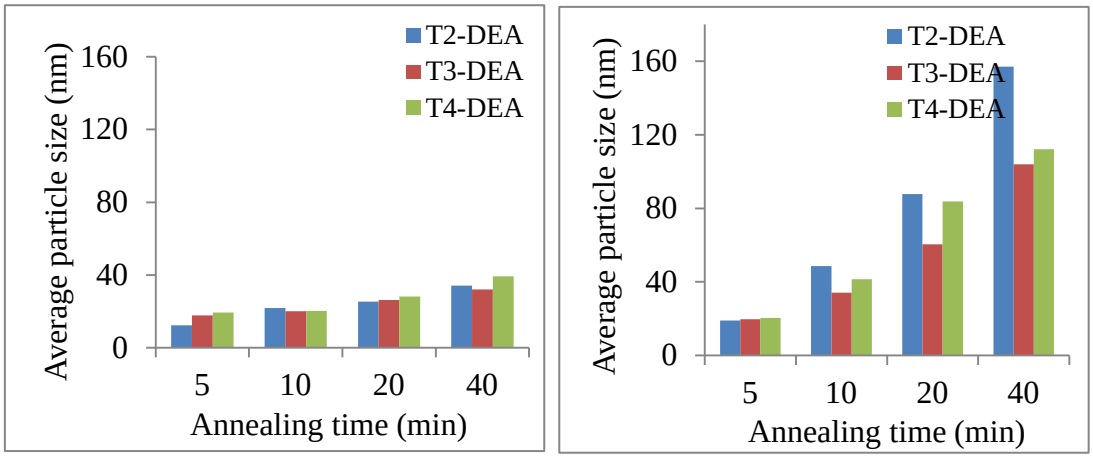

Fig. 3. 14 Average crystallite size of rutile TiO_2 films (left) and powders (right) prepared from TiO_2 sol and fired at 600 °C for time shown.

When the comparison between the crystallite sizes prepared with acidic catalyst and no modifier, or using the DEA modifier system were made, the anatase crystallite sizes of the films and powders under acidic catalyst were larger than modified with DEA due to the chloride ion was prevented to the formation of the rutile nuclei; the anatase particle was growing completely without any transformation to rutile phase (Fig. 3.15).

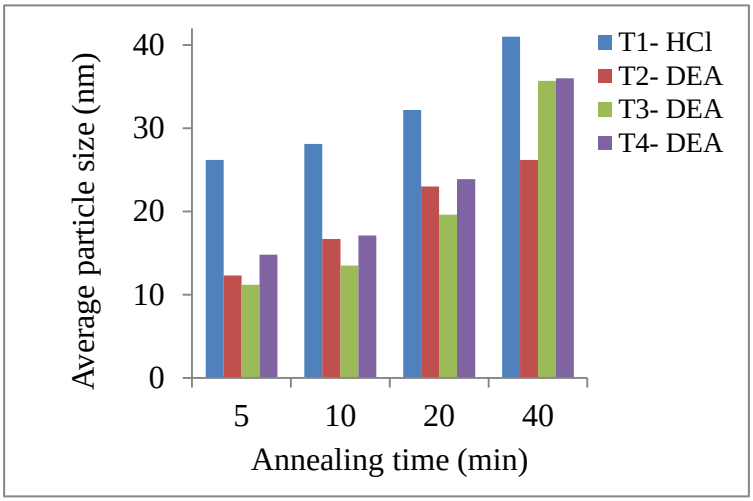

Fig. 3. 15 Average crystallite size anatase TiO_2 films prepared from TiO_2 sol and fired at 600 °C for various time.

Therefore, the transformation from anatase to rutile phase depended on the sols composition, crystallite size and the packing density of the particles.

3.4 Speciation in TiO_2 precursor sols

The study of the speciation in the TiO_2 sols will provide us a better understanding of why the differences in the film morphology and phase behaviour observed in TiO_2 occur, and could allow us to improve the behaviour of TiO_2.

3.4.1 MS studies

ESI-MS is a soft technique for detecting non-volatile ionic or easy ionised species in solution. The morphology, particle size and phase behaviour of TiO_2 films were found to depend on the sol synthesis conditions. The higher stability of the titanium precursors in the presence of a modifier has been suggested to be due to differences in the cluster size of the primary building blocks created during the synthesis.[62] Therefore, ESI-MS was used in an attempt to observe what species are present in the sol prior to production of films.

ESI-MS of the $Ti(O^iPr)_4$ with DEA in ethanol sol

An example of the mass spectra obtained by injection $Ti(O^iPr)_4$ with DEA in ethanol sol with aging for 24 hours were showed in Fig. 3.16. Based on multiple attempts a series of the same distinct cluster sizes were observed in the mass range 50 -1500 *m/z* and the highest mass cluster with significant intensity was observed at 1359. An accurate mass plot (Fig. 3.17) shows an isotopic splitting pattern with the most intense peak at 1359.03 *m/z*.

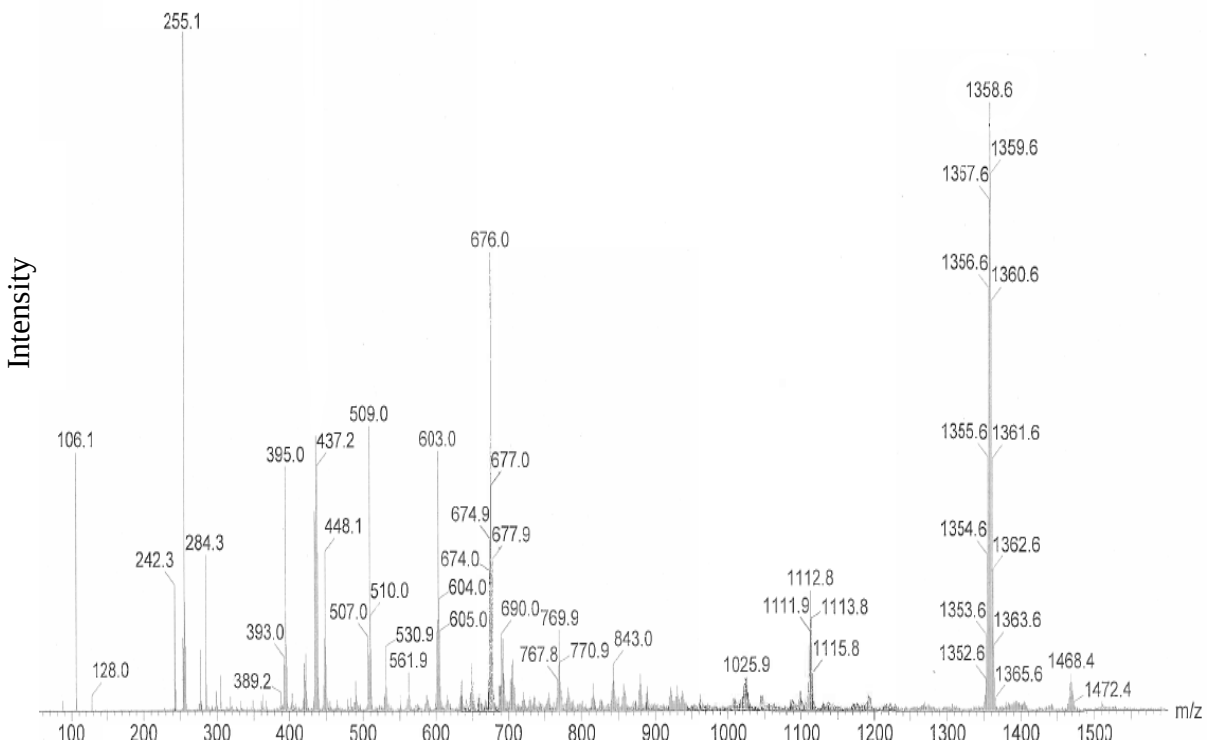

Fig. 3. 16 ESI-MS spectrum of the sol-gel reaction solution prepared from $Ti(O^iPr)_4$ with DEA.

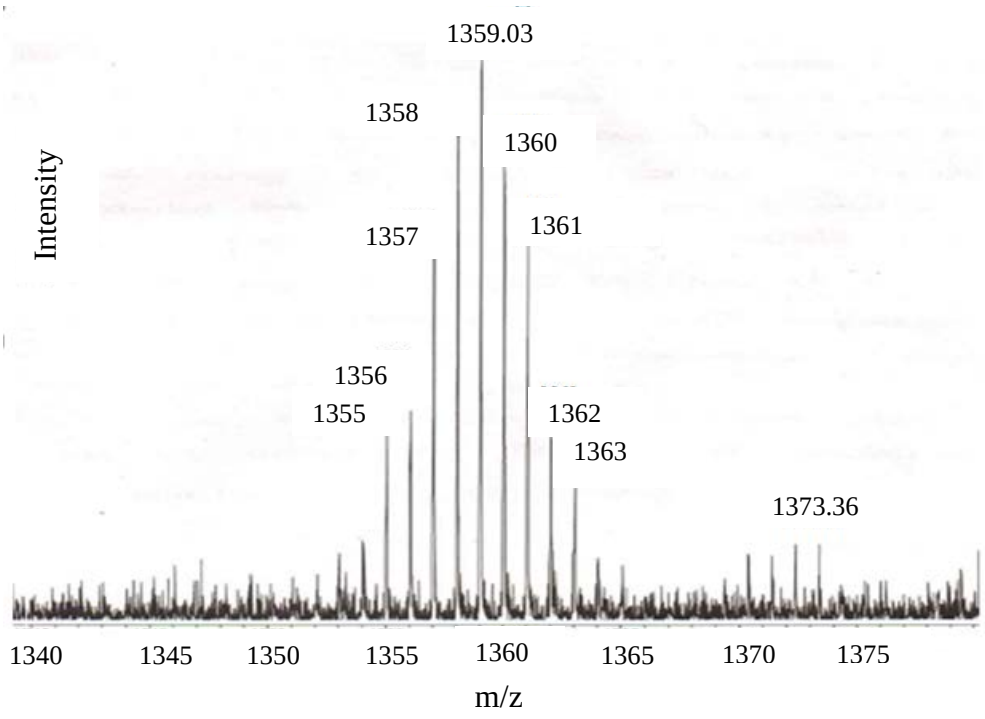

Fig. 3. 17 The accurate mass plot of isotopic splitting pattern.

The element with the most significant isotope splitting is Ti. The isotopic patterns in Fig. 3.17 are consistent with cluster containing around 8-10 Ti atoms. This is illustrated in Fig. 3.18 although the exact content of these clusters could not be determined. Hence they have been modelled $Ti_8O_{32}H_{79}C_{32}$,$Ti_9O_{27}H_{87}C_{34}$ or $Ti_{10}O_{23}H_{80}C_{36}$ based on comparison with simulated splitting patterns that account for the effect of the different titanium isotopes. Comparison with Fig. 3.17 shows that the observed cluster at *m/z* 1359.03 likely contains 8 or 9 Ti atoms.

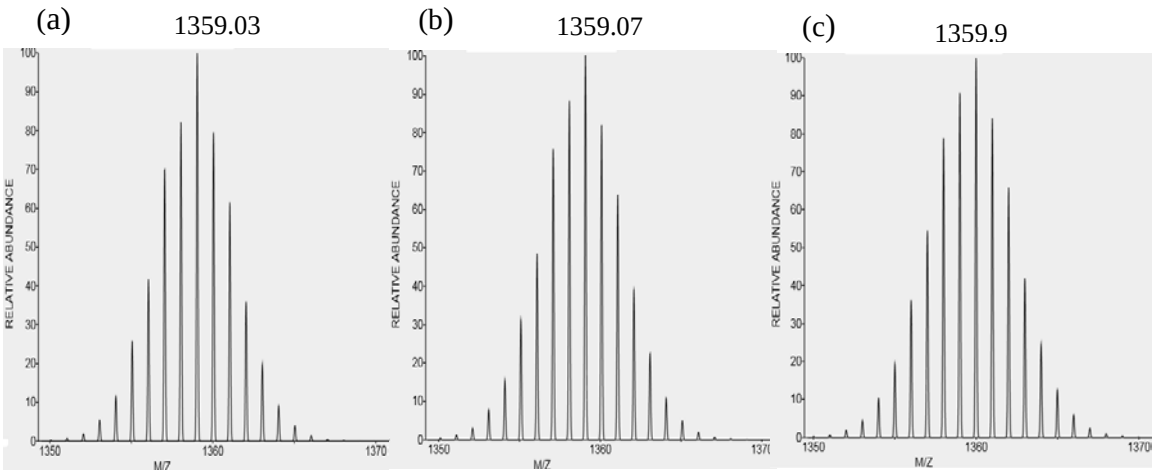

Fig. 3. 18 Simulated splitting patterns for TiO_2 cluster observed by ESI-MS.

ESI+ also observes positively charged species, and that requires either protonation or for other common cations to be picked up by the mass spectrometry chamber. So, the positive ion mass spectrum of TiO_2 sol in acetonitrile solution containing sodium nitrate (1.8×10^{-7}) M was displayed in Fig. 3.19. Clearly singly charged ion of *m/z* 1359.05 and in comparison to the species observed at *m/z* 1359.03, it was evident that there was not any effect of adding Na^+ to the titania sol. Hence the masses observed in Figs. 3.16- 3.18 are due to sodiated species.

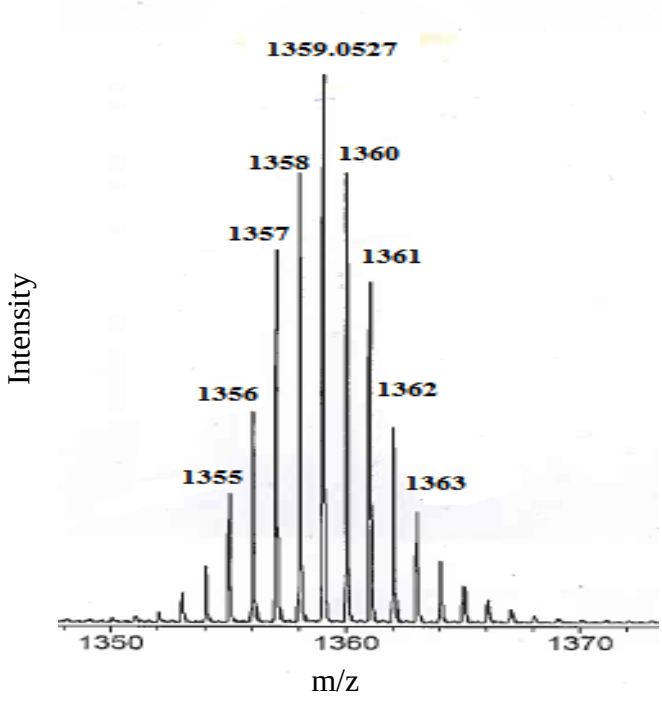

Fig. 3. 19 ESI-MS spectra of the sol-gel reaction solution prepared from $Ti(O^iPr)_4$ with DEA and sodium.

The evolution of high mass peaks with sol aging time has been investigated (Fig. 3.20). As it was found in the sol some stable cluster, the mass spectrum after 1 hour of the reaction provided an increase in species with absence of the observed species at *m/z* 1359.03 and 1373.36. As the reaction evolves, spectra taken at 2 hours showed a continuous increase in the number of mass with dominate species observed at *m/z* 1359.03, but the intensity was decreased significantly which may suggest aggregation of the cluster resulting in the formation of cluster larger than *m/z* 1359.03 and therefore undetectable by ESI+. Further increasing in reaction time for 5 hours, the number of species was decreased with no observation for the observed cluster at *m/z* 1359.03, whereas after 48 hours and 1 week of the reaction the spectrum showed an increase again in the species. Therefore, reappearance of some species after long periods could be due to sodium uptake from the glass containers used to store the sols.

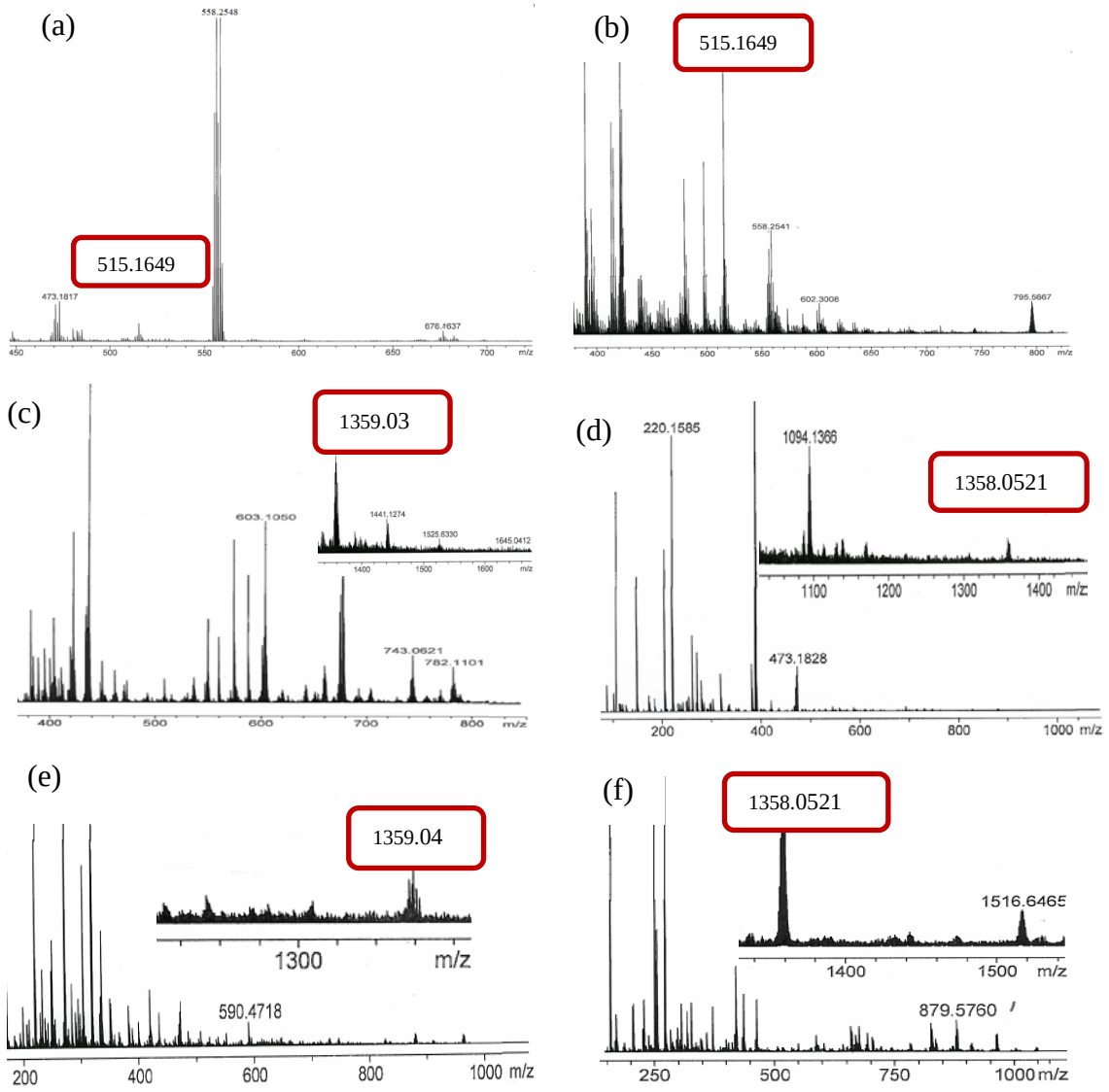

Fig. 3. 20 Time evolution of the ESI-MS spectra of the reaction solution prepared from $Ti(O^iPr)_4$ with DEA: (a) 0 hour, (b) 1 hour,(c) 2 hours , (d) 5 hours, (e) 48 hours and (f) 1 week.

It should be noted that, the relative abundances are not necessarily indicative of the concentrations of species in solution, or whether the species present in solution. The mass spectrometer could be detecting the ions containing excess alcohol or diethanolamine molecules, and molecules that could not be ionized will not be observed by this technique. The rapid hydrolysis of titanium isopropoxide depends on the solvent and the substitution of the DEA (moderator) ligands. However, a number of defined species with distinct composition were observed in different sols. Splitting patterns show these contain multiple Ti atoms, with 8-9 Ti atom species showing up prominently.

3.4.2 NMR study

The influence of additives like DEA on the hydrolysis and polycondensation properties, and the changes induced by the moderator on the TiO_2 sols, were studied by NMR. The investigation has tried to establish whether the alcohol exchange occurred and whether the N-atom in the DEA was bonded to the Ti atom. Both ^{1}H and $^{13}C\{^{1}H\}$NMR spectra were recorded, and peak assignments were accomplished by comparison with the spectra of the precursors used. $CDCl_3$ and CD_2Cl_2 were used as solvents.

3.4.2.1 Initial ambient temperature of titanium isopropoxide modified with DEA sol

The TiO_2 sols that were aged for 24 hours consisted of $Ti(O^{i}Pr)_4$ and DEA in 1:2 molar ratio in the presence of ethanol (Table 3.2). The solvent was pumped off completely and the yellowish viscous solid was dissolved in $CDCl_3$ for NMR measurements at room temperature. Attempts to grow single crystals from the NMR solution were not successful.

Table 3.10 lists the chemical shift value of the peaks observed in ^{1}H NMR spectra of a sol prepared with 2 equivalents of DEA. Fig. 3.21 shows alcohol CH_3 signals only in the 1.0 to 1.5 ppm region, with the two sets of triplet and doublet signals for EtOH and ^{i}PrOH alcohols in agreement with the standard chemical shift at 1.25 and 1.22 ppm. Two sets of quartets at 3.7 ppm and septet at 4.0 ppm correspond to CH_2 and CH protons and are in the same position for the standards exactly at 3.7 and 4.0 ppm (EtOH and ^{i}PrOH). The CH_2 protons of DEA are shifted from 2.5 ppm (NCH_2) and 3.4 ppm (OCH_2), to 2.7 and 3.7 ppm, with loss of the splitting patterns. The 3.7 ppm signal is overlapped with the CH_2 of ethanol.

No sharp features due to sol oligomers are seen, although broad features are observed in the 4.0-4.7 ppm region that may be due to C*H* protons from propoxide groups or CH_2 protons from ethoxide groups (Fig. 3.21, f). The complete exchange of the isopropoxide groups when Ti(O^iPr)$_4$ is reacted with ethanol suggests the latter. CH_3 groups due to sol oligomers are unlikely to be observed due to the overlap with the CH_3 proton signals from ethanol and isopropanol. Further broad, unidentifiable features are seen at 3.0-3.5 ppm.

The use of commercial Ti(OEt)$_4$ in place of Ti(O^iPr)$_4$ results in very similar products being observed in the ^{1}H NMR spectra.

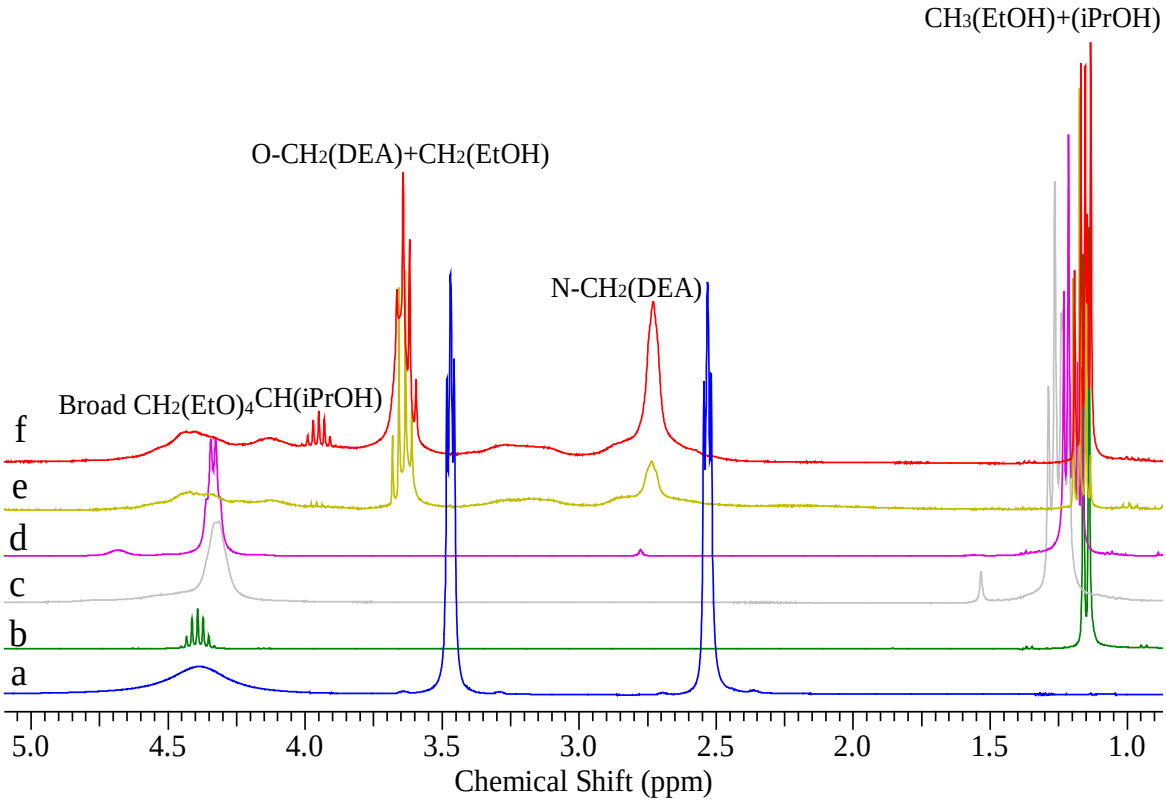

Fig. 3.21 ^{1}H NMR spectra measured at 22 °C for Ti(O^iPr)$_4$ in EtOH and DEA sols: (a) DEA, (b) Ti(O^iPr)$_4$, (c) Ti(O^iPr)$_4$ + EtOH, (d) Ti(OEt)$_4$, (e) Ti(OEt)$_4$ + EtOH + 2 eq DEA and (f) Ti(O^iPr)$_4$ + EtOH + 2 eq DEA.

Table 3. 10 Chemical shift values of the peaks in ^{1}H NMR spectra of the mixture of $Ti(O^iPr)_4$ in EtOH and DEA sols. (*) trace of titanium isopropoxide.

Solution	Ethoxide		Isopropoxide		DEA	
	CH_3	CH_2	CH_3	CH	N-CH_2	O-CH_2
a) DEA	-	-	-	-	2.5	3.4
b) $Ti(O^iPr)_4$	-	-	1.16	4.4		
c) $Ti(O^iPr)_4$ + EtOH	1.24-1.28	4.31-4.33	1.21-1.23	-		
d) $Ti(OEt)_4$	1.19-1.23	4.31-4.36	1.16-1.18 *	4.7 (broad) *		
e) $Ti(OEt)_4$ + EtOH + 2 eq DEA	1.15-1.19	3.7	1.13-1.15	4.0	2.7	3.7
f) $Ti(O^iPr)_4$ + EtOH + 2 eq DEA	1.15-1.19	3.7	1.13-1.15	4.0	2.7	3.7

Fig. 3.22 shows that the product of reacting $Ti(O^iPr)_4$ with EtOH and commercial $Ti(OEt)_4$ both have a shift in the CH_2 position relative to pure $Ti(OEt)_4$ (prepared). The ethanolysis product peak is also somewhat broader, with the splitting pattern not resolved as the propoxide CH signal would be observed close by. The CH_3 region of the pure ethoxide (prepared) contains only the expected triplet structure, but the commercial and ethanolysis samples also contain a propoxide signal. These are not at identical shift values as the spectra are corrected vs the solvent peak and therefore comparing integrals between the two regions suggests average compositions of the commercial "$Ti(OEt)_4$" to be $[Ti(OEt)_{3.66}(O^iPr)_{0.34}]$, and the ethanolysis product to be $[Ti(OEt)_{3.72}(O^iPr)_{0.28}]$.

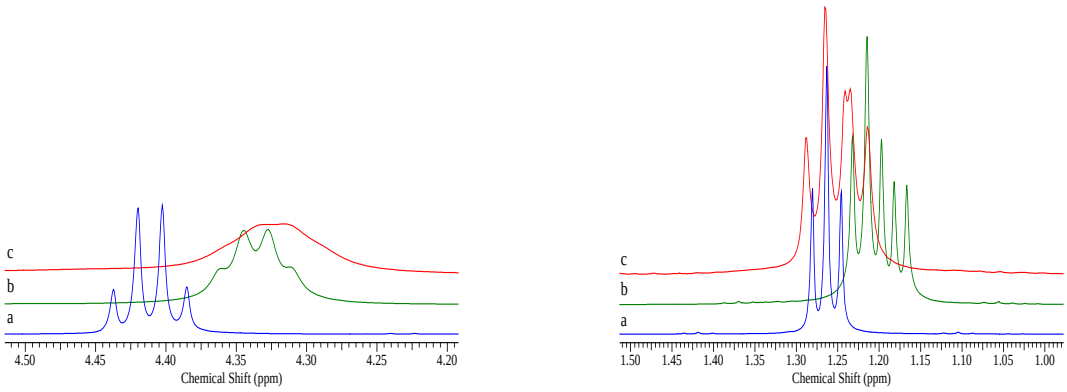

Fig. 3. 22 ^{1}H NMR spectra measured at 22 °C for: (a) Pure $Ti(OEt)_4$, (b) commercial $Ti(OEt)_4$ and (c) $Ti(O^iPr)_4$ + EtOH.

The $^{13}C\{^1H\}$ spectrum of the Ti-containing products of the sol prepared with 2 equivalents DEA and aged for 24 hours shows the presence of DEA, ethanol and isopropanol only and their chemical shift value shown in Table 3.11.

Fig. 3.23 demonstrated the isopropoxide exchanges almost completely to ethoxide after ethanol treatment, and closely resembles the commercial ethoxide. Both contain an isopropoxide signal at 26.2 ppm, but this was shifted slightly downfield from the neat isopropoxide position of 26.5 ppm toward the isopropanol at 25.1 ppm by the addition of DEA, suggesting the presence of an intermediate composition such as $[Ti(O^iPr)(OEt)_3]$. The presence of the isopropanol in the isopropoxide were observed could be due to hydrolysis while samples were waiting to be run on the autosampler because they were not seen in the proton data.

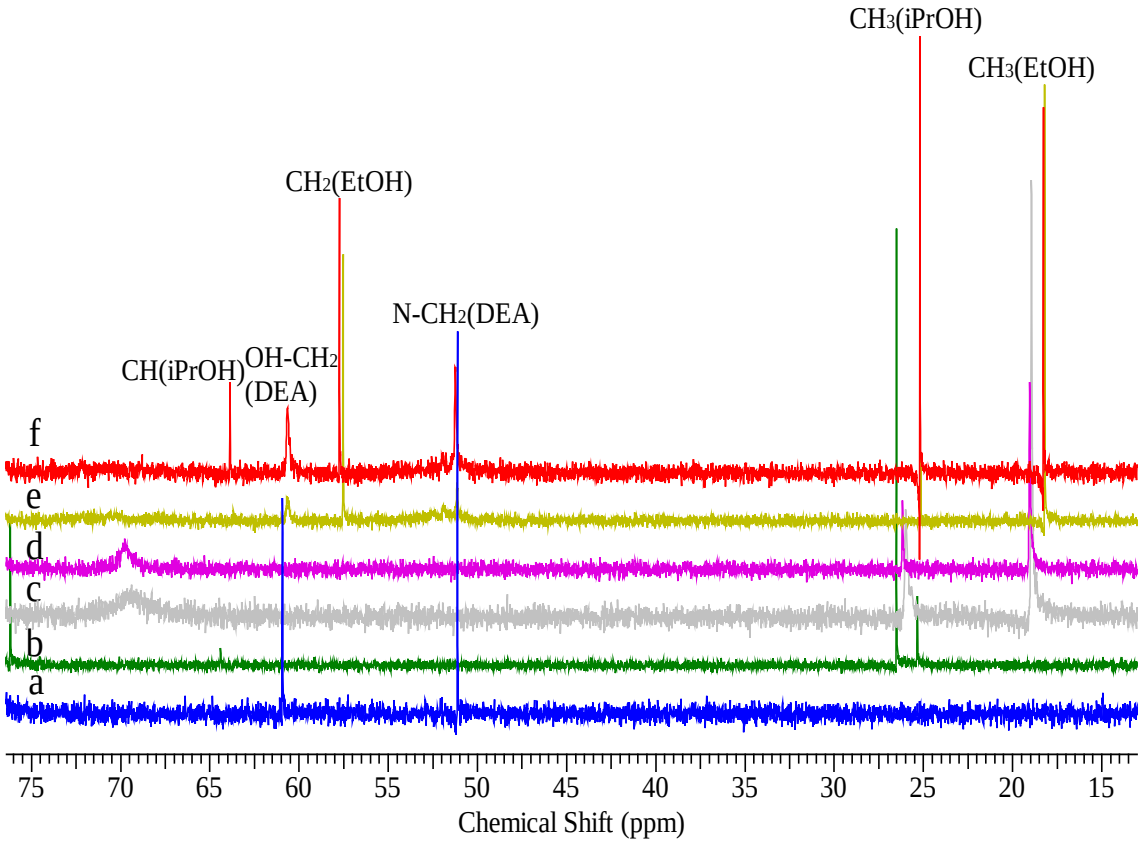

Fig. 3.23 $^{13}C\{^1H\}$NMR spectra measured at 22 °C for $Ti(O^iPr)_4$ in EtOH and DEA sols: (a) DEA, (b) $Ti(O^iPr)_4$, (c) $Ti(O^iPr)_4$ + EtOH, (d) $Ti(OEt)_4$, (e) $Ti(OEt)_4$ + EtOH + 2 eq DEA and (f) $Ti(O^iPr)_4$ + EtOH + 2 eq DEA.

Table 3. 11 Chemical shift values of the peaks in $^{13}C\{^1H\}$NMR spectra of the mixture of $Ti(O^iPr)_4$ in EtOH and DEA sols.

Solution	Ethoxide		Isopropoxide		DEA	
	CH_3	CH_2	CH_3	CH	$N\text{-}CH_2$	$O\text{-}CH_2$
a) DEA	-	-	-	-	51	61
b) $Ti(O^iPr)_4$	-	-	26.5	76.1		
c) $Ti(O^iPr)_4$ + EtOH	19	69	26.1	-		
d) $Ti(OEt)_4$	19	69.5	26.2	-		
e) $Ti(OEt)_4$ + EtOH +2 eq DEA	18.2	57.7	25.2	64 (weak)	51	60.6
f) $Ti(O^iPr)_4$ + EtOH +2 eq DEA	18.2	57.5	25.2	64	51	60.6

3.4.2.2 Initial ambient temperature spectra of $Ti(OEt)_4$ with DEA mixture

The ^1H NMR spectra of the $Ti(OEt)_4$ mixture with DEA (Fig. 3.24) shows the same behaviour as the 2 equivalent sample described above, as the DEA peaks shifted from the first addition and formation of ethanol and isopropanol. The ethoxide:isopropoxide ratio observed in the C*H*$_3$ region remained relatively constant up to 1.0 molar equivalents DEA, suggesting neither alkoxide was displaced more readily than the other.

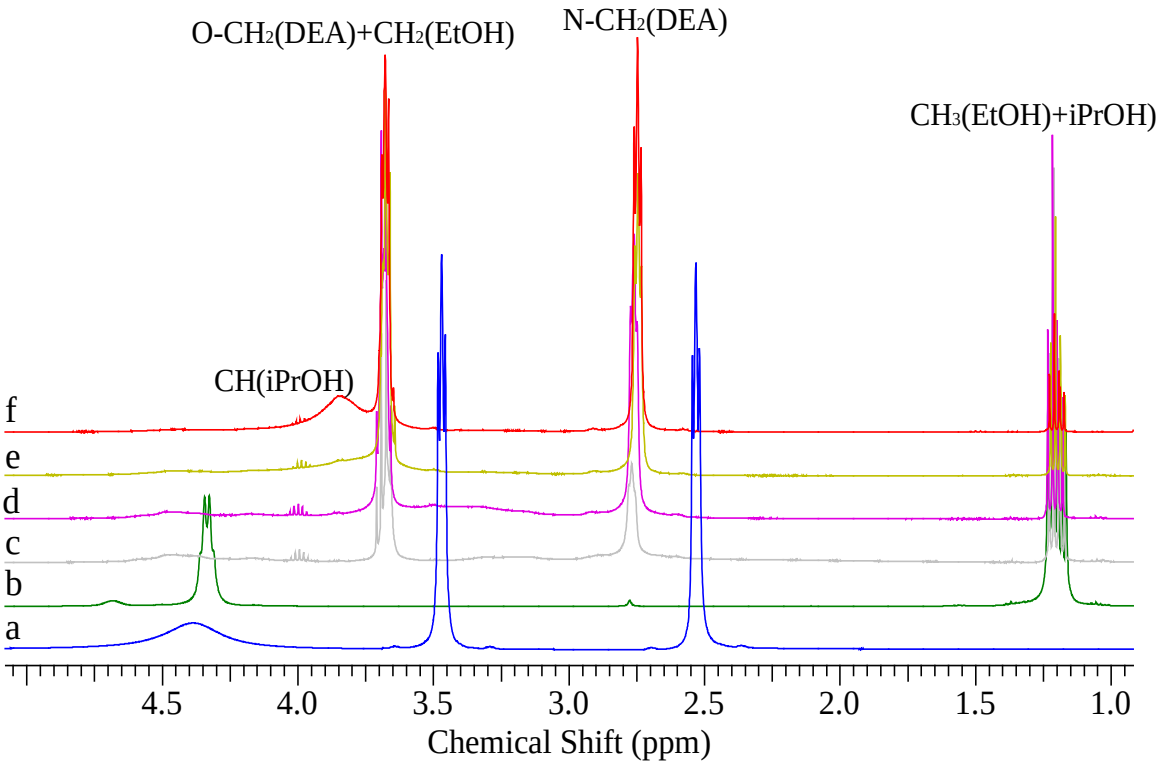

Fig. 3. 24 ^{1}H NMR spectra measured at 22 °C for $Ti(OEt)_4$ and DEA mixed ligand: (a) DEA, (b) $Ti(OEt)_4$, (c) $Ti(OEt)_4$ + 0.25 eq DEA, (d) $Ti(OEt)_4$ + 0.5 eq DEA, (e) $Ti(OEt)_4$ + 0.75 eq DEA and (f) $Ti(OEt)_4$ + 1 eq DEA.

The $^{13}C\{^{1}H\}$ NMR spectra (Fig. 3.25) also show basically the same features as the 2 equivalent sol above, even addition of 0.25 equivalent DEA results in conversion of ethoxide and isopropoxide to ethanol and isopropanol. Therefore, mixed ligand species are not observed.

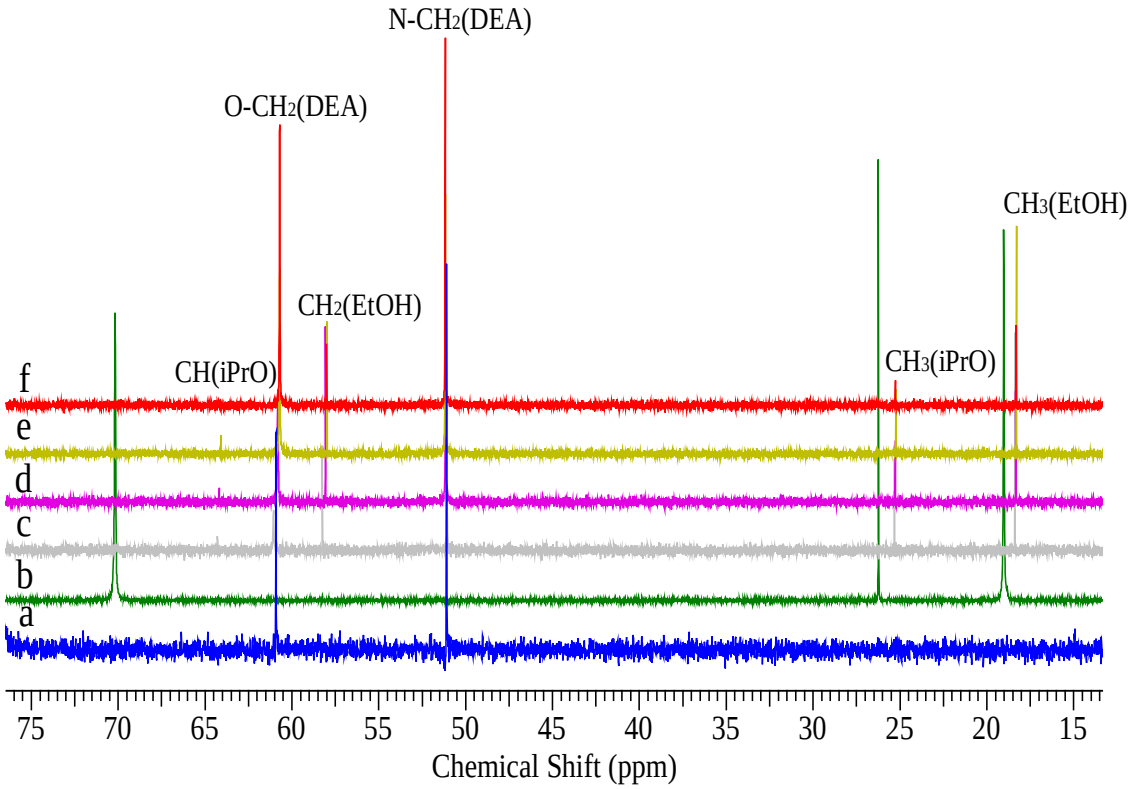

Fig. 3. 25 $^{13}C\{^1H\}$NMR spectra measured at 22 °C for $Ti(OEt)_4$ and DEA mixed ligand: (a) DEA, (b) $Ti(OEt)_4$, (c) $Ti(OEt)_4$ + 0.25 eq DEA, (d) $Ti(OEt)_4$ + 0.5 eq DEA, (e) $Ti(OEt)_4$ + 0.75 eq DEA and (f) $Ti(OEt)_4$ + 1 eq DEA.

Comparing the ^1H and $^{13}C\{^1H\}$ NMR spectra prepared from the sols or mixtures, it can be observed the C*H*$_2$ protons of DEA signal are shifted and that same species cannot be seen in the $^{13}C\{^1H\}$ NMR spectra. This can be explained by the time scale of ^1H NMR, which is faster than $^{13}C\{^1H\}$ NMR. Therefore the lability of the DEA ligands will have a larger effect on the $^{13}C\{^1H\}$ NMR spectra.

3.4.2.3 Low temperature NMR for $Ti(OEt)_4$ with DEA mixtures

In order to investigate the molecular structure of the Ti species in the DEA with $Ti(OEt)_4$ system, NMR measurements were carried out at low temperature with various DEA molar equivalents, and CD_2Cl_2 was used as a solvent. As the measurement temperature decreased the rate of the exchange reactions, therefore the understanding of the sol species and molecular structure can be possible.

The $^{13}C\{^1H\}$ NMR spectrum of $Ti(OEt)_4$ was − 90 °C (Fig. 3.26) shows the peak splittings due to oligomerisation in comparison to room temperature spectrum showed just two peaks at 19.1 (C*H*$_3$) and 70.5 (C*H*$_2$) ppm. While, DEA has recorded ambient temperature spectra only, which has peaks at 51 (N-C*H*$_2$-) and 61 (O-C*H*$_2$-) ppm.

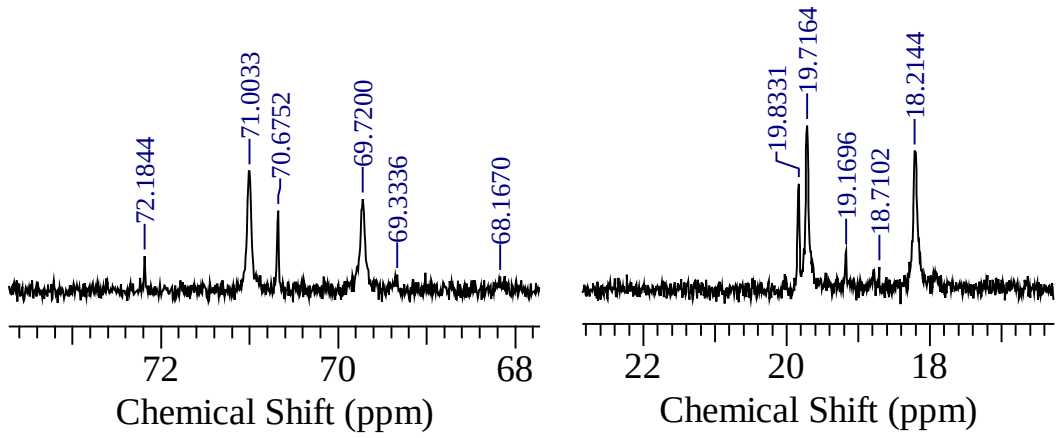

Fig. 3. 26 $^{13}C\{^1H\}$NMR spectra of $Ti(OEt)_4$ measured at − 90 °C.

The $^{13}C\{^1H\}$ NMR spectra after the addition of various equivalents DEA (Fig. 3.27) show the C*H*$_3$ region of ethoxide/ethanol to have been changed in the ethoxide speciation from the first addition (0.25 eq), and ethanol appearing from 0.5 eq onwards, shifting from 18.1 to18 ppm as more DEA was added. The ethanol O-C*H*$_2$ peak also appeared (although broad) at 0.5 equivalent, shifting from 57.2 to 56.9 ppm with further DEA additions. These shifts appeared to be real as the spectra have been referenced to the CD_2Cl_2 signal at 54.0 ppm, therefore the shifts in ethanol peaks may be due to coordination or hydrogen bonding to the Ti atom.

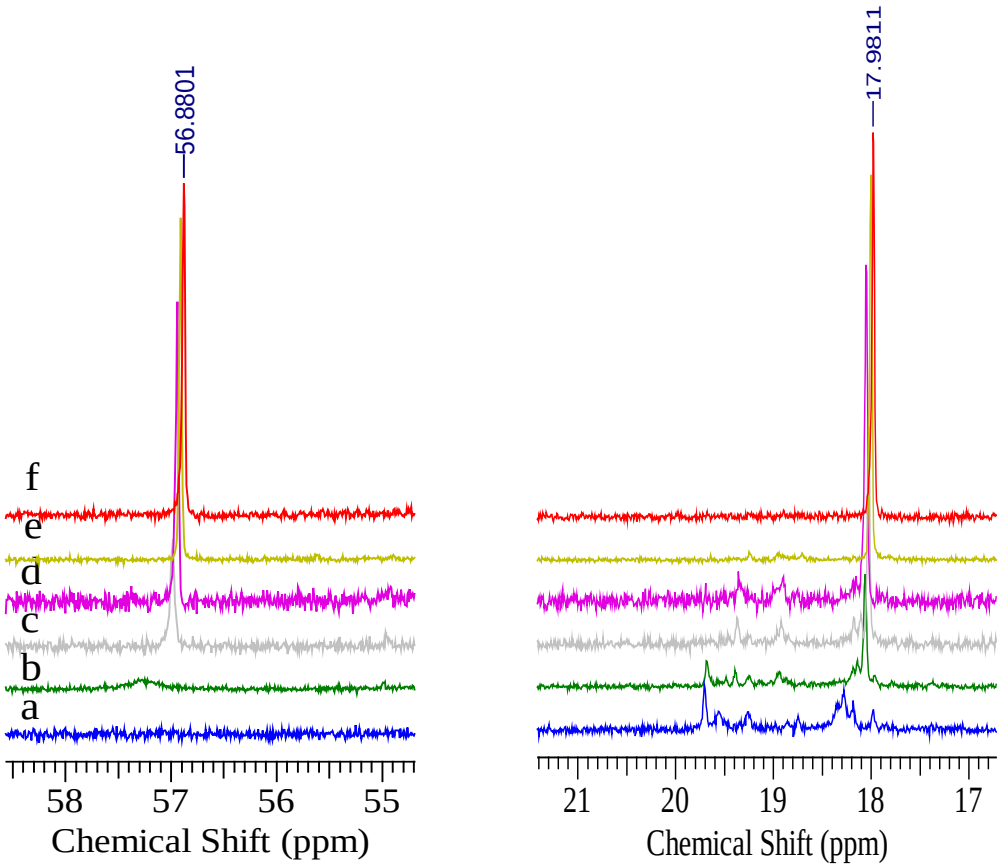

Fig. 3.27 $^{13}C\{^1H\}$NMR spectra measured at − 90 °C for $Ti(OEt)_4$ with various equivalent of DEA: (a) 0.25 eq, (b) 0.5 eq, (c) 0.75 eq, (d)1 eq, (e)1.25 eq and (f)1.5 eq.

The DEA (O-CH_2) signal only appeared at the two highest DEA concentrations used, where signals are seen at 59.6 and 60.0 ppm and the presence of more than one signal suggested, as with the ethanol, that coordination or hydrogen bonding occurred. The O-CH_2 signal from deprotonated and coordinated DEA appeared to move upfield to the same region as the ethoxide O-CH_2 signal (69.9 ppm), although it then also diminished at the highest concentration due to reduced solubility at − 90 °C (Fig. 3.28).

A number of weak signals were observed in the DEA N-CH_2 region, suggesting that amide coordination to the titanium was significant. The multiple signals do, however, suggest that DEA was present as more than one species (Fig. 3.28).

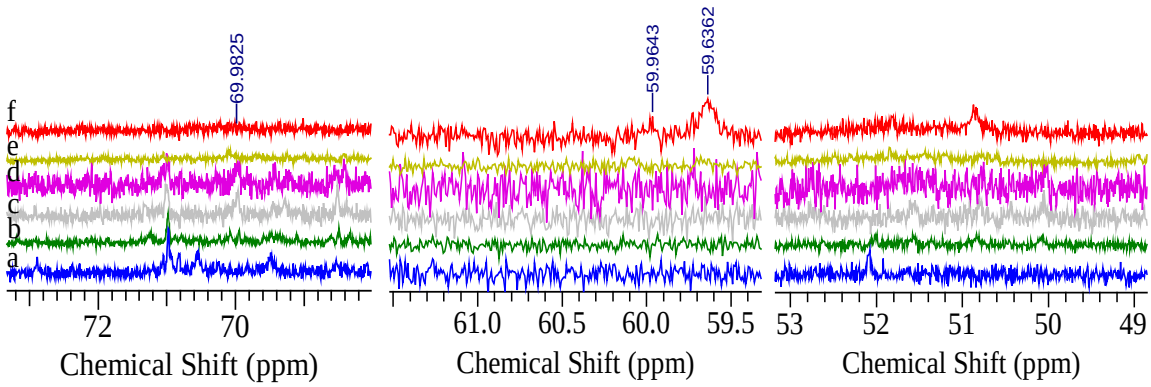

Fig. 3.28 $^{13}C\{^1H\}$NMR spectra measured at − 90 °C for $Ti(OEt)_4$ with various eq of DEA: (a) 0.25 eq, (b) 0.5 eq, (c) 0.75 eq, (d) 1 eq, (e) 1.25 eq and (f) 1.5 eq.

$Ti(OEt)_4$ with 1.5 eq of DEA at various temperatures

Some signals in the $^{13}C\{^1H\}$ NMR spectra were diminished at − 90 °C in samples with higher DEA concentrations and some solid was observed in samples, so a varied temperature study was carried out at − 90 , − 70, − 40, − 20 and 22 °C.

The EtOH -CH_3 signal moves from 18.7 ppm at 22 °C to 18 ppm at − 90 °C, though these shifts are not significant as the solvent-referencing took no account of temperature shifts. Ethoxide -CH_3 signals were absent throughout suggested all $Ti(OEt)_4$ had reacted. The DEA signals at ~51 and ~60 ppm shifted similarly with temperature, becoming more distinct at − 40 °C and above, however the DEA O-CH_2 and N-CH_2 remain too broad to observe properly at 22 °C (Fig. 3.29).

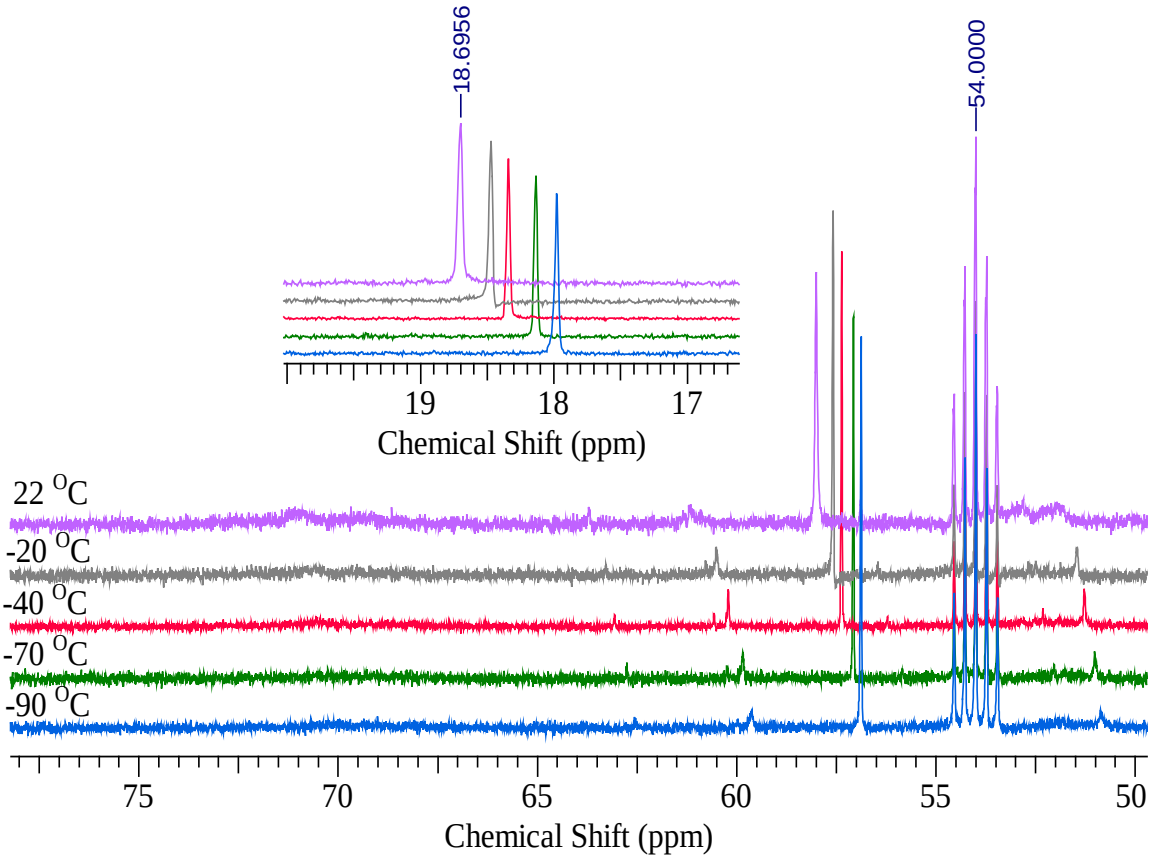

Fig. 3. 29 $^{13}C\{^1H\}$NMR spectra of $Ti(OEt)_4$ with 1.5 equivalents of DEA and measured at various temperatures of − 90, − 70, − 40, − 20 and 22 °C.

^{1}H NMR of $Ti(OEt)_4$ shows splitting due to oligomerisation only in the O-CH_2 proton signal at ~4.25 ppm (Fig. 3.31a), with the -CH_3 protons at 1.16 ppm. On addition of DEA 0.25 equivalents to 1.5 equivalents, the ethoxide -CH_3 signal was smoothly replaced by that of ethanol at 1.11 – 1.05 ppm and it is close to the standard position of the ethanol (CH_3) at 1.25 (Fig. 3.30, inset). As above, the shift in the position of this signal could imply some H-bonding or neutral binding to Ti. The ethanol O-CH_2 signal shifts from 3.76 ppm at 0.25 equivalents to 3.57 ppm at 0.5 equivalents then smoothly to 3.50 pm at 1.25 equivalents (Fig. 3.30, inset).

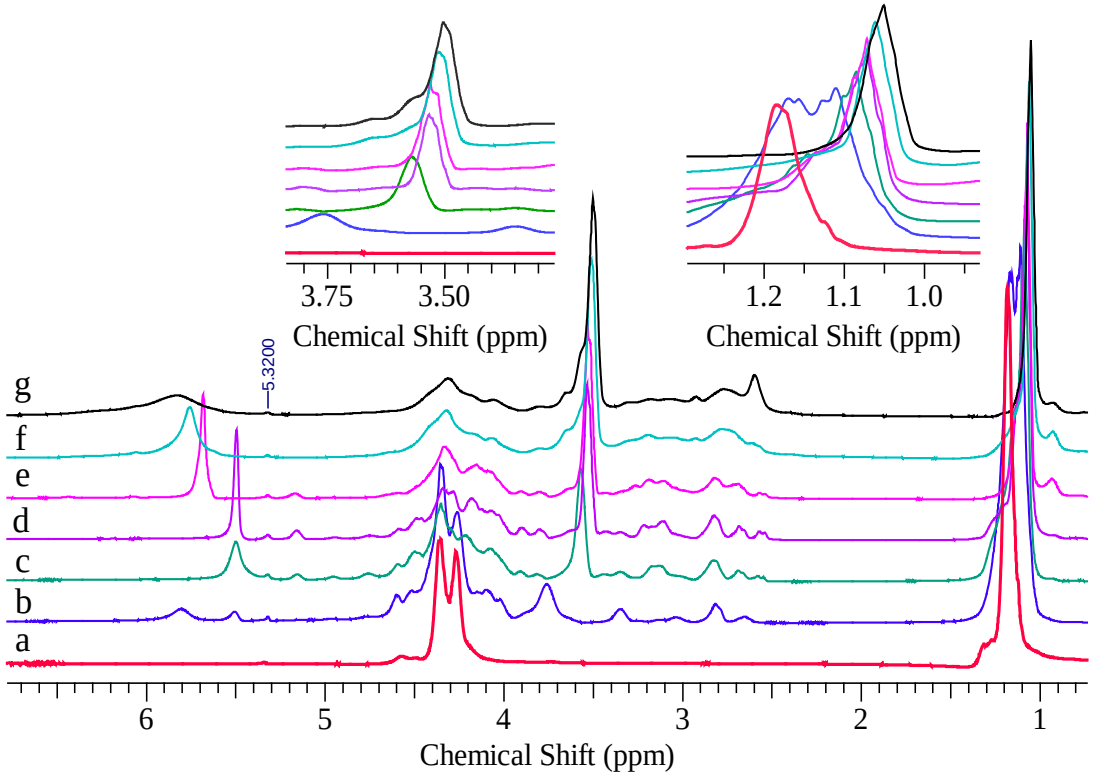

Fig. 3. 30 ^{1}H NMR spectra measured at – 90 °C for $Ti(OEt)_4$ (a) with various equivalents of DEA (b) 0.25 eq, (c) 0.5 eq, (d) 0.75 eq, (e) 1 eq, (f) 1.25 eq and (g) 1.5 eq.

The ethoxide O-CH_2 signal ~4.3 ppm broadens as DEA is added and never disappears, suggesting that it overlapped with the O-CH_2 signal of deprotonated and bonded DEA in comparison to $^{13}C\{^1H\}$ NMR (Fig. 3.30) (the CH_3 signal has disappeared). The N-H shift ~5.7 ppm did change, but this was small suggesting it might be due to variations in H-bonding. The DEA (N-CH_2) signal ~3 ppm changes with DEA addition and especially in the most DEA-rich samples, suggesting some unbound DEA, but the spectra are so broad that it was difficult to explain (Fig. 3.31).

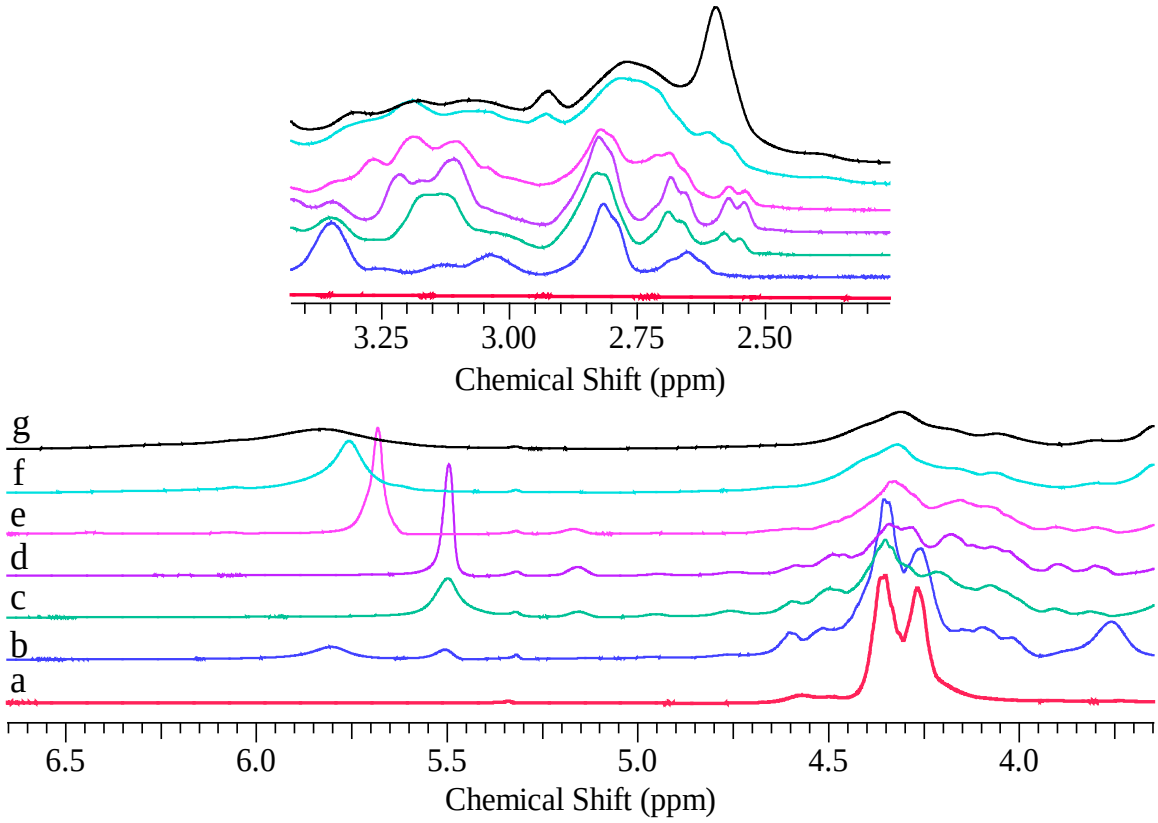

Fig. 3.31 ^1H NMR spectra measured at − 90 °C for $Ti(OEt)_4$ with various eq of DEA: (a) 0.25 eq, (b) 0.5 eq, (c) 0.75 eq, (d) 1 eq, (e) 1.25 eq and (f) 1.5 eq.

In comparison between all the NMR results, it can be seen that the reaction of $Ti(OEt)_4$ with the organic ligand (DEA) are still unclear, because it was difficult to determine the molecular structure of metal-containing species in a solution. However based on the NMR results, the $Ti(OEt)_4$ peaks were lost from the ^{1}H and $^{13}C\{^{1}H\}$ NMR spectra measured at room temperature suggesting the $Ti(OEt)_4$ groups were more labile at room temperature than at lower temperature. The determination of the molecular structure of the metal alkoxide modified with DEA is very complex. The current work is in agreement with Takayuki et al.[63] and [64] they found it is difficult to find the molecular structure of DEA system with $Ti(O^{i}Pr)_4$ in $Pr^{i}OH$ or with $Zr(O^{n}Pr)$ compound.[65] The tendency of metal to achieve its maximum coordination number, which results in an oligomeric system, is different by steric force branches that increase by increasing the alkoxy group. Therefore, the results suggested that the Ti species in the solution with DEA was present as a monomeric complex, which may have the structure as tridentate (Fig. 3. 32).

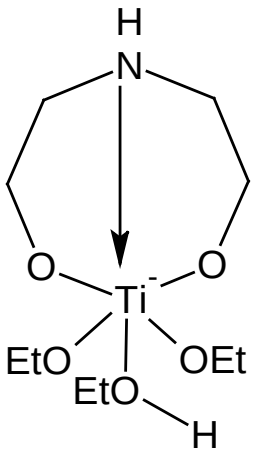

Fig. 3. 32 Proposed molecular structure of Ti species in the DEA system.

3.5 Mesoporous TiO_2 films

The self-organization of TiO_2 nanoparticles in the sol was directly related to the P123 templating quantity. P123 amphiphilic triblock copolymer is a nonionic surfactant and the driving force for creating the micelle for mesoporous structure is due to the hydrophilicity between the polyethylene oxide (PEO) and polypropylene oxide (PPO) block. The solution of TiO_2 has affinity binding to the P123 unit which then forms the self-assembled mesoporous structures.[66] Therefore, P123 acts as a structure directing agent while concentrated HCl inhibits the rapid condensation of the TiO_2 precursor.

Fig. 3.33 shows small-angle XRD (SXRD) patterns for the TiO_2 films prepared with 0.35 g of P123 and heat treated at different temperatures. It can be seen that each film fired at 300 to 600 °C exhibited one broad diffraction peak in the intensities of d_{200} in the low 2θ = 1.85º, while 100 (0.9º) and 110(1.4º) reflections associated with for cubic[67] or hexagonal symmetry of mesoporous structure[68] have disappeared. These results suggested a worm-like pore structure that assembled from a surfactant could be from non-completed self-assembly of P123 micelles.[69, 70]

The primary peak was not observed due to the large pores, because the beam stop on the C2 cut off the signal at 2θ = 0.9° and even then the edges of the direct beam scattered by air spill over the edge of the beam stop giving an intense signal to 2θ = 1.85°. As the temperature increased to 600 °C, a marked decreased in intensity and a broadening of the 200 peak occurred. This could be due to the reflection of a partial degradation of the assembled pores in the films and in agreement with Yu et al.[40].

Wide angle XRD in Fig. 3.33 displays a gradual increasing narrowing in the anatase TiO_2 101 peaks at 2θ = 25.4º with increasing calcination temperature. This was clearly the transition from amorphous to- anatase TiO_2 and subsequent growth of anatase-TiO_2 particles. At 300 °C, the film is typically amorphous and it converted to anatase-TiO_2 at around 400 °C. The amorphous-anatase transition and particle growth were accelerated by annealing the films at higher temperatures of 500 and 600 °C, as shown by the increasing and sharpening of the 101 peaks.

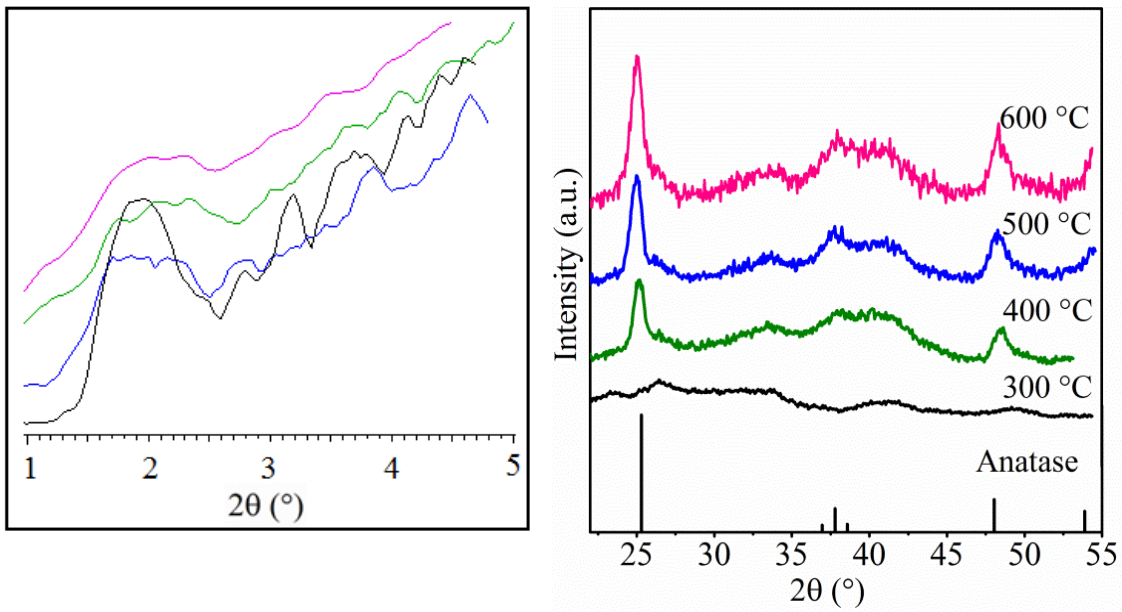

Fig. 3. 33 Small-angle (left) and wide-angle (right) XRD patterns of TiO_2 films with 0.35 g of P123 and fired for 4 hours at 300, 400, 500 or 600 °C from bottom to top.

As the P123 volume fraction was increased to 0.56 g, small and wide-XRD patterns for TiO_2 mesoporous film shows no difference than that previously mentioned by using 0.35 g of P123. Therefore, no ordered TiO_2 mesoporous structure was observed (Fig. 3.34).

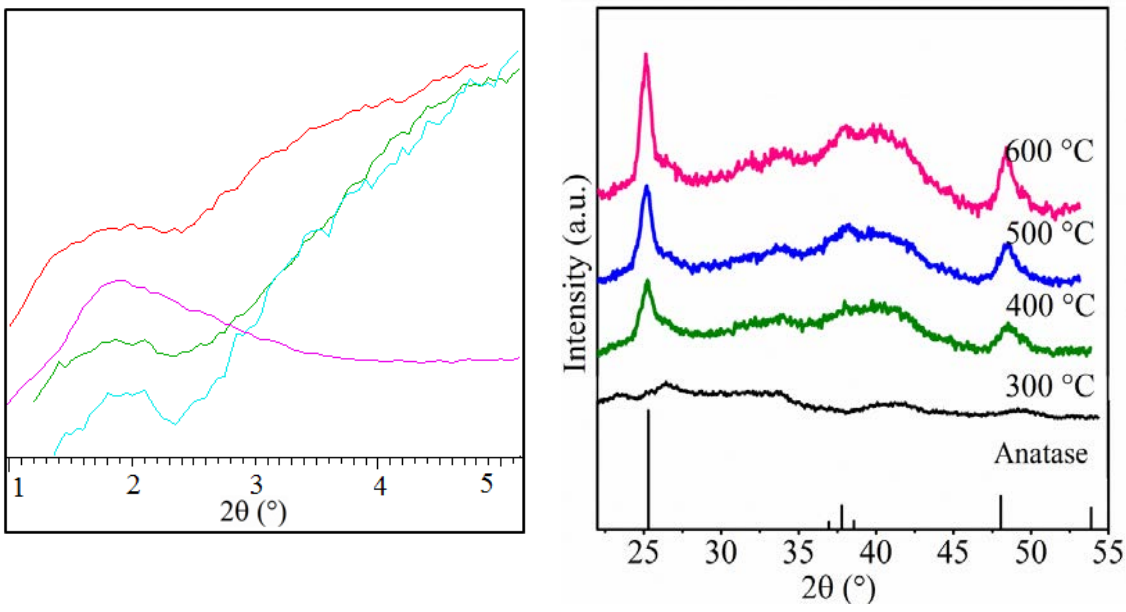

Fig. 3. 34 Small-angle (left) and wide-angle (right) XRD patterns of TiO_2 films with 0.56 g of P123 and fired for 4 hours at 300, 400, 500 or 600 °C from bottom to top.

Mesostructured TiO_2 powders were prepared by drying the sol after the dip-coating was completed and then it was used for BET measurements. Fig. 3.35 shows the Barrett−Joyner−Halenda (BJH) pore size distribution plots and N_2-sorption isothermals for the mesoporous TiO_2 prepared by 0.35 g of P123 and fired at 400 °C for 4 hours. (Fig. 3.35, inset). The hysteresis loop for the relative partial pressure (P/P_0) of the mesoporous TiO_2 was large in the range from 0.4 to 0.7 and it is typical of mesoporous materials, corresponding to the type-IV isotherm. A BJH analysis of the adsorption branch showed that the 400 °C-calcined sample exhibited a mean pore size (D_{BJH}) of 3.9 nm. The specific surface area and the pore volume of the powder were 187.9 $m^2\ g^{-1}$ and 0.99 $cm^3\ g^{-1}$, respectively.

According to BET measurements, there was an indication of a pore size of 3.9 nm in the sample prepared by 0.35 g of P123 and annealed at 400°C. However, the ordered pores were not observed from XRD results, and it is possible that the pore structure was just completely disordered.

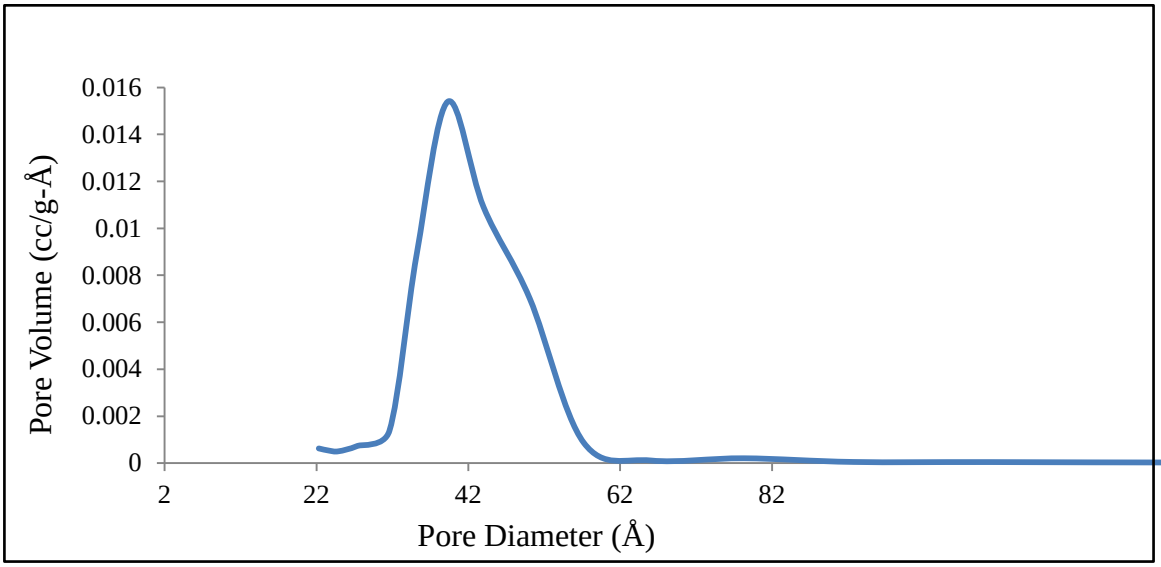

Fig. 3. 35 BJH pore size distribution of mesoporous TiO_2 and nitrogen adsorption/desorption isotherm (*inset*).

On the other hand, the influence of varying temperature on TiO_2 mesoporous film can be observed. As the temperature was increased from 4 to 34 °C in the preparation process of films for allowing the mesosphase to be formed, it was observed the crystallization of anatase titania network was almost kept constantly with increasing the temperature (Fig. 3.36, right), while no significant change for SAXRD patterns (Fig. 3.36, left).

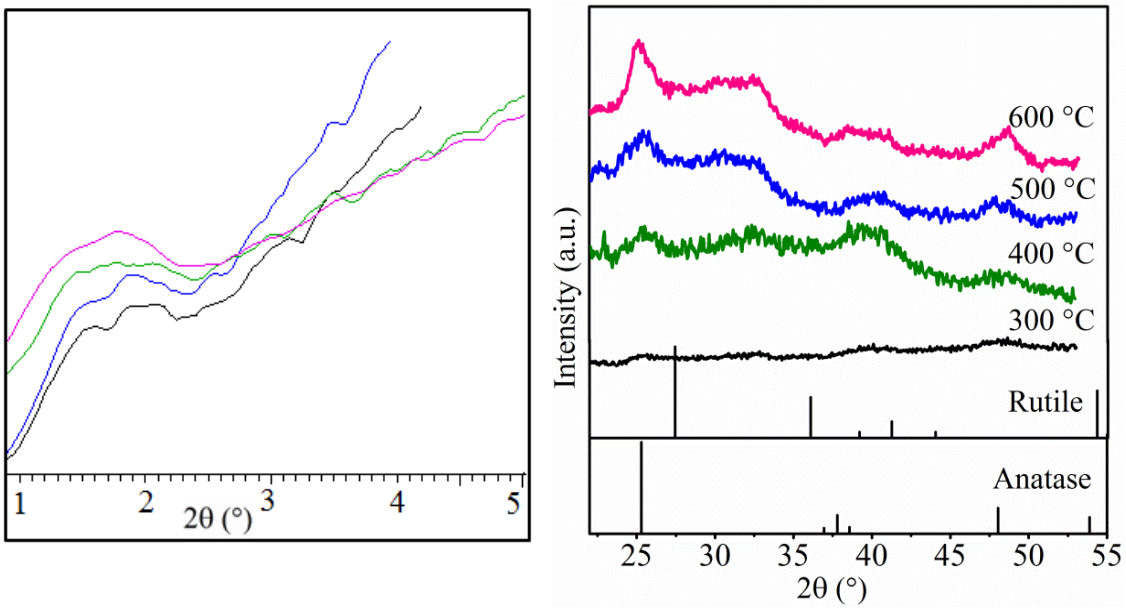

Fig. 3. 36 Small-angle (left) and wide-angle (right) XRD patterns of TiO_2 films prepared by 0.35 g of P123 and fired for 4 hours at 300 °C ,400 °C , 500 °C and 600 °C from bottom to top.

3.6 Conclusion

Anatase TiO_2 films and mixed anatase/rutile films were successfully synthesised using various types of sols with a dip-coating method. Ti $(O^iPr)_4$ and Ti$(OBu^n)_4$ sols modified with DEA, and Ti$(O^iPr)_4$ sols with HCl catalyst were investigated. Formation of complex ions between diethanolamine and titanium isopropoxide by using the optimum content of DEA was responsible for the stability of the precursor sol and producing good films with few cracks.

The mixture of anatase and rutile TiO_2 films and powders were obtained by the hydrolysis of $Ti(O^iPr)_4$ sol and $Ti(OBu^n)_4$ sol modified with (DEA), whereas when HCl was used as a catalyst, the anatase phase was observed and its crystallisation was increased by increasing the temperature.

With all sol types, the particle size of anatase was increased with increasing temperature, while the particle size of the rutile was extended due to agglomeration of the primary particles. The thickness of the films decreased as a function of temperature due to the aggregation and densification of the particles.

The composition and the chemical formula of TiO_2 sols prepared using $Ti(O^iPr)_4$ modified with DEA have been studied by the combinations between MS and NMR technique. ESI-TOFMS offered a good ability to identify masses of species in the TiO_2 sols with peak intensity at *m/z* 1359.03 being particularly prominent. The determination of its composition was difficult to obtain as the sol has many species. NMR measurements have shown that all the isopropoxide groups were substituted by ethoxy group and DEA ligands are bound to the titania in a monomeric structure.

Attempts to synthesise mesoporous TiO_2 thin films by EISA-sol-gel method using tri-block copolymer P123 as a template were accomplished. The crystallisation of titania from amorphous to anatase form was caused by heating at 400 °C and the wall of mesoporous titania was formed. The pore size of the samples prepared at 400 °C based on BET was 3.9 nm, however it has not detected by XRD instrument may be the pore was not organised. Mesoporous TiO_2 films having excellent potential for some application in catalysis, therefore it required effective equipment to investigate the pore structure.

3.7 References

1. N. Avci, P. Smet, H. Poelman, N. Velde, K. Buysser, I. Driessche and D. Poelman, *J. Sol-Gel Sci. Technol.*, 2009, **52**, 424-431.
2. B. I. Kharisov, O. V. Kharissova and H. V. R. Dias, *Nanomaterials for Environmental Protection*, Wiley, 2014.
3. D. S. Bhachu, S. Sathasivam, G. Sankar, D. O. Scanlon, G. Cibin, C. J. Carmalt, I. P. Parkin, G. W. Watson, S. M. Bawaked, A. Y. Obaid, S. Al-Thabaiti and S. N. Basahel, *Adv. Funct. Mater.*, 2014, **24**, 5075-5085.
4. W. Q. Wu, Y. F. Xu, H. S. Rao, C. Y. Su and D. B. Kuang, *J. Am. Chem. Soc.*, 2014, **136**, 6437-6445.
5. A. D. Lisenkov, S. K. Poznyak, M. F. Montemor, M. J. Carmezim, M. L. Zheludkevich and M. G. S. Ferreira, *J. Electrochem. Soc.*, 2014, **161**, D73-D78.
6. Y. Tsuge, K. Inokuchi, K. Onozuka, O. Shingo, S. Sugi, M. Yoshikawa and S. Shiratori, *Thin Solid Films*, 2006, **499**, 396-401.
7. T. K. Ghorai and P. Dhak, *Adv. Mater. Lett.*, 2013, **4**, 121-130.
8. Y. Chimupala, G. Hyett, R. Simpson and R. Brydson, *J. Phys.: Conf. Ser.*, 2014, **522**, 012074.
9. N. Rausch and E. P. Burte, *J. Electrochem. Soc.*, 1993, **140**, 145-149.
10. E. Noori, N. Mir, M. Salavati-Niasari, T. Gholami and M. Masjedi-Arani, *J. Sol-Gel Sci. Technol.*, 2014, **69**, 544-552.
11. A. Mills, A. Graham and C. O'Rourke, *Sens. Actuators, B*, 2014, **190**, 907-912.
12. H. Kochkar, M. Triki, K. Jabou, G. Berhault and A. Ghorbel, *J. Sol-Gel Sci. Technol.*, 2007, **42**, 27-33.
13. Y. Hu, H. L. Tsai and C. L. Huang, *Mater. Sci. Eng., A*, 2003, **344**, 209-214.
14. E. György, G. Socol, E. Axente, I. N. Mihailescu, C. Ducu and S. Ciuca, *Appl. Surf. Sci.*, 2005, **247**, 429-433.
15. S. Sen, S. Mahanty, S. Roy, O. Heintz, S. Bourgeois and D. Chaumont, *Thin Solid Films*, 2005, **474**, 245-249.
16. G. San Vicente, A. Morales and M. T. Gutierrez, *Thin Solid Films*, 2001, **391**, 133-137.
17. K. Murugan, T. N. Rao, G. V. N. Rao, A. S. Gandhi and B. S. Murty, *J. Mater. Chem. Phys.*, 2011, **129**, 810-815.
18. T. Imao, N. Noma and S. Ito, *J. Sol-Gel Sci. Technol.* , 2006, **38**, 197-202.
19. J. A. Galaviz-Perez, F. Chen, J. R. Vargas Garcia, Q. Shen and L. Zhang, *12th International Symposium on Multiscale, Multifunctional and Functionally Graded Materials (Fgm 2012)*, 2013, **419**.
20. C. Legrand-Buscema, C. Malibert and S. Bach, *Thin Solid Films*, 2002, **418**, 79-84.
21. A. Verma and S. A. Agnihotry, *Electrochim. Acta*, 2007, **52**, 2701-2709.
22. Y. Takahashi and Y. Matsuoka, *J. Mater. Sci.*, 1988, **23**, 2259-2266.
23. J. Hu, C. Zhang, B. Cui, K. Bai, S. Guan, L. Wang and S. Zhu, *Appl. Surf. Sci.* , 2011, **257**, 8772-8777.
24. J. Yu, X. Zhao and Q. Zhao, *J. Mater. Sci. Lett.*, 2000, **19**, 1015-1017.
25. T. Nishide, M. Sato and H. Hara, *J. Mater. Sci.*, 2000, **35**, 465-469.
26. D. J. Kim, S. H. Hahn, S. H. Oh and E. J. Kim, *Mater. Lett.*, 2002, **57**, 355-360.
27. J. Godovac-Zimmermann and L. R. Brown, *Mass. Spectrom. Rev.*, 2001, **20**, 1-57.
28. M. E. Simonsen and E. G. Sogaard, *J. Sol-Gel Sci. Technol.*, 2010, **53**, 485-497.

29. M. E. Simonsen and E. G. Sogaard, *Eur. J. Mass Spectrom.*, 2013, **19**, 265-273.
30. M. L. Naklicki, S. I. Gorelsky, W. Kaim, B. Sarkar and R. J. Crutchley, *Inorg. Chem.*, 2012, **51**, 1400-1407.
31. M. Jung, H. Oh, J. Yang and Y. Shul, *Bull. Korean Chem. Soc.*, 1999, **20**, 1394-1398.
32. M. Jung, *Int. J. Inorg. Mater.*, 2001, **3**, 471-478.
33. S. Benfer, U. Popp, H. Richter, C. Siewert and G. Tomandl, *Sep. Purif. Technol.* , 2001, **22**, 231-237.
34. A. M. Urbas, M. Maldovan, P. DeRege and E. L. Thomas, *Adv. Mater.*, 2002, **14**, 1850-1853.
35. C. J. Brinker, Y. Lu, A. Sellinger and H. Fan, *Adv. Mater.*, 1999, **11**, 579-585.
36. J. C. Yu, X. Wang and X. Fu, *Chem. Mater.*, 2004, **16**, 1523-1530.
37. J. H. Koh, J. A. Seo, S. H. Ahn and J. H. Kim, *Thin Solid Films*, 2010, **519**, 158-163.
38. W. Gan, M. Lee, R. Amal, H. Zhao and K. Chiang, *J. Appl. Electrochem.*, 2008, **38**, 703-712.
39. J. Hong Pan and W. In Lee, *New J. Chem.*, 2005, **29**, 841-846.
40. J. C. Yu, X. Wang and X. Fu, *Chem. Mater.*, 2004, **16**, 1523-1530.
41. A. C. Larson and R. B. V. Dreele, *Los Alamos National Laboratory Report LAUR* 2004, 86-748.
42. *Inorganic Crystal Structure Database (ICSD, Fiz Karlsruhe) accessed via the National Chemical Database Service hosted by the Royal Society of Chemistry.*
43. R. B. V. Dreele and A. C. Larson, *LANSCE MS-H805, Los Alamos National Laboratory, NM87545*, 2000.
44. D.W. Park, Y.K. Choi, K.J. Hwang, J.W. Lee, J. K. Park, H. D. Jang, H.S. Park and S. J. Yoo, *Adv. Powder Technol.*, 2011, **22**, 771-776.
45. G. Balasubramanian, D. D. Dionysiou, M. T. Suidan, V. Subramanian, I. Baudin and J. M. Laîné, *J. Mater. Sci.*, 2003, **38**, 823-831.
46. C. Urh, L. S. Urska, T. Polonca and R. R. Primoz., *Acta. Chimica .Slovenica.*, 2006.
47. Y. Chen and D. D. Dionysiou, *Appl. Catal., B*, 2006, **69**, 24-33.
48. S. Attia, J. Wang, G. Wu, J. Shen and J. Ma, *J. Mater. Sci. Technol.*, 2002, **18**, 31-33.
49. H. M. Rietveld, *Acta Crystallogr.*, 1966, **20**, 508-513.
50. C. R. Brundle, C. A. Evans and S. Wilson, *Encyclopedia of materials characterization : surfaces, interfaces, thin films*, Butterworth-Heinemann ; Manning, Boston; Greenwich, C.T, 1992.
51. M. Horn, C. Schwebdtfeger and E. Meagher, *Z. Kristallogr.*, 1972, **136**, 273-281.
52. W. Gonschorek, *Z. Kristallogr.* , 1982, **160**, 187-204.
53. Y. U. Ahn, E. J. Kim, H. T. Kim and S. H. Hahn, *Mater. Lett.*, 2003, **57**, 4660-4666.
54. A. G. Amy and F. B. JillIian, *Am. Mineral.*, 1997, **82**, 717-728.
55. T. Hashimoto, T. Yoko and S. Sakka, *Bull. Chem. Soc. Jap.*, 1994, **67**, 653-660.
56. N. Negishi and K. Takeuchi, *Mater. Lett.*, 1999, **38**, 150-153.
57. S. Funda, A. meltem, H. Sayilkan, Y. Onal, M. Akarsu and E. Arpac, *Turk. J. Chem.*, 2005, 697-706.
58. W. W. So, S. B. Park and S. J. Moon, *J. Mater. Sci. Lett.*, 1998, **17**, 1219-1222.
59. H. Zhang and J. F. Banfield, *J. Mater. Res.* , 2000, **15**, 437-448.
60. R. Nechache, M. Nicklaus, N. Diffalah, A. Ruediger and F. Rosei, *Appl. Surf. Sci.* , 2014, **313**, 48-52.
61. J.G. Yu, H.G. Yu, B. Cheng, X.J. Zhao, J. C. Yu and W.K. Ho, *J. Phys. Chem. B*, 2003, **107**, 13871-13879.

62. C. J. Brinker and G. W. Scherer, *Sol-gel Science: The Physics and Chemistry of Sol-gel Processing*, Academic Press, 1990.
63. T. Ban, Y. Ohya and Y. Takahashi, *J. Sol-Gel Sci. Technol.*, 2003, **27**, 363-372.
64. A. Verma, M. Kar and D. P. Singh, *J. Sol-Gel Sci. Technol.*, 2010, **54**, 129-138.
65. G. I. Spijksma, L. Kloo, H. J. M. Bouwmeester, D. H. A. Blank and V. G. Kessler, *Inorg. Chim. Acta.* , 2007, **360**, 2045-2055.
66. M. Yong, A. Wong and G. Ho, *Mater. Chem. Phys.*, 2009, **116**, 563-568.
67. J. Hong Pan and W. In Lee, *New J. Chem.*, 2005, **29**, 841-846.
68. N. P. Hung, N. T. Hoan and N. V. Nghia, *Nanosci. Nanotech.*, 2013, **3**, 19-25.
69. X. P. Cao, D. Li, W. H. Jing, W. H. Xing and Y. Q. Fan, *J. Mater. Chem.*, 2012, **22**, 15309-15315.
70. W. Jing, W. Huang, W. Xing, Y. Wang, W. Jin and Y. Fan, *ACS Appl. Mater. Interfaces.*, 2009, **1**, 1607-1612.

4. Sol-gel route for barium titanate ($BaTiO_3$) and bismuth titanate ($Bi_2Ti_2O_7$) films

4.1 Introduction

In order for multimetallic oxide thin films to be successfully used in microelectronic applications and also be integrated into silicon device technology, it is necessary to synthesise high-quality, pure phase films. Moderate crystallization temperatures are desired in porous films to facilitate the creation of durable pore structures. There are different techniques for synthesizing $BaTiO_3$ and $Bi_2Ti_2O_7$ by various researchers, the quality of the film is not only affected by the synthesis method but also by the precursor materials used. Sol-gel methods can provide low temperature crystallization and low cost. This chapter describes the synthesis of $BaTiO_3$ and $Bi_2Ti_2O_7$ films.

Existing sol-gel routes to $BaTiO_3$ films typically employ $Ti(O^iPr)_4$ and barium acetate.[1-4] hydroxide,[5] isopropoxide[6] or ethylhexanoate[7] in acetic acid[4] alcohols[5, 6] or mixtures of acetic acid and alcohols.[1-3, 7] A reaction moderator such as acetylacetone,[7] diethanolamine[6] or ethylene glycol[5] may be added to control the hydrolysis of the $Ti(O^iPr)_4$, although this functionality can also be achieved via acetate groups from the acetic acid or by using methoxyethanol in the solvent mixture[2, 3] which can displace isopropoxide groups from the titanium and block additional coordination sites via coordination of the ether group. A final variation is that some researchers have added water to the mixture in order to gain better control of its concentration rather than relying on moisture from the reagents and the atmosphere as a source of this component, which is critical in all cases for the hydrolysis of the precursors.

It is not typical to combine all of the controls described above in a single process. In most cases very thin films, of the order of tens of nm per coating, are produced and procedures rely on multiple coating/ drying cycles to build film thickness. An exception to this is the work of Yuk et al.[4] who produced heavily cracked 7.5 μm thick coatings from acetic acid sols with no added alcohol.[4]

The ability to produce good quality thicker films in a single coating is useful because it would then be possible to dilute sols with extra alcohol to control the film thickness over a wide range. Hence in this work water was added to sols in order to increase the concentration of hydrolysed species and enhance condensation during solvent evaporation. Stabilisation of these sols required a strongly coordinating environment and sols containing acetate and acetylacetone diluted with methoxyethanol were found to be stable and clear. Kamalasanan *et al* previously applied a similar approach, but with methanol as the solvent.[7] They did produce thicker films by reducing the methanol content of the sols, but suffered from poor adhesion in the thicker films.

$Bi_2Ti_2O_7$ has been deposited from a mixture of the chlorides in acidified ethanol[8] and the images of the films showed the $Bi_2Ti_2O_7$ films were homogeneous with an average grain size of about 2-10 nm, or from citrate solutions stabilised by ammonia and diethanolamine[9] or from bismuth nitrate solutions with $Ti(O^iPr)_4$ or $Ti(O^nBu)_4$ in acetic acid[10] with the addition of methoxyethanol,[11, 12] methoxyethanol and acetylacetone,[13] or acetylacetone and ethylene glycol monoethyl ether.[14] Typically very thin films are produced by spin coating and built up by multiple coating/firing cycles. In most cases the films are also observed to exhibit a strong <111> orientation.[9, 11, 13, 14] In one case yttria-stabilised zirconia single crystal substrates with a similar lattice spacing to that of the pyrochlore phase were used, and films could be produced that were aligned with substrates that were cut along various different crystal faces[10]. Thicker films were heavily textured and porous.[11, 13, 14]

Part of $Bi_2Ti_2O_7$ film works were contributed jointly by the project student, Jack Brewer.

4.2 Experimental procedure

All reagents were purchased from Sigma-Aldrich and solvents from Fisher Scientific.

4.2.1 Preparation of $BaTiO_3$ sol using barium nitrate

Initially the precursor chosen was barium nitrate (Ba $(NO_3)_2$) which is a white solid compound. This precursor has been dissolved in acetic acid or in 2-methoxyethanol at room temperature with and without heating, however both attempts failed to produce clear solutions of Ba $(NO_3)_2$.

4.2.2 Preparation of $BaTiO_3$ sol using barium acetate

Variations in the $BaTiO_3$ precursor sol composition are discussed in the results and discussion, but typically barium acetate ($Ba(OAc)_2$, 2.5 g) was dissolved in acetic acid (15 mL) with stirring at 60 °C for 10 minutes to obtain a clear and homogenous solution. A measured amount of water (Table 5.1) was added to the Ba solution and stirred for a further 10 minutes. Titanium isopropoxide (3 mL) was dissolved in anhydrous 2-methoxyethanol (15 mL) and acetylacetone (1.46 mL) was added as a moderator to control the hydrolysis rate of the titanium isopropoxide. The barium acetate solution was added drop-wise to the titanium isopropoxide solution with stirring over a period of ~1 hour and the resultant transparent and light yellow sol was aged in a sealed bottle at room temperature for 24 hours.

4.2.3 Preparation of $Bi_2Ti_2O_7$ sol

In a typical $Bi_2Ti_2O_7$ sol preparation, $Bi(NO_3)_3 \cdot 5H_2O$ (6.8869 g) was dissolved in glacial acetic acid (15 mL) at 50 °C and the solution was allowed to cool to room temperature in a sealed glass bottle. Titanium n-butoxide (5 mL) was dissolved in a mixture of 2- methoxyethanol (15 mL) and acetylacetone (1.46 mL) and stirred for 5 minutes. The bismuth nitrate solution was added drop wise to the titanium butoxide solution over ~1 hour and the resultant transparent, dark yellow sol was aged in a sealed bottle at room temperature for 24 hours.

4.2.4 Fabrication of $BaTiO_3$ and $Bi_2Ti_2O_7$ films

Microscope glass slides or (100) silicon were cut to10 mm × 20 mm and used as substrates for $BaTiO_3$ or $Bi_2Ti_2O_7$ (respectively) film depositions. The slides were cleaned in piranha etch (40 mL, 3:1 H_2SO_4: H_2O_2) until the bubbles had ended completely (roughly 3 hours) to remove organic contamination (note this can produce explosive mixtures if incorrectly prepared), rinsed with water then ethanol, and blown dry with nitrogen. Using a Nima Technology D1L dip-coater a 10 × 10 mm region of the substrate was immersed into the sol for 5 seconds and then withdrawn at a rate of 65 mm minutes^{-1}. The drop of excess sol at the bottom of the substrate was removed with tissue and then films were placed horizontally on a petri dish to age/dry in air for ~30 minutes. The films were annealed in air by placing into a pre-heated furnace at various temperatures for 40 or 30 minutes.

4.2.5 Dielectric measurements

For dielectric measurement samples were deposited on 200 nm gold deposited by vacuum evaporation. The dielectric constant was determined from the capacitor equation, with a dielectric layer averaged-thickness obtained from SEM characterisation. After coating and firing the $BaTiO_3$ film, 2.5×10^{-3} m^2 of copper foil was pressed onto the surface using a silicone sheet through mechanical force on the $BaTiO_3$ (Fig. 4.1).
Dielectric measurement has been carried out using Biologic SP150 Impedance /Gain-phase analyser. The frequency range for the dielectric measurement was varied in the range of 1 kHz to1 mHz.

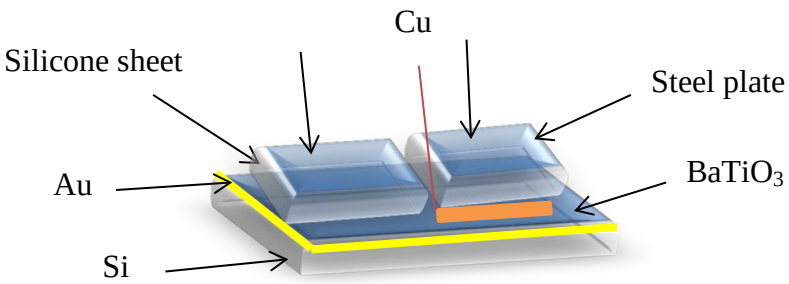

Fig. 4. 1 Schematic drawing of $BaTiO_3$ films for dielectric measurement.

4.3 Results and discussion

$BaTiO_3$ and $Bi_2Ti_2O_7$ films were produced from sols in acetic acid/methoxyethanol mixtures. Films with thickness of ~5 μm were produced by dip coating once and firing the resultant films, and multiple dip/dry cycles could be used to build up larger thickness.

4.3.1 $BaTiO_3$ films

For capacitance application it is essential that $BaTiO_3$ films have both structural and compositional stability and therefore $BaTiO_3$ films were optimised in terms of the purity and the quality of the films as a function of temperature, water content and aging time.

Table 4. 1 Different $BaTiO_3$ films preparation.

Experiment number	Experimental procedure
1	Aging variation at 900 °C
2	Water and temperature variation
3	Thermal stability
4	Varied number of dip-coating at 750 °C
5	Variation in preparation at 750 °C

4.3.1.1 Aging variation

The influence of the aging time was investigated on the $BaTiO_3$ film structure which annealed at 900 °C as shown in the stacked XRD patterns (Fig. 4.2). Shortening the sol aging time resulted in changes to the film composition and phase content. A film produced from an unaged sol and heated at 900 °C for 40 minutes contained mainly $BaTi_2O_5$ with some hexagonal $BaTiO_3$. EDX shows this film have a 1:2 ratio of Ba:Ti, suggesting that the sol itself is inhomogeneous at this point (the bulk content of the sol has 1:1 Ba:Ti ratio). 3 hours sol aging time resulted in a decrease in the intensity of the $BaTi_2O_5$ peaks in a film heated under the same conditions, and after 9 or 24 hours sol aging the $BaTi_2O_5$ peaks were not observed, although peaks due to the $Ba_2TiOSi_2O_7$ (fresnoite phase) were observed. This phase has previously been shown to grow at the $BaTiO_3$/Si interface when films are heated above 730 °C.[15]

This importance of sol aging time suggests a certain level of development of the oligomer structure is necessary in order to retain barium in the meniscus during coating, either by direct bonding to the titanium-containing species by carriage of barium-rich solution into a network structure formed by titanium containing species.

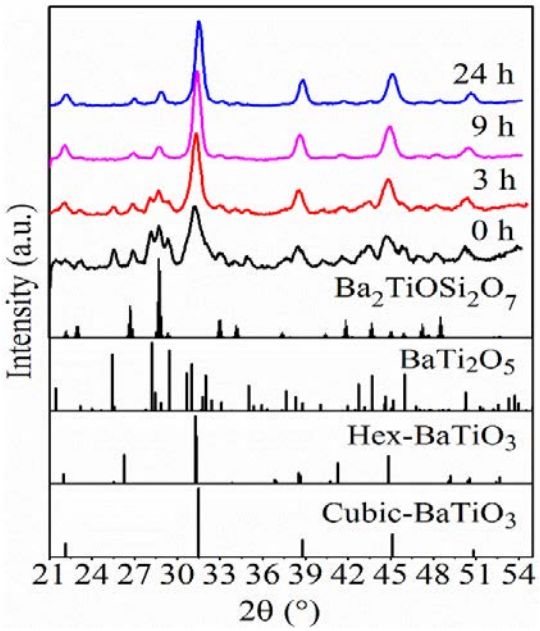

Fig. 4. 2 XRD patterns of $BaTiO_3$ films prepared by different aging and sintered at 900 °C for 40 minutes, compared with standard patterns from ICSD for cubic phase,[16] hexagonal phase,[17] $BaTi_2O_5$[18] and $Ba_2TiOSi_2O_7$.[19]

4.3.1.2 Water and temperature variation

Initially, two $BaTiO_3$ experiments were carried out using 0.7 mL and 1 mL, and then fired at 750 °C and 850 °C for 40 minutes. The $BaTiO_3$ films prepared by 0.7 mL of H_2O, contained cubic $BaTiO_3$ with a trace of hexagonal-$BaTiO_3$ and an impurity peak at 29º due to the $BaTi_2O_5$ phase (Fig. 4.3a and b). The micrographs of the 750 °C fired film (Fig. 4.4a) show that it was smooth with small particles and pinholes in the surface, while at 850 °C the $BaTiO_3$ was partially delaminated from the substrate (Fig. 4.4b).
By increasing the water content to 1 mL and firing at 750 °C (Fig. 4.3c), the $BaTiO_3$ films were almost pure $BaTiO_3$ cubic phase and the film were smooth and well adhered and crack free (Fig. 4.4c). However at 850 °C some $BaTi_2O_5$ has grown (Fig. 4.3d) and SEM depicts the film as smooth with small particles in the top surface (Fig. 4.4d). This is in agreement with Valdez-Nava.[20]

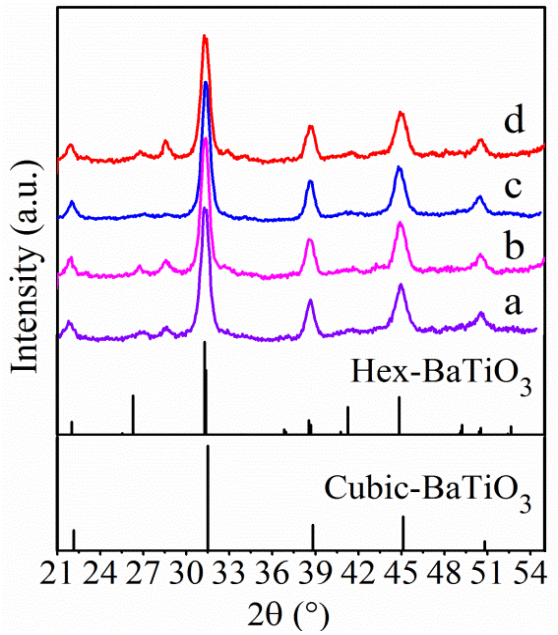

Fig. 4. 3 XRD patterns of $BaTiO_3$ prepared by different amounts of H_2O and annealed for 40 minutes: (a) 0.7 mL, 750 °C, (b) 0.7 mL, 850 °C (c) 1 mL, 750 °C and (d) 1 mL, 850 °C, compared with standard patterns from ICSD for cubic phase[16] and hexagonal phase.[17]

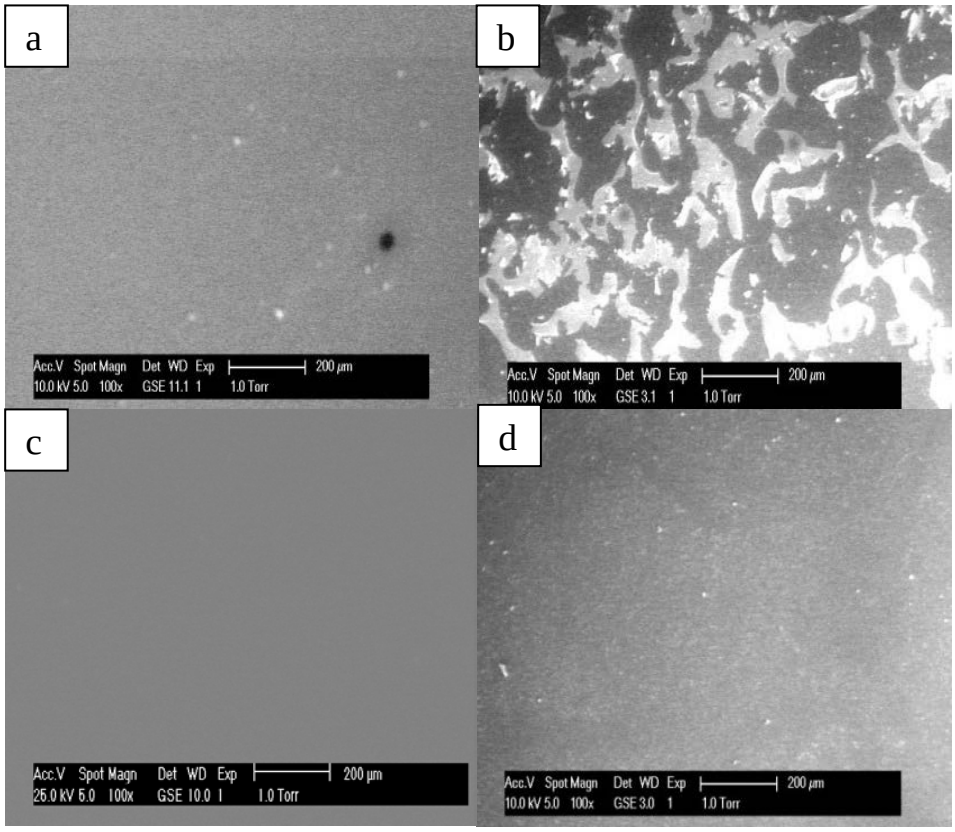

Fig. 4. 4 Microstructure of $BaTiO_3$ films calcined for 40 minutes and prepared with different amounts of water (a) 0.7 mL, 750 °C, (b) 0.7 mL, 850 °C, (c) 1 mL, 750 °C (d) 1 mL, 850 °C.

4.3.1.3 Firing temperature variation

After optimising the best preparation route for the synthesis of good quality $BaTiO_3$ films, the films was investigated in terms of firing temperature variation. Fig. 4.5 shows the XRD patterns of $BaTiO_3$ films which were fired at temperatures ranging from 300 °C to 1000 °C. As expected, the sol-gel deposited $BaTiO_3$ framework is completely amorphous at 300 °C and 400 °C. The onset of crystallisation was exhibited after 500 °C and it is worth noting that $BaTiO_3$ with hexagonal structure formed with broadening of the reflections that were not shared with cubic phase. This suggests some disorder consistent with the low processing temperature. These reflections reduced in intensity in samples produced at 600 °C and 700 °C, and were very weak in samples annealed at 750 °C. The composition profile of the Ba/Ti ratio is 1.00 from EDX data (Fig. 4.5). So, the single cubic (tetragonal) $BaTiO_3$ phase was observed at 750 °C fired film which is only found in agreement with Kamalasanan paper[7] who used barium ethylhexanoate as a precursor, whereas other papers[4-6] obtained cubic (tetragonal) $BaTiO_3$ at 600 °C or 650 °C.

The films fired at temperatures above 800 °C, however, exhibited peaks corresponding to $BaTi_2O_5$ and peaks due to growth of the fresnoite $Ba_2SiOTi_2O_7$ phase were observed as well as the peaks relevant to $BaTiO_3$. There were also some cracks on the films.

The hexagonal $BaTiO_3$ phase is usually obtained at high temperature (1460 °C) for bulk materials.[21] The threshold of hexagonal phase crystallisation was observed in this study at 500 °C and thus it can be explained by the high surface free energy which may be sufficient to the growing of the hexagonal phase by increasing the temperature to 500 °C.[21] The present result is in agreement with Andrade et al.[22] who synthesised hexagonal $BaTiO_3$ films at low temperature. Nièpce et al.[23] explained the formation of hexagonal phase based on $BaTiO_3$ to the planar defects can be created due to the complex phenomena associated with Ti^{+3} and oxygen and/or barium vacancies.

In samples prepared at low temperature it is often difficult to observe the small tetragonal splitting in $BaTiO_3$. Rietveld fitting of the data collected on a film heated at 750 °C for 40 minutes, showed good fits to both cubic and tetragonal $BaTiO_3$, with a very small contribution (<2%) from hexagonal $BaTiO_3$. The tetragonal phase delivered a slightly better fit, most notably in the 200/002 reflection at ~45°.

In comparable refinements the cubic phase fit statistics were R_{wp} = 9%, R_p = 7.1%, whereas the tetragonal phase was fitted with R_{wp} = 8.3%, R_p = 6.6% and χ^2 = 6.1. The tetragonal fit is shown in Fig. 4.5 and the lattice parameters were close to those quoted in this study used to define the structural model of a = 4.0022(1) and c = 4.0318(5) Å.[24] The average crystallite size was refined as 29(1) nm.

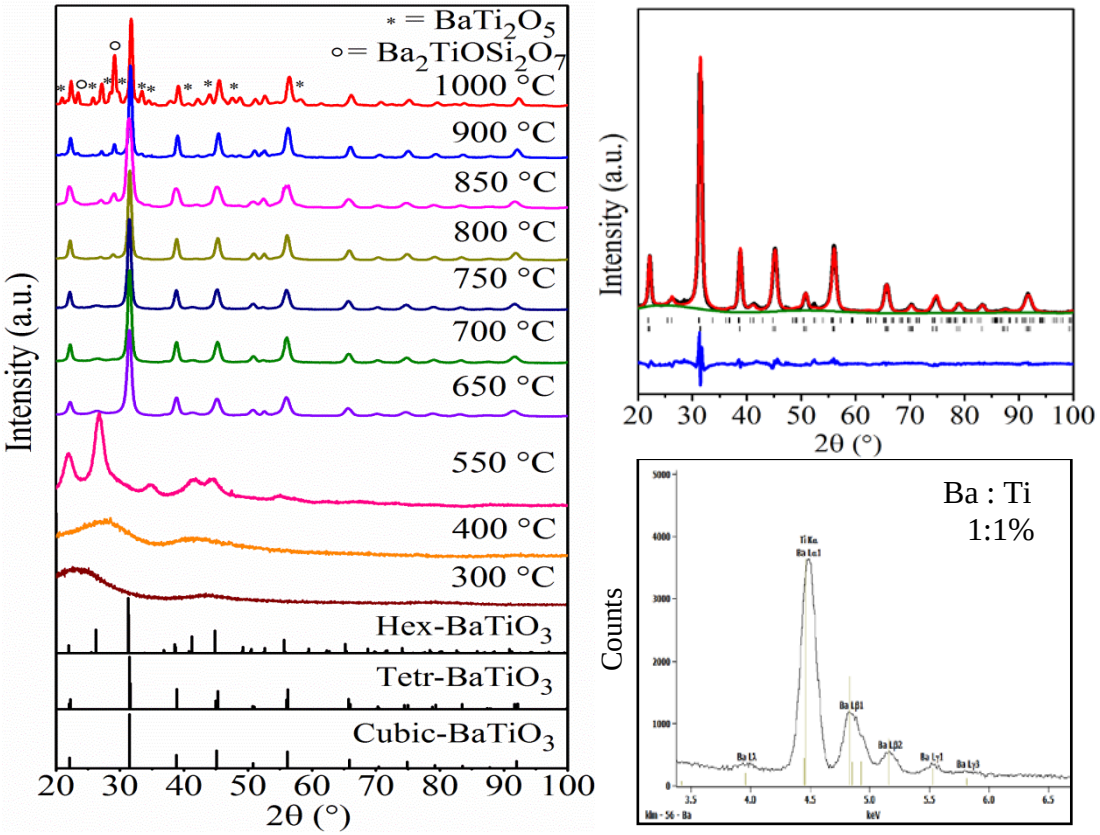

Fig. 4. 5 Temperature variation of the XRD patterns of $BaTiO_3$ films fired at various temperatures compared with standard patterns from ICSD(left) for cubic phase,[25] hexagonal[17] and tetragonal phase.[24] A Rietveld fit to the XRD for a film heated at 750 °C (right). Rietveld fit results: tetragonal $BaTiO_3$ (93%, lower tick marks) P_4mm,[24] a = 4.0100(5) and c = 4.04326(8) Å, Ba 0, 0, 0, U_{iso} = 0.0105(10), Ti ½, ½, 0.451(5), U_{iso} = 0.008(3), O ½, ½, − 0.037, U_{iso} = 0.05(2), O ½, 0, 0.518, U_{iso} = 0.05(2). Oxygen positions not refined; Hexagonal $BaTiO_3$ (7 % upper tick marks) $P6_3/mmc$,[17] a = 5.735(2) and c =14.000(12) Å and EDX spectrum of $BaTiO_3$ film calcined at 750 °C for 40 minutes (bottom right).

4.3.1.4 Varied number of dip-coating cycles followed by firing at 750 °C

After 24 hours aging time of fired $BaTiO_3$ films at 750 °C for 40 minutes, produced by dipping the substrate into the sol once were found to be around 5 µm thick (Fig. 4.6a).

The films were largely smooth and free from cracks and pinholes, although both of these deficiencies were found close to the edges of the films.

The film thickness could be increased by dipping the substrate multiple times with 30 minutes aging time between dippings, with no appreciable change in XRD phase behaviour or the Ba:Ti ratio (1:1 by EDX) observed in the thicker films. The XRD peak shapes were also very consistent, suggesting crystallite size to be unchanged with thickness. After 4 dippings the thickness of the fired films was around 20 µm and the central parts remained smooth (Fig. 4.6d), although the presence of cracks and pinholes around the edges of the films does become more significant with thickness.

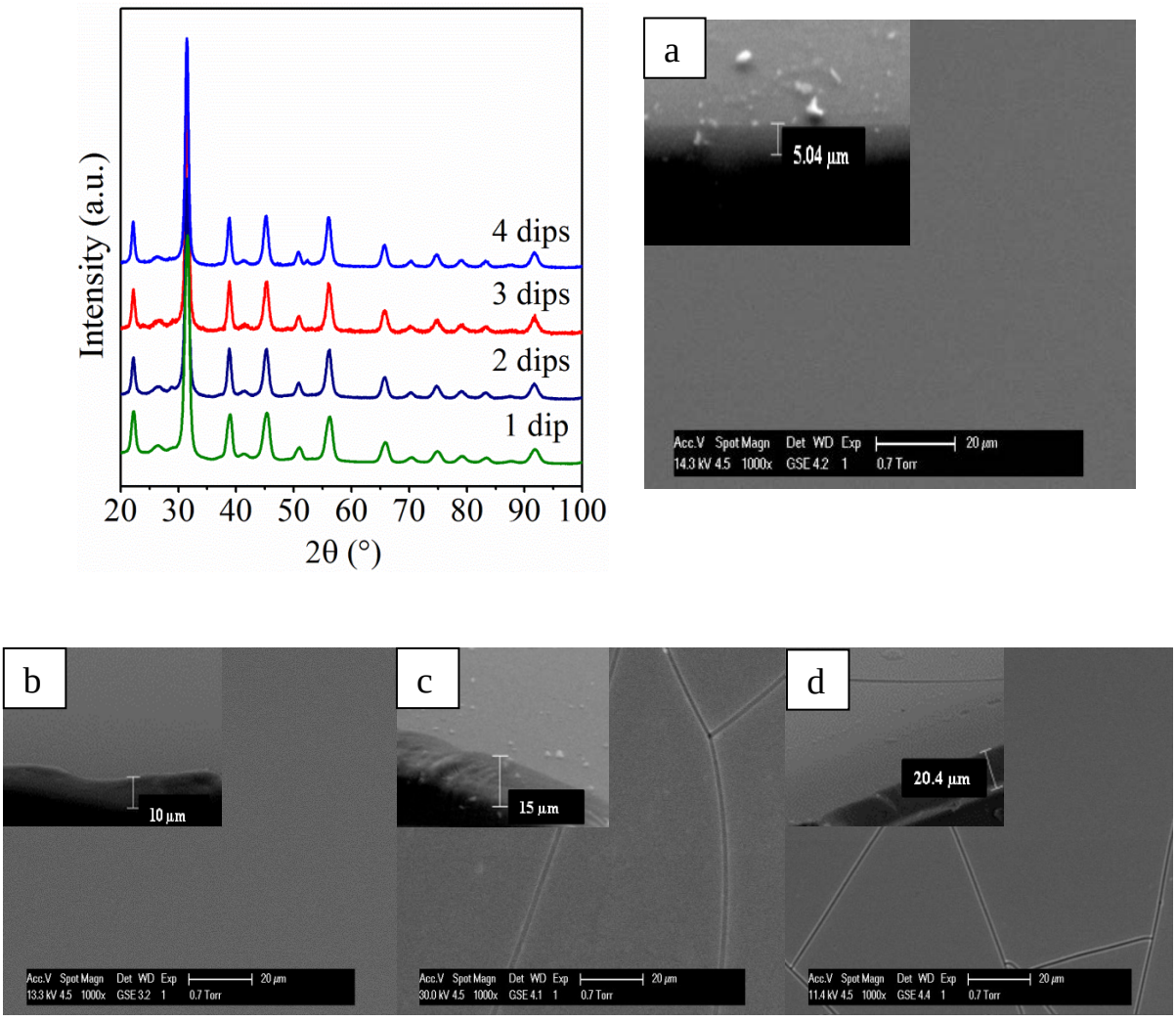

Fig. 4. 6 Multiple-dips of the XRD patterns of $BaTiO_3$ films fired at 750 °C for 40 minutes and SEM images of the front face and a cross section(top right and bottom) of a film prepared by (a) 1 dip, (b) 2 dips, (c) 3 dips and (d) 4 dips and fired at 750 °C for 40 minutes .

4.3.1.5 Variations in sol composition followed by firing at 750 °C

Different preparation routes for synthesis of $BaTiO_3$ films, such as increasing the amount of the moderator, using basic solution to clean the substrate, without using 2-ME as co-solvent for preparing the sol and also annealing the film under inert gas (N_2), were investigated to study its effect on the $BaTiO_3$ composition.

From XRD data, comparison between 111 peak width which positioned at 2θ 38º, and 002 associated with 200 peaks around 45º in 2θ shows that a phase of tetragonal symmetry is predominant in all films with a cubic phase (Fig. 4.7 insets). A small contribution of hexagonal $BaTiO_3$ was also observed. Peak shapes were consistent throughout suggesting no significant change in crystallite sizes from that calculated earlier from Rietveld refinement as 29(1) nm.

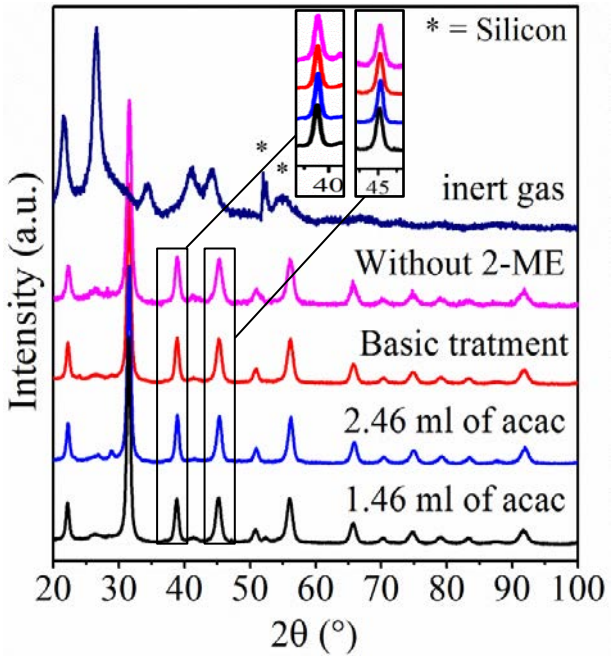

Fig. 4. 7 XRD patterns of $BaTiO_3$ films annealed at 750 °C for 40 minutes prepared by different routes.

Trace amount of $BaTi_2O_5$ phase impurities at 2θ 29º were only observed on XRD $BaTiO_3$ pattern when prepared by increasing the amount of the acac moderator to 2.46 mL, hence this could be due to a stoichiometric deviation in the precursor solution (Fig. 4.7). Pinholes and small cracks measuring up to ~100 μm were observed across the entire film (Fig. 4.8a).

Cleaning the substrate by basic solution resulted in no significant change in the XRD pattern, which remained tetragonal phase beside cubic $BaTiO_3$ and a trace of hexagonal phase (Fig. 4.7). The SEM image showed crack free flat films, and some individual small particles were observed on the surface of the film (Fig. 4.8b).

Leaving the methoxyethanol out of the sol resulted in thinner films (~1 μm per dip) with a much more extensive crack network in which only the very centre of the films ~100 μm was crack free (Fig. 4.8c and Fig. 4.9a). This change also caused adhesion problems in films produced using multiple dips, with ~3 μm films produced from 3 dips showing peeled regions (Fig. 4.9c). The solvent 2-methoxyethanol is the most widely used in the sol preparations of perovskite materials as it forms metal-oxygen-metal (M-O-M) bonds causing a decrease in the hydrolysis sensitivity of the precursor such $Ti(O^iPr)_4$ by the alcohol-exchange reaction. The XRD pattern has not changed (Fig. 4.7).

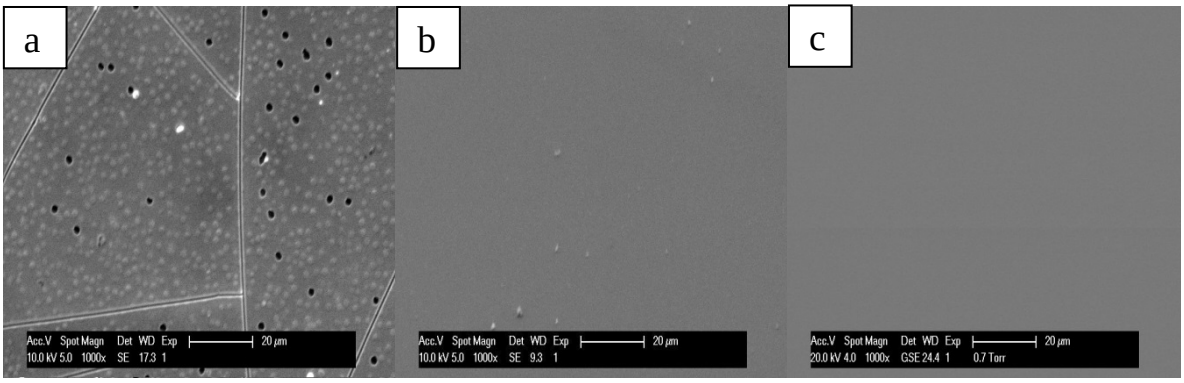

Fig. 4. 8 Different routes of SEM images of $BaTiO_3$ films prepared by: (a) 2.46 mL acac, (b) basic treatment for the substrate and (c) without 2-ME and fired at 750 °C for 40 minutes.

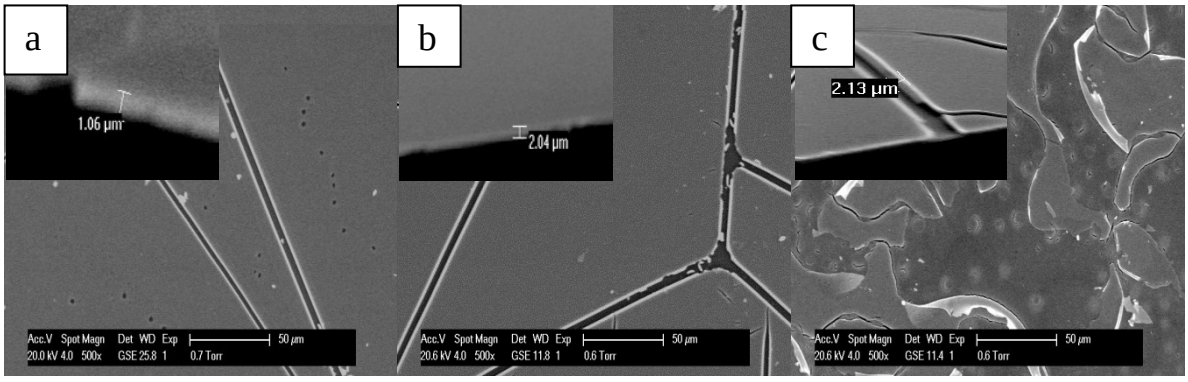

Fig. 4. 9 Multiple dips of SEM images of the front face and a cross section of a $BaTiO_3$ film prepared without 2-ME by (a) 1 dip, (b) 2 dips, (c) 3 dips and fired at 750 °C for 40 minutes.

Pure $BaTiO_3$ hexagonal phase was obtained under inert gas (N_2). Commonly hexagonal phase formed at higher temperature (>1460 °C), however can be produced at low temperature in air by quenching or stabilised by oxygen deficiency under N_2 gas and it is in agreement with Andrade et al.[22]. Silicon peaks (310) and (311) at 2θ 52º and 56º, respectively were overlapped with hexagonal peaks (116) and (611) at the same 2θ position (Fig. 4.7).

In this work, $BaTiO_3$ films were successfully prepared from sols in acetic acid/ methoxyethanol and acac mixtures resulted in tetragonal/cubic phase beside a trace of hexagonal phase. Good quality films without crack were observed.

4.3.2 Dielectric properties

The dielectric properties have been investigated in this work to study the quality of barium titanate films. It is a characteristic perovskite-type ferroelectric material with tetragonal symmetry and possesses high dielectric constant. $BaTiO_3$ is well known material for capacitors due to its high permittivity and dielectric constant, low dispersion and wide frequency response for multilayer ceramic capacitors.[26]

Dielectric behaviour has been studied as a function of the temperature[27] and the thicknesses.[28, 29] Some of the example studied that correlated the higher dielectric constant to the temperature. Mimura et al.[30] achieved a dielectric constant value of 3000 for $BaTiO_3$ films by deposited on Pt-coated Si with adhesion layer of TiO_2/SiO_2 and firing at 850°C in O_2 atmosphere. A dielectric constant value of 720 was found in $BaTiO_3$ films fired at 850°C has been obtained by Kumazawa et al.[31], and Stawski et al.[32] found a maximum dielectric constant value of 680.

Other studies linked higher dielectric constants to an-increase in the film thickness. Hayashi et al.[6]obtained a dielectric constant value of 1000 for $BaTiO_3$ films by using 0.58 µm thick film on $Pt(111)/SiO_2/Si(100)$ and they correlated the higher dielectric constant to the increasing of the thickness. Parker et al.[32] were in agreement in which the dielectric constant was increased with increasing the film thickness.

Stawski et al.[33] attributed the low dielectric constant of the $BaTiO_3$ films on $Pt(111)/SiO_2/Si(100)$ and gold-palladium electrodes sputtered on the top surface of the film to the asymmetric properties of the upper-lower electrode-dielectric interfaces. One study is in agreement with the findings in this study[34] as they related the lower value of the dielectric constant to the smaller grain size and lower packing density in the $BaTiO_3$.

Therefore, to investigate the certain thicknesses for which dielectric properties could be measured, $BaTiO_3$ films with thicknesses ranging from 5 to 9 μm were coated by repeating the process 3 times at room temperature on gold coated on silicon. From XRD (Fig. 4.10) patterns of the $BaTiO_3$ films with thickness ranging from 5 to 9 μm, it was confirmed that all the synthesized $BaTiO_3$ were crystalline in the cubic perovskite phase with minor hexagonal phase.

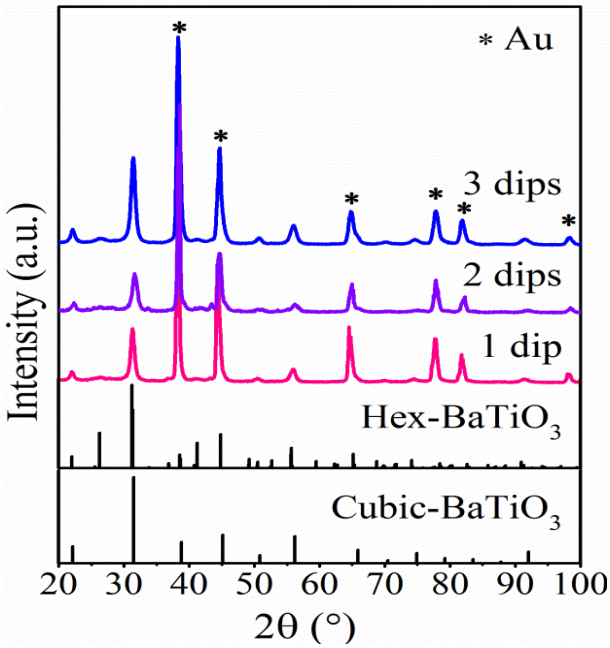

Fig. 4. 10 XRD patterns of $BaTiO_3$ films on gold coated silicon fired at 750 °C for 40 minutes, compared with standard patterns from ICSD for cubic phase[25] and hexagonal phase.[17]

For dielectric constant measurement, the phase of the impedance of $BaTiO_3$ films with upper electrode $2.4 \times 10^{-5}\,m^2$ in dimension was measured by an impedance analyzer. The capacitance density and the dielectric properties were calculated from equation 4.1 as 13 $nF\,m^{-2}$ and 295 at 1 kHz at room temperature; however it decreased to 58 as the thickness increased to 9 μm (Table 4.2).

$$C = \frac{\varepsilon_0 \varepsilon_r A}{d} \qquad (4.1)$$

where C is measured capacitance in Farads, A is the area of the capacitor and d is the thickness of the film in m and then applied in the equation.

Table 4. 2 The relationship between film thickness and dielectric constant.

Thickness of the films(μm)	Cap. density (nFm^{-2})	ε_r
5	13.00	295
8	3.36	114
9	1.36	58

Fig. 4.11 shows Nyquist plots of the impedance of the highest dielectric constant value (295) in parallel with the resistance. The fits to the experimental data are quite good in semicircle shape.

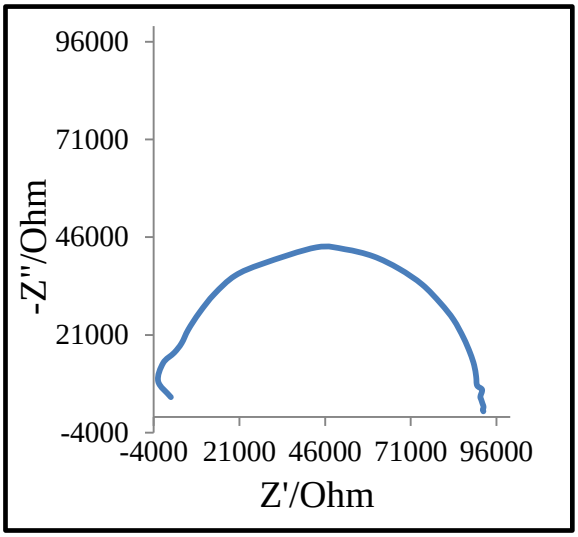

Fig. 4. 11 Nyquist plot of the impedance of $BaTiO_3$ film of 91K Ω, a capacitance of 13 nF m^{-2} and annealed at 750 °C for 40 minutes.

In order to investigate the major reason why dielectric properties decreased based on their thickness, the SEM was used to study the morphology of $BaTiO_3$ films (Fig. 4.12). 5 μm flat and crack free $BaTiO_3$ film were observed (Fig. 4.12a).

The extremely fine grain structure as mentioned earlier from the Rietveld fit (29 nm) could be responsible for the low value of the dielectric constant. The splitting around 45º 2θ from the XRD due to the tetragonal phase was not obvious (Fig. 4.10) although the tetragonal phase was provided good fit in the refinement of 750 °C $BaTiO_3$ films (Fig. 4.5, right).

It has been suggested that there is a critical size for the $BaTiO_3$ crystallite (<0.1 μm) to transform from cubic to tetragonal phase[35] and if the crystallite size is smaller than the critical size of the grain, the tetragonal phase will be less effective than cubic phase and therefore splitting of the tetragonal peak in the XRD will not be obvious.[6] Similar dielectric measurements results have been reported for $BaTiO_3$ films prepared by sol-gel method and they attributed the lower dielectric constant to the lower packing densities of the particles. It may also be that the tetragonal regions were focused in some domains and that others were cubic.[3, 34]

As thicker films (8 and 9 μm) were produced by repeating the coating more than once, cracking in the films was clear in the third coating. Some craters, observed in Fig. 4.12c could be due to the non-uniformity of the particles resulted from some small pores filled by particles and other large pores not filled completely during increasing the thickness. Thus, if upper electrodes are coated onto the regions which have cracks or craters, the resulting $BaTiO_3$ films would exhibit high leakage current densities and the dielectric constant would decrease.

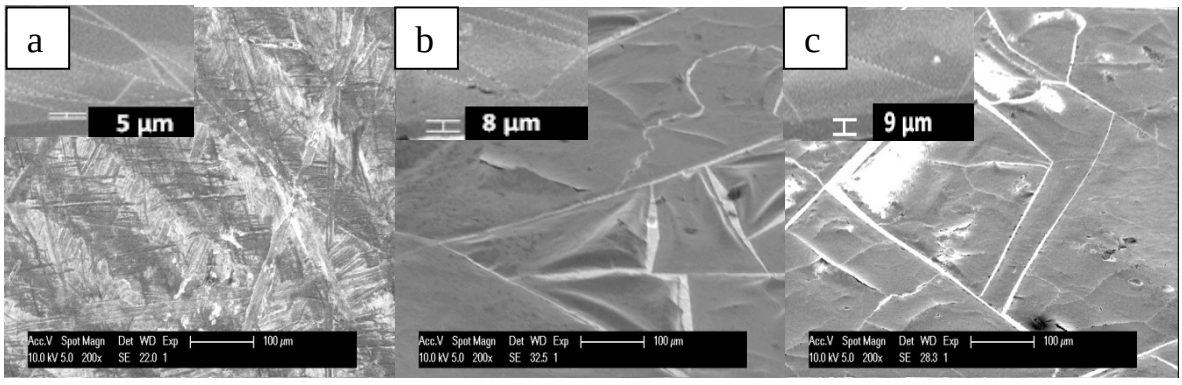

Fig. 4. 12 Multiple dips of SEM images of the front face and a cross section of a $BaTiO_3$ film on gold coated silicon fired at 750 °C for 40 minutes.

Therefore, due to the smaller crystallite size (29 nm) the dielectric constant of the $BaTiO_3$ was low for the single coated films and the surface defects for the multiple dips films.

4.3.3 $Bi_2Ti_2O_7$ films

$Bi_2Ti_2O_7$ films were produced in this study from $Bi(NO_3)_3.5H_2O$, $Ti(OBu)_4$, acetic acid and 2-methoxyethanol. No water was added to the sol as the hydrated bismuth nitrate introduced a significant quantity of water. A wide range of different conditions were investigated to find the optimum conditions for the production of pure phase $Bi_2Ti_2O_7$ thin films. All the experiments performed are summarised (Tabl 4.3).

Table 4. 3 Conditions investigated in the preparation of the $Bi_2Ti_2O_7$ thin films.

Experiment number	Experimental procedure
1	Firing temperature
2	Firing period variation
3	Sol preparation variation

4.3.3.1 Firing temperature

To find out the best temperature for obtaining pure pyrochlore $Bi_2Ti_2O_7$, the films were annealed at various temperatures for 30 minutes (Fig. 4.13). It is clear that the pyrochlore structure only forms in a relatively narrow temperature window. Annealing for 30 minutes at 500 °C the diffraction pattern resembles that of the Aurivillius-type $Bi_4Ti_3O_{12}$ phase. At 550 °C it is single phase pyrochlore $Bi_2Ti_2O_7$ and at higher temperature a mixture of the Aurivillius and pyrochlore-type structures is found. Hector et al.[36] showed that bulk $Bi_2Ti_2O_7$ is only stable in powder form in a very narrow temperature stability window around 470 °C, but EDX analysis (Fig. 4.13, right) showed a 1:1 ratio of bismuth:titanium so the substrate-supported material appears to have a slightly better thermal stability.

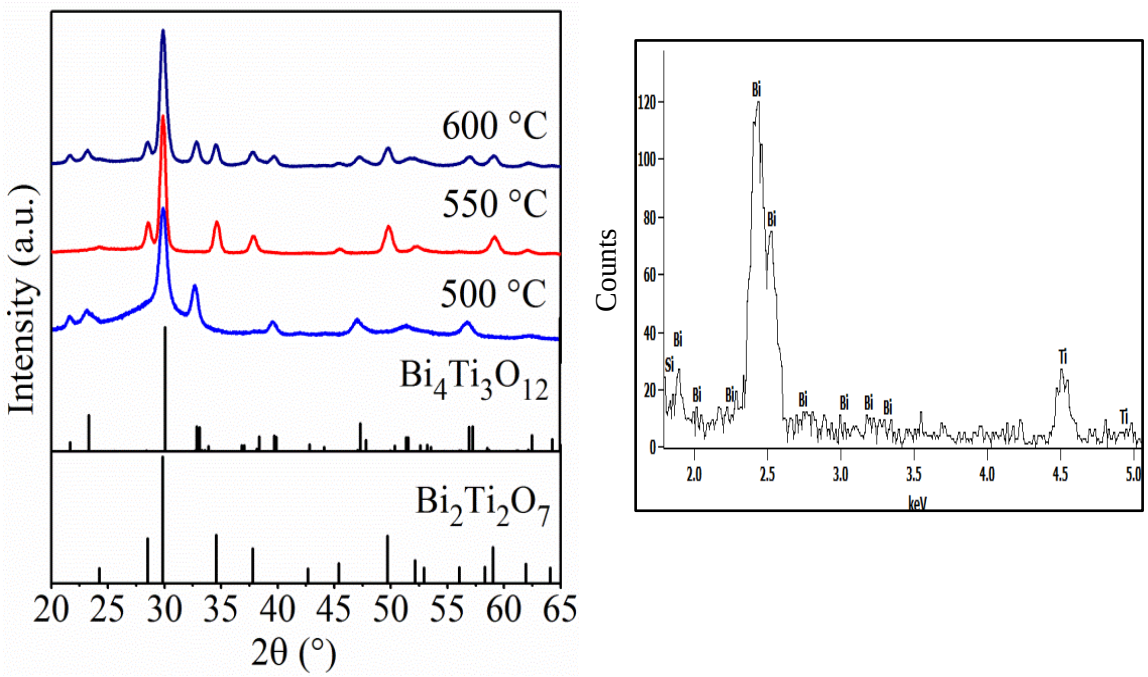

Fig. 4. 13 XRD patterns of temperature variation of $Bi_2Ti_2O_7$ films fired at various temperatures compared with standard patterns from ICSD (left) for pyrochlore phase[36] and Aurivillius phase,[37] and EDX spectrum of $Bi_2Ti_2O_7$ film calcined at 550 °C for 30 minutes (right).

The SEM image for the pyrochlore $Bi_2Ti_2O_7$ film (Fig. 4.14, right) shows smooth film with no individual particles visible within the high magnification resolution of the SEM, but a network of cracks on the long-range scale across the entire surface, with the largest crack-free islands measuring up to ~200 μm. Rietveld refinement of the XRD pattern of a $Bi_2Ti_2O_7$ film (Fig. 4.14) resulted in a good fit with a lattice parameter close to previously reported values of 10.3794(4) Å[36] and a crystallite size of 86.4(13) nm. A film produced from a single dip into the sol had a thickness of ~5 μm.

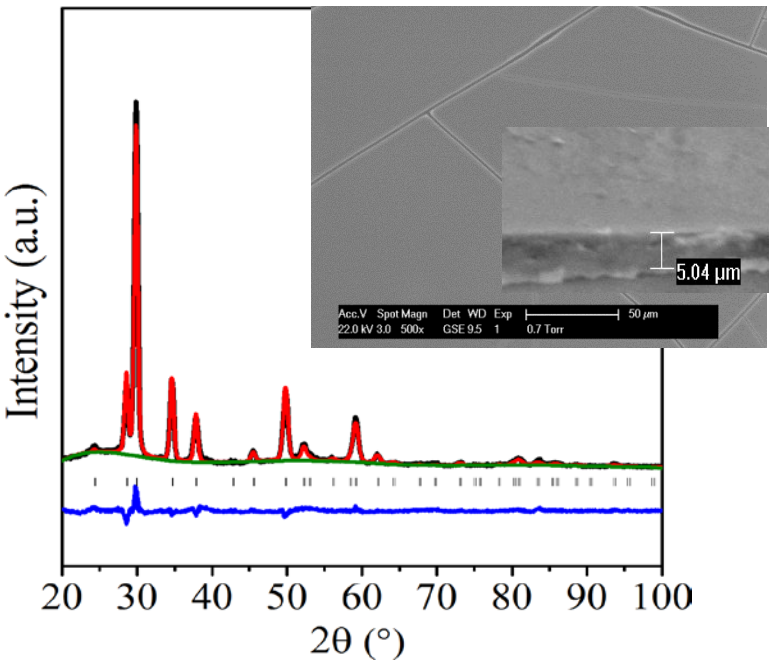

Fig. 4. 14 A Rietveld fit to the XRD for a film heated at 550 °C and SEM images of the front face and a cross section of a film fired at 550 °C (inset right). Rietveld fit results: R_{wp} = 7.4%, R_p 5.9%, *Fd*$\bar{3}$*mz*, *a* = 10.3658(17) Å, Bi 0.0208(14), 0.0208(14), – 0.0339(14), $^1/_6$ occupancy, U_{iso} = 0.027(3), Ti ½, ½, ½, U_{iso} = 0.001(3), O $^1/_8$, $^1/_8$, 0.4259(13), U_{iso} 0.045(4), O' $^1/_8$, $^1/_8$, $^1/_8$, U_{iso} 0.045(4).[36]

Shorter firing times resulted in an increase in the Aurivillius content (Fig. 4.15), similarly to previous findings with $Bi_2Ti_2O_7$ powders.[36]

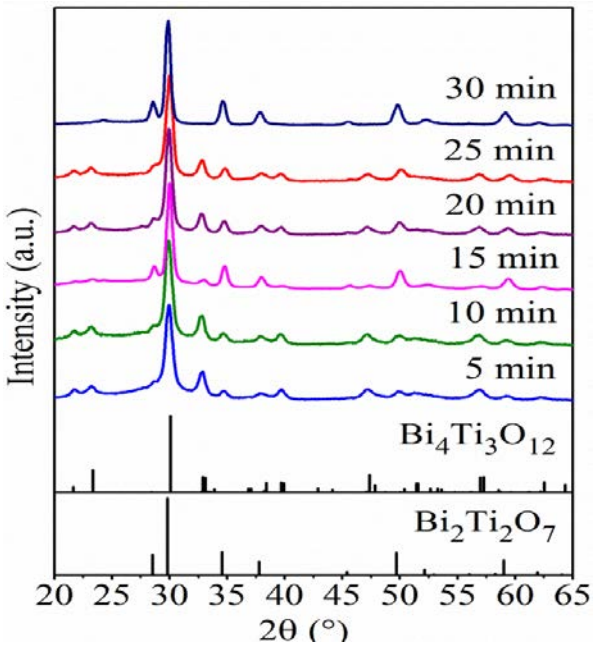

Fig. 4. 15 XRD patterns of $Bi_2Ti_2O_7$ films fired at 550 °C for various times, with standard patterns from ICSD for pyrochlore phase[36] and Aurivillius phase.[37]

4.3.3.2 Sol preparation variation

To examine the effect of the aging period and the composition of the sol on the $Bi_2Ti_2O_7$ films (see Fig. 4.16). The XRD showed the sol aging time had less effect on the $Bi_2Ti_2O_7$ films than observed in $BaTiO_3$ and little differences in the films were observed with aging times as short as 2.5 hours compared with the 24 hours standard time period. Sols only aged for 1 hour, however, did show an increase in the Aurivillius content even using the standard firing conditions of 550 °C for 30 minutes. Also deviations in the sol composition by 5% either direction away from 1:1 Bi:Ti also resulted in an increase in the Aurivillius content.

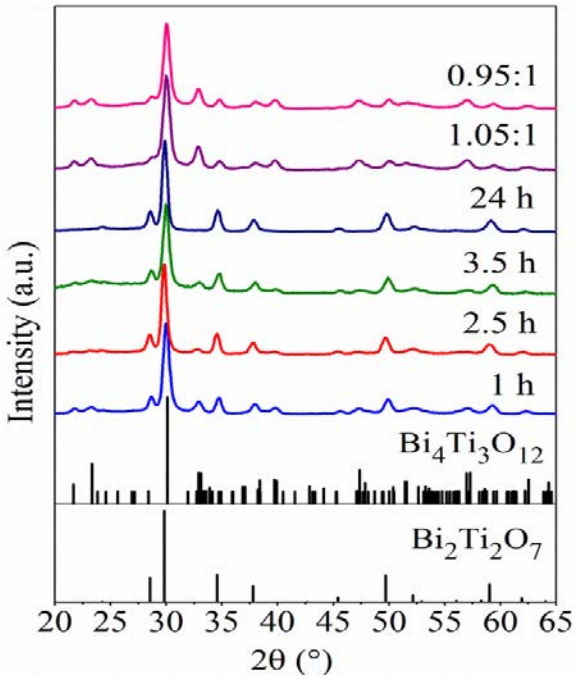

Fig. 4. 16 XRD patterns of sol preparation variation of $Bi_2Ti_2O_7$ films fired at 550 °C with standard patterns from ICSD for pyrochlore phase[36] and Aurivillius phase.[37]

4.4 Conclusion

Sol formulations based on titanium alkoxides, acetic acid, acetylacetone and methoxyethanol with simple barium or bismuth salts were found to be effective for the controlled formation of films. Dip coating produced ~5 µm solid film per coating cycle and these could be built up using multiple cycles. Tetragonal-$BaTiO_3$ was shown a good fit of Rietveld refinement to the XRD pattern of $BaTiO_3$. Due to the smaller crystallite size (29 nm), the dielectric constant of the $BaTiO_3$ was low for the single coated films and the surface defects for the multiple dips films as the thickness increased.

Good quality pyrochlore $Bi_2Ti_2O_7$ film were optimised by aging the sol for 24 hours and firing at 550 °C for 30 minutes, which showed smooth film in ~100 µm with no individual particles on the top surface. The Aurivillius phase was increased by changing the sol composition from 1:1 Bi:Ti.

4.5 References

1. R. Ashiri, A. Nemati and M. Sasani Ghamsari, *Ceram. Int.*, 2014, **40**, 8613-8619.
2. A. Solanki, S. Choudhary, V. R. Satsangi, R. Shrivastav and S. Dass, *J. Alloys Compd.*, 2013, **561**, 114-120.
3. H. Basantakumar Sharma and A. Mansingh, *J. Phys. D, Appl. Phys.*, 1998, **31**, 1527-1533.
4. J. Yuk and T. Troczynski, *Sens. Act. B*, 2003, **94**, 290-293.
5. C. R. Cho, S. I. Kwun, T. W. Noh and M. S. Jang, *Jpn. J. Appl. Phys.*, 1997, **36**, 2196.
6. T. Hayashi, N. Oji and H. Maiwa, *Jpn. J. Appl. Phys.*, 1994, **33**, 5277-5280.
7. M. N. Kamalasanan, N. D. Kumar and S. Chandra, *J. Appl. Phys.*, 1993, **74**, 5679-5686.
8. T. Kidchob, L. Malfatti, D. Marongiu, S. Enzo and P. Innocenzi, *J. Am. Ceram. Soc.*, 2010, **93**, 2897-2902.
9. A. Hardy, S. VanElshocht, C. Dedobbelaere, J. Hadermann, G. Pourtois, S. De Gendt, V. V. Afanas'ev and M. K. Van Bael, *Mar. Pollut. Bull.*, 2012, **47**, 511-517.
10. F. E. Oropeza, I. J. V.Garcia, R. G. Palgrave and D. J. Payne, *J. Mater. Chem. A*, 2014, **2**, 18241-18245.
11. S. W. Wang, H. Wang, X. Wu, S. Shang, M. Wang, Z. Li and W. Lu, *J. Cryst. Growth.*, 2001, **224**, 323-326.
12. S. W. Wang, W. Lu, N. Li, Z. F. Li, H. Wang, M. Wang and X. C. Shen, *Mater. Res. Bull.* , 2002, **37**, 1691-1697.
13. Y. Hou, T. Lin, Z. Huang, G. Wang, Z. Hu, J. Chu, X. Xu and M. Wang, *Appl. Phys. Lett.* , 2004, **85**, 1214-1216.
14. Z. Wang, C. H. Yang, D. L. Sun, J. F. Hu, H. Wang, H. C. Chen and C. S. Fang, *Mater. Sci. Eng., B*, 2003, **102**, 335-338.

15. T. M. Stawski, W. J. Vijselaar, O. F. Göbel, S. A. Veldhuis, B. F. Smith, D. H. Blank and E. Johan, *Thin solid films*, 2012, **520**, 4394-4401.
16. R. Buttner and E. Maslen, *Acta Crystallogr. Sect. B: Struct. Sci.*, 1992, **48**, 764-769.
17. J. Akimoto, Y. Gotoh and Y. Oosawa, *Acta Crystallogr., Sect. C: Cryst. Struct. Commun.*, 1994, **50**, 160-161.
18. E. Tillmanns, *Acta Crystallogr., Sect. B:* , 1974, **30**, 2894-2896.
19. P. B. Moore and S. Louisnathan, *Zeitschrift für Kristallographie-Crystalline Materials*, 1969, **130**, 438-448.
20. Z. V.Nava, C. Tenailleau, S. G.Fritsch, N. E. Horr, T. Lebey, P. Dufour, B. Durand and J. Y. C.Ching, *J. Phys. Chem. Solids.*, 2011, **72**, 17-23.
21. Y. C. Wu, N. J. Ho and H. Y. Lu, *J. Microsc.*, 2005, **220**, 205-220.
22. H. R. C. S. Andrade, L. M. Seara, W. J. Fadgen and N. D. S. Mohallem, *J. Sol-Gel Sci. Technol.*, 2012, **64**, 543-548.
23. J. C. Nièpce and L. Pizzagalli, in *Nanomaterials and Nanochemistry*, eds. C. Bréchignac, P. Houdy and M. Lahmani, Springer Berlin Heidelberg, Editon edn., 2007, pp. 35-54.
24. Y.I. Kim, J. K. Jung and K.-S. Ryu, *Mater. Res. Bull.*, 2004, **39**, 1045-1053.
25. R. Buttner and E. Maslen, *Acta Crystallogr., Sect. B: Struct. Sci.*, 1992, **48**, 764-769.
26. A. Visinoiu, R. Scholz, M. Alexe and D. Hesse, *Appl. Phys. A*, 2005, **80**, 229-235.
27. K. i. Mimura and K. Kato, *Appl. Phys. Express.*, 2014, **7**, 061501.
28. Y. Yano, K. Iijima, Y. Daitoh, T. Terashima, Y. Bando, Y. Watanabe, H. Kasatani and H. Terauchi, *J. Appl. Phys.*, 1994, **76**, 7833-7838.
29. T. Hayashi, N. Oji and H. Maiwa, *Jap. J. Appl. Phys.*, 1994, **33**, 5277.
30. K.i. Mimura and K. Kato, *Appl. Phys. Express.*, 2014, **7**, 061501.
31. H. Kumazawa and K. Masuda, *Thin Solid Films*, 1999, **353**, 144-148.
32. C. B. Parker, J.P. Maria and A. I. Kingon, *Appl. Phys. Lett.*, 2002, **81**, 340-342.
33. T. M. Stawski, W. J. C. Vijselaar, O. F. Gobel, S. A. Veldhuis, B. F. Smith, D. H. A. Blank and J. E. ten Elshof, *Thin Solid Films*, 2012, **520**, 4394-4401.
34. B. Lee and J. Zhang, *Thin Solid Films*, 2001, **388**, 107-113.
35. M. H. Frey and D. A. Payne, *Phys. Rev. B*, 1996, **54**, 3158-3168.
36. A. L. Hector and S. B. Wiggin, *J. Solid. State. Chem.*, 2004, **177**, 139-145.
37. J. F. Dorrian, R. E. Newnham, D. K. Smith and M. I. Kay, *Ferroelectrics*, 1972, **3**, 17-27.

5. Mesoporous $BaTiO_3$ and $Bi_2Ti_2O_7$ powdered and films

5.1 Introduction

Mesoporous metal oxide materials have attracted growing interest due to their dielectric[1] and photocatalytic properties[2] which can be enhanced by the pore structure. Very little progress has been made in the syntheses of mesoporous $BaTiO_3$ and $Bi_2Ti_2O_7$, and there are not report in mesoporous films.

The evaporation-induced self-assembly (EISA) method is one of the most useful techniques for synthesizing mesoporous single-metal oxide films but it has not been extended to mesoporous multimetal oxides due to several problems. One of these is the phase separation that can result from heterogeneity in the solubility of the nonvolatile components through the solvent evaporation process. Hence, secondary phases appear.[3] Modifiers such as acetylacetone,[4] ethylene glycol,[5] and ethanolamine[6] are usually utilised to obtain homogeneous sols. Yet, these moderators commonly lead to the generation of poor mesostructure blocks. Thermal instability of the porous structure is a serious problem as they often collapse due to pore-wall crystallization and the lack of support at high firing temperatures during the transition from amorphous to crystalline phase by annealing. The common organic surfactants applied in the EISA routes usually burn below the crystallization temperatures of the multimetal oxides.[7] There are limited papers dealing with the syntheses of mesoporous $BaTiO_3$[7-9] and $Bi_2Ti_2O_7$[10] powders but they obtained disordered porous structures. Wen et al.[8] synthesized mesoporous $BaTiO_3$ powders using tetradecylamine with 2.2 nm pore size, and 29.1 nm pore sizes were prepared using CTAC and P123 as surfactants.[7, 9] Additionally, P123 was used to fabricate mesoporous $Bi_2Ti_2O_7$ with pore size of 6.1 nm.[10]

Research has moved to the use of combinations of different materials to stabilise the pore structure by prefilling the pores with carbon prior to crystallization in inert gas and then removing the carbon matrix by calcination, referred to as a "nanocasting strategy".[7]

The preparation of mesoporous ferroelectric materials by the integration into mesoporous silica could offer some advantages, such as preserving its properties due to confinement.[11] Carbon materials made from sucrose were successfully used for the nanocasting strategy due to the presence of -OH groups in sucrose which can form hydrogen bonds with the silanol groups of the mesoporous silica template.

There are a few papers related to mesoporous $BaTiO_3$ powders by impregnation into mesoporous silica.[11-13] All of these papers produced mesoporous $BaTiO_3$ powders with $\geq$ 3 nm pore size. Kohiki et al.[12] prepared mesoporous $BaTiO_3$ powders with 3 nm by using mesoporous silica prepared from (MCM-41). Hou et al.[13] synthesized 3.4 nm pore using SPA-15, whereas Kinka et al.[11] obtained a larger pore size of 3.8 nm by using MCM-41. Thus, much attention has been paid to the synthesis and characterization of nano-sized mesoporous $BaTiO_3$ since its morphology is preparation dependent.

To the best of our knowledge no papers were found related to the mesoporous $BaTiO_3$ and $Bi_2Ti_2O_7$ films and it is still quite challenging to achieve functional multi-metal-oxides having highly ordered porous structure.

5.2 Experimental procedure

All reagents were purchased from Sigma-Aldrich and solvents from Fisher Scientific.

F127 template

5.2.1 Synthesis of mesoporous $BaTiO_3$ and $Bi_2Ti_2O_7$ films using F127 surfactant

A number of experiments were carried out using different quantities of the surfactant F-127 as a structure directing agent to synthesise mesoporous $BaTiO_3$ and $Bi_2Ti_2O_7$ films. The surfactant (Table 5.1) was added to the sols prepared as described in section 4.2.2 and 4.2.3 before addition of the barium acetate or bismuth nitrate, respectively. The resulting mixture was left stirring for 1 hour at room temperature.

The dip-coating method was carried out on silicon as described in section 4.2.4. Calcination was achieved by slowly increasing temperature from room temperature to 750 or 550 °C (heating rate 0.5°C minutes^{-1}) for 40 or 30 minutes to remove organic templates and crystallize the pore wall of barium or bismuth titanate, respectively.

Table 5. 1 Quantities of F-127 used for mesoporous $BaTiO_3$ (a) and $Bi_2Ti_2O_7$ (b) thin film preparations.

(a)

Experiment	F127 (g)	Experiment	F127 (g)
1	0.6	7	2
2	0.8	8	2.3
3	1	9	2.6
4	1.2	10	2.9
5	1.4	11	-
6	1.6	12	-

(b)

Experiment	F127 (g)
1	0.3
2	0.4
3	0.6
4	0.8
5	1
6	1.2

Mesoporous-SiO_2

5.2.2 Synthesis of mesoporous $BaTiO_3$ powders by hard template

Attempts were made to synthesize mesoporous $BaTiO_3$ powders in the following steps adapted from the methodology reported by Hou et al.[13]

5.2.2.1 MCM-41 molecular sieve synthesis

Mesoporous silica powder was prepared based on the literature.[14] 0.279 g of CTAB was dissolved in 110.5 mL of H_2O and 9.8 mL of NH_4OH at 50 °C and left stirring for 90 minutes. The solution was allowed to cool to room temperature in a sealed round flask and 1.394 g of TEOS was added with rapid stirring for 30 minutes and then the solution became thick and turbid. Finally the sample was filtered and calcined at 550 °C for 2 hours to burn the surfactant.

5.2.2.2 Silica-carbon composite preparation by sucrose

MCM-41 was used as the template and sucrose as the carbon source. The synthetic procedure reported by Jun et al.[15] were followed with modifications to the starting composition such as template, the sucrose quantity and the carbonization mode. 1g of calcined MCM-41was dissolved in the aqueous solution containing a measured quantity of sucrose (Table 5.2) and 0.07 mL of H_2SO_4 to catalyse the carbonization in 5 mL of H_2O. The solution was stirred for 10 minutes to obtain homogenous mixture and then kept in a drying oven at 100 °C for 6 hours, before the temperature was increased to 160 °C for a further 6 hours. The product was dark brown or black after drying in the oven. The process was repeated again at 100 °C for 6 hours and then at 160 °C for 6 hours as well to confirm the polymerisation of the silica sample and carbonisation of the sucrose inside the pore after the addition of the measured quantity of sucrose (Table 5.2) and 0.05 mL of H_2SO_4. The solid product was completely carbonised by pyrolysis at 900 °C for 6 hours under N_2 gas (heating rate 5°C $minutes^{-1}$). The silica template was removed from the carbon-silica composite by washing twice at 100 °C with 1 M NaOH solution consisting of 1:1 ethanol: water by volume in closed bottle and covered with para film. The resulting template free is filtered, washed with ethanol and finally dried in oven at 100 °C for 24 hours.

Table 5. 2 Different quantities of sucrose used for mesoporous silica-carbon powders composite powders.

Experiment	Sucrose (g)	Additional sucrose (g)
1	1.25	0.8
2	1.5	1.05
3	1.8	1.35
4	2.25	1.8

5.2.2.3 Incorporation of $BaTiO_3$ into mesoporous silica

0.1 g of carbon template was impregnated with the $BaTiO_3$ precursor solutions (the $BaTiO_3$ sol was prepared the same as in section 4.2.2. The mixture was kept stirring for 2 hours and then the excess of solution was removed by the centrifuge. The wet powders were kept in a drying oven at 100 °C for 24 hours and then fired in flowing nitrogen at 750 °C (heating rate 5 °C $minutes^{-1}$) for 40 minutes to crystallize the $BaTiO_3$ wall.

Finally, $BaTiO_3$-carbon composite powders were heat treated at different temperatures in air (heating rate 0.5°C $minutes^{-7}$) for 2 hours to obtain porous $BaTiO_3$ (Fig. 5.1).

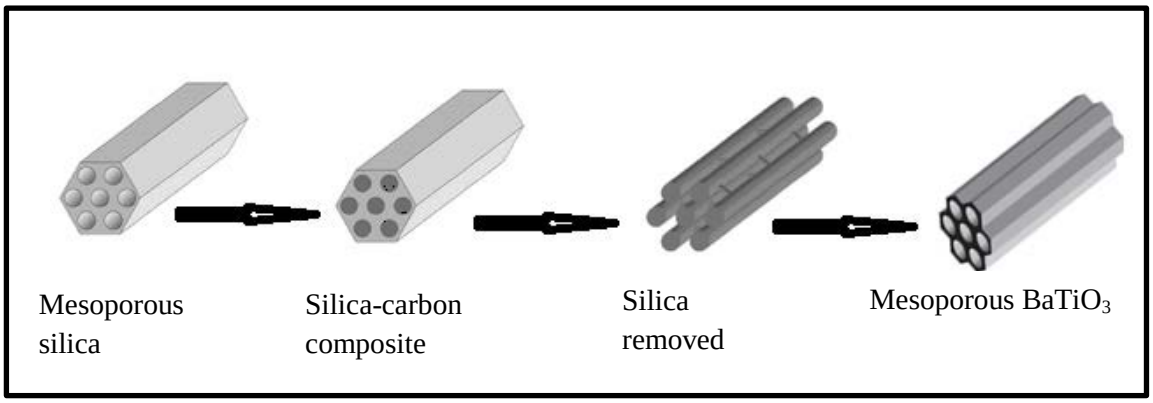

Fig. 5. 1 Schematic synthesis strategy of mesoporous $BaTiO_3$ by hard template.

5.2.3 Synthesis of mesoporous $BaTiO_3$ films by hard template method

Mesoporous $BaTiO_3$ films were attempted by infiltrating into mesoporous silica deposited onto an ITO electrode by the electrochemically assisted surfactant assembly (EASA) method. Perpendicularly aligned mesoporous silica films were adapted from Goux et al.[16] and Walcarius et al.[17] with some variations.

5.2.3.1 Mesoporous silica films by EASA route

Mesoporous silica preparation by the EASA route was adapted from the previous literature.[16] An aqueous sodium nitrate solution (0.1 M, 20 mL) was mixed with ethanol (20 mL) and adjusted to pH 3 using an aqueous 0.2 M HCl solution. TEOS (0.905 mL) was added and the solution allowed to stir at room temperature for 90 minutes.

Then, CTAB (0.47 g) was added to the solution and left stirring for a further 30 minutes. Electrochemical cells used a silver rod pseudo-reference electrode (3.175 mm diameter, hard) and a large area stainless steel counter electrode.

Electrochemical experiments were accomplished using a Biologic SP150 potentiostat. A potential of −1.3 V was applied for 20 seconds for 1 × 1 cm area of ITO as the working electrode. The electrode was rinsed immediately with deionized water after deposition and dried overnight at 130 ºC. Surfactant extraction was typically carried out by calcination in air at 450 °C for 5 hours (heating rate 0.5 °C minutes^{-1}).

5.2.3.2 Silica-carbon composite films preparation by sucrose through dip-coating process

Silica-carbon composite films were prepared by using different quantities of sucrose as a carbon source (Table 5.3) previously described in section 5.2.2.2, however, mesoporous silica was dipped into the sucrose solution and left in the solution for 1 hour and dried overnight at 130 ºC. The carbonization was performed at 550 °C for 6 hours (heating rate 5 °C min^{-1}) for ITO on glass. The silica was removed by dipping into 1 M NaOH solution one time for 30 seconds without heating.

Table 5. 3 Different quantites of sucrose used for mesoporous silica-carbon films composite.

Experiment	Sucrose (g)	Additional sucrose (g)
1	3	2
2	4	3
3	5	4
4	6	5
5	7	6

5.2.3.3 Silica-carbon composite films preparation by Polypyrrole through electrodeposition

Silica-carbon composite films were prepared by using polypyrrole as a carbon source, following the synthetic procedure reported by Kang et al.[18].

Pyrrole solution was prepared by mixing 0.7 mL pyrrole solution (0.1 M in water) with 1.49 g KCl in water (0.2 M) in a volumetric flask (100 mL). Polypyrrole solution was infiltrated into mesoporous silica films by electrochemical experiments using a Biologic SP150 potentiostat. These experiments were carried out with a three electrode system using a saturated calomel electrode (SCE) as a reference electrode, and platinum mesh as a counter electrode. N_2 gas was flushed through the pyrrole solution before the deposition to remove O_2 gas. A current of 570 µA was applied for 0.5 second for 1 × 1 cm area of mesoporous silica on ITO surface as working electrode. The silica-carbon composite electrode was rinsed immediately with deionized water after deposition and dried overnight at 130 ºC. The next steps were the same as in section 5.2.2.2. Therefore, polypyrrole was deposited as a carbon source into the silica template.

5.2.3.4 Incorporation of $BaTiO_3$ into mesoporous silica

Mesoporous $BaTiO_3$ films were attempted by sol infiltrating through a dip-coating process into a carbon template film replicated from mesoporous silica onto an ITO surface and then followed the same procedure as section 5.2.2.3.

5.3 Results and discussion

The EISA route was adopted to synthesize mesoporous $BaTiO_3$ and $Bi_2Ti_2O_7$ films using amphiphilic triblock copolymers (PEO-PPO-OEO), F127 as a soft template. $BaTiO_3$ and $Bi_2Ti_2O_7$ films were made from sols in acetic acid/methoxyethanol mixture. In a self-assembly process, the poly (ethylene oxide) (PEO) parts are integrated into a rigid matrix composed of barium, bismuth and titanium ions, whereas the poly (propylene oxide) (PPO) parts create the rigid hydrophobic core.[19] High molecular weight copolymers with long hydrophobic parts are achieved to template the large-pore mesoporous $BaTiO_3$ film.

5.3.1 Mesoporous $BaTiO_3$ films templated by F127

Effect of the amount of surfactant

Recently, block copolymers have been utilised to organise mesostructured materials.

The architectures of the block copolymers can be adjusted rationally to control the interactions between the inorganic and organic species, leading to self-assembly. The surfactant quantity was varied to observe the influence of the molar ratio of surfactant to the barium and titanium ratio on the mesostructured of the films since the liquid crystal phases of the mesoporous materials is sensitive to the relative ratios.

Evidence for ordered pore structures were sought using in-plane grazing incidence small angle X-ray scattering experiments (GI-SAXS). The variation of the surfactant from 0.6-2.9 g showed no signs of the pore structures as observed from in-plane SAXS (Fig. 5.2a). This may be due to the condensation and hydrolysis rates of the inorganic species (barium and titanium precursors) not having met the kinetics condition for the surfactant micelles to form the mesostructures.[20]

Mesoporous $BaTiO_3$ did not have retained any mesostructured during calcination. Fig. 5.2b shows the wide-angle XRD pattern of mesoporous $BaTiO_3$ film, illustrating well-resolved peaks characteristic of cubic or tetragonal phase with a trace of hexagonal phase. However, when the surfactant was dissolved in ethanol the crystallisation of $BaTiO_3$ film was combined with another phase of $BaTi_2O_5$ which would hinder the properties of $BaTiO_3$ (Fig. 5.2b).

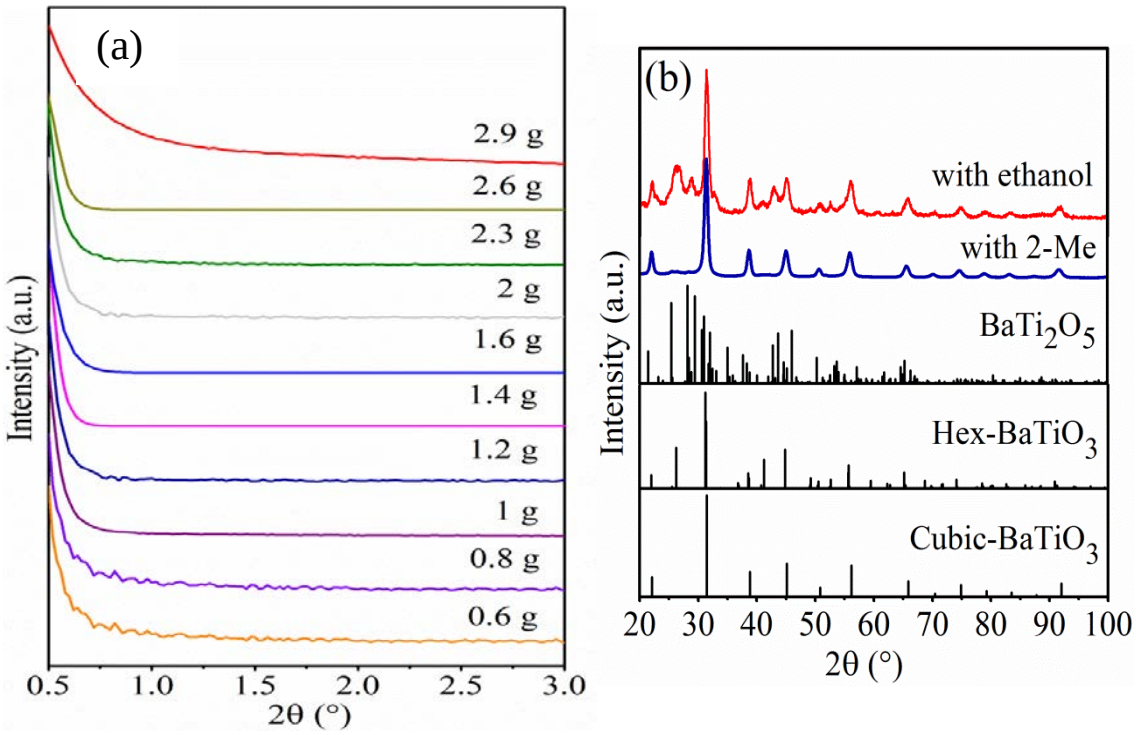

Fig. 5. 2 In-plane small angle (a) XRD patterns of mesoporous $BaTiO_3$ films with different amounts of F127 and fired at 750 °C for 40 minutes, and wide- angle (b) for 1.6 g of F127.

Rietveld refinement was used to distinguish between the cubic (R_{wp} 10%, R_p 8%) and the tetragonal (R_{wp} 8%, R_p 6%) phases of films fired at 750 °C. The tetragonal model (Fig. 5.3, left) gave a clearly better fit, with the most obvious difference again being observed in the 200/002 reflections. The hexagonal phase was present at low concentration (~22%) for two phase fitting. Refined parameters for tetragonal $BaTiO_3$ ($P4mm$)[21] where: a = 4.0049(4) and c = 4.0412(6) Å; atom positions were not refined, and the average crystallite size was extracted from the profile coefficients as 34.5(8) nm. For cubic phase $BaTiO_3$ ($Pm\bar{3}m$)[22] (Fig. 5.3, right) where: a = 4.0141(4) Å ; atom positions were not refined, and the average crystallite size was 41(1) nm.

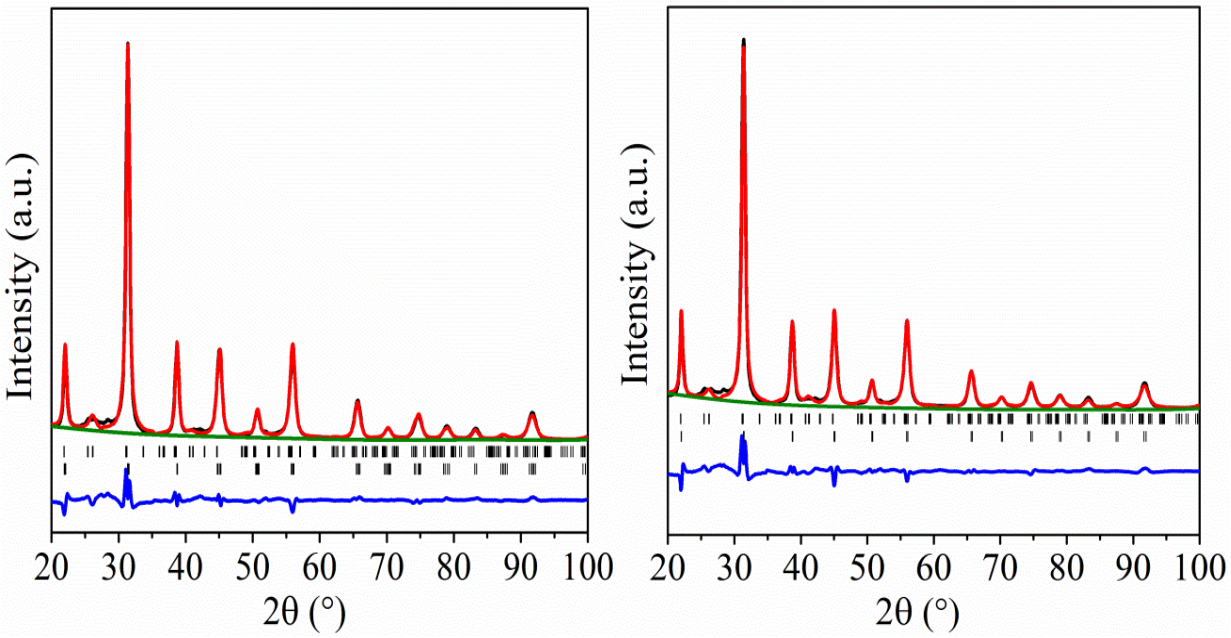

Fig. 5. 3 A Rietveld fit to the XRD for a tetragonal (left) and cubic (right) $BaTiO_3$ film heated at 750 °C for 40 minutes. The black line shows the data points, the red solid line the fit and the lower continuous line the difference.

5.3.2 Mesoporous $Bi_2Ti_2O_7$ films template with F127

Effect of the amount of the surfactant

Mesoporous $Bi_2Ti_2O_7$ films were attempted by using different quantities of the surfactant F127 as shown in GISAXS. Fig. 5.4a shows no observation of pore structure over different quantities of the F127 surfactant. Wide -angle XRD clearly showed the formation of pyrochlore phase when 0.8 g of F127 was used, while the Aurivillius phase was present when using 0.6 and 1 g of F127 (Fig. 5.4b).

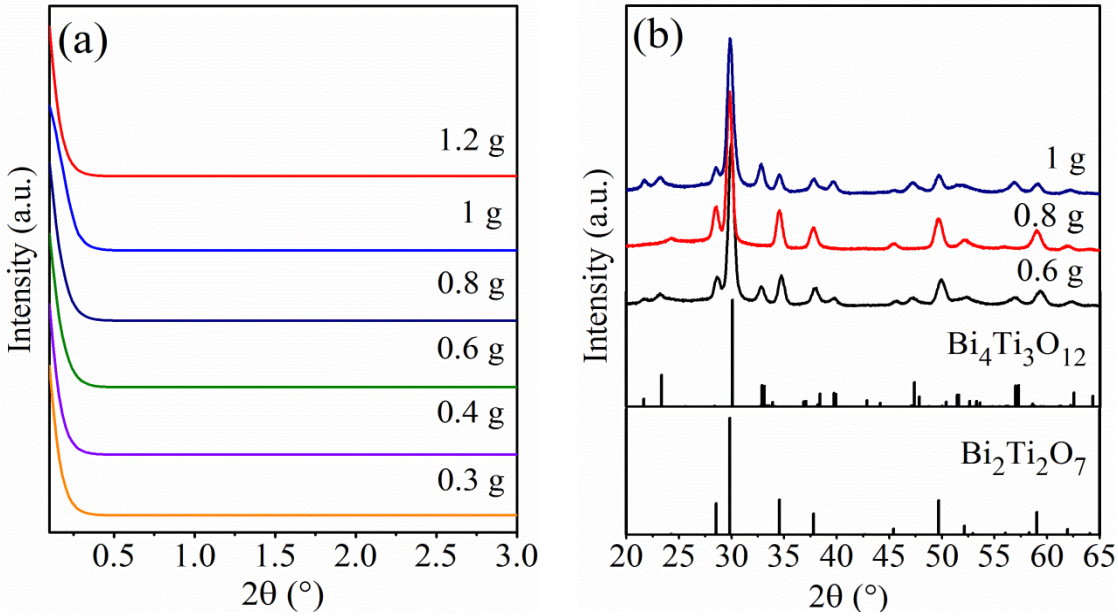

Fig. 5. 4 In plane small-angle (a) and wide-angle (b) XRD patterns of $Bi_2Ti_2O_7$ films produced with different amounts of F127 and fired at 550 °C for 30 minutes.

Effect of aging time

The effect of aging time of the sol at room temperature on the mesostructure of the $Bi_2Ti_2O_7$ film was studied by in-plane GI-SAXS analysis. The pore structure was not observed for different aging time (data not shown) of the films.

Fig. 5.5 displays wide-angle XRD of the templated films. With no sol aging the film was completely amorphous and the film was still amorphous even after 1 and 2.5 hours aging sol, with the commencement of the pyrochlore phase after 3.5 hours.

Further aging of the sol to 24 hours, however, did show an increase in the Aurivillius content even using the standard annealing conditions of 550 °C for 30 minutes.

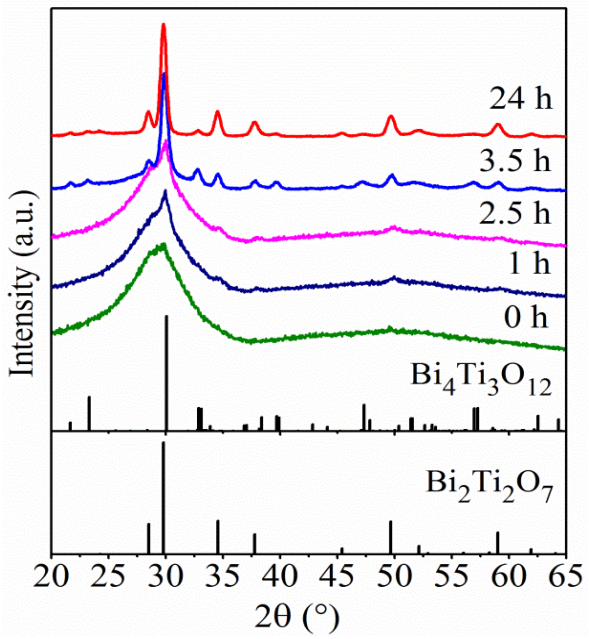

Fig. 5. 5 Wide-angle XRD patterns of $Bi_2Ti_2O_7$ film prepared by 1 g of F127, aged for different times and fired at 550 °C for 30 minutes.

There are some suggested reasons for the failure to observe of the pore structure:

1. The condensation and hydrolysis rate of the metal ions and the surfactant micelles is required to be under kinetic control in order to form mesostructured materials.[23]
2. The crystallization temperature requires in some materials high temperature and that results in the simultaneous collapse of the pore structure.[24]
3. The harsh processing conditions which had a negative impact on the growing of micelle to mesoporous bismuth/ barium titanate sols. 2-ME was used as a solvent and may be it was harsh to disperse the surfactant in the multimetal oxide sols.

5.3.3 Mesoporous $BaTiO_3$ powders by hard template

Mesoporous silica MCM-41 with a uniform pore diameters of 1.5-30 nm[25] are a new type of promising host for the synthesis of $BaTiO_3$ ultrafine nanostructures. 4.05 g of sucrose was used to produce carbon nanorods as this quantity was found to maximize the intensity of the SAXS signal.

Powder GISAXS patterns of the MCM-41 sample are depicted in Fig. 5.6a. Three peaks are present which can be indexed to a hexagonal unit cell with a sharp d_{100} reflection with additional 110 and 200 reflections revealing a long range ordered hexagonal framework. The XRD of the carbon-silica nano-composite prior to the framework removal was identical to that for the template except for lattice contraction and some intensity loss. Removal of the silicate templates using 1 M NaOH solution produced ordered amorphous carbon nanorod assemblies that showed Bragg diffraction in the small angle region with the same *d*-spacing as the carbon-silica composite, implying that the carbon nanorods replicating the mesoporous silica MCM-41still possess ordered mesostructure (Fig. 5.6c). Similar work has been conducted by Hou et al.[13] and Abdel-Fattah et al.[26] but they failed to obtain ordered carbon nanorod, whereas Yang[27] prepared carbon nanorods by using microwave radiation to remove the silica template.

Earlier researchers thought that some types of mesoporous silica materials were not appropriate for the preparation of mesoporous carbon. For MCM-41without micropore and mesopore in the wall, the resultant replicated carbon nanorods possess no interconnecting pillars, and separate disordered carbon nanorods can be gained after removing the silica templates based on Ryoo's method.[28] This is the first example of the carbonisation of carbon inside the pores of mesoporous silica occurring under N_2 with a slow heating programme, resulted in dense carbon filling of the pores. Removing the silica template with 1 M NaOH in a closed bottle and covering with para films led to an increase in the pressure inside the bottle which resulted in change of micro-domains in the silica walls. Thus, abundant silanols can be formed in the thin pore walls of MCM-41 which assist the stability of the carbon.

Fig. 5.6d-f shows the GISAXS for mesoporous $BaTiO_3$ powders. It was hard to infiltrate $BaTiO_3$ sols around the carbon template after removing the silica template, however it was achieved by using different temperature such as 500 °C, 550 °C or 600 °C and the last temperature was the best temperature to produce well replicated structured $BaTiO_3$ without carbon as it was seen by EDX.

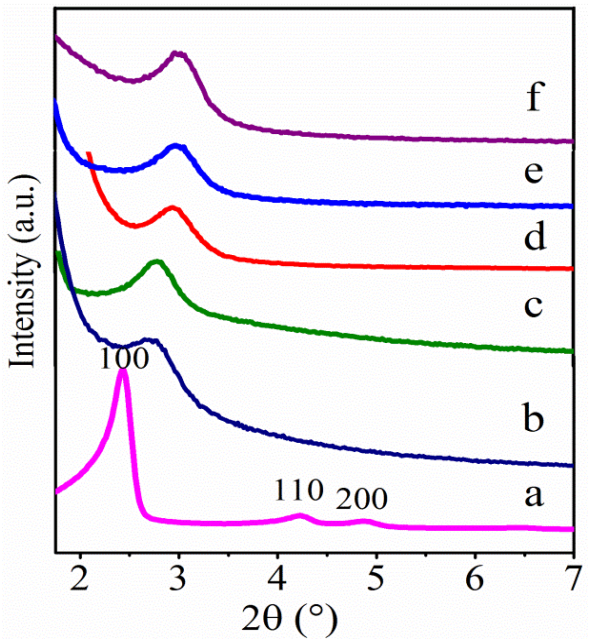

Fig. 5. 6 In-plane GI-SAXS patterns of (a) mesoporous silica (MCM-41),(b) carbon-silica composite prepared by 4.05 g of sucrose, (c) carbon nanorods, (d-f) mesoporous $BaTiO_3$ fired at 750 °C and at 500 °C, 550 °C or 600 °C to remove the carbon .

The crystallization of mesoporous $BaTiO_3$ powders prepared by 4.05 g of sucrose adopted a cubic or tetragonal phase for the same reason as mentioned in section 5.3.1, whilst a small amount of hexagonal phase was also present (Fig. 5.7).

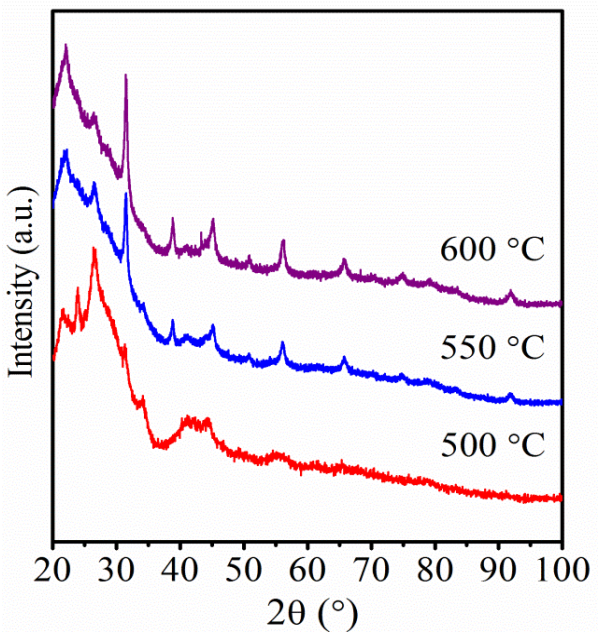

Fig. 5. 7 Wide-angle XRD of mesoporous $BaTiO_3$ powders fired at 500 °C, 550 °C or 600 °C.

To the best of our knowledge, it is the first result to prepare mesoporous $BaTiO_3$ powders by using MCM-41.

The d_{100} spacing for all samples was around ~3 nm (Table 5.4). The lattice shrinkage commonly takes place when the MCM-41 undergoes to firing at high temperature,[27] however, the intensity reduction could be due to the pore filling by carbon.[26]

Table 5. 4 Powder XRD data of (a) mesoporous silica (MCM-41), (b) carbon-silica nanocomposite, (c) carbon nanorods, (d-f) mesoporous $BaTiO_3$ fired at 500, 550 and 600 °C.

Sample	peak	2θ	d (nm)
a	100	2.46	3.5
b	100	2.8	3.2
c	100	2.8	3.2
d	100	3	3
e	100	3	3
f	100	3	3

EDX was used to determine the composition of the sample (Table 5.5). The result showed that the silica-carbon composite contains 10 % silicon atoms and 90 % carbon atoms, whereas 99.5 % carbon atoms still remained in the sample after removal of the silica template with 0.5% of silica still observed. The atomic ratio was 50/50 for Ba/Ti for mesoporous $BaTiO_3$ powders.

Table 5. 5 EDX analysis data (left) and spectrum (right) for mesoporous silica-carbon composite powders.

Element (atom %)	Silica-carbon composite	Silica removed	Mesoporous $BaTiO_3$
Si	10	0.5	-
C	90	99.5	-
Ba	-	-	50
Ti	-	-	50

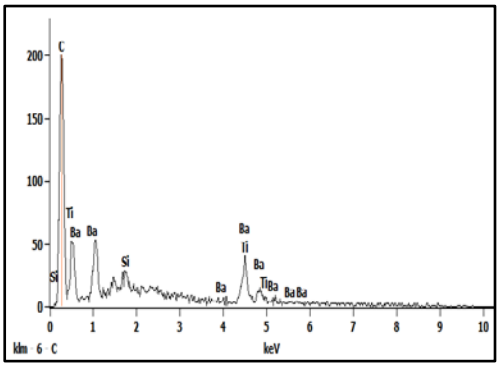

5.3.4 Mesoporous $BaTiO_3$ films by hard template

Powders of $BaTiO_3$ with hexagonal pore structure have been obtained in section 5.3.3. A similar hard template method based on hexagonal ordered mesoporous silica was used similarly in an attempt to produce $BaTiO_3$ nanocomposites and mesoporous $BaTiO_3$ films. The EASA process established by Walcarius and co-workers[17] applies a cathodic potential to the electrode in order to induce a surfactant at a conductive substrate (an electrode surface) to self-assemble. Hydroxide ions are generated due to the current passed at the electrode surface, and they catalyse the condensation of the silica gel around the surfactant assemblies. This work accomplished the deposition of silica onto ITO electrode at -1.3 V for 20 seconds, as previously reported[29] resulting in mesoporous silica films with strong in-plane GISAXS features at 2.46, 4.1 and 4.65º, that could be indexed as the 100, 110 and 200 reflections of a hexagonal lattice of cylinders with a lattice parameter of 3.5 (10) nm.

5.3.4.1 Investigation of pore filling by sucrose

The pore filling route initially depends on the mobility of the carbon precursor. The sucrose quantity controls the viscosity of the synthesis solution. Additionally, the oligomerisation rate of the sucrose molecules has its effect on the pore diffusion. Increasing the oligomerisation rate can produce bulky molecules and result in a hindrance of diffusion.[30] Therefore, the influence of sucrose quantities whilst other parameters were fixed studied by GI-SAXS (Fig. 5.8, left). In-plane GI-SAXS was used to investigate the regular vertical orientation of mesopores silica deposited on the ITO surface at -1.3 V for 20 seconds (Fig. 5.8). The in-plane GI-SAXS exhibits well resolved diffraction features at 2.46, 4.1 and 4.65º which can be indexed to a hexagonal unit cell with reflections of 100, 110, 200, 210 and a lattice parameter of 3.5 nm. Moreover, the SEM image of mesoporous silica (Fig. 5.8, right) shows a flat with aggregation-free surface. Some small particles on the top surface were observed.

The silica- carbon composites obtained with different quantities of sucrose (Table 5.3) (Fig. 5.8), showed the ordered arrangement of the carbon nanorods in the silica-carbon composites gives rise to the well-defined XRD peaks that can be indexed to 100, 110, 200 and 210 reflections of the hexagonal structure, similar to the mesoporous silica template without impregnation, with the same d_{100} spacing as 3.5 nm with minor shrinkage due to pore filing but still in the range of 2θ of 2.5º. Clearly, the carbon content of the silica–carbon composite over different quantities of sucrose was not enough to form carbon walls which can stabilize the pores. After silica removal the pore walls collapse and no pores can be observed.

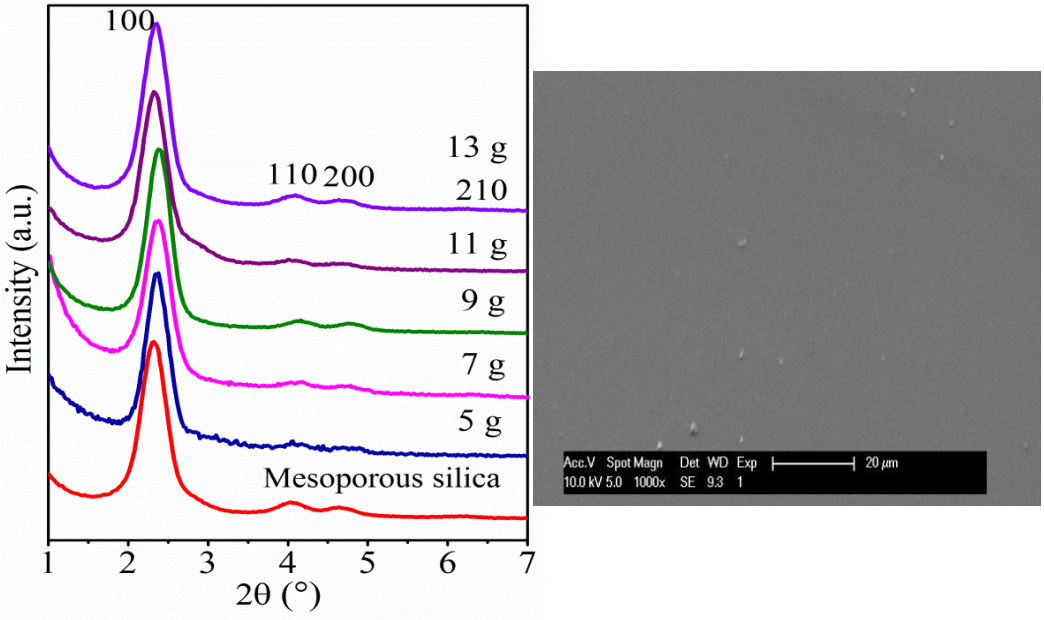

Fig. 5. 8 In plane GI-SAXS patterns of mesoporous silica and variation of sucrose amount used to prepare silica-carbon composite (left). SEM image of the mesoporous silica surface morphology of the film (right).

Use of 9 g (Fig. 5.9b, left) and 13 g of sucrose (Fig. 5.9b, right) resulted in the best replicated structure in terms of d_{100} spacing, especially by using 13 g of sucrose. However, ordered structures were difficult to prepare due the requirement of high temperature to pyrolyse the carbon inside the pore which led to dense pores. It was accomplished in this study by increasing the temperature to 550 °C for 6 hours. The carbon generated from temperatures lower than 550 °C resulted in featureless GI-SAXS patterns due to incomplete cross linking of the carbon into mesoporous silica film.

It was interesting to maintain the hexagonal ordered into the composite film. Carbon nano-rods obtained after removing the silica template (Fig. 5.9c) resulted in broad peaks for both cases whether using 9 or 13 g of sucrose; however using 9 g of sucrose led to a shift in the peak for 100 reflection to the same position as for the original mesoporous silica. This can indicate a good replication of the structure as the whole silica framework has removed or the overfilled of carbon into mesoporos silica which led to decrease the pore size of the composite. No pore structure for $BaTiO_3$ films was observed for both quantity of 9 and 13 g of sucrose incorporated into mesoporous silica, which could be due to the thickness of the $BaTiO_3$ film as 5 µm and therefore the carbon nanorods were crushed and destroyed. Therefore, mesoporous $BaTiO_3$ prepared from the nanocasting route is still quite challenging.

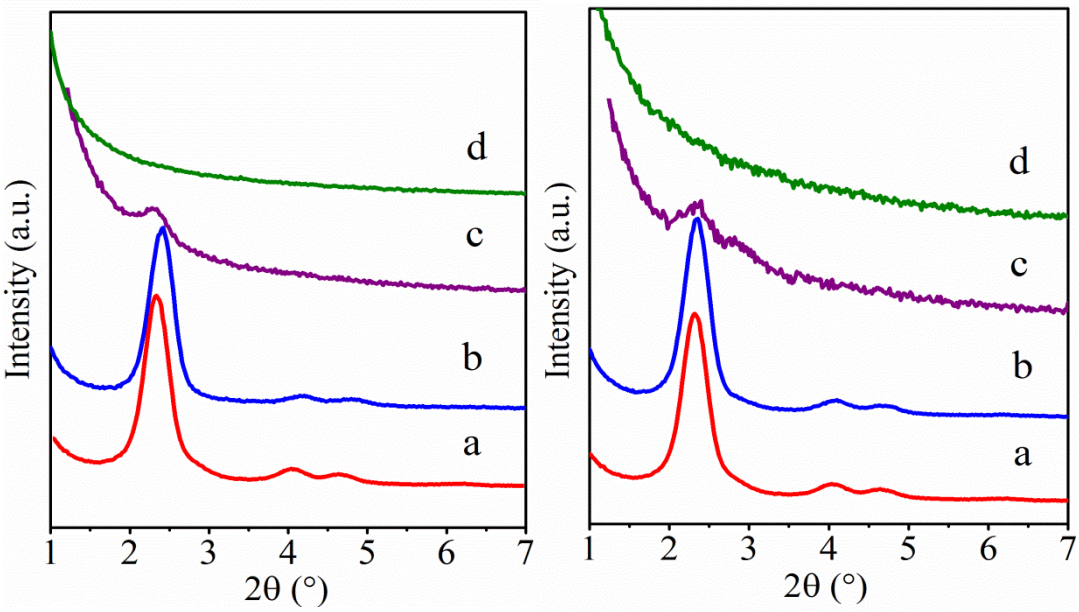

Fig. 5. 9 In-plane GI-SAXS patterns of different quantity of sucrose 9 g (left) and 13 g (right): (a) mesoporous silica film,(b) carbon-silica composite, (c) carbon nanorods and (d) mesoporous $BaTiO_3$ fired at 750 °C.

EDX analysis (Table 5.6) confirmed that the carbon filled the pores of the mesoporous silica and as well the silica template was removed completely as shown from the atomic percentage (74.1%) being the same as the original ITO coated glass (74%).

Table 5. 6 EDX analysis data for mesoporous silica-carbon composite and after silica removed. Film prepared using 13 g of sucrose.

Element (atom)	ITO-silica electrode	Silica-carbon composite on ITO-silica electrode	Silica template removed
% Si	74	77	74.1
% C	5.6	7.8	9
% Na	16.3	12.0	12.1
% In	4.1	3.2	4.8

5.3.4.2 Investigation of pore filling by polypyrrole (electrochemistry process)

Polypyrrole was used as a carbon precursor. The Ppy was electrodeposited on mesoporous silica- ITO electrode from an aqueous solution containing 0.1 M of pyrrole and 0.2 M of KCl and was elucidated by cyclic voltammogram (CV) (Fig. 5.10). In the electropolymerization, the potential was swept from the free potential of electrode (−0.2 V/SCE to 1.2 V/SCE) at a potential sweep rate of 100 mV s^{-1}. An increase in the current density was seen at 570 µA cm^{-2} in the cyclic voltammogram and that explained the formation of pyrrole radical cations from the pyrrole monomer aqueous.

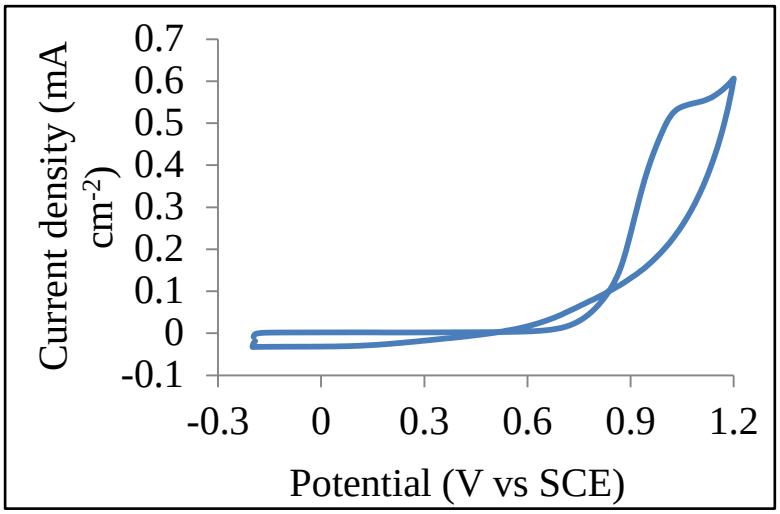

Fig. 5. 10 Cyclic voltammogram of polypyrrole electrodeposited in mesoporous silica on ITO electrode at scan rate100 mV s^{-1}.

Based on the CV, 570 µA cm^{-2} was selected as the maximum current density for the oxidation of pyrrole monomer to perform the electrodeposition of pyrrole. However smaller (500 µA cm^{-2}) was also examined to determine the best current density for the deposition of polypyrrole inside mesoporous silica pores.

Cronopotentiomentry deposition process was applied based on cyclic voltammetry due to the easy determination of the quantity of the potential that consumed to fill the pores of mesoporous silica by polypyrrole. Different current densities were applied during 600 seconds (data not shown) and then fixed for 5 seconds to allow the electropolymerization of polypyrrole inside the pores (Fig. 5.11, left). It is worth noting that the shape of the cronopotentiomentry curve was quite the same, whilst the current density of 570 µA cm^{-2} was the best to provide filled pores by polypyrrole as confirmed by XRD and EDX (which will be discussed in following section). The potential required to keep constant current increased by increasing the deposition progress. After obtaining the maximum in the potential-time curve, the voltage decreased to flatten around 1.1V. The increase in potential was required to grow polypyrrole nano -rods through the mesopors. After the pores were filled by polypyrrole nano–rods completely, additional growth of polypyrrole occurred and therefore required less potential than before. Furthermore, the 570 µA cm^{-2} was run for 0.5 second (Fig.5.11, right) to address the time effect on the deposition, and it was observed that 0.5 second was enough to deposit polypyrrole inside mesoporous silica and it is in agreement with Kang et al.[18], however they used 80 seconds and the current work used 0.5 second of the deposition time.

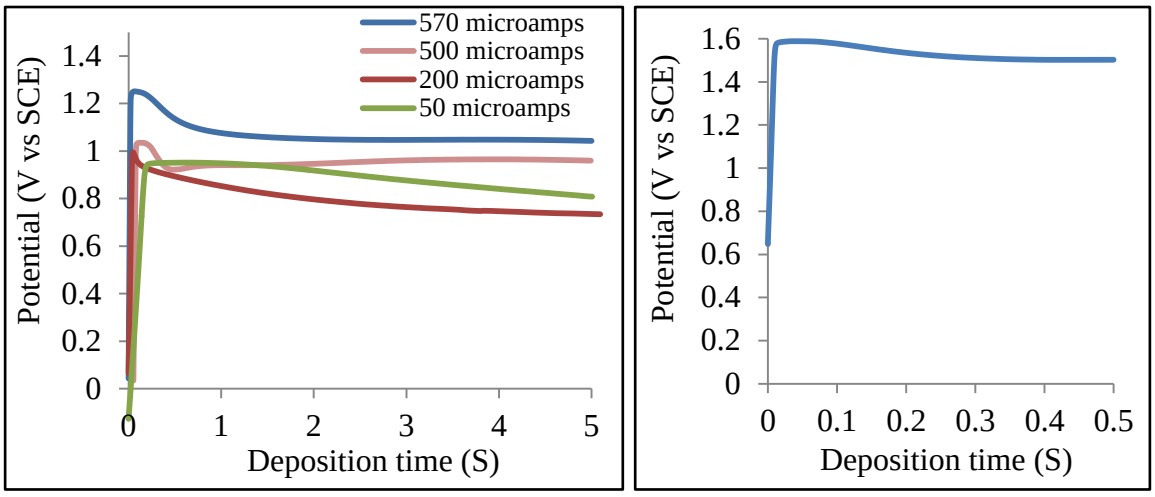

Fig. 5. 11 Cronopotentiomentry curve for 5seconds with shown potential of polypyrrole solution containing 0.1M pyrrole and 0.2M KCl solution, deposition on silica/ITO composit electrode (left). Potential-time of 570 µA/cm^2 on silica/ITO composit electrodes for 0.5 second (right).

In plane GI-SAXS was used to characterise the replicated structured of carbon and $BaTiO_3$ films from mesoporous silica deposited on ITO surface (Fig. 5.12). The in-plane pattern of the carbon- silica composite was well-resolved and the reflection can be indexed to 100,110 and 210 reflections of the 2-D hexagonal *p6mm* space group, indicating a retention of the ordered structure of mesoporous silica host (Fig. 5.12b). Furthermore, the amount of pyrolysed carbon inside the pores of mesoporous silica was not overfilled; therefore it was sufficient to keep the pore structure and prevented the collapse of the carbon replicated after dissolving the host silica (Fig. 5.12c). Similar work has also been reported for preparing carbon replicated SPA-15 powders.[31] EDX analysis (Table 5.7) confirmed that the carbon filled the pores of the mesoporous silica and as that the silica template was removed completely as shown from the atomic percentage was (71.1%) being the same as the original ITO coated glass (71%).

Fig. 5.12d shows in-plane GI-SAXS of mesoporous $BaTiO_3$ films, so it can be seen that the weak and small peak at 2θ of 2.6º indicated pore structure but with little shift in the reflection to higher angle with *d* spacing of 3.4 nm, indicating considerable shrinkage of the pore structure comparable to the original mesoporous silica template used with *d* spacing of 3.5 nm.

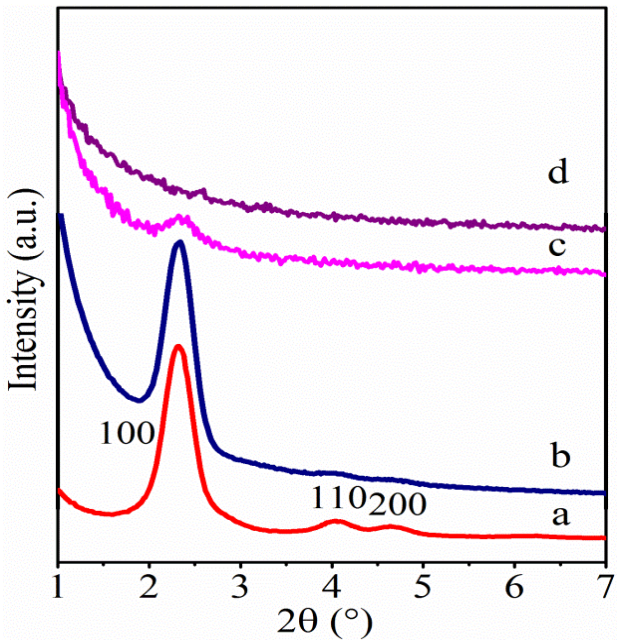

Fig. 5. 12 In-plane GI-SAXS patterns of: (a) mesoporous silica film, (b) carbon-silica composite, (c) carbon nanorods and (d) mesoporous $BaTiO_3$ fired at 750 °C.

Table 5. 7 EDX analysis data for mesoporous silica-carbon composite.

Element (atom %)	ITO-silica electrode	Silica-carbon composite on ITO-silica electrode	Silica template removed
Si	71	74	71.1
C	7.7	9	12
Na	16.5	12.2	12.1
In	4.8	4.8	4.8

5.4 Conclusions

Mesoporous titanate compounds have been attempted by several methods by using soft and hard templates. Nanocrystalline $BaTiO_3$ and $Bi_2Ti_2O_7$ films were synthesized by using F127 surfactant. All the hydrolysis, condensation and assembly processes were self-adjusting without using any extra preparation. Hard template by using mesoporous silica MCM-41 prepared from aqueous TEOS solution containing CTAB by EISA and EASA routes, and variation of sucrose quantities as a carbon source were applied successfully by using (4.05) or 13 g of sucrose to prepare mesoporous $BaTiO_3$ (powders) and films via the impregnation or infiltration of the $BaTiO_3$ precursor sols around the carbon replicated silica template. Electrochemistry method by cronopotentiomentry process was used to grow polypyrrole nanorods through the silica mesopores on ITO electrode. Crystallisation and pore structures have been monitored by in-plane XRD. The elemental analysis and surface morphology were investigated by EDX and SEM tools. The mesoporous $BaTiO_3$ films, are expected to have remarkable properties in areas such as power storage and gas sensor.[13]

5.5 References

1. M. Moniruzzaman and C. K. Das, *Macromol. Symp.*, 2010, **298**, 34-42.
2. H. Choi, E. Stathatos and D. D. Dionysiou, *Appl. Catal., B*, 2006, **63**, 60-67.
3. X. Fan, Y. Wang, X. Chen, L. Gao, W. Luo, Y. Yuan, Z. Li, T. Yu, J. Zhu and Z. Zou, *Chem. Mater.*, 2010, **22**, 1276-1278.
4. M. N. Kamalasanan, N. D. Kumar and S. Chandra, *J. Appl. Phys.*, 1993, **74**, 5679-5686.
5. E. J. H. Lee, F. M. Pontes, E. R. Leite, E. Longo, J. A. Varela, E. B. Araujo and J. A. Eiras, *J. Mater. Sci. Lett.*, 2000, **19**, 1457-1459.

6. H. Kozuka, S. Takenaka, H. Tokita, T. Hirano, Y. Higashi and T. Hamatani, *J. Sol-Gel Sci. Technol.*, 2003, **26**, 681-686.
7. R. Hou, P. Ferreira and P. Vilarinho, *Microporous Mesoporous Mater.*, 2008, **110**, 392-396.
8. H.W. Wang, C.H. Kuo, T.-H. Liao, R.-J. Lin and S.-Y. Cheng, *J. Mater. Res.*, 2006, **21**, 941-946.
9. W. Jiang, C. Jiang, X. Gong and Z. Zhang, *J. Sol-Gel Sci. Technol.*, 2009, **52**, 8-14.
10. L. Kong, H. Chen, W. Hua, S. Zhang and J. Chen, *Chem. Commun.*, 2008, 4977-4979.
11. M. Kinka, J. Banys, W. Bohlmann, E. Bierwirth, M. Hartmann, D. Michel, G. Volkel and A. Poppl, *Ultrasonics, Ferroelectrics, and Frequency Control, IEEE Transactions on*, 2006, **53**, 2305-2308.
12. S. Kohiki, S. Takada, A. Shimizu, K. Yamada, H. Higashijima and M. Mitome, *J. Appl. Phys.*, 2000, **87**, 474-478.
13. R. Z. Hou, P. Ferreira and P. M. Vilarinho, *Cryst. Growth Des.*, 2011, **11**, 5215-5220.
14. R. I. Nooney, D. Thirunavukkarasu, Y. Chen, R. Josephs and A. E. Ostafin, *Chem. Mater.*, 2002, **14**, 4721-4728.
15. S. Jun, S. H. Joo, R. Ryoo, M. Kruk, M. Jaroniec, Z. Liu, T. Ohsuna and O. Terasaki, *J. Am. Chem. Soc.*, 2000, **122**, 10712-10713.
16. A. Goux, M. Etienne, E. Aubert, C. Lecomte, J. Ghanbaja and A. Walcarius, *Chem. Mater.*, 2009, **21**, 731-741.
17. A. Walcarius, E. Sibottier, M. Etienne and J. Ghanbaja, *Nat. Mate.r*, 2007, **6**, 602-608.
18. H. Kang, H. Lee and J. Kwak, *J. Korea.n Chem. Soc.*, 2011, **14**, 22-26.
19. S. W. Boettcher, M. H. Bartl, J. G. Hu and G. D. Stucky, *J. Am.Chem. Soc.*, 2005, **127**, 9721-9730.
20. L. Zhao, Y. Yu, L. Song, M. Ruan, X. Hu and A. Larbot, *Appl. Catal., A*, 2004, **263**, 171-177.
21. Y.I. Kim, J. K. Jung and K.-S. Ryu, *Mar. Pollut. Bull.*, 2004, **39**, 1045-1053.
22. R. Buttner and E. Maslen, *Acta Crystallogr., Sect. B: Struct. Sci.*, 1993, **49**, 62-66.
23. K. Cassiers, T. Linssen, M. Mathieu, Y. Q. Bai, H. Y. Zhu, P. Cool and E. F. Vansant, *J. Phys. Chem. B*, 2004, **108**, 3713-3721.
24. D. Grosso, G. J. de A. A. S. Illia, F. Babonneau, C. Sanchez, P. A. Albouy, A. Brunet-Bruneau and A. R. Balkenende, *Adv. Mater.*, 2001, **13**, 1085-1090.
25. C. Robertson, R. Beanland, S. A. Boden, A. L. Hector, R. J. Kashtiban, J. Sloan, D. C. Smith and A. Walcarius, *Phys. Chem. Chem. Phys.*, 2015, **17**, 4763-4770.
26. T. AbdelFattah, E. J. Siochi and R. E. Crooks, *Fullerenes, Nanotubes, and Carbon Nonstructures*, 2006, **14**, 585-594.
27. H. Yang and D. Zhao, *J. Mater. Chem.*, 2005, **15**, 1217-1231.
28. R. Ryoo, S. H. Joo and S. Jun, *J. Phys. Chem. B*, 1999, **103**, 7743-7746.
29. A. Goux, M. Etienne, E. Aubert, C. Lecomte, J. Ghanbaja and A. Walcarius, *Chem. Mater.*, 2009, **21**, 731-741.
30. K. Böhme, W.D. Einicke and O. Klepel, *Carbon*, 2005, **43**, 1918-1925.
31. C. M. Yang, C. Weidenthaler, B. Spliethoff, M. Mayanna and F. Schüth, *Chem. Mater.*, 2005, **17**, 355-358.

6. Macroporous $BaTiO_3$ and $Bi_2Ti_2O_7$ films

6.1 Introduction

Macroporous materials with regular periodicity can be formed either as two (2D) or three dimensional (3D) films. These are of considerable interest for catalysis,[1] separation[2] hosting molecular species for high surface area battery electrodes[3] and photonic band gap materials for use in optoelectronic devices. The most studied ordered macroporous structures are inverse opals due to their periodic structures that can manipulate light transmission by localizing light and adjusting spontaneous emission. These materials exhibit Bragg diffraction from the planes which generate photonic stop bands in the visible spectra that are suitable for pigment applications. The diameter of the pores is sufficient to allow liquids to diffuse, and high specific surface areas are achieved by the open porous structures.[4]

Inverse opal materials with periodicities in the sub micrometer size range are a challenge to fabricate using techniques such as emulsion templating,[5] which leads to foam-like materials with lower structural order. Therefore, colloidal crystal templates are necessary. The self-assembled template replication process has been established for the fabrication of inverse opal materials, using arrays of close-packed spheres (typically silica or polystyrene). The interstitial voids between the spheres are infiltrated with precursors to the desired material. Template removal by thermal processing or solvent extraction provides a highly ordered, interconnected, porous spheroid matrix. However, the resultant macroporous inverse opal material replicates some defects present in the original packed spheres, with extra defects generated from incomplete the infiltration and cracking during template removal. By using monodisperse colloidal spheres, the colloidal crystal defects can be reduced by controlling the packing mechanisms. Other defects can be controlled by selecting the proper method to infiltrate the spheres and gentle burn-off of the template, which is difficult to control.[6]

Inverse opals of ternary titanates have been produced to achieve high phase contrast in photonic crystals.[7] Our interest stems from investigations into porous electrodeposition hosts,[8] however many ternary oxide materials provide very high dielectric constants that could improve properties of a number of functional electronic materials deposited in such hosts. $BaTiO_3$ inverse opals have previously been produced by electrophoretic deposition into polystyrene sphere opal templates,[9] or infiltration of a number of different alkoxide-based sol formulations into polystyrene[10, 11] PMMA[12] or silica[7] opal templates.

Inverse opal $BaTiO_3$ films with ~5 μm thick mass have been prepared by Soten et al.[11] they prepared films with 280-330 nm pores. Preparing a template by the sedimentation method, infiltrating by dip-coating and calcining at 750 ^oC, the shrinkage factor was 17 %. Jin et al.[13] have prepared 330 nm inverse opal films of cerium-doped $BaTiO_3$ with short-range hexagonal order and the pore diameter reduced on firing by 32.65 % relative to that of the original spheres. Inverse opal Pb-doped $Ba_{0.7}Sr_{0.3}TiO_3$ films with 600 nm pores were synthesised by sedimentation method and infiltration by spin-coating, in which the films exhibited long-range pore structure.[14]

Although the sol-gel method yields extremely high quality materials, all of the preparations in the literature have some defects, such as short range order or cracks. Therefore, it is necessary to control other parameters as mentioned previously such as the mechanism of formation of the colloidal sphere into colloidal crystals and the heating process during template removal, as well the precursor infiltration between the voids.

No previous examples of $Bi_2Ti_2O_7$ inverse opal film production were found in the literature, although Yang and co-workers[15, 16] have reported lanthanide-doped $Bi_2Ti_2O_7$ inverse opals for use in up-conversion luminescence.

The work reported in this chapter describes synthesis of inverse opal $BaTiO_3$ and $Bi_2Ti_2O_7$ films by self-assembly of polystyrene spheres on vertical substrates, and sol-gel infiltration of the precursor into the voids. These were fired at various temperatures with programmed heating rate. The technique defined herein is effective for yielding new ternary compound films with the inverse opal morphology. Part of inverse opal $Bi_2Ti_2O_7$ film works were contributed jointly by the project student, Jack Brewer.

6.2 Experimental procedure

6.2.1 Generation of polystyrene arrays

Templates were generated on 22 × 22 × 1 mm silica tiles. The size of the tiles defined the angle of the surface relative to the polystyrene suspension during the solvent evaporation process, to yield a uniform layer over the substrate surface. Silica tiles for coating were cleaned by sonication in saturated $KOH_{(aq)}$, H_2O, propan-2-ol, and acetone for 10 minutes before drying under a stream of N_2.

Thin film arrays of polystyrene (PS) spheres were generated as follows. Divinylbenzene-cross-linked and amidine capped polystyrene microspheres (500 nm Invitrogen, 42 cm^3 of 0.04 %, 0.08 % and 0.1 % by mass in deionized water) were sonicated for 2-3 hours to attain an even dispersion. The suspension was then utilised to generate a batch of seven templates. Individually cleaned silica tiles were placed into a 25 mm diameter specimen tubes with the tile an angle of ~ 70^o to the base of the tube. A measured amount (6 cm^3) of the polystyrene sphere suspension was carefully syringed into the base of the tube. The seven specimen tubes were positioned on an insulating tray, equally spaced in a circle around an 8^{th} tube having water (6 cm^3) in order to control the humidity through the evaporation process. The tray was transferred into an oven at 65 ^oC without a fan for 72 hours to allow for slow solvent evaporation. After the evaporation of water to dryness a striated, opalescent film of 500 nm polystyrene sphere beads was deposited on the silica substrate (Fig. 6.1). After that the templates were completely dried, removed from the tube vials and stored in a desiccator till further required.

Films produced with 0.1 % PS had highly uniform PS spheres and exhibited a typical iridescent behaviour due to Bragg diffraction. Hence these were used for most inverse opal preparations.

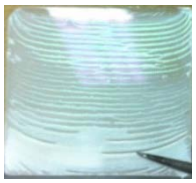

Fig. 6. 1 A photograph showing the opalescence of the PS array templates prepared from a 0.1 % suspension.

6.2.2 Array filling

Two different methods (dipping and capillary infiltration) were used in order to infiltrate the interstitial spaces between the polystyrene spheres.

A $BaTiO_3$ sol and $Bi_2Ti_2O_7$ sol were prepared using the same procedure as in section 4.2.2 and 4.2.3, respectively.

For the dipping process the template was dipped vertically into the sol at a rate of 150 mm $minutes^{-1}$, held for 3 minutes and withdrawn at a controlled rate of 75 mm $minutes^{-1}$. Due to capillary action the sol infiltrates the space between the voids of the template. The dip-coating process was repeated up to 2 or 3 times with 30 minutes drying periods before the next coating to ensure the complete infiltration between the polystyrene spheres on the substrate.

Capillary infiltration was accomplished by submerging only the side edge of the tiles (~1−2 mm) into the $BaTiO_3$ sol so that the liquid was drawn by capillary force along the striated structure and the solvent was evaporated from the surface. The polystyrene sphere templates were left to infiltrate for 2 hours, and so during the process of infiltration the sol volume reduced to around 20 % of its original value. The films were allowed to dry for 30 minutes.

6.2.3 Firing conditions

The pyrolysis of the arrays was performed using a box furnace heated at a rate of 5 ^oC $minutes^{-1}$ followed by calcination at various temperatures for 40 minutes or 30 minutes before the furnace was allowed to cool down. This process yields macroporous multimetal oxide films with various thicknesses according to the firing temperatures.

6.3 Results and discussion

The effects of different preparation conditions, including concentration of PS suspension and precursor sol, template filling mechanisms, firing temperature, and varied number of coating on the morphologies of the macroporous oxide films with 500 nm sphere size, were investigated using SEM. Initially, the array of PS spheres was studied to reveal polycrystalline lattices with close-packed domains and amorphous regions, Fig. 6.2. The diameters of the spheres were confirmed by SEM as 500 nm.

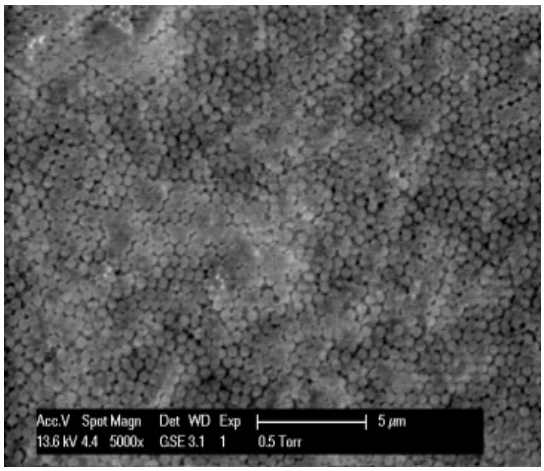

Fig. 6. 2 SEM micrographs of an array of DVB cross-linked PS microspheres displaying regions of close-packing.

6.3.1 $BaTiO_3$ inverse opal film formation

6.3.1.1 Variation of PS and precursor sol concentration

Polystyrene arrays producing from suspensions containing 0.04 %, 0.08 % and 0.1 % polystyrene by mass were filled with precursor sols containing 0.28 mol dm^{-3} or 0.14 mol dm^{-3} Ba and Ti, and fired at 550 ^oC in air in order to determine which conditions gave the best inverse opal $BaTiO_3$ films. The effect of each sol on the morphology of the products was investigated using SEM.

Initially, arrays produced from 0.04 % PS beads were infiltrated with different concentrations of $BaTiO_3$ precursor sol. Fig. 6.3a shows a typical SEM image of the resulting films. A thin layer is present over the surface of the inverse opal film, with some remnants of the initial ordered porosity still visible. The films showed minor and medium cracks, with local disruption in the pore ordering as the porous structure is too fragile to sustain its morphology after removing the PS spheres by calcination. The precursor solution was diluted by a factor of 2 to attempt to remove the thin layer in the top of the inverse opal film (Fig. 6.3b), and SEM revealed the inverse opal film to be improved, and formation of an ordered macroporous structure in large areas. However it also showed disruption and deformation of the ordered macroporous structure in other areas with cracks coming partly from formation of the sphere arrays as a result of drying induced strains, and partly from incomplete filling of the template. A white colour is observed in some areas due to the densification of the $BaTiO_3$ film, as previously reported by Lytle.[17]

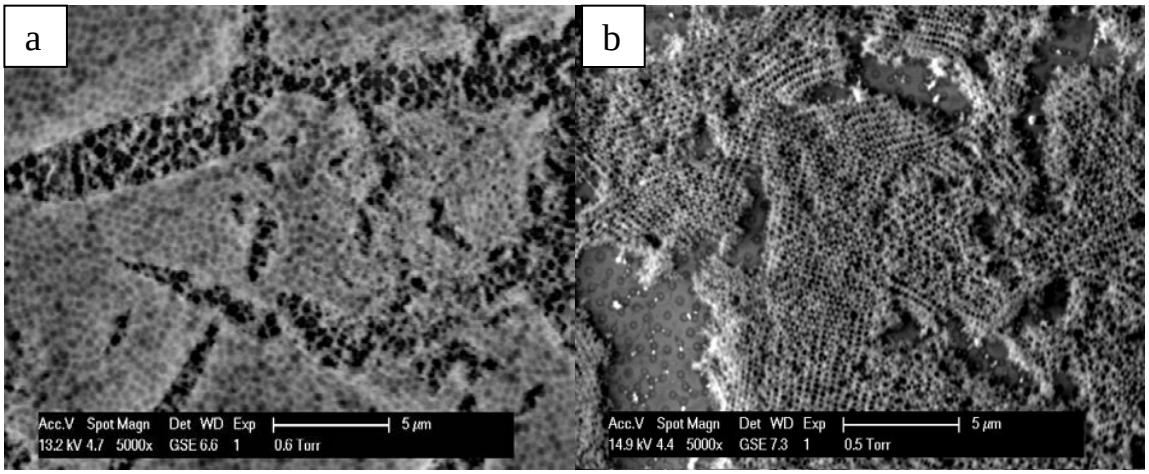

Fig. 6. 3 SEM images of 0.04 % PS arrays infiltrated with 0.28 mol dm^{-3} (a) and 0.14 mol dm^{-3} (b) of $BaTiO_3$ sol then fired at 550 ^oC.

Polystyrene arrays were produced from 0.08 % suspensions were then dipped into 0.28 and 0.14 mol dm^{-3} $BaTiO_3$ sols. Fig. 6.4a shows SEM image of the infiltrated inverse opal film from the 0.28 mol dm^{-3} sol. The opal inverse structure has an ordered 3D-interconnected porous architecture containing open windows between pores, however this is only present in short regions with cracks separating adjacent inverse opal regions. Notably the surface coating in Fig. 6.3a is not present, as the template presumably is thicker. When a diluted sol (0.14 mol dm^{-3}) was used, incomplete filling of the template voids resulted in incomplete macroporous coatings (Fig. 6.4b).

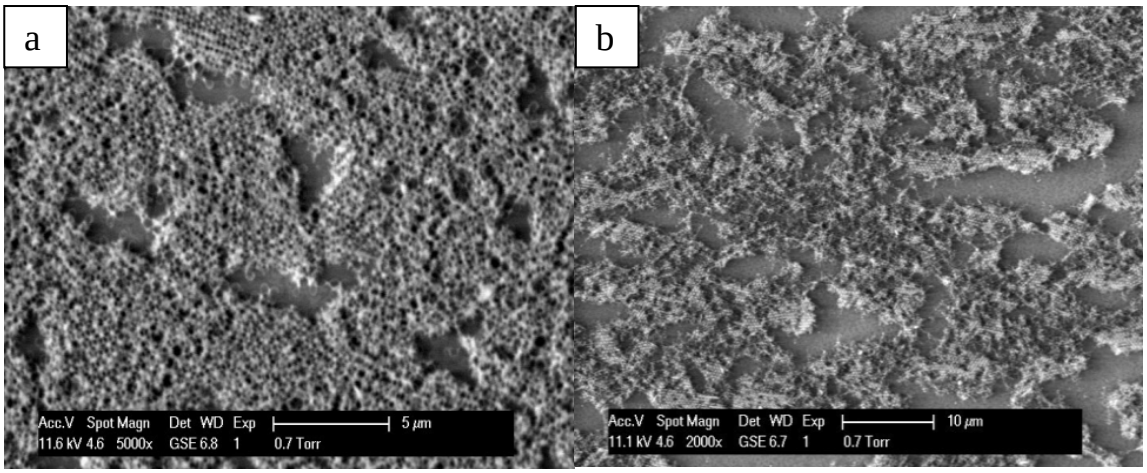

Fig. 6. 4 SEM images of 0.08 % PS arrays infiltrated with 0.28 mol dm^{-3} (a) and 0.14 mol dm^{-3} (b) $BaTiO_3$ sols then fired at 550 ^oC.

Template produced from 0.1 % PS beads and infiltrated by 0.28 and 0.14 mol dm^{-3} $BaTiO_3$ sols resulted in the films shown in Fig. 6.5. Long-range alignment of the hexagonal close packed spheres array were exhibited in Fig. 6.5a and b, but the white colour was still observed due to the densification. Long and short-range order was present when using the diluted $BaTiO_3$ sol (0.14 mol dm^{-3}) but the presence of cracks was more pronounced (Fig. 6.5c and d).

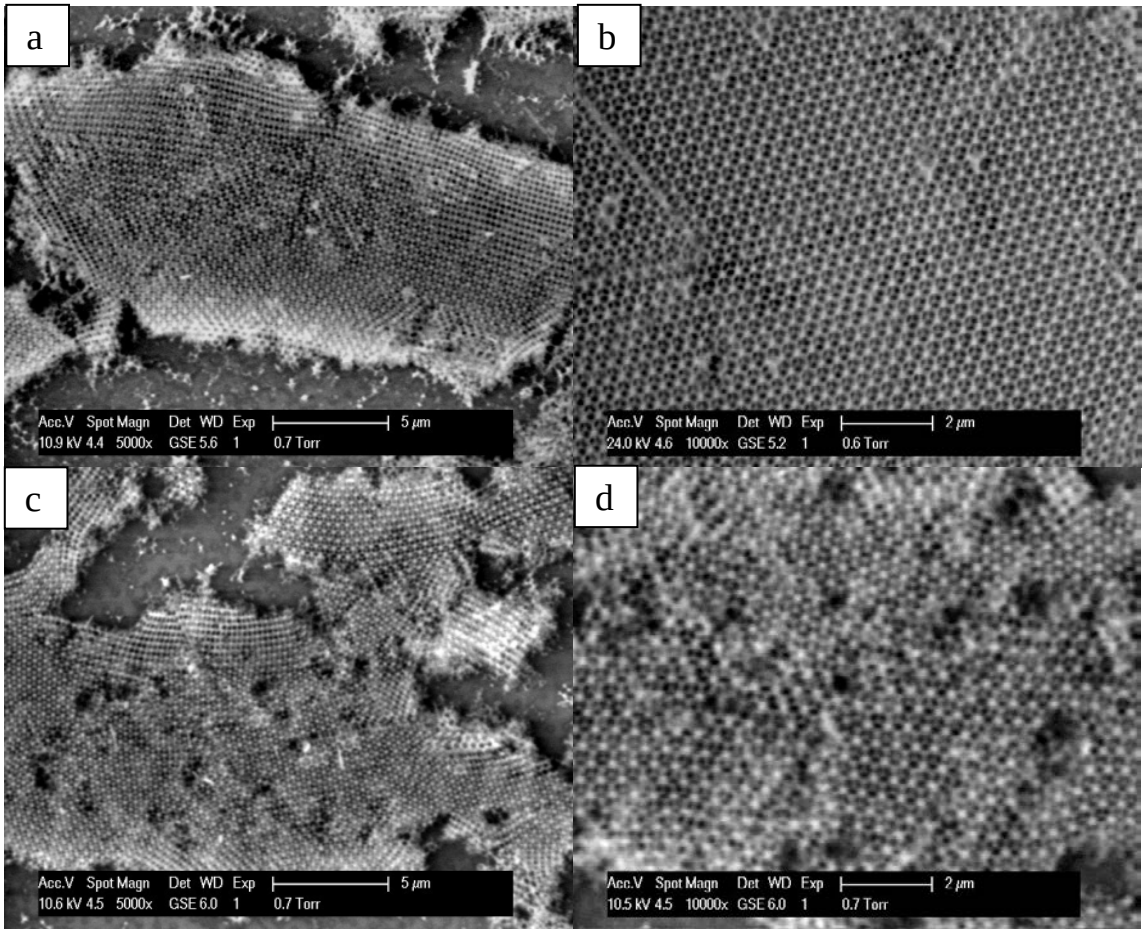

Fig. 6. 5 SEM images of 0.1 % PS arrays infiltrated with 0.28 mol dm^{-3} (a and b) or 0.14 mol dm^{-3} (c and d) of $BaTiO_3$ sol then fired at 550 ^oC.

Overall templates prepared frrom 0.1 % polystyrene infiltrated with 0.28 mol dm^{-3} sol provided the best $BaTiO_3$ inverse opal films, so most further work developed from these conditions.

6.3.1.2 Effect of firing temperature

To study the effect of the temperature on the inverse opal films, $BaTiO_3$ films prepared from 0.1 % PS and infiltrated once with 0.28 mol dm^{-3} of $BaTiO_3$ sols were fired at 500 ^oC, 600 ^oC and 700 ^oC.

Firing at 500 °C (Fig. 6.6a) and 600 °C (Fig. 6.6b) resulted in crack-free, long-range, well-ordered hexagonal arrangements with interconnected pores reflecting the colloidal crystal template. Each large cavity in the surface layer has three internal windows corresponding to the contact points with the three particles in the layer below of the original spheres. The presence of these features along with the minimal cracking and long range order, show that a filling of the void took place imply that the precursor solution completely filled the volume between the spheres prior to solidification.[18] Typically ordered regions of at ~25 μm were present between cracks.

Firing films at 700 °C led to an irregular pore structure and destruction of the porous network, with the presence of significant further crack (Fig. 6.6c).

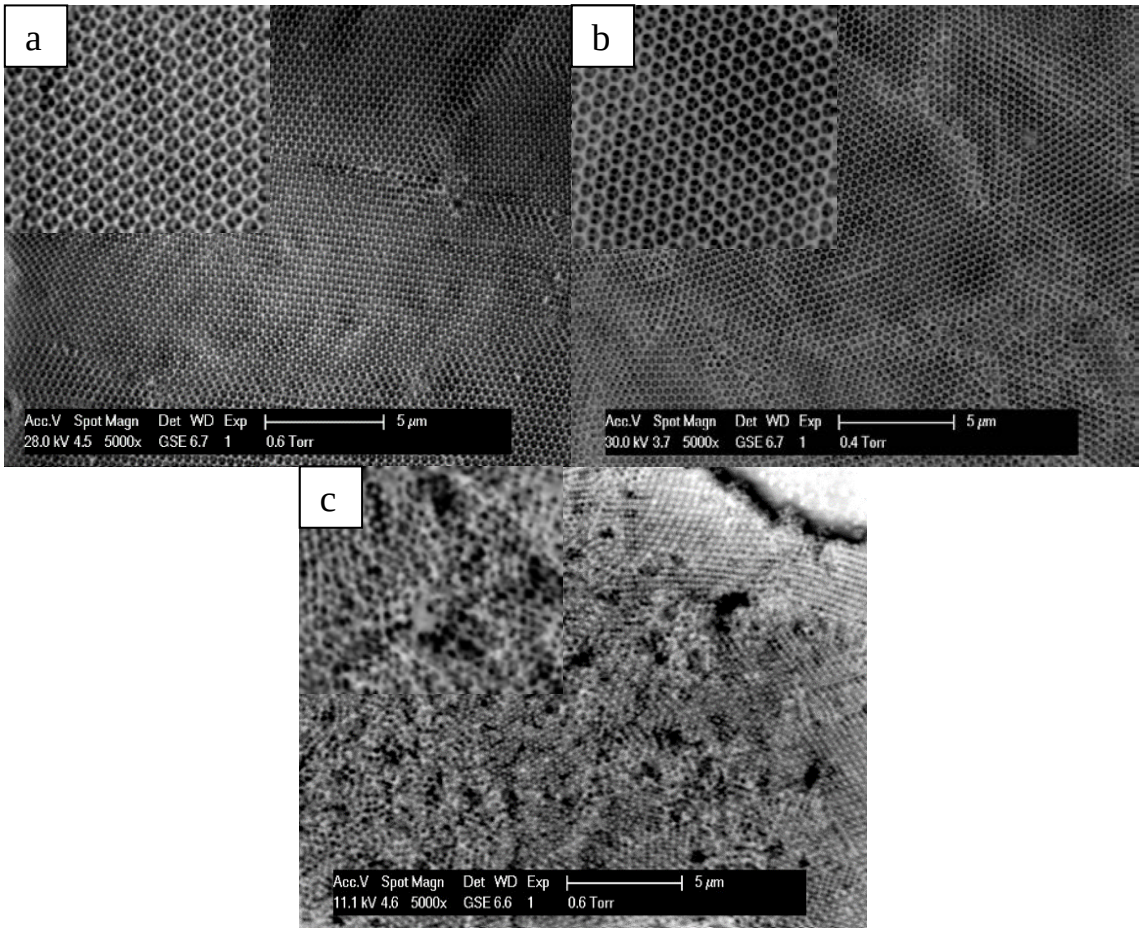

Fig. 6. 6 SEM images of 0.1 % of inverse opal films fired at 500 °C (a), 600 °C (b) and 700 °C (c).

6.3.1.3 Effect of template filling process

In an attempt to extend the macroporous regions over larger areas of the $BaTiO_3$ films, the infiltration of $BaTiO_3$ sols was increased up to 3 coatings, and fired at 500 ^oC, 600 ^oC and 700 ^oC and their influences on the morphology were investigated by SEM.

At 500 ^oC (Fig. 6.7a) and 600 ^oC (Fig. 6.7b) the SEM images shows continuous inverse opal $BaTiO_3$ films in large areas were covered up to ~55-100 µm and very good of ordering pores and further layers of open pores clearly visible with miner defects were observed. Films thickness were 5-6 µm and the Ba:Ti ratio was measured as 1:1.0 from EDX data.

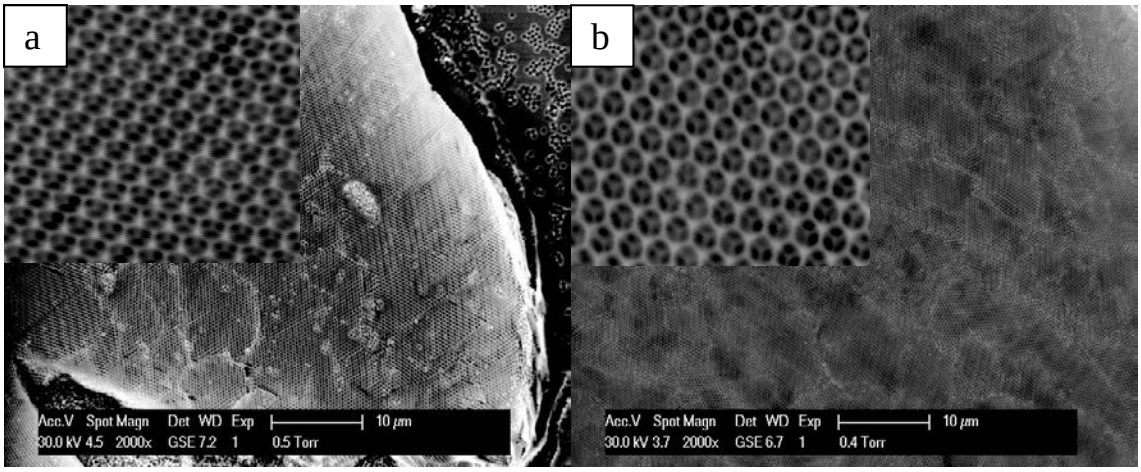

Fig. 6. 7 SEM images of 0.1 % PS arrays infiltrated by 3 dippings of $BaTiO_3$ sol then fired at 500 (a) and 600 ^oC (b).

Films fired at 700 °C developed a series of cracks (Fig. 6.8), although the regions of inverse opal between the cracks were again well ordered. It is likely that some densification is occurring at this temperature, causing strains which result then formation of new cracks.

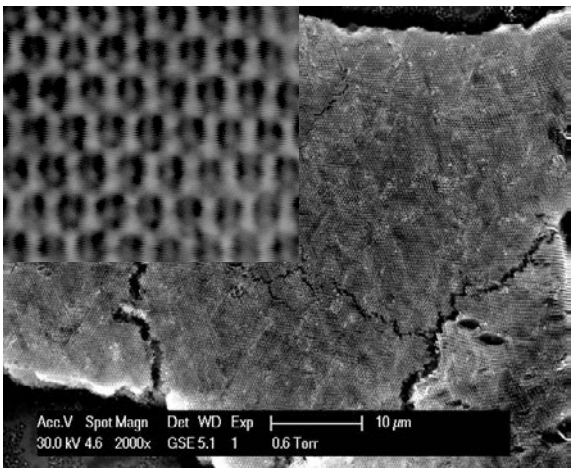

Fig. 6. 8 SEM images of 0.1 % PS arrays infiltrated by 3 dippings of $BaTiO_3$ sol then fired at 700 ^oC.

Visibly, all the patterns had well-ordered and minor defects with high fidelity inverse opal films under optimized conditions, which contributed to the well-ordered periodicity of PS arrays and this was observed over larger length scales than other published studies.[7, 10, 11] In all cases three dark regions were observed inside each pore corresponding to the air spheres of the underlying layer of PS were observed. The pore spacing varied from ~390 nm at 500 °C, to ~370 nm at 600 °C, and ~360 nm at 700 °C. This is a reduction of ~25% relative to the original 500 nm spheres.

Capillary infiltration

Capillary infiltration involved placing the edge of the template into the sol and allowing liquid to be drawn into the pore structure. With metal nitride inverse opals it was more effective than dip-coating.[19]

Fig. 6.9b shows ~ 50 µm regions of well-ordered inverse opal $BaTiO_3$ film produced by capillary infiltration followed by firing at 600 °C. A high number of wide cracks were observed, suggesting that the density of precursors in the templates after infiltration was insufficient. The well-ordered hexagonal structure was depicted by SEM (Fig. 6.9a).

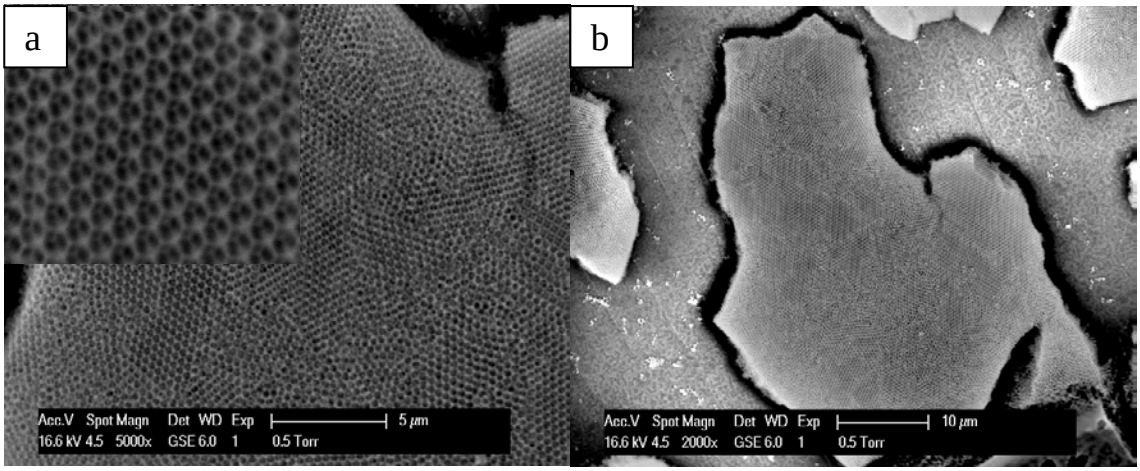

Fig. 6. 9 SEM images of 0.1 % PS arrays infiltrated by capillary method with a $BaTiO_3$ sol then fired at 600 ^oC.

In comparison between dipping and capillary infiltration methods, the dipping route was very effective in providing longe range and well-ordered inverse opal $BaTiO_3$ films in larger areas (~100 µm) than the capillary infiltration route.

6.3.2 $Bi_2Ti_2O_7$ inverse opal film results

$Bi_2Ti_2O_7$ inverse opal films have only previously been reported in the literature when doped with lanthanide elements.[15, 16] These used sol formulations comprising of bismuth and lanthanide nitrates, titanium butoxide, ethanol, ethylene glycol and acetic acid. Herein $Bi_2Ti_2O_7$ precursor sols, as used in section 4.2.3 for films, were used to fill cross-linked PS templates to make inverse opals.

6.3.2.1 Variation of PS concentration

$Bi_2Ti_2O_7$ inverse opal films were produced from three different concentrations of PS templates as described for $BaTiO_3$ inverse opal films.

With 0.04 % PS template, SEM shows inverse opal $Bi_2Ti_2O_7$ films with a hexagonal order which covered ~ 5-10 µm at a time (Fig. 6.10a). However, large open cracks were observed between distorted regions on inverse opal islands (Fig. 6.10b).

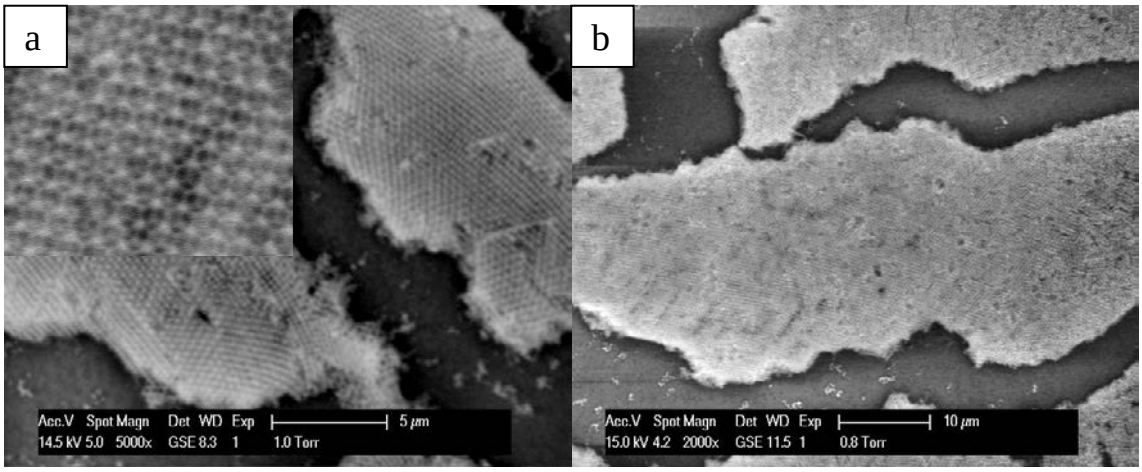

Fig. 6. 10 SEM images of 0.04 % of PS arrays infiltrated by $Bi_2Ti_2O_7$ sol then fired at 550 ^oC.

With 0.08 % PS arrays, the films were improved as the cracks between the islands were reduced in size (Fig. 6.11b) although micro cracks were still present (Fig.6.11a).

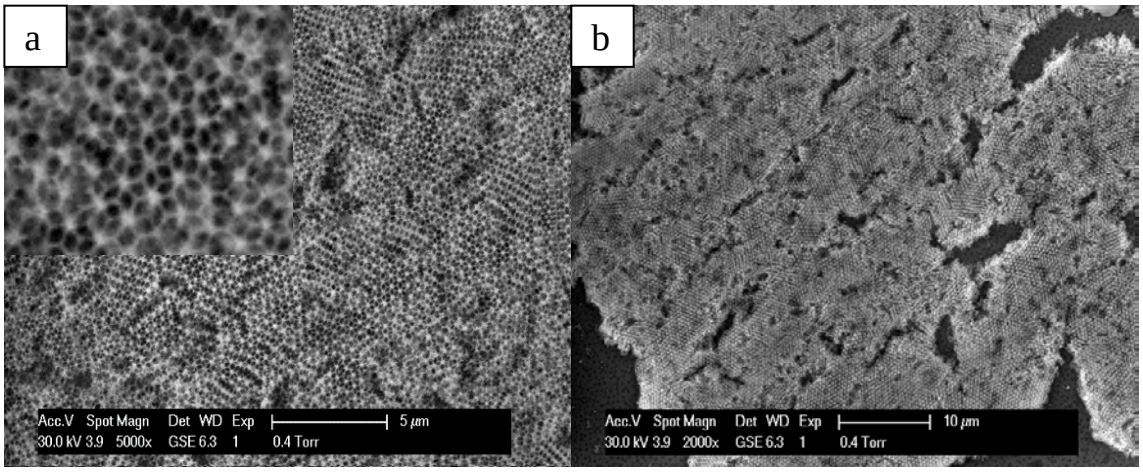

Fig. 6. 11 SEM images of 0.08 % PS arrays infiltrated by $Bi_2Ti_2O_7$ sol then fired at 550 ^oC.

With 0.1 % PS arrays, uniform inverse opal $Bi_2Ti_2O_7$ films characterized by a hexagonal close packed ordered crack-free domains of up to 20 μm (Fig. 6.12a and inset) and it extended over ~120 μm of the whole film with micro-cracks (Fig. 6.12b).

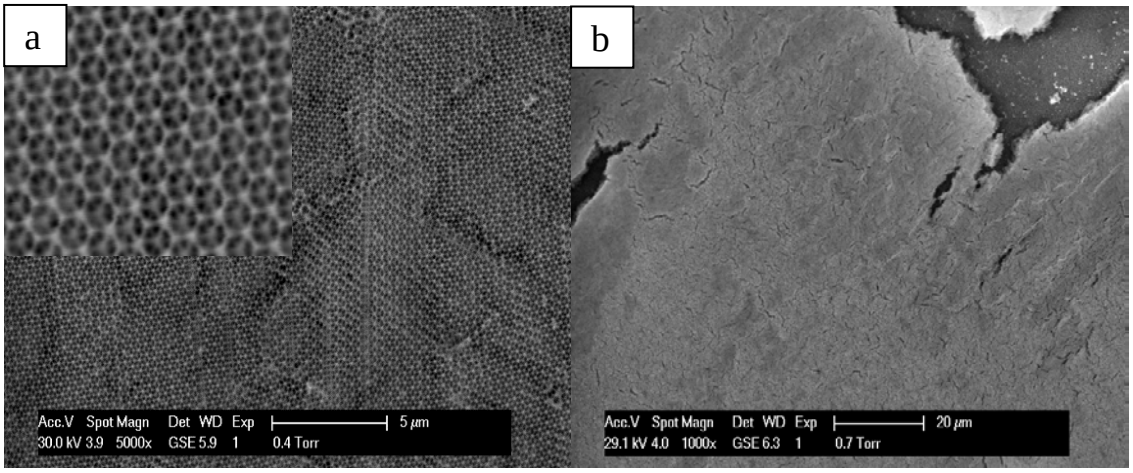

Fig. 6. 12 SEM images of 0.1 % of PS arrays infiltrated by $Bi_2Ti_2O_7$ sol and fired at 550 ^oC, (a) medium magnification (higher magnification, inset) and (b) low magnification.

In comparison between the different concentrations of PS template used, it was obvious that 0.1% PS template provided a good replica of the template over large region of the film.

6.3.2.2 Effect of firing temperature

$Bi_2Ti_2O_7$ inverse opal films prepared from 0.1% PS templates were subjected to firing at 450 ^oC and 650 ^oC, and the films were examined by SEM. At 450 ^oC the inverse opal films had long range order and were crack free over 25 μm (Fig. 6.13a), as well it extended to ~ 140 μm of the entire film (Fig. 6.13b and inset).

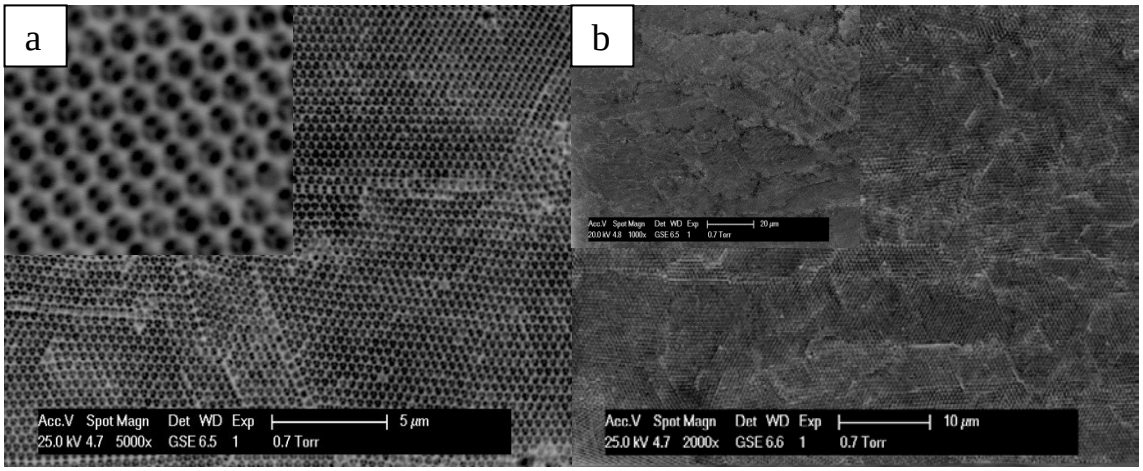

Fig. 6. 13 SEM images of 0.1 % of PS arrays infiltrated by $Bi_2Ti_2O_7$ sol and fired at 450 ^oC.

Significant cracking of the films was observed when it fired at 650 ^oC (Fig. 6.14b) again presumably due to densification, while the pore structure was still preserved in small regions (Fig. 6.14a and inset).

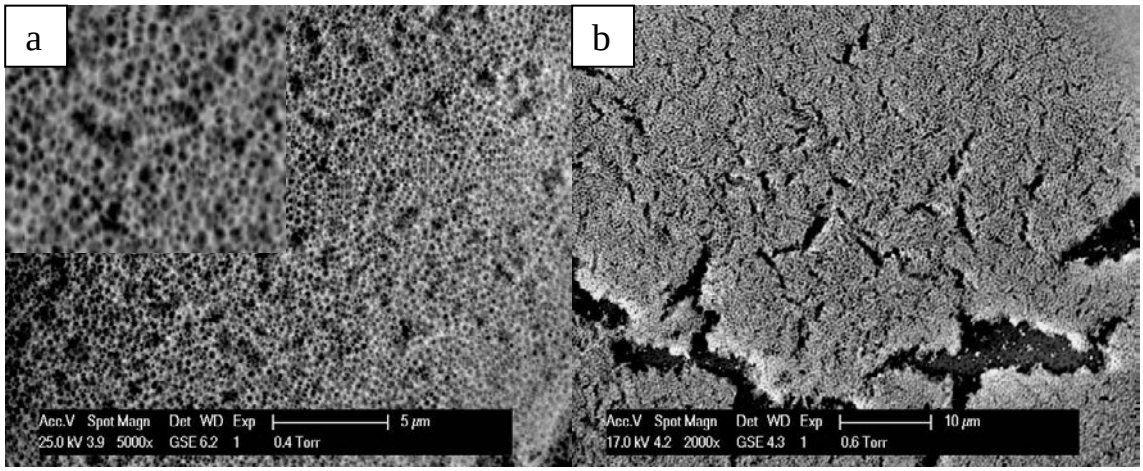

Fig. 6. 14 SEM images of 0.1 % PS arrays infiltrated by $Bi_2Ti_2O_7$ sol and fired at 650 ^oC.

6.3.2.3 Effect of template filling process

In order to obtain well-ordered $Bi_2Ti_2O_7$ inverse opal film over large area with fewer defects, 2 dippings were used. At 450 ^oC, the SEM depicts a long range order of close packed hexagonal film (Fig. 6.15a). These pores structure were extended over ~ 100 µm cracks-free and only minor defects were observed reflecting the original PS arrays.

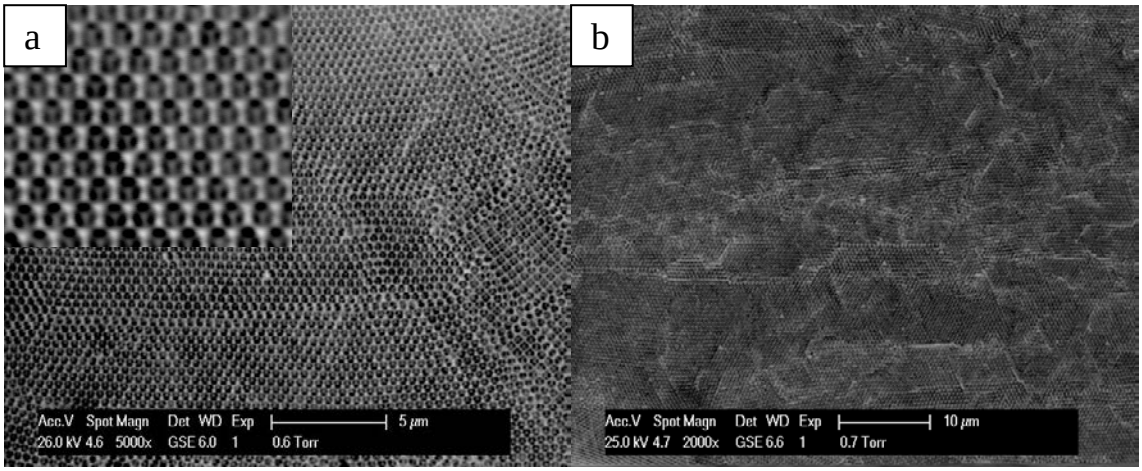

Fig. 6. 15 SEM images of 0.1 % of PS arrays infiltrated by 2 dippings of $Bi_2Ti_2O_7$ sol and fired at 450 ^oC.

The hexagonal pore structures were retained when firing at 550 ^oC (Fig. 6.16a), with preserving the order of the pores in areas as large as ~ 140 µm (Fig. 6.16b).

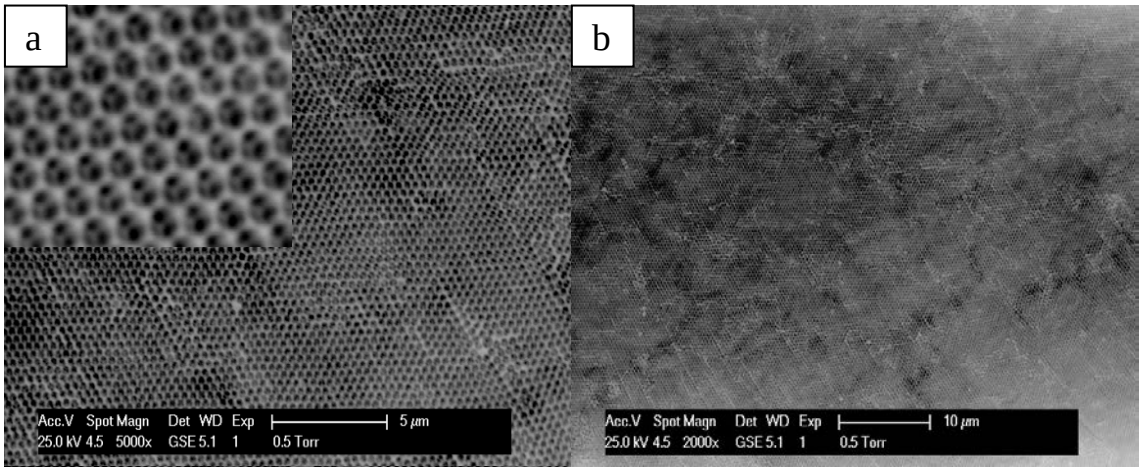

Fig. 6. 16 SEM images of 0.1 % PS arrays infiltrated by 2 dippings of $Bi_2Ti_2O_7$ sol and fired at 550 ^oC.

Major cracks were observed when the film fired at 650 ^oC (Fig. 6.17a), however the film still showed short range regions of well-ordered $Bi_2Ti_2O_7$ film (Fig. 6.17a).

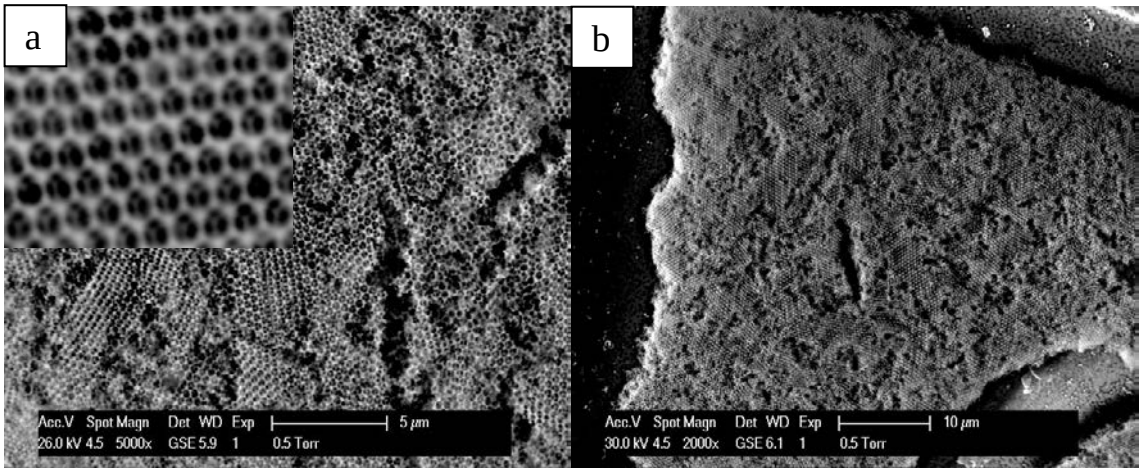

Fig. 6. 17 SEM images of 0.1 % of PS arrays infiltrated by 2 dippings of $Bi_2Ti_2O_7$ sol then fired at 650 ^oC.

The influence of multiple dips on the inverse opal $Bi_2Ti_2O_7$ films prepared by 0.1% PS arrays and fired at 550 ^oC was investigated by SEM (Fig. 6.18). A very thin layer on the top of the inverse opal film was observed.

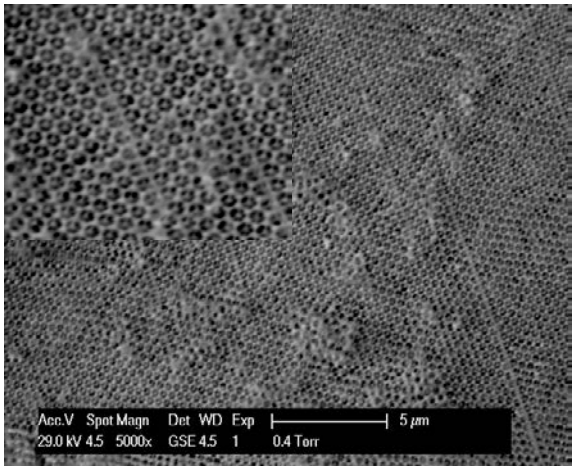

Fig. 6. 18 SEM images 0.1 % of PS arrays infiltrated by 3 dippings of $Bi_2Ti_2O_7$ sol and fired at 550 ^oC.

In comparison between the 450, 550 and 650 ^oC inverse opal films, 450 and 550 ^oC were the best temperatures for the precursor to cross link within the PS template. The pore spacing was 400 nm at 450 °C, 400 nm at 550 °C and 390 nm at 650 °C, hence the shrinkage was a little less (~20%) than that observed with $BaTiO_3$.

Capillary infiltration was also used as well to infiltrate $Bi_2Ti_2O_7$ inverse opal films, but resulted in a high level of film cracking as was observed in the $BaTiO_3$ inverse opal films.

6.3.2.4 Optimised $Bi_2Ti_2O_7$ inverse opal films

The thickness of the best $Bi_2Ti_2O_7$ inverse opal films prepared from 0.1% PS arrays were studied after firing at various temperature .Fig. 6.19a represents the thickness of the $Bi_2Ti_2O_7$ inverse opal film when fired at 450 ^oC as 5 µm; however the thickness was decreased to 3.4 µm and 2.7 µm when the temperature was increased to 550 ^oC and 650 ^oC (Fig. 6.19b and c) due to the wall shrinkage during the densification by the temperature, respectively. The 550 °C film had a 1:1.0 ratio of Bi:Ti by EDX.

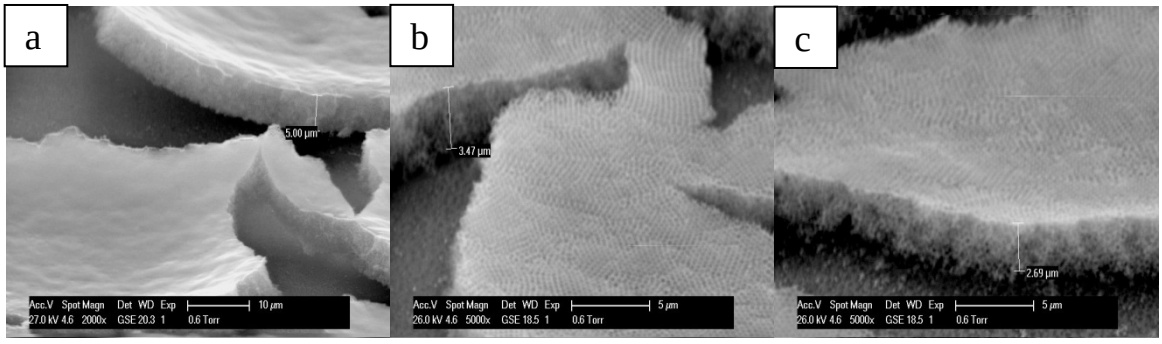

Fig. 6. 19 SEM images of 0.1 % $Bi_2Ti_2O_7$ invers opal films then fired at 450 ^oC (a), 550 ^oC (b) and 650 ^oC (c).

6.3.3 X-ray diffraction

The optimum $BaTiO_3$ and $Bi_2Ti_2O_7$ invers opal films, which were synthesised using 0.1 % PS suspensions and infiltrated 3 or 2 times, respectively with the precursors sols and fired at various temperatures, were characterised by XRD to study the chemical structure and the crystallization of the films.

6.3.3.1 $BaTiO_3$ inverse opal films

$BaTiO_3$ inverse opal films fired at 500 °C were close to amorphous, with only broad features observed. These did have some resemblance to the hexagonal $BaTiO_3$ phase, suggesting that some small nanocrystals may be present. At 600 °C a mixture of hexagonal and tetragonal $BaTiO_3$ was obtained. The XRD pattern of 700 °C fired film showed cubic or tetragonal $BaTiO_3$ with a trace of hexagonal phase (Fig. 6.20).

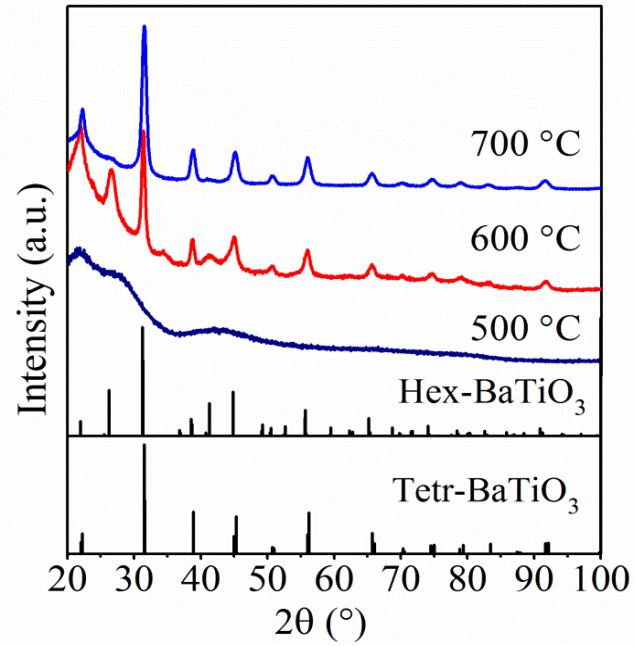

Fig. 6. 20 XRD patterns of $BaTiO_3$ invers opal films sintered at different temperatures compared with standard patterns from ICSD for tetragonal phase[20] and hexagonal phase.[21]

Rietveld fitting of the 600 °C pattern (R_{wp} 4.5%, R_p 3.5%) revealed 23% tetragonal $BaTiO_3$ (P_4mm,[20] a = 4.0091(9) and c = 4.0432(14) Å) and 77% hexagonal $BaTiO_3$ ($P6_3/mmc$,[21] a = 5.726(4) and c = 13.508(11) Å) (Fig. 6.21).

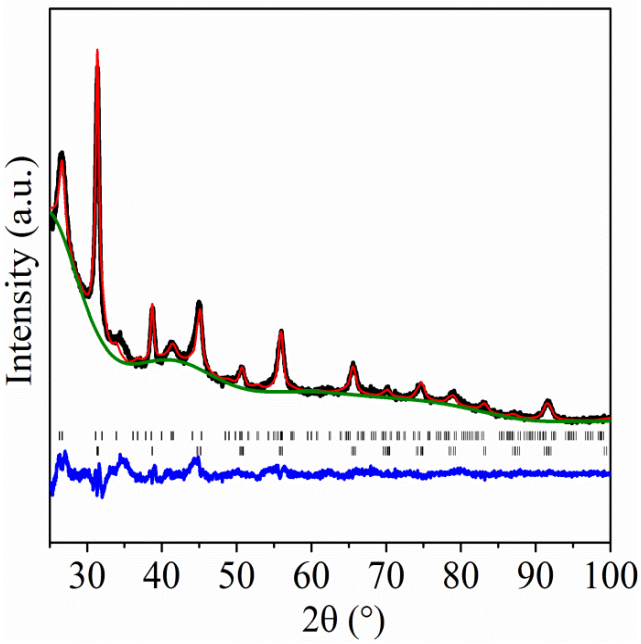

Fig. 6. 21 A Rietveld fit to the XRD for a $BaTiO_3$ film heated at 600 °C. The hexagonal phase is indicated by upper tick marks, the tetragonal phase by lower tick marks. The black line shows the data points, the red solid line, the fit and the lower continuous line the difference.

Rietveld refinement was used to distinguish between the cubic (R_{wp} 8.3%, R_p 6.5%) and the tetragonal (R_{wp} 5.2%, R_p 4.1%) phases of film fired at 700 °C (Fig. 6.22). The tetragonal model gave a clearly better fit, with the most obvious difference being observed in the 200/002 reflections. The hexagonal phase was present at too low a concentration (~1%) for two phase fitting. Refined parameters for tetragonal $BaTiO_3$ (P_4mm)[20] where: a = 4.0012(6) and c = 4.0391(10) Å; Ba 0, 0, 0, U_{iso} = 0.0533(12); Ti ½, ½, 0.531(10), U_{iso} = 0.045(4); O ½, ½, −0.037, U_{iso} = 0.084(3); O ½, 0, 0.518, U_{iso} = 0.084(3). Oxygen positions were not refined, and the average crystallite size was extracted from the profile coefficients as 17.4(17) nm.

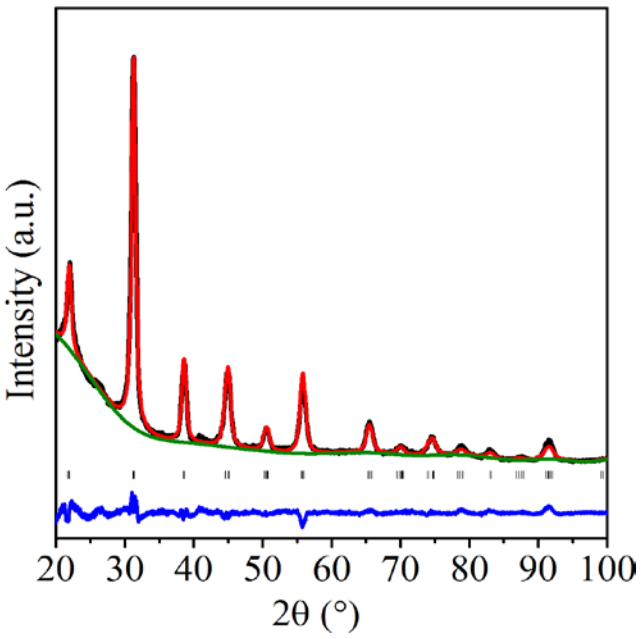

Fig. 6. 22 A Rietveld fit to the XRD for a $BaTiO_3$ film heated at 700 °C. The black line shows the data points, the red solid line the fit and the lower continuous line the difference.

Combining the microscopy and the XRD data it can be seen that the tetragonal $BaTiO_3$ phase was prepared in inverse opal form at 700 °C, with a good ordering of the pore structure and reasonable film quality. However, better long-range order was achieved at 600 °C, where a mixture of hexagonal and tetragonal $BaTiO_3$ were present.

6.3.3.2 $Bi_2Ti_2O_7$ inverse opal films

XRD patterns of $Bi_2Ti_2O_7$ inverse opal films fired at 450 °C contained some $Bi_2Ti_2O_7$ but also a primitive cubic phase that matched literature patterns for a phase of Bi_2O_3[22] (Fig. 6.23). This had the same lattice parameter as the more common fluorite-type Bi_2O_3, but the primitive cell suggests some degree of ion ordering within the defective fluorite lattice. The pyrochlore structure adopted by $Bi_2Ti_2O_7$ is an ordered, defective variation of the fluorite structure and the presence of the extra primitive reflections in the diffraction patterns relative to fluorite suggests some ordering is present here, which could suggest that a primitive cubic bismuth titanate phase is responsible for those reflections. Films fired at 550 °C showed phase pure $Bi_2Ti_2O_7$. At 650 °C the Aurivillius $Bi_4Ti_3O_{12}$ phase was observed as an impurity.

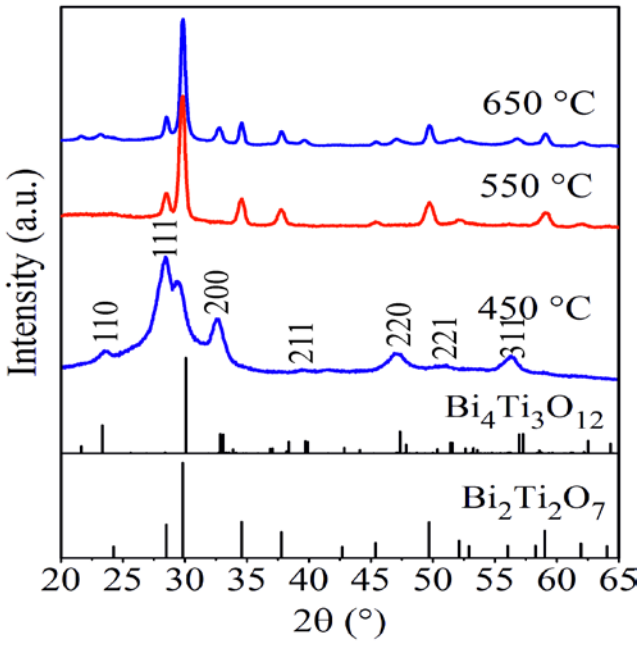

Fig. 6. 23 XRD patterns of $Bi_2Ti_2O_7$ inverse opal films sintered at different temperatures compared with standard patterns from ICSD. The Miller indices labelled on the 450 °C pattern are those of the primitive cubic phase of Bi_2O_3.[22]

Rietveld fitting for a film fired at 550 °C (R_{wp} = 7.1%, R_p = 5.7%) confirmed the expected pyrochlore structure in *Fd3̄mz*, with refined parameters as follows: *a* = 10.3817(4) Å; Bi 0.0214(18), 0.0214(18), −0.0344(17), $^1/_6$ occupancy, U_{iso} = 0.038(3); Ti ½, ½, ½, U_{iso} = 0.008(2); O $^1/_8$, $^1/_8$, 0.4309(12), U_{iso} 0.018(4); O' $^1/_8$, $^1/_8$, $^1/_8$, U_{iso} 0.018(4) (Fig. 6.24).

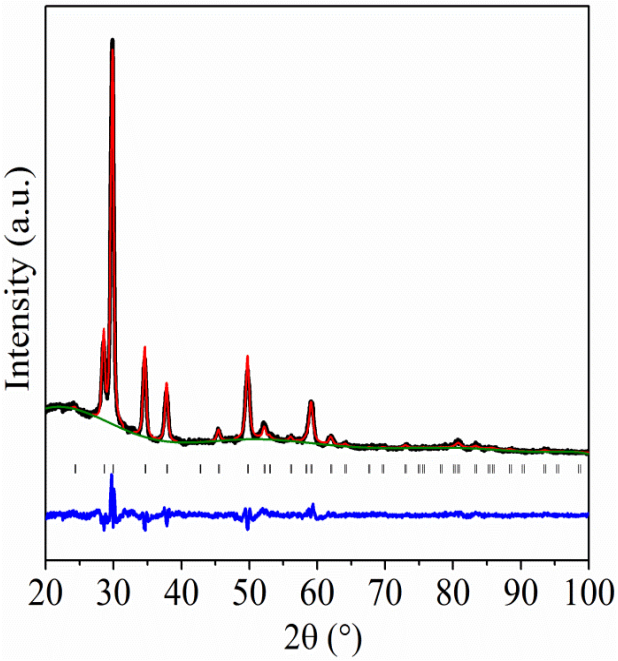

Fig. 6. 24 A Rietveld fit to the XRD for a $Bi_2Ti_2O_7$ film heated at 550 °C for 30 minutes. The black line shows the data points, the red solid line the fit and the lower continues line the difference.

Combining the microscopy and XRD it was clear that very high quality pyrochlore $Bi_2Ti_2O_7$ inverse opals are produced by dip coating the sols under investigation herein into cross-linked polystyrene opal templates and then firing at 550 °C.

6.3.4 UV-visible spectroscopy

The long-range order observed in $BaTiO_3$ and $Bi_2Ti_2O_7$ inverse opal films fired at 600 °C and 550 °C was reflected in strong light green opalescence visible over regions of several mm. This colour results from Bragg optical diffraction from the periodic spacing of the macroscopic lattice, and its intensity is related to the dielectric properties of the films. The UV−vis transmission spectrum of these films (Fig. 6.25) shows a dip in the transmittance centred at around 540 nm which is consistent with the expected photonic stop band.

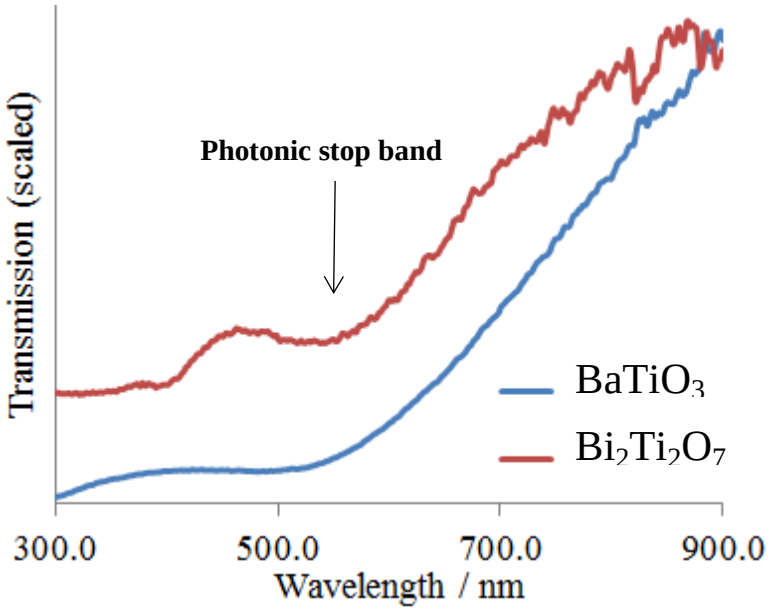

Fig. 6. 25 Transmission UV-visible spectra of $BaTiO_3$ (600 °C) and $Bi_2Ti_2O_7$ (550 °C) inverse opal films.

6.4 Conclusions

Sol formulations based on titanium alkoxides, acetic acid, acetylacetone and methoxyethanol with simple barium or bismuth salts were found to be effective for the controlled formation of inverse opal films of $BaTiO_3$ and $Bi_2Ti_2O_7$. Dip coating of 0.1 % PS arrays produced ~5 µm thickness of well-ordered crack free inverse opal films in large area ~ 100 µm. The template thickness and the density of pore filling could be adjusted to minimise film cracking. The $Bi_2Ti_2O_7$ inverse opal films could be produced phase pure, with long range order and very little cracking. Tetragonal $BaTiO_3$ inverse opal films contained some cracks, consistent with the higher crystallisation temperature of $BaTiO_3$, but contained larger regions of ordered porosity than those currently in the literature.[23] This work represents a significant advance as the first time reported the synthesis of $Bi_2Ti_2O_7$ inverse opal film using 500 nm of PS template in large areas. Due to their high dielectric constants, $BaTiO_3$ and $Bi_2Ti_2O_7$ inverse opals are expected to find a range of dielectric, optical and optoelectric applications, as well as applications in separation and catalysis.

6.5 References

1. W. Q. Fan, H. Y. Bai, G. H. Zhang, Y. S. Yan, C. B. Liu and W. D. Shi, *Cryst. Eng. Comm.*, 2014, **16**, 116-122.
2. M. E. Davis, *Nature*, 2002, **417**, 813-821.
3. R. E. Hummel, *Electronic Properties of Materials*, Springer, New York, 2011.
4. K. Edagawa, *Sci. Technol. Adv. Mater.*, 2014, **15**, 034805.
5. V. N. Manoharan, A. Imhof, J. D. Thorne and D. J. Pine, *Adv. Mater.*, 2001, **13**, 447-450.
6. M. Sadakane, T. Horiuchi, N. Kato, K. Sasaki and W. Ueda, *J. Solid. State. Chem.*, 2010, **183**, 1365-1371.
7. J. Zhou, C. Q. Sun, K. Pita, Y. L. Lam, Y. Zhou, S. L. Ng, C. H. Kam, L. T. Li and Z. L. Gui, *Appl. Phys. Lett.*, 2001, **78**, 661-663.
8. C. Robertson, R. Beanland, S. A. Boden, A. L. Hector, R. J. Kashtiban, J. Sloan, D. C. Smith and A. Walcarius, *Phys. Chem. Chem. Phys.* , 2015, **17**, 4763-4770.
9. B. Li, J. Q. Wang, R. Fujiwara, M. Kuwabara, M. Fu and J. Zhou, Key Eng. Mater. , 2010, **434,** 247-252.
10. A. Xiang, G. Jian Ping, C. Hong Kui, Y. Jiu Gao and R. X. Liu, *Chin. Chem. Lett.*, 2004, **15**, 228-230.
11. I. Soten, H. Miguez, S. M. Yang, S. Petrov, N. Coombs, N. Tetreault, N. Matsuura, H. E. Ruda and G. A. Ozin, *Adv. Funct. Mater.*, 2002, **12**, 71-77.
12. Y. N. Kim, E. O. Chi, J. C. Kim, E. K. Lee and N. H. Hur, *Sol. St. Commun.*, 2003, **128**, 339-343.
13. Y. Jin, Y. Zhu, X. Yang, C. Li and J. Zhou, *J. Solid. State. Chem.* , 2007, **180**, 301-306.
14. N. Matsuura, S. Yang, P. Sun and H. E. Ruda, *Appl. Phys. A*, 2005, **81**, 379-384.
15. Y. Cun, Z. Yang, J. Liao, J. Qiu, Z. Song and Y. Yang, *Mater. Lett.*, 2014, **131**, 154-157.
16. D. Yan, Z. Yang, J. Liao, H. Wu, J. Qiu, Z. Song, D. Zhou, Y. Yang and Z. Ying, *Chin. Opt. Lett.*, 2013, **11**, 1-4.
17. J. C. Lytle, H. Yan, N. S. Ergang, W. H. Smyrl and A. Stein, *J. Mater. Chem.*, 2004, **14**, 1616-1622.
18. Z. Zhong, Y. Yin, B. Gates and Y. Xia, *Adv. Mater.*, 2000, **12**, 206-209.
19. C. F. Mallinson, B. M. Gray, A. L. Hector, M. A. McLachlan and J. R.Owen, *Inorg. Chem.*, 2013, **52**, 9994-9999.
20. Y.I. Kim, J. K. Jung and K.-S. Ryu, *Mar. Pollut. Bull* , 2004, **39**, 1045-1053.
21. J. Akimoto, Y. Gotoh and Y. Oosawa, *Acta. Crystallogr., Sect. C: Cryst. Struct. Commun*, 1994, **50**, 160-161.
22. A. A. Zav'yalova and R. M. Imamov, *J. Struct. Chem.*, 1973, **13**, 811-814.
23. S. M. Hant, *Characterization and Fabrication of Nanoporous Materials by Template-Directed Sol-Gel Methods.* PhD thesis. University of Southampton, 2008.

7. Conclusions

TiO_2, $BaTiO_3$ and $Bi_2Ti_2O_7$ films and powders have been synthesized. Film formation used a dip-coating sol-gel method. Mesoporous $BaTiO_3$ and $Bi_2Ti_2O_7$ films were produced using a soft template, and a hard template method was attempted for preparing ordered mesoporous $BaTiO_3$ films. Macroporous $BaTiO_3$ and $Bi_2Ti_2O_7$ films were obtained by templated deposition a round PS sphere template.

Mixed phase anatase and rutile TiO_2 films and powders were successfully synthesized using $Ti(O^iPr)_4$ and $Ti(OBu^n)_4$ based sols modified with DEA. Ti $(O^iPr)_4$ based sols with HCl catalyst and no modifier resulted in phase pure anatase after firing in the same conditions. The optimum content of DEA improved the crystallinity and flat, crack-free films were produced. The phase change from anatase to rutile phase in this study was dependent on synthesis conditions. The DEA modifier accelerated the transformation whereas chloride ions have a tendency to supress the transformation unless higher concentration of the HCl was applied. The transformation from anatase into rutile has been suggested to be assisted by interface boundary defects of the anatase particles, which allow the growth of rutile phase during heating process.[1] Using the optimum amount of DEA led to induce the breaking of Ti-O of anatase particles and removal of oxygen ion and formed defects along with creation of new Ti-O bond for rutile phase.[1] Therefore, 7 mL of DEA produced thicker and denser TiO_2 films which increase the transformation from anatase to rutile phase due to the nanoparticles to be contacted with each other and thus interface boundary defects happened at the interface of the neighbouring anatase nanocrystallites.[2] The transformation from anatase to rutile was increased in powders than films due to the stabilisation of SiO_2 phase from the substrate used.[3]

Crystallite sizes were calculated from Rietveld refinement, and increased largely with increasing firing temperature. The rutile crystallite size increase faster with temperature due to the rutile crystallite mechanism formation, it is grows from anatase particle (the primary particles) and increased significantly. The crystallite sizes in the films were smaller than that in powders, which could be due to substrate effects.

The thickness of TiO_2 films were found to increase by increasing the number of coating cycles, the concentration of the sol and the substrate withdrawal speed, but to decrease with increasing firing period.

The speciation of TiO_2 sols modified by DEA was investigated by ESI-TOFMS, and ^{1}H and $^{13}C\{^{1}H\}$NMR in order to determine the molecular structure and the composition. As the sol was very complicated and many species were shown, the ESI-TOFMS failed in determining the molecular structure. NMR measurements were useful in understanding the species. It was observed that all the isopropoxide groups were substituted by ethoxy groups and DEA ligands were bound to the titania in a monomeric structure from ^{1}H NMR spectra. The same effects were observed from $^{13}C\{^{1}H\}$NMR, which could be due to the time scale of exchange process of ^{1}H NMR is faster than $^{13}C\{^{1}H\}$NMR and therefore the lability of the ligands, has a large effect in the case of $^{13}C\{^{1}H\}$ NMR. Therefore, the NMR results suggested that the Ti species in the solution with DEA was present as a tridentate monomeric complex, but with significant lability.

Attempts to obtain mesoporous TiO_2 films by EISA-sol-gel method using tri-block copolymer P123 as a template were not successful, partly due to the lack of effective means at that time to investigate large pore size. The crystallisation of titania from amorphous to anatase form was caused by heating at 400 °C.

Tetragonal-$BaTiO_3$ and pyrochlore $Bi_2Ti_2O_7$ films were synthesised based on titanium alkoxides, acetic acid, acetylacetone and methoxyethanol with simple barium or bismuth salts. Single dip-coating provided ~5 μm solid films which were largely smooth and free from crack and pinholes with 1:1 Ba:Ti and Bi:Ti ratios were found using EDX analysis and the thickness could be increased by using multiple coating. Rietveld refinement program was used to distinguish between cubic and tetragonal-$BaTiO_3$ in the XRD pattern. The tetragonal phase delivered a slightly better fit, most notably in the 200/002 reflection at ~45° in comparison to the cubic phase refinements. The dielectric constant measurements of $BaTiO_3$ film were studied by an impedance analyzer with upper electrode of $2.4 \times 10^{-5}\,m^2$ in dimension. The dielectric constants were calculated as low, due to the smaller crystallite size for the single coated films and the surface defects for the multiple dips films.

Good quality pyrochlore $Bi_2Ti_2O_7$ films were obtained by aging the sol for 24 hours and firing at 550 °C for 30 minutes and the SEM showed flat film in ~100 µm with no individual particles on the top surface. The Aurivillius phase content was increased by varying the sol composition in either way from 1:1 Bi:Ti. The crystallite size was calculated as 86.4(13) nm based on Rietveld refinement.

Mesoporous $BaTiO_3$ and $Bi_2Ti_2O_7$ films have been tried by several methods by using soft and hard templates. The pore structure of mesoporous $BaTiO_3$ and $Bi_2Ti_2O_7$ films was not observed through in plane GI-SAXS by using soft template (F127 surfactant). This could be due to the harsh processing conditions that the 2-ME solvent was not able to disperse the surfactant in the multimetal oxide sols, so it was difficult to grow the micelle of F127 surfactant into barium / bismuth titanate sols, thus, another solvent are required. Alternatively the variation in the condensation and hydrolysis rate of the metal ions and the surfactant micelles could be problematic. However, both $BaTiO_3$ and $Bi_2Ti_2O_7$ films were crystalline into tetragonal and pyrochlore phases, respectively.

A hard template was applied to prepare $BaTiO_3$ films and powders by using mesoporous silica MCM-41 prepared by EISA and EASA routes through impregnation or infiltration of the precursor sols around the carbon prepared from different quantity of sucrose, replicating a silica template. Electrochemistry method by cronopotentiomentry process was used to grow polypyrrole as a carbon source inside the mesopores silica on ITO electrode in attempt to adequate to fill the pore structure by the carbon in effective way. However, it was a challenge to maintain the mesoporous $BaTiO_3$ films after removing the silica template due to the thickness of the $BaTiO_3$ film was 5 µm and therefore the carbon nanorods were crashed when the infiltration by the sols was took place, therefore thinner films would be useful for preparing mesoporous $BaTiO_3$ films. The mesoporous $BaTiO_3$ films are predictable to have significant properties in areas such as power storage.[4]

Tetragonal $BaTiO_3$ and pyrochlore $Bi_2Ti_2O_7$ inverse opal films were synthesised by using 500 nm of PS spheres as a template by sol-gel dip-coating process successfully. 0.1 % PS arrays produced ~5 µm thickness of excellent-ordered and crack-free inverse opal films in large area ~100 µm after firing the film at 600 °C for 30 minutes, so it showed very good 3 dimensional ordering of pores. The template thickness and the density of pore filling could be controlled to minimise film cracking.

The pore size varied from ~390 nm at 500 °C, to ~370 nm at 600 °C, and ~360 nm at 700 °C. This is a reduction of ~25 % relative to the original 500 nm spheres. Tetragonal $BaTiO_3$ inverse opal films contained some cracks, consistent with the higher crystallisation temperature of $BaTiO_3$, but contained larger regions of ordered porosity than those currently in the literature.[5-7] The $Bi_2Ti_2O_7$ inverse opal films were phase pure, with long range order and very little cracking. They covered ~100 μm of the entire surface at a time after firing at 550 °C for 30 minutes. The pore size was 400 nm at 450 °C, 400 nm at 550 °C and 390 nm at 650 °C, thus the shrinkage was a little less (~20 %) than that observed with $BaTiO_3$. The current work is a significant advance as the first time reported the synthesis of $Bi_2Ti_2O_7$ inverse opal film using 500 nm of PS template with high specification, e.g the macroporous covered large areas with preserving the well ordering. Because of their high dielectric constants, $BaTiO_3$ and $Bi_2Ti_2O_7$ inverse opals are likely to find a range of dielectric, separation,[8] catalysis applications and hosting molecular species for high surface area battery electrodes.[9, 10] So this is significant future potential to expand the range of macroporous materials especially for ternary compounds by using other techniques, e.g. electrochemistry.

7.1 References

1. B. Choudhury and A. Choudhury, *Int. Nano Lett.*, 2013, **3**, 1-9.
2. N. Avci, P. Smet, H. Poelman, N. Velde, K. Buysser, I. Driessche and D. Poelman, *J. Sol-Gel Sci. Technol.*, 2009, **52**, 424-431.
3. J. G. Yu, H. G. Yu, B. Cheng, X. J. Zhao, J. C. Yu and W. K. Ho, *J. Phys. Chem. B*, 2003, **107**, 13871-13879.
4. R. Z. Hou, P. Ferreira and P. M. Vilarinho, *Cryst. Growth. Des.* , 2011, **11**, 5215-5220.
5. J. Zhou, C. Q. Sun, K. Pita, Y. L. Lam, Y. Zhou, S. L. Ng, C. H. Kam, L. T. Li and Z. L. Gui, *Appl. Phys. Lett.*, 2001, **78**, 661-663.
6. A. Xiang, G. Jian Ping, C. Hong Kui, Y. Jiu Gao and R. X. Liu, *Chin. Chem. Lett.*, 2004, **15**, 228-230.
7. I. Soten, H. Miguez, S. M. Yang, S. Petrov, N. Coombs, N. Tetreault, N. Matsuura, H. E. Ruda and G. A. Ozin, *Adv. Funct. Mater.*, 2002, **12**, 71-77.
8. M. E. Davis, *Nature*, 2002, **417**, 813-821.
9. R. E. Hummel, *Electronic Properties of Materials*, Springer, New York, 2011.
10. E. Armstrong and C. O'Dwyer, *J. Mater. Chem C*, 2015, **3**, 6109-6143.

Rietveld refinement patterns of TiO_2 films and powders

A. T1- HCl

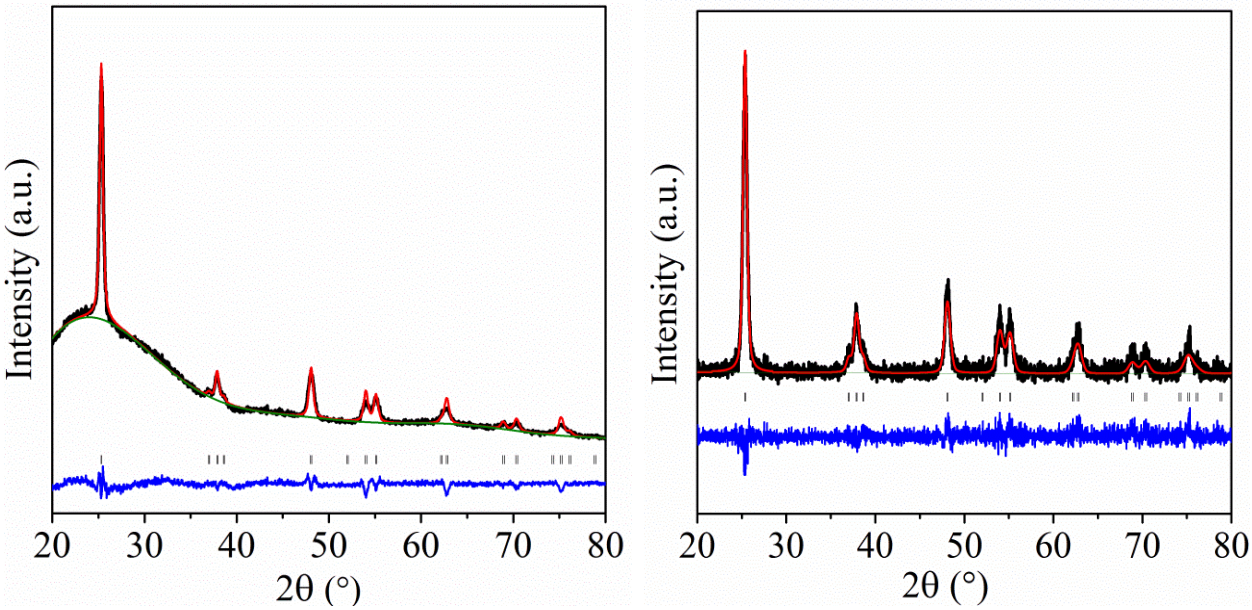

A Rietveld fit to the XRD pattern for film (left) and powder (right) produced from sol T1-HCl and heated at 600 °C for 5 minutes (page 68).

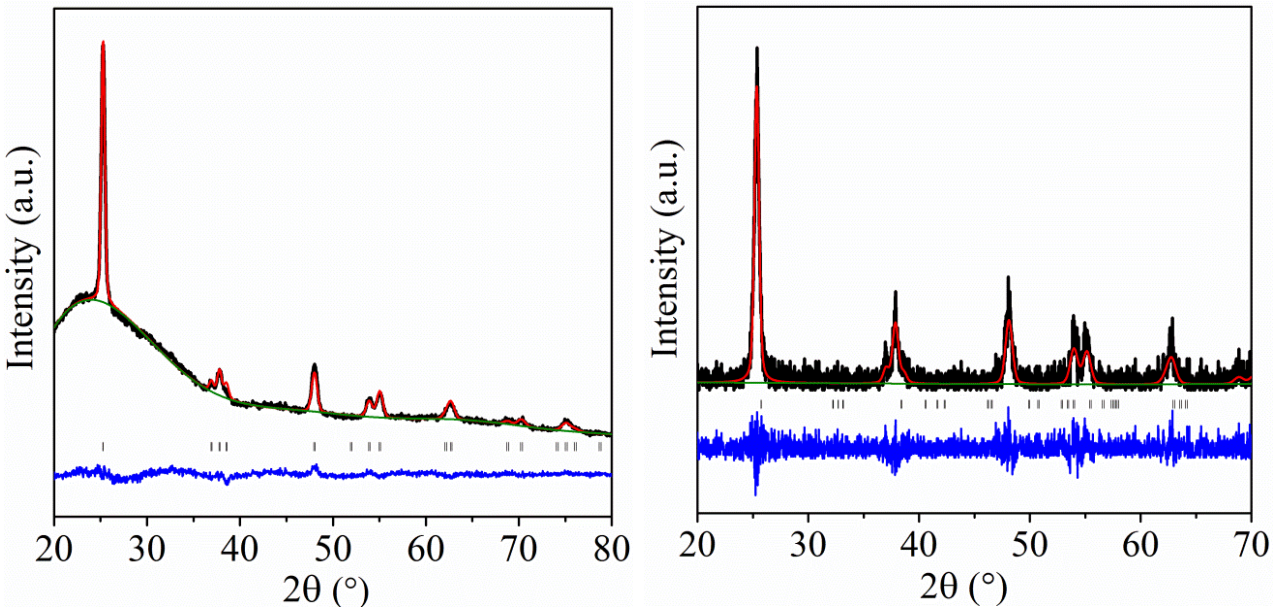

A Rietveld fit to the XRD pattern for film (left) and powder (right) produced from sol T1-HCl and heated at 600 °C for 10 minutes (page 68).

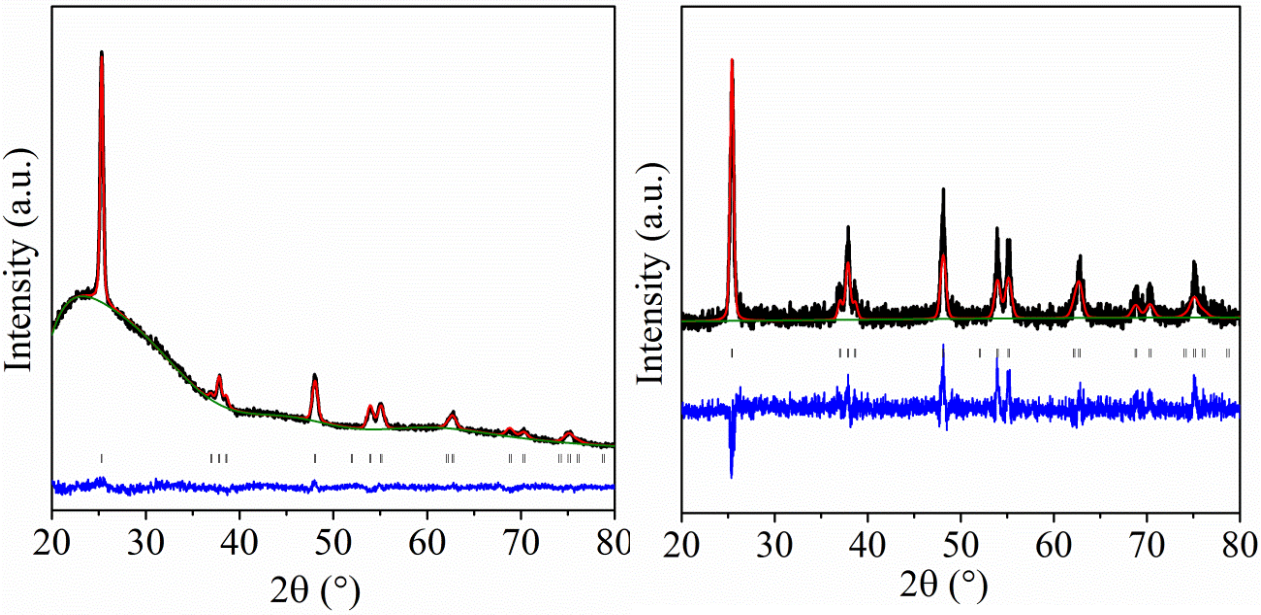

A Rietveld fit to the XRD for film (left) and powder (right) produced from sol T1-HCl and heated at 600 °C for 40 minutes (page 68).

B. T2-DEA

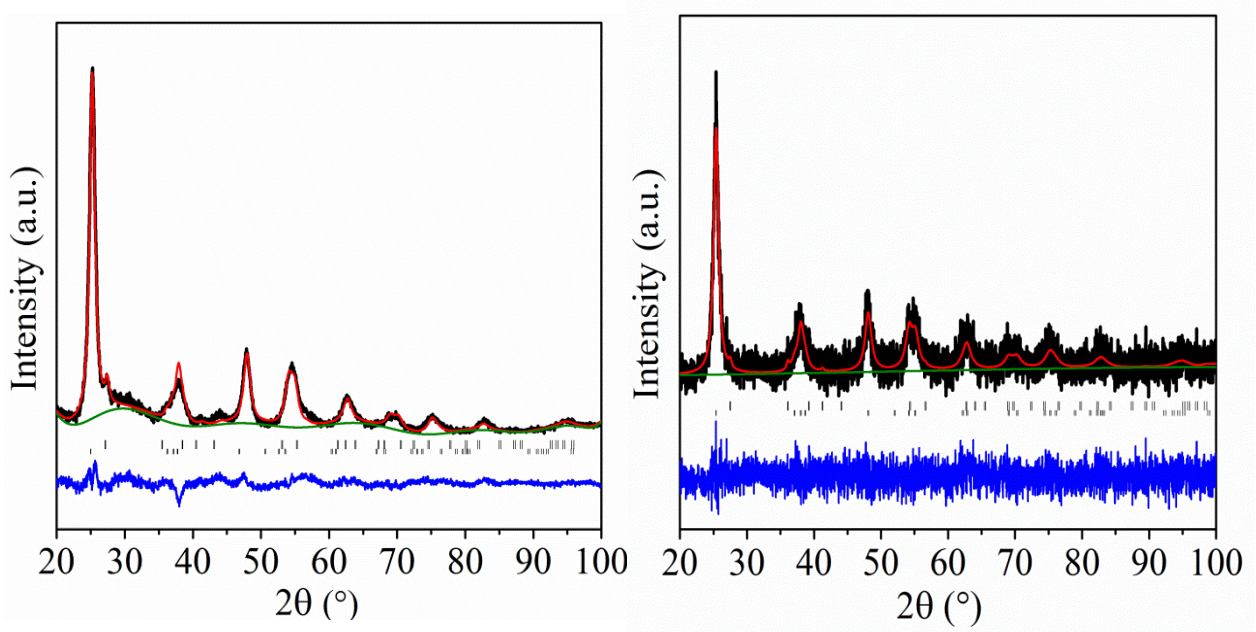

A Rietveld fit to the XRD for film (left) and powder (right) produced from sol T2-DEA and heated at 600 °C for 5 minutes (page 71).

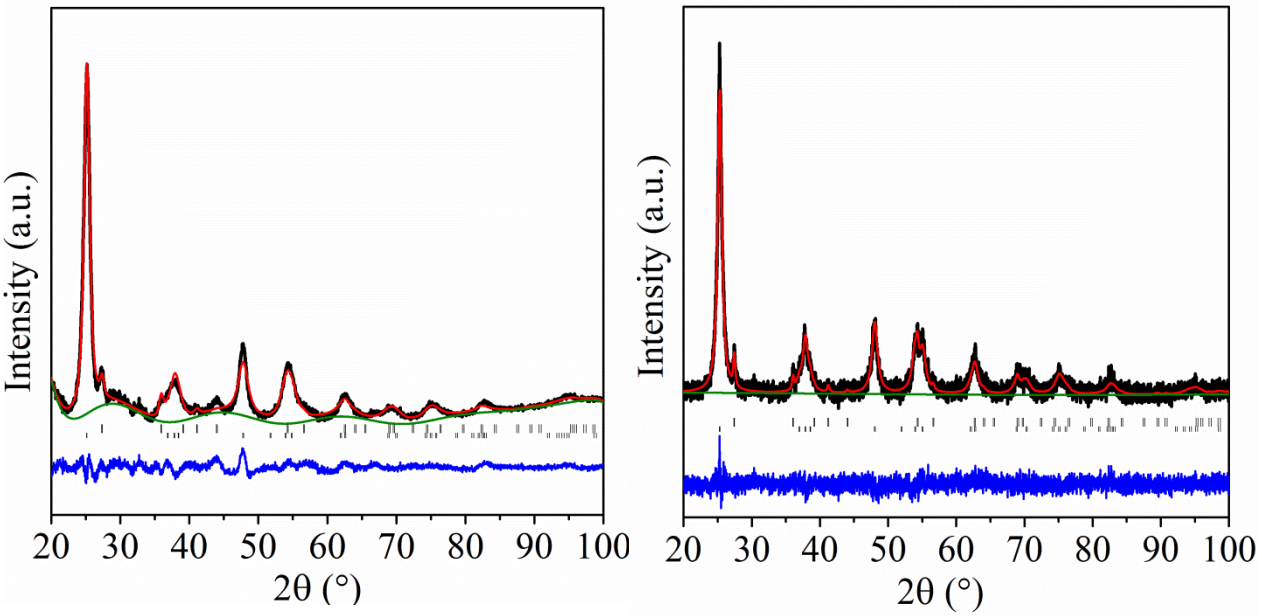

A Rietveld fit to the XRD for film (left) and powder (right) produced from sol T2-DEA and heated at 600 °C for 10 minutes (page 71).

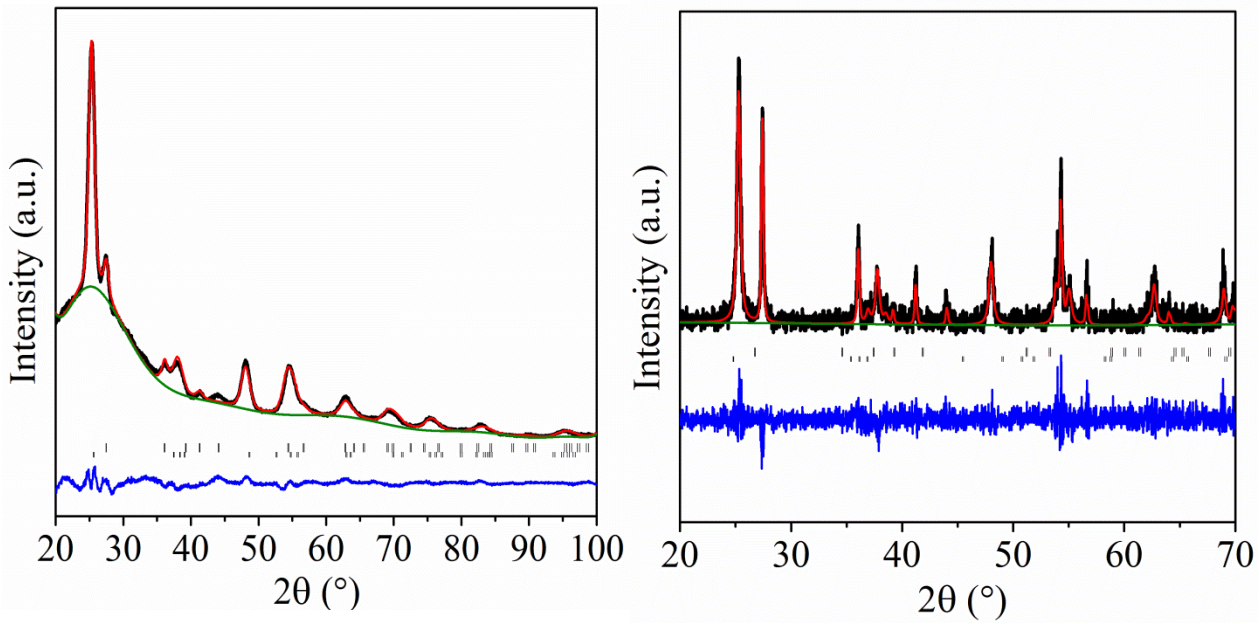

A Rietveld fit to the XRD for film (left) and powder (right) produced from sol T2-DEA and heated at 600 °C for 40 minutes (page 71).

C. T3-DEA

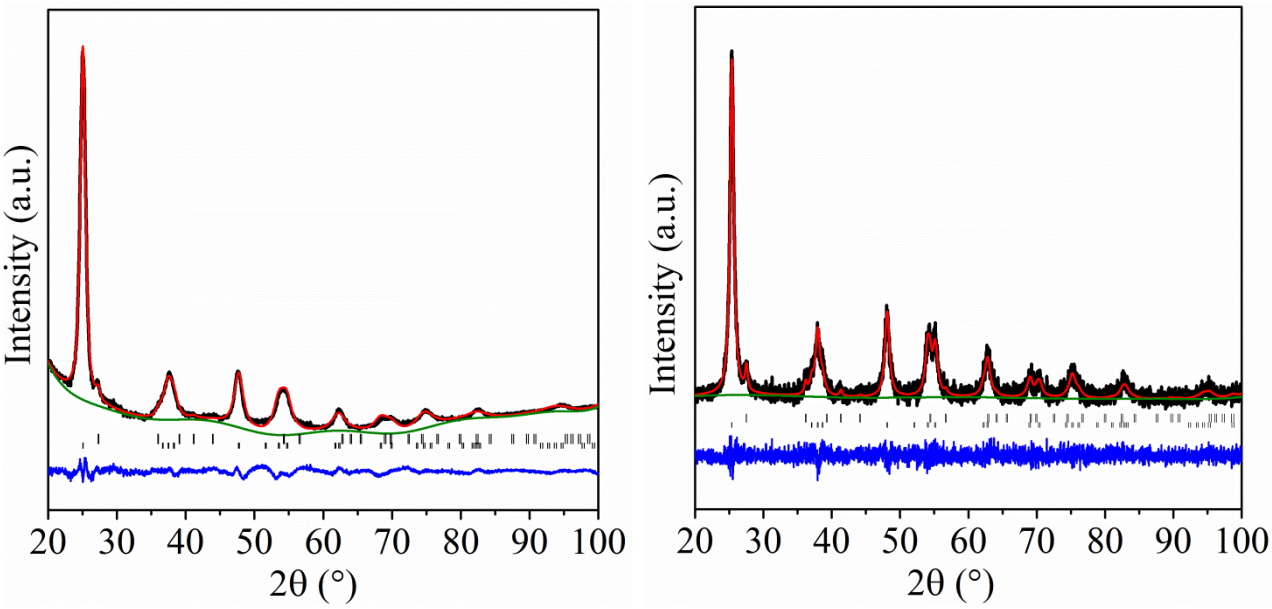

A Rietveld fit to the XRD for film (left) and powder (right) produced from sol T3-DEA and heated at 600 °C for 5 minutes (page 73).

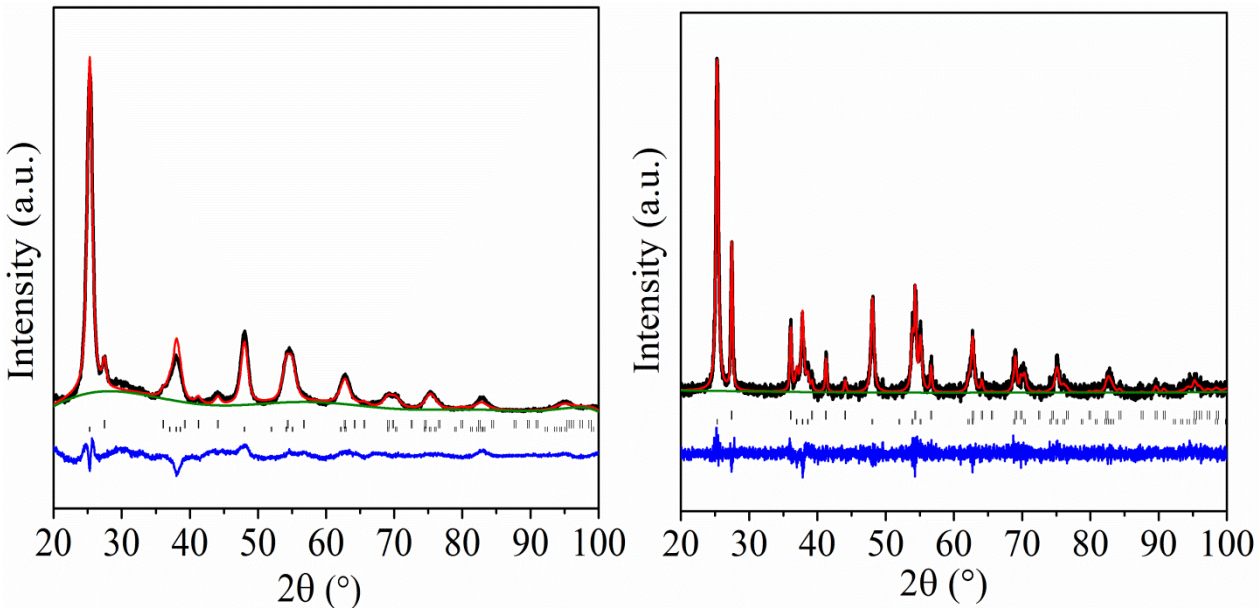

A Rietveld fit to the XRD for film (left) and powder (right) produced from sol T3-DEA and heated at 600 °C for 10 minutes (page 73).

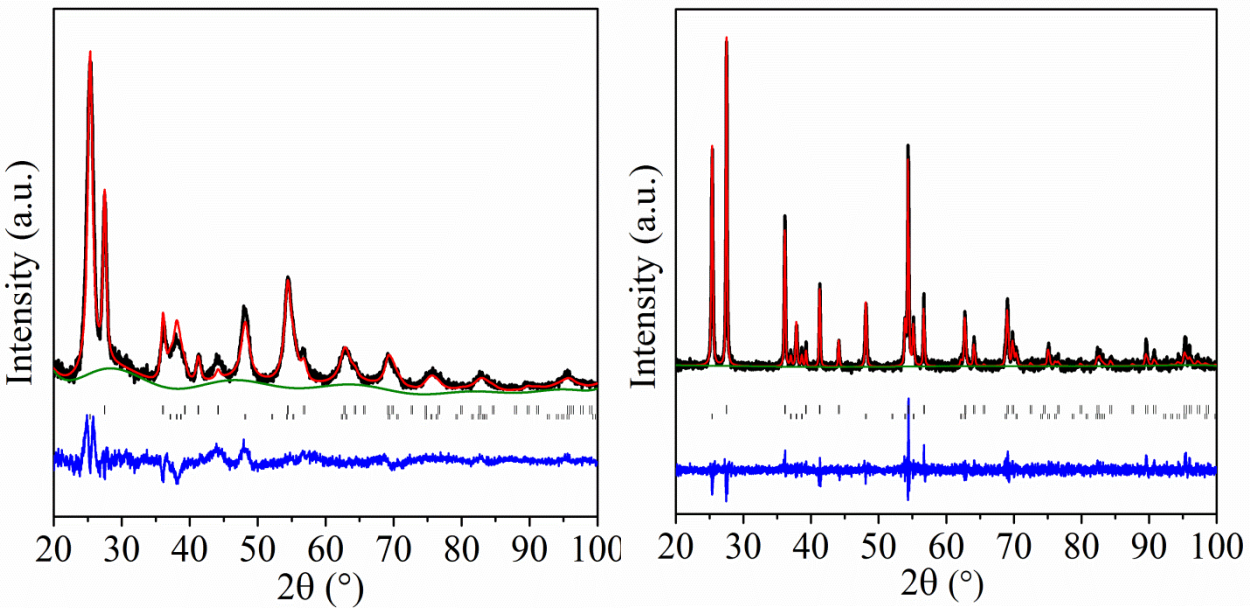

A Rietveld fit to the XRD for film (left) and powder (right) produced from sol T3-DEA and heated at 600 °C for 40 minutes (page 73).

D. T4-DEA

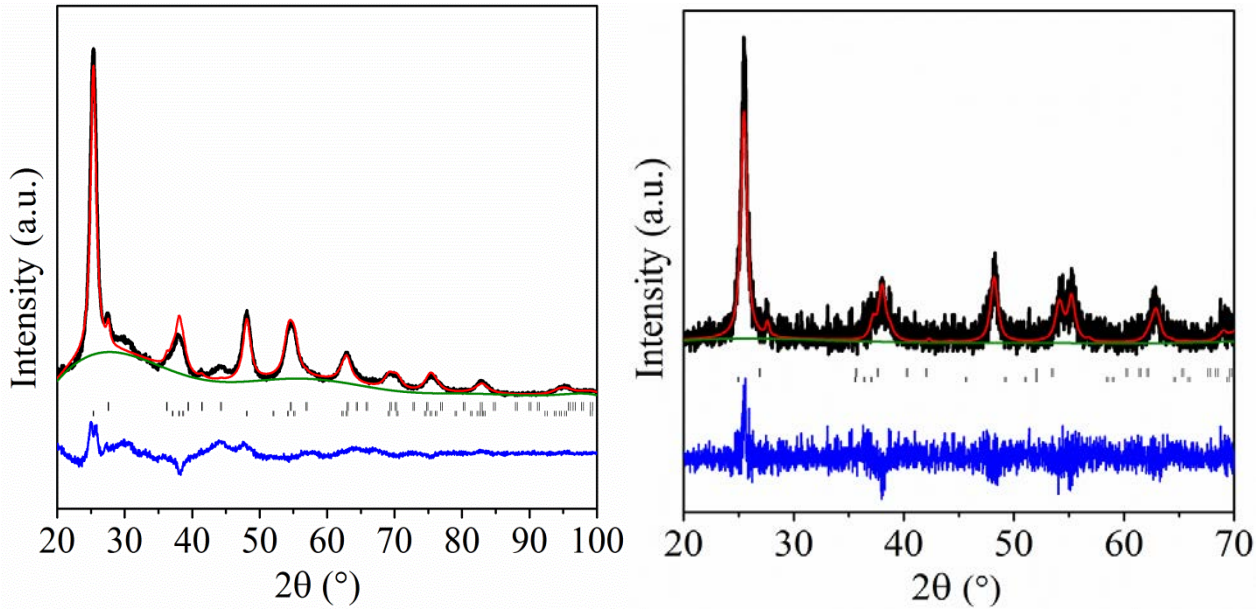

A Rietveld fit to the XRD for film (left) and powder (right) produced from sol T4-DEA and heated at 600 °C for 5 minutes.

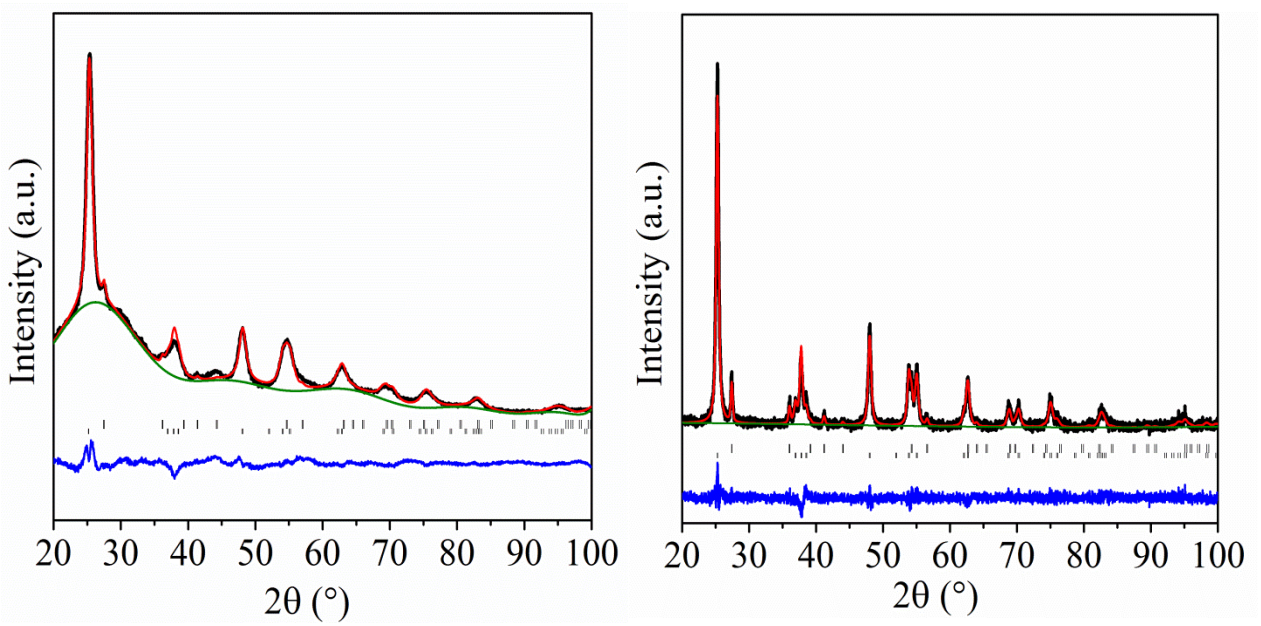

A Rietveld fit to the XRD for film (left) and powder (right) produced from sol T3-DEA and heated at 600 °C for 10 minutes.

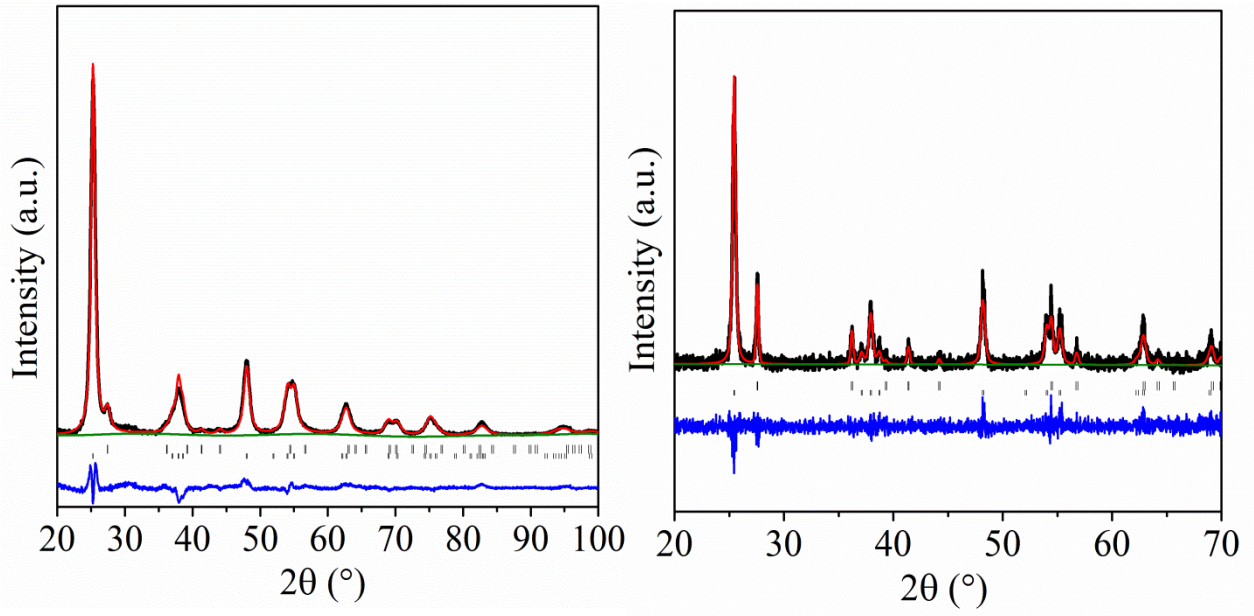

A Rietveld fit to the XRD for film (left) and powder (right) produced from sol T3-DEA heated at 600 °C for 40 minutes.

Crystallite size calculation

Crystallite size can be estimated by a Rietveld refinement method in particular related to the peak shape.

$$p = \frac{18000K\lambda}{\pi X}$$

where K is the Scherrer constant (0.891), λ is the X-ray wavelength (0.154 nm), π is 3.14 and X is the Lorentzian component value (Lx) that is extracted from a GSAS refinement.

So, for example if the Lx= 26.7

P = 18000 × 0.891 × 0.154 / 3.14 × 26.7

P = 2469.85/ 83.83

P = 29.4 nm.

Error calculation

Error can be calculated from a Rietveld refinement method specifically from liststview.

For example: if error is 0.59

So, error = 0.59 + LX

Error = 0.59 + 26.7

Error = 27.29

So LX + error = 27.29

P = 28.8 nm

The real error 29.4 – 28.82 = 0.6

Errors below 2 are written to 2 significant figures.

And therefore, the crystallite size will be 29.4 (6) nm.

Unite cell error calculation

Based on the Rietveld refinement method, the error can be calculated as:

For example: a = 3.782682 and the error value = 0.000256

So, the error will be written as 3.7827(3).